Numerical and analytical studies for stagnation point flows of Newtonian and non-Newtonian fluids

By

ABDUL REHMAN

Department of Mathematics

Quaid-i-Azam University, Islamabad

PAKISTAN

2014

Numerical and analytical studies for stagnation point flows of Newtonian and non-Newtonian fluids

By

ABDUL REHMAN

Supervised

By

DR. SOHAIL NADEEM

Department of Mathematics

Quaid-i-Azam University, Islamabad

PAKISTAN

2014

Numerical and analytical studies for stagnation point flows of Newtonian and non-Newtonian fluids

By

ABDUL REHMAN

A Dissertation Submitted in the Partial Fulfilment of the requirements for the degree of

DOCTOR OF PHILOSOPHY

IN

MATHEMATICS

Supervised By

DR. SOHAIL NADEEM

Department of Mathematics

Quaid-i-Azam University, Islamabad

PAKISTAN

2014

DEDICATION

TO ALL FRIENDS

Acknowledgement

All praises to almighty Allah, the most beneficent, the most merciful, who created this universe and gave us the idea to discover. I am highly grateful to Almighty Allah for His blessing, guidance and help in each and every step of my life.

I am grateful to my supervisor, **Dr. SohailNadeem** for his knowledgeable and valuable guidance throughout my research. His encouragement gave me strength to work with concentration. I feel honor to have him as supervisor and to have **Dr. Malik Muhammad Yousaf**my teacher.

I am also thankful to theChairman Department of Mathematics, Prof. **Dr. TasawarHayat** and Prof. **Dr. Muhammad Ayub**.

I am grateful to my dearest friends, Muhammad Zulfiqar and Muhammad Naseer. I enjoyed each day of my stay at the Quaid-i-Azam University in their company.

I also acknowledge the support of Higher Education Commission (HEC) Pakistan and the University of Balochistan, Quetta for providing me financial assistance and granting me leave.

I am also thankful to my parents, my family members and all my friends and teachers in the University of Balochistan for their continuous encouragement.
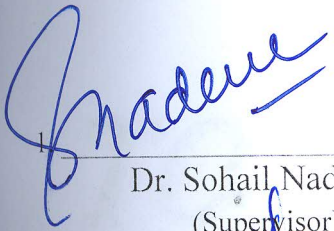
CERTIFICATE

NUMERICAL AND ANALYTICAL STUDIES FOR STAGNATION POINT FLOWS OF NEWTONIAN AND NON-NEWTONIAN FLUIDS
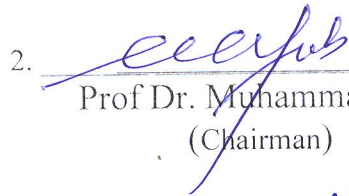
By

ABDUL REHMAN

A thesis submitted in the partial fulfillment of the requirement for the degree of doctor of philosophy
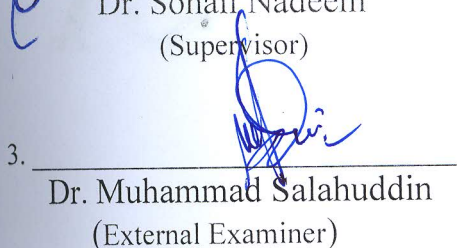
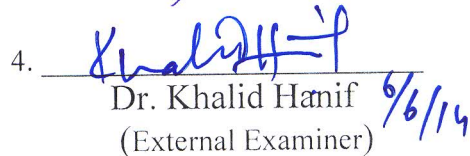**We accept this thesis as conforming to the required standard.**

Dr. Sohail Nadeem
(Supervisor)

2. Prof Dr. Muhammad Ayub
(Chairman)

3. Dr. Muhammad Salahuddin
(External Examiner)

4. Dr. Khalid Hanif 6/6/14
(External Examiner)

**Department of Mathematics
Quaid-i-Azam University, Islamabad
PAKISTAN
2014**

Contents

Chapter 0

Introduction

The study of fluid flow associated with the different physical situations has been a field of interest from the last five decades due to its extensive common applications in different daily life situations. Recently, fluid flows of viscous and non-Newtonian fluids are investigated in many important areas, like subsonic, transonic, supersonic and hypersonic flows in aerodynamics [1], food flow through human throat [2], microchannel flows [3] associated with some chemical and biological species in different microchips, hydraulic fracturing containing chemical additives [4], peristaltic flows due to contraction and expansion of arteries [5, 6], blood circulation [7] and the study of blood as a mixture of constituent components that causes cardiovascular diseases [8], fluid flow through annular regions [9], fluid flow through parallel disks [10], fluid flow through inflatable or collapsible tubes [11], fluid flow along wavy surfaces [12] and the dilatant flows [13, 14].

Stagnation points are the points where the fluid is brought to rest by the surface of the object. The concept of two dimensional fluid flow near the stagnation point was first initiated by Hiemenz [15], while the three dimensional axisymmetric stagnation flow was primarily deliberated by Homann [16]. After the initiation of [15, 16], extensive research has been carried out by various researchers because of its tremendous technological and industrial applications. Stagnation point flows are investigated for viscous or inviscid fluids [17, 18], steady or unsteady flows [19, 20], two dimensional and three dimensional geometries [21, 22], normal and oblique [23, 24] and forward or reverse [25, 26] flows. The notion is also debated for finite and infinite domain problems [27, 28]. In some cases, fluid flow is assumed to be stagnationed by a solid

wall, while in other a free stagnation point or line exist interior to the fluid domain [29].

Stagnation-point flows have numerous engineering applications. Crane et al. [26] have developed stagnation-point reverse flow (SPRF) combustors that in case of burning liquid fuels (with low emissions in gas turbines) which can be used in aircraft engines, land based power generation and marines. Craft et al. [30] have developed a new wall function that is applicable for complex turbulence flows (channel flow, axisymmetric impinging jet flow) using both linear and nonlinear turbulence models. Wang [31] have investigated the problem of axisymmetric stagnation point flow impinging on a plate that is moving in its own plane with partial slip condition on the solid boundary. Such flows are important in convective cooling processes. Renardy [32] has debated the problem of viscoelastic (Oldroyd B) fluid flowing away from a wall for both the axisymmetric and the planer cases. Weidman and Ali [33] have discussed the problem of laminar radial stagnation point flow impinging on a stretching/shrinking cylinder when the strain rates of the stagnation flow and that of the stretching cylinder are arbitrary constants. Such flows are relevant in manufacturing processes of the metallic or polymer solid cylinders. Hong and Wang [34] have presented the solutions for the problem of annular axisymmetric stagnation point flow when the inner cylindrical rod is rotating about and translating along the axial axis with constant angular and linear velocities, respectively. The fluid was also assumed to be injected with a constant velocity from the fixed outer cylinder towards the inner cylindrical rod. Such annular geometry flows are pertinent to the study of externally pressure lubricated journal bearings. They [34] have discussed the problem asymptotically for small Reynolds numbers Re, solutions for large Reynolds numbers Re, perturbation solutions for small radial gap width from the outer to the inner cylinder and the numerical solutions are also presented. They [34] also found that the injection effects were more dominant in case of the large Reynolds numbers Re and that the drag coefficient, the moment at the surface of the inner cylinder increases with the increase in the Reynolds numbers Re, while increase in the gap width decreases the drag coefficient and the moment at the surface of the inner cylinder. Ishak et al. [35] have investigated the suction/injection effects over the steady, incompressible mixed convection boundary layer flow over a vertical slender cylinder having mainstream velocity/surface wall temperature proportional to the axial distance from the stagnation point along the surface of the cylinder and concluded that the boundary layer separation was delayed by the

5

suction or curvature parameters, while injection enhances the boundary layer separation. Wang [36] has also studied the axisymmetric stagnation point flow that impinges on a moving plate with anisotropic slip condition. Such flows are relevant with the flow over super hydrophobic strips. Loc et al. [37] have observed the unsteady mixed convection boundary layer flow of a non-Newtonian micropolar fluid near the region of the stagnation point on a vertical flat plate where the time dependence is due to the impulsive motion of the free stream velocity and due to a sudden change in the surface temperature from the uniform ambient temperature. Nadeem and Rehman [38] and Nadeem et al. [39] have extended the work of [34] for viscous nanofluids and the non-Newtonian micropolar fluids, respectively. Martin and Boyd [40] have studied the Falkner-Skan boundary layer wedge flow with slip boundary condition when a modified boundary layer Knudsen number is used. Zhu et al. [41] have analyzed the hydromagnetic plane and axisymmetric stagnation point flow with velocity slip towards a stretching sheet and showed that the flow and skinfriction coefficient depend upon the velocity slip condition. Nadeem et al [42] and Rehman and Nadeem [43] have also discussed the boundary layer flow and heat transfer of viscous based nanofluids and the non-Newtonian microplar fluids flowing over a vertical slender cylinder and had shown that as a special case their results are consistent with the results obtained by Ishak et al. [35]. In another study, Nadeem et al. [44] have also presented the solutions of the problem for the boundary layer flow of a non-Newtonian second grade fluid flowing over a horizontal cylinder and have observed that the curvature parameter decreases the velocity flow rate near the surface of the cylinder.

Fluid flow over a stretching surface was initiated by Crane [45], since then the concept is studied vigorously by different researchers for stretching sheet [46, 47] and stretching cylinder [48, 49] problems due to its wide range of engineering applications. Such applications include glass blowing, paper production, metal spinning, and manufacturing of polymeric sheets [50, 51]. In many cases, the surface of the object is assumed to be stretched linearly with a velocity proportional to the distance from the stagnation point [52, 53], while in some cases nonlinear (polynomial, exponential) surface stretching velocity is also studied [54, 55]. Wong et al. [56] have analyzed the problem of boundary layer stagnation point flow over an exponentially stretching sheet. Bhallacharyya and Vajrauelu [57] have studied heat transfer analysis over the boundary layer stagnation point flow of a viscous fluid flowing over an exponentially stretching

surface. Further, Nadeem and Lee [58] have presented the nanoparticles effect over the flow of a viscous fluid flowing over a stretching surface. The work [56] was extended by Rehman et al. [59] for the case of couple stress nanofluid flowing over an exponentially stretching sheet. Jat and Chand [60] have investigated the viscous dissipation and radiation effects over the flow and heat transfer of a viscous fluid flowing over an exponentially stretching sheet that is assumed to be experiencing a uniform transverse magnetic field. Elbashbeshy et al. [61] have evaluated the suction and internal heat generation or absorption effects over the flow of an unsteady mixed convection boundary layer flow and heat transfer of a viscous fluid flowing over an exponentially stretching surface in presence of thermal radiation and magnetic field. Ishak [62] has presented the magnetohydrodynamic effects over the boundary layer flow due to an exponentially stretching sheet under the influence of thermal radiation. Pramanik [63] has examined the thermal radiation effects over the flow and heat transfer of a Casson fluid flowing over a porous surface that is stretched exponentially. Bhattacharyya [64] has obtained the solutions for the problem of boundary layer flow, heat transfer and reactive mass transfer over an exponentially stretching surface moving in an exponential free stream. In another effort, Bhattacharyya [65] has measured the problem of boundary layer flow and heat transfer over an exponentially shrinking sheet.

The notion of nanofluids was introduced by Choi [66, 67], since then the theory of nanofluids has gained much importance due to the enhanced heat transfer rate ability of these nanofluids [68]. Nanoparticle suspensions are used as coolants, lubricants and microchannel heat sinks. One of the very common model for nanofluids used also in this dissertation is the Buongiorno model that exhibits slip mechanism of the nanoparticles and the base fluid The study of non-Newtonian fluids is important and has many applications. There is no single model which exhibits all the properties of non-Newtonian fluids, therefor many models are reported and discussed by different researchers. Micropolar fluid model was proposed by Eringen [69, 70] and is capable of describing the microstructure of fluids [71, 72]. The Williamson fluid model is a pseudoplastic fluid model that has important role in the field of polymer solution and powder suspensions over a wide range of shear stresses and shear rates [73, 74]. A Casson fluid model represents shear thinning fluids that has an infinite viscosity at zero shear rate and a zero viscosity at an infinite shear rate [75-77]. Couple stress fluid model has a competency

of describing some important features of fluid such as the presence of couple stresses, body couples and a non-symmetric stress tensor that enables to study the particle size effects [78, 79]. Second grade fluid model is a simple non-Newtonian viscoelastic fluid model that can predict the influence of normal stress difference [80-82]. A third grade fluid model is also a viscoelastic fluid model that can be used to observe the effects of shear thinning/thickening [83-85].

Motivated from the above studies the purpose of the present thesis is to discuss the stagnation point flow of Newtonian and different non-Newtonian fluids flowing through annular cylindrical regions, or towards cylinder and stretching sheets and cylinders. The problems are modeled according to the physical geometries and then solved analytically and numerically. The analytical solutions are obtained through the homotopy analysis method [86-93], while the numerical solutions are obtained with the aid of the Keller-box scheme [94-96], the Runge-Kutta Fehlberg and the Shooting methods [97-100]. The chapter wise breakdown of this thesis is presented as follow:

Chapter 1 concerns with the study of axisymmetric stagnation point flow of a viscous based nanofluid flowing through the annular region between the concentric cylinders. The inner cylinder is assumed to be translating along and rotating about the axial axis with constant linear and angular velocities. The solutions of the nondimensional problem are acquired through the homotopy analysis method. A brief discussion about the effects of the skinfriction coefficient, the Nusselt numbers and the Sherwood number is also presented. Contents of the chapter are published in **Computational Mathematics and Modeling 24(2) (2013) 293-306.**

Chapter 2 contains an analysis for the problem of boundary layer stagnation point flow and heat transfer of a nanofluid flowing over a vertical slender cylinder. The problem of highly nonlinear partial differential equations is converted into a system of ordinary differential equations with the aid of similarity transformation. The resulting system is then solved the help of homotopy analysis method. The behavior of important parameters such as the curvature parameter and the natural convection parameter is debated through sketches. Contents of the chapter are published in the **Journal of Nanoengineerings and Nanosystems 226(4) (2012) 165-173.**

Chapter 3 covers an investigation for the problem of boundary layer stagnation point flow

of a viscous fluid flowing over a stretching cylinder. The surface stretching velocity of the cylinder and the fluid velocity at infinity are assumed to be exponentially proportional to the distance from the stagnation point. The outcomes of the problem are obtained by converting the partial differential equations into a system of first order ordinary differential equations and finally solved by using the block elimination procedure of the Keller-box scheme. The work is equipped with the impact of dissipation over the heat transfer and Nusselt numbers. The content of this chapter are submitted for publication in **International Journal of Heat and Mass Transfer.**

Chapter 4 provides an analysis for the problem of axisymmetric stagnation point flow of a Casson fluid flowing through porous media in a moving cylinder. Fluid is assumed to be injected with a constant injection velocity from the fixed outer cylinder towards the rotating and translating inner cylinder. The conclusions of the problem are obtained by means of the Runge-Kutta Fehlberg method. The porosity effects over the flow and heat transfer are analyzed. The work is submitted for publication in journal of **Transport in porous media.**

Chapter 5 is relevant to the study of nanoparticles effect over the micropolar fluid flow through the annular region formed between two concentric cylinders, where the outer cylinder is kept fixed while the inner cylinder is rotating about and translating along the axial axis with some constant velocities. The solutions of the problem are obtained with the aid of Runge-Kutta Shooting method. A comparison of the problem as a special case with the available literature is also presented Contents of the chapter are published in **Mathematical Problems in Engineering (2012) doi:10.1155/2012/378259.**

Chapter 6 is concerned with the problem of natural convection boundary layer stagnation point flow and heat transfer of a micropolar fluid containing nanoparticles and flowing over a vertical slender cylinder. The results of the problem are obtained through the homotopy analysis method. A detailed discussion about the behavior of different parameters over the velocity, microrotation, heat transfer and the nanoparticle concentration profiles is presented. Contents of the chapter are published in **Chines Physics Letters 29(12) (2012) 124701-5.**

Chapter 7 offers an investigation for the problem of boundary layer stagnation point flow of a nan-Newtonian Couple stress fluid flowing over an exponentially stretching sheet through porous media. The couple stress parameter and porosity effects are observed over the fluid and

heat transfer. The solutions of the problem are obtained using both the homotopy analysis method and the Runge-Kutta Fehlberg algorithm. Both the homotopy and numerical solutions are compared in tabular form. Contents of the chapter are published in the **Journal of Power Technologies 93 (2) (2013) 1–11.**

Chapter 8 contains an analysis for the problem of boundary layer stagnation point flow of a Williamson fluid flowing over an exponentially stretching cylinder. The problem of partial differential equations associated with the Williamson fluids along with the boundary conditions are simplified with the help of similarity transformations and the resulting system is then solved with the help of Runge-Kutta Fehlberg method. The chapter contains a detailed analysis for the important physical features such as the skinfriction coefficient and the local Nusselt numbers. The work is currently submitted for publication in the journal of **Computers and Fluids**.

Chapter 9 describes the study of boundary layer stagnation point flow and heat transfer of a second grade fluid flowing over a horizontal cylinder. The results of the problem are obtained through the homotopy analysis method. A brief account of the dissipation effects over the flow and heat transfer and the physical quantities like the skinfriction coefficient and the local Nusselt numbers is presented. Contents of the chapter are published in **Mathematical Problems in Engineering (2012) doi:10.1155/2012/640289.**

Chapter 10 concerns with the study of boundary layer stagnation point flow of a third grade fluid flowing over a stretching sheet. The surface stretching velocity of the sheet is assumed to be an exponential function of the distance from the stagnation point. The solutions of the problem are acquired through the Keller-box scheme and the homotopy analysis method. A comparison of both the solutions is counted in. Contents of the chapter are published in the **Brazilian Journal of Chemical Engineering 30(3) (2013) 611-618.**

Chapter 1

Axisymmetric stagnation flow of a nanofluid in a moving cylinder

1.1   Introduction

This chapter contains analysis for the steady, incompressible axisymmetric stagnation flow of viscous fluid containing nanosized particles and flowing over a moving cylinder. The fluid is assumed to be flowing through the annular region between the two concentric cylinders such that the infinite inner cylinder is translating along and rotating about the axial direction. The governing equations of conservation of mass, momentum, energy and nanoparticle concentration associated with this finite radial domain stagnation point flow problem are simplified with the aid of suitable similarity transformations. The resulting system of five dimensionless coupled ordinary differential equations is then solved analytically using the homotopy analysis method (HAM). The convergence of HAM solutions are examined through the $\hbar$ curves. A comparison of a special case of present results with the existing work is also presented. The physical features of pertinent parameters have been studied and discussed through graphs.

1.2   Formulation

Consider the stagnation point flow of viscous based nanofluid flowing through the annular region between two concentric cylinders. The outer cylinder is assumed fixed while the inner

cylinder is translating along and rotating about z axis with constant velocities. The velocity, temperature and concentration functions are of the form

$$\mathbf{V}(r,z) = (V_r(r,z), V_\theta(r,z), V_z(r,z)), \tag{1.1}$$

$$T = T(r,z), \tag{1.2}$$

$$\phi = \phi(r,z), \tag{1.3}$$

where (V_r, V_θ, V_z) are the velocity components along the (r, θ, z) axes.
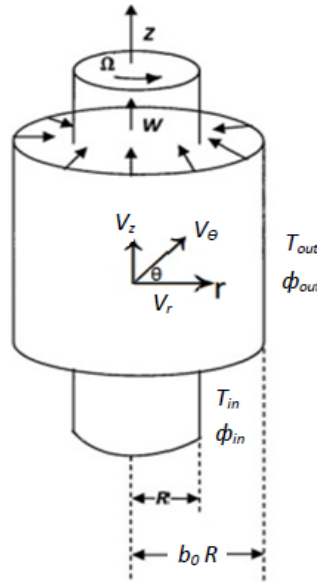
$Fig.$(1.1). Flow geometry

The inner cylinder is rotating with angular velocity Ω and translating axially with velocity W. The outer cylinder is fixed with fluid injected from the top surface of the outer cylinder towards the inner cylinder.

The inner cylinder of radius R is assumed to be translating along the axial direction with a constant velocity W and rotating about the $z-$axis with a constant angular velocity Ω, while the constant fluid injunction velocity from the outer towards the inner cylinder is U. The associated

12

boundary conditions are

$$V\left(R, z\right) = \left(0, l_0\Omega, W\right), \qquad V\left(b_0R, z\right) = \left(-U, 0, 0\right), \tag{1.4}$$

$$T\left(R, z\right) = T_{in}, \qquad T\left(b_0R, z\right) = T_{out} \tag{1.5}$$

$$\phi\left(r, z\right) = \phi_{in}, \qquad \phi\left(b_0R, z\right) = \phi_{out}, \tag{1.6}$$

where T_{in} and T_{out} are the surface temperatures, while ϕ_{in} and ϕ_{out} are the surface concentrations at the inner and outer cylinders, respectively, b_0 is the scaling parameter and l_0 is the reference length.

The governing equations of conservation of mass, momentum, energy and nanoparticle concentration are

$$\text{div } V = 0, \tag{1.7}$$

$$\rho\frac{dV}{dt} = \text{div } S, \tag{1.8}$$

$$\rho c_p\frac{dT}{dt} = -\text{div } q + \rho^* c_p^* \left(D_B \boldsymbol{\nabla}\phi \cdot \boldsymbol{\nabla}T + \frac{D_T}{T_{in}}\boldsymbol{\nabla}T \cdot \boldsymbol{\nabla}T\right), \tag{1.9}$$

$$\frac{d\phi}{dt} = D_B\boldsymbol{\nabla}^2\phi + \frac{D_T}{T_{in}}\boldsymbol{\nabla}^2T, \tag{1.10}$$

where V is the velocity profile, ρ is the density, S is the Cauchy stress tensor, c_p is the specific heat at constant pressure, T is the temperature, q is the heat flux, ρ^* is the nanoparticle mass density, c_p^* is the effective heat of the nanoparticle material, ϕ is the nanoparticle volume fraction, D_B is the Brownian diffusion coefficient and D_T is the thermophretic diffusion coefficient. The Cauchy stress tensor for viscous fluid is

$$S = -pI + \mu A_1, \tag{1.11}$$

where p is pressure, I is the unit tensor, μ is the coefficient of viscosity and A_1 is the first Rivlin Ericksen tensor and is defined as

$$A_1 = \boldsymbol{\nabla}V + \left(\boldsymbol{\nabla}V\right)^{T_1}, \tag{1.12}$$

13

in which T_1 represent the transpose.

Invoking $Eqs.\,(1.1)$, (1.2), (1.9) and (1.10), in $Eqs.\,(1.5)$ to (1.8) and neglecting the dissipation effects we get

$$r\frac{\partial V_z}{\partial z} + \frac{\partial(rV_r)}{\partial r} = 0, \tag{1.13}$$

$$V_r\frac{\partial V_r}{\partial r} + V_z\frac{\partial V_r}{\partial z} - \frac{V_\theta^2}{r} = -\frac{1}{\rho}\frac{\partial p}{\partial r} + \nu\left(\frac{\partial^2 V_r}{\partial r^2} + \frac{1}{r}\frac{\partial V_r}{\partial r} + \frac{\partial^2 V_r}{\partial z^2} - \frac{V_r}{r^2}\right), \tag{1.14}$$

$$V_r\frac{\partial V_\theta}{\partial r} + V_z\frac{\partial V_\theta}{\partial z} + \frac{V_r V_\theta}{r} = \nu\left(\frac{\partial^2 V_\theta}{\partial r^2} + \frac{1}{r}\frac{\partial V_\theta}{\partial r} + \frac{\partial^2 V_\theta}{\partial z^2} - \frac{V_\theta}{r^2}\right), \tag{1.15}$$

$$V_r\frac{\partial V_z}{\partial r} + V_z\frac{\partial V_z}{\partial z} = -\frac{1}{\rho}\frac{\partial p}{\partial z} + \nu\left(\frac{\partial^2 V_z}{\partial r^2} + \frac{1}{r}\frac{\partial V_z}{\partial r} + \frac{\partial^2 V_z}{\partial z^2}\right), \tag{1.16}$$

$$V_r\frac{\partial T}{\partial r} + V_z\frac{\partial T}{\partial z} = \alpha\left(\frac{\partial^2 T}{\partial r^2} + \frac{1}{r}\frac{\partial T}{\partial r} + \frac{\partial^2 T}{\partial z^2}\right) + \frac{\rho^* c_p^*}{\rho c_p}[D_B\left(\frac{\partial\phi}{\partial r}\frac{\partial T}{\partial r} + \frac{\partial\phi}{\partial z}\frac{\partial T}{\partial z}\right)$$
$$+\frac{D_T}{T_{in}}\left(\left(\frac{\partial T}{\partial r}\right)^2 + \left(\frac{\partial T}{\partial z}\right)^2\right)], \tag{1.17}$$

$$V_r\frac{\partial\phi}{\partial r} + V_z\frac{\partial\phi}{\partial z} = D_B\left(\frac{\partial^2\phi}{\partial r^2} + \frac{1}{r}\frac{\partial\phi}{\partial r} + \frac{\partial^2\phi}{\partial z^2}\right) + \frac{D_T}{T_{in}}\left(\frac{\partial^2 T}{\partial r^2} + \frac{1}{r}\frac{\partial T}{\partial r} + \frac{\partial^2 T}{\partial z^2}\right), \tag{1.18}$$

where ν is the kinematic viscosity and α is the thermal conductivity.

To simplify the set of above equations the following similarity transformations [34] are introduced

$$V_r = -\frac{Uf(\eta)}{\sqrt{\eta}}, \qquad V_\theta = \Omega l_0 h(\eta), \tag{1.19}$$

$$V_z = 2Uf'(\eta)\xi + Wg(\eta), \tag{1.20}$$

$$\theta = \frac{T - T_{in}}{T_{out} - T_{in}}, \quad \eta = \frac{r^2}{R^2}, \quad \xi = \frac{z}{R}, \tag{1.21}$$

$$\Psi = \frac{\phi - \phi_{in}}{\phi_{out} - \phi_{in}}. \tag{1.22}$$

With the help of transformations defined in $Eqs.\,(1.19)$ to (1.22), $Eq.\,(1.13)$ is identically satisfied while $Eqs.\,(1.14)$ to (1.18) take the following form

$$\eta f^{(IV)} + 2f''' + \text{Re}(ff''' - f'f'') = 0, \tag{1.23}$$

$$\eta g'' + g' + \text{Re}\left(fg' - f'g\right) = 0, \tag{1.24}$$

14

$$4\eta h'' + 4h' - \frac{h}{\eta} + \mathrm{Re}\left(4fh' + \frac{2fh}{\eta}\right) = 0, \tag{1.25}$$

$$\eta\theta'' + \theta' + \Pr\mathrm{Re}\, f\theta' + Nb\eta\theta'\Psi' + Nt\eta\theta'^2 = 0, \tag{1.26}$$

$$\eta\Psi'' + \Psi' + Le\Pr\mathrm{Re}\, f\Psi' + \frac{Nt}{Nb}\left(\eta\theta'' + \theta'\right) = 0, \tag{1.27}$$

in which $Re = UR/2\nu$ is the cross-flow Reynolds number, $\Pr = v/\alpha$ is the Prandtl number, $Le = \alpha/D_B$ is the Lewis number, $Nb = \rho^* c_p^* D_B\left(\phi_{out} - \phi_{in}\right)/\rho c_p \alpha$ is the Brownian motion parameter and $Nt = \rho^* c_p^* D_T\left(T_{out} - T_{in}\right)/\rho c_p \alpha T_{in}$ is the thermophoresis parameter. The boundary conditions in nondimensional form are

$$f(1) = 0, \quad f'(1) = 0, \quad f(b_0) = \sqrt{b_0}, \quad f'(b_0) = 0, \tag{1.28}$$

$$g(1) = 1, \quad g(b_0) = 0, \quad h(1) = 1, \quad h(b_0) = 0, \tag{1.29}$$

$$\theta(1) = 0, \quad \theta(b_0) = 1, \tag{1.30}$$

$$\Psi(1) = 0, \quad \Psi(b_0) = 1. \tag{1.31}$$

1.3 Solution of the problem

The solutions of the above boundary value problem presented in $Eqs.$ (1.23) to (1.31) are obtained with the help of HAM. For HAM solution we choose the initial guesses as [86, 87]

$$f_0(\eta) = \frac{\sqrt{b_0}}{b_0 - 1}\left((3b_0 - 1) - 6b_0\eta + 3\left(b_0 + 1\right)\eta^2 - 2\eta^3\right), \tag{1.32}$$

$$g_0(\eta) = \frac{b_0 - \eta}{b_0 - 1}, \quad h_0(\eta) = \frac{b_0 - \eta}{b_0 - 1}, \tag{1.33}$$

$$\theta_0(\eta) = \frac{\eta - 1}{b_0 - 1}, \quad \Psi_0(\eta) = \frac{\eta - 1}{b_0 - 1}. \tag{1.34}$$

The corresponding auxiliary linear operators are

$$L_f = \frac{d^4}{d\eta^4}, \quad L_g = \frac{d^2}{d\eta^2}, \quad L_h = \frac{d^2}{d\eta^2}, \tag{1.35}$$

$$L_\theta = \frac{d^2}{d\eta^2}, \quad L_\Psi = \frac{d^2}{d\eta^2}, \tag{1.36}$$

15

satisfying

$$L_f[c_1 + c_2\eta + c_3\eta^2 + c_4\eta^3] = 0, \tag{1.37}$$

$$L_g[c_5 + c_6\eta] = 0, \quad L_h[c_7 + c_8\eta], \tag{1.38}$$

$$L_\theta[c_9 + c_{10}\eta] = 0, \quad L_\Psi[c_{11} + c_{12}\eta] = 0, \tag{1.39}$$

where c_i $(i = 1, ..., 12)$ are arbitrary constants. The zeroth order deformation equations are

$$(1 - q) L_f[\hat{f}(\eta; q) - f_0(\eta)] = q\hbar_1 N_f[\hat{f}(\eta; q)], \tag{1.40}$$

$$(1 - q) L_g[\hat{g}(\eta; q) - g_0(\eta)] = q\hbar_2 N_g[\hat{g}(\eta; q)], \tag{1.41}$$

$$(1 - q) L_h[\hat{h}(\eta; q) - h_0(\eta)] = q\hbar_3 N_h[\hat{h}(\eta; q)], \tag{1.42}$$

$$(1 - q) L_\theta[\hat{\theta}(\eta; q) - \theta_0(\eta)] = q\hbar_4 N_\theta[\hat{\theta}(\eta; q)], \tag{1.43}$$

$$(1 - q) L_\Psi[\hat{\Psi}(\eta; q) - \Psi_0(\eta)] = q\hbar_5 N_\Psi[\hat{\Psi}(\eta; q)], \tag{1.44}$$

in which

$$N_f[\hat{f}(\eta; q)] = \eta\hat{f}^{iv} + 2\hat{f}''' + \mathrm{Re}(\hat{f}\hat{f}''' - \hat{f}'\hat{f}''), \tag{1.45}$$

$$N_g[\hat{g}(\eta; q)] = \eta\hat{g}'' + \hat{g}' + \mathrm{Re}(\hat{f}\hat{g}' - \hat{f}'\hat{g}), \tag{1.46}$$

$$N_h[\hat{h}(\eta; q)] = 4\eta^2\hat{h}'' + 4\eta\hat{h}' - \hat{h} + \mathrm{Re}(4\eta\hat{f}\hat{h}' + 2\hat{f}\hat{h}), \tag{1.47}$$

$$N_\theta[\hat{\theta}(\eta; q)] = \eta\hat{\theta}'' + \hat{\theta}' + \mathrm{Pr}\,\mathrm{Re}\,\hat{f}\hat{\theta}' + Nb\eta\hat{\theta}'\hat{\Psi}' + Nt\eta\theta'^2, \tag{1.48}$$

$$N_\Psi[\hat{\Psi}(\eta; q)] = \eta\hat{\Psi}'' + \hat{\Psi}' + Le\,\mathrm{Pr}\,\mathrm{Re}\,\hat{f}\hat{\Psi}' + \frac{Nt}{Nb}\left(\eta\hat{\theta}'' + \hat{\theta}'\right). \tag{1.49}$$

The boundary conditions for the zeroth order system are

$$\hat{f}(1; q) = 0, \quad \hat{f}'(1; q) = 0, \quad \hat{f}(b_0; q) = \sqrt{b_0}, \quad \hat{f}'(b_0; q) = 0, \tag{1.50}$$

$$\hat{g}(1; q) = 1, \quad \hat{g}(b_0; q) = 0, \quad \hat{h}(1; q) = 1, \quad \hat{h}(b_0; q) = 0, \tag{1.51}$$

$$\hat{\theta}(1; q) = 0, \quad \hat{\theta}(b_0; q) = 1, \quad \hat{\Psi}(1; q) = 0, \quad \hat{\Psi}(b_0; q) = 1. \tag{1.52}$$

The mth order deformation equations can be obtained by differentiating the zeroth-order deformation equations (1.40) to (1.44) and the boundary conditions (1.50) to (1.52), m-times with

16

respect to q, then dividing by $m!$, and finally setting $q = 0$, we get

$$L_f[f_m(\eta) - \chi_m f_{m-1}(\eta)] = \hbar_1 R_{mf}(\eta), \tag{1.53}$$

$$L_g[g_m(\eta) - \chi_m g_{m-1}(\eta)] = \hbar_2 R_{mg}(\eta), \tag{1.54}$$

$$L_h[h_m(\eta) - \chi_m h_{m-1}(\eta)] = \hbar_3 R_{mh}(\eta), \tag{1.55}$$

$$L_\theta[\theta_m(\eta) - \chi_m \theta_{m-1}(\eta)] = \hbar_4 R_{m\theta}(\eta), \tag{1.56}$$

$$L_\Psi[\Psi_m(\eta) - \chi_m \Psi_{m-1}(\eta)] = \hbar_5 R_{m\Psi}(\eta), \tag{1.57}$$

$$f_m(1) = 0, \quad f'_m(1) = 0, \quad f_m(b_0) = 0, \quad f'_m(b_0) = 0, \tag{1.58}$$

$$g_m(1) = 0, \quad g_m(b_0) = 0, \quad h_m(1) = 0, \quad h_m(b_0) = 0, \tag{1.59}$$

$$\theta_m(1) = 0, \quad \theta_m(b_0) = 0, \quad \Psi_m(1) = 0, \quad \Psi_m(b_0) = 0, \tag{1.60}$$

where

$$R_{mf}(\eta) = \eta^2 f''''_{m-1} + 2f'''_{m-1} + \operatorname{Re} \sum_{j=0}^{m}(f_j f'''_{m-1-j} - f'_j f''_{m-1-j}), \tag{1.61}$$

$$R_{mg}(\eta) = \eta g''_{m-1} + g'_{m-1} + \operatorname{Re} \sum_{j=0}^{m}(f_j g'_{m-1-j} - f'_j g_{m-1-j}), \tag{1.62}$$

$$R_{mh}(\eta) = 4\eta^2 h''_{m-1} + 4\eta h'_{m-1} - h_{m-1} + \operatorname{Re} \sum_{j=0}^{m}(4\eta f_j h'_{m-1-j} + 2f_j h_{m-1-j}), \tag{1.63}$$

$$R_{m\theta}(\eta) = \eta \theta''_{m-1} + \theta'_{m-1} + \operatorname{Pr} \operatorname{Re} \sum_{j=0}^{m} f_j \theta'_{m-1-j} + Nb\eta \sum_{j=0}^{m} \theta'_j \Psi'_{m-1-j}$$
$$+ Nt\eta \sum_{j=0}^{m} \theta'_j \theta'_{m-1-j}, \tag{1.64}$$

$$R_{m\Psi}(\eta) = \eta \Psi''_{m-1} + \Psi'_{m-1} + Le \operatorname{Pr} \operatorname{Re} \sum_{j=0}^{m} f_j \Psi'_{m-1-j} + \frac{Nt}{Nb}\left(\eta \theta''_{m-1} + \theta'_{m-1}\right), \tag{1.65}$$

$$\chi_m = \begin{cases} 0 & m \leq 1 \\ 1 & m > 1. \end{cases} \tag{1.66}$$

With the help of MATHEMATICA, the solutions of $Eqs.$ (1.23) to (1.27) subject to the boundary conditions (1.28) to (1.31) can be written as

$$f(\eta) = \lim_{Q\to\infty} [\sum_{m=1}^{Q} f_m(\eta)], \quad g(\eta) = \lim_{Q\to\infty} [\sum_{m=1}^{Q} g_m(\eta)], \tag{1.67}$$

$$h(\eta) = \lim_{Q\to\infty} [\sum_{m=1}^{Q} h_m(\eta)], \quad \theta(\eta) = \lim_{Q\to\infty} [\sum_{m=1}^{Q} \theta_m(\eta)], \tag{1.68}$$

$$\Psi(\eta) = \lim_{Q\to\infty} [\sum_{m=1}^{Q} \Psi_m(\eta)], \tag{1.69}$$

where

$$f_m(\eta) = f_m^*(\eta) + C_1 + C_2\eta + C_3\eta^2 + C_4\eta^3, \tag{1.70}$$

$$g_m(\eta) = g_m^*(\eta) + C_5 + C_6\eta, \quad h_m(\eta) = h_m^*(\eta) + C_7 + C_8\eta, \tag{1.71}$$

$$\theta_m(\eta) = \theta_m^*(\eta) + C_9 + C_{10}\eta, \quad \Psi_m(\eta) = \Psi_m^*(\eta) + C_{11} + C_{12}\eta. \tag{1.72}$$

In which $f_m^*(\eta), g_m^*(\eta), h_m^*(\eta), \theta_m^*(\eta)$ and $\Psi_m^*(\eta)$, are the special solutions, and can be stated as

$$f_m(\eta) = \sum_{n=1}^{\infty} a_{mn}\eta^{4n+3}, \quad g_m(\eta) = \sum_{n=1}^{\infty} b_{mn}\eta^{4n+1}, \tag{1.73}$$

$$h_m(\eta) = \sum_{n=1}^{\infty} c_{mn}\eta^{4n+1}, \tag{1.74}$$

$$\theta_m(\eta) = \sum_{n=1}^{\infty} d_{mn}\eta^{4n+1}, \quad \Psi_m(\eta) = \sum_{n=1}^{\infty} e_{mn}\eta^{4n+1}, \tag{1.75}$$

where, $a_{mn}, b_{mn}, c_{mn}, d_{mn}, e_{mn}$ are the arbitrary constants.

1.4 Results and discussion

The solutions of the problem of nanofluid flow through the annular region between the two concentric cylinders are obtained through the homotopy analysis method (HAM). The convergence of the solutions associated with the non-dimensional velocities, temperature and nanoparticle concentration functions are examined through the convergence curves in $Figs.$ (1.2) to (1.6).

$Fig.$ (1.2) shows the convergence region for the non-dimensional radial velocity profile f plotted for different values of the Reynolds number Re. From the figure, increase in Reynolds number Re decreases the convergence region for f. The acceptable convergence region when Reynolds number Re $= 2$ is $-0.6 \leq \hbar_1 \leq -0.2$. $Figs.$ (1.3) and (1.4) contain the $\hbar$ curves for non-dimensional velocity profiles g and h graphed for different values of the Reynolds number Re. From $Fig.$ (1.3) acceptable convergence region for velocity profile g when Reynolds number Re $= 3$ is $-0.8 \leq \hbar_2 \leq -0.2$. $Fig.$ (1.5) is plotted to observe the convergence regions associated with the non-dimensional temperature profile θ for different values of the Prandtl number Pr at the 15$^{\text{th}}$ order of approximation. From $Fig.$ (1.5) with Prandtl number Pr $= 1$, the acceptable convergence region is $-0.9 \leq \hbar_4 \leq -0.3$.

The behavior of non-dimensional velocities, temperature and nanoparticle concentration profiles f, g, h, θ and ψ are graphed in $Figs.$ (1.6) to (1.17) for different values of the Reynolds number Re, the Prandtl number Pr, the Brownian motion parameter Nb, the thermophoresis parameter Nt and the Lewis number Le. $Fig.$ (1.6) displays the influence of radial velocity profile f and the velocity gradient f' graphed for different values of the Reynolds number Re. From the figure it is observed that increase in the Reynolds number Re increases the velocity profile f. This increase in the radial velocity profile f reveals the fact that higher Reynolds number Re corresponds to higher radial injection fluid velocity from outer towards the inner cylinder that bring increase in the fluid radial velocity. $Fig.$ (1.7) gives the impact of axial velocity profile g for different values of the Reynolds number Re. From the sketch it is noted that increase in the Reynolds number Re increases the velocity profile g. The behavior of Reynolds number Re over the velocity profile h is presented in $Fig.$ (1.8). From the plot it is observed that increase in the Reynolds number Re decreases the velocity profile h. The impact of Reynolds number Re over the temperature flow function θ is sketched in $Fig.$ (1.9). From the figure it is noticed that increase in the Reynolds number Re increases the temperature profile θ. $Fig.$ (1.10) gives the impact of Prandtl number Pr over the temperature profile θ. From the graph, increase in the Prandtl number Pr increases the temperature flow rate θ. $Fig.$ (1.11) provides the influence of Brownian motion parameter Nb over the temperature profile θ. From the figure it is observed that increase in the Brownian motion parameter Nb increases the temperature function θ. $Fig.$ (1.12) shows the impact of thermophoresis parameter Nt over the temperature profile

θ. From the sketch it is noted that increase in the thermophoresis parameter Nt increases the temperature flow θ because of the fact that increase in the thermophoresis parameter Nt tends to warm the boundary layer fluid near the surface of the cylinder that enhances the temperature difference and hence increase the temperature flow rate θ. The influence of Reynolds number Re over the nanoparticle concentration profile ψ is graphed in $Fig.\,(1.13)$. The observed behavior of ψ is increasing with increase in Re. $Fig.\,(1.14)$ gives the impact of Prandtl number Pr over the nanoparticle concentration function ψ. The observed behavior in $Fig.\,(1.14)$ is increasing with increase in the Prandtl number Pr. The influence of Lewis number Le over the nanoparticle concentration function ψ is shown in $Fig.\,(1.15)$. From the graph it is observed that increase in the Lewis number Le increases the nanoparticle concentration function ψ. The impact of Brownian motion parameter Nb over the nanoparticle concentration profile ψ is presented in $Fig.\,(1.16)$. From the plot it is noted that increase in the Brownian motion parameter Nb increases nanoparticle concentration function ψ. $Fig.\,(1.17)$ shows the behavior of thermophoresis parameter Nt over the nanoparticle concentration function ψ. From the figure, increase in the thermophoresis parameter Nt decreases the nanoparticle concentration function ψ.

$Table.\,(1.1)$ shows a comparison of the behavior of boundary derivatives for velocity profiles with the available work of Wang [34] for different values of the Reynolds number Re. Entries in $Table.\,(1.1)$ also gives an insight for the behavior of shear stress at the surface corresponding to the skinfriction coefficient for different values of the Reynolds number Re. From the table it is noted that both the results are in good agreement. It is also observed that increase in the Reynolds number Re increases the skinfriction coefficient. $Table.\,(1.2)$ shows the boundary derivatives for temperature profile θ at the surface of the inner cylinder for different values of the Prandtl number Pr and the Brownian motion parameter Nb also corresponding to the heat flux at the surface and the Nusselt numbers. From the table it is observed that increase in both the Prandtl number Pr and the Brownian motion parameter Nb increases the Nusselt numbers. $Table.\,(1.3)$ gives the entries for the boundary derivatives of the nanoparticle concentration profile at the surface of the inner cylinder that corresponds to the Sherwood numbers tabulated for different values of the Lewis number Le and the thermophoresis parameter Nt. From the table, increase in the thermophoresis parameter Nt decreases the Sherwood number.
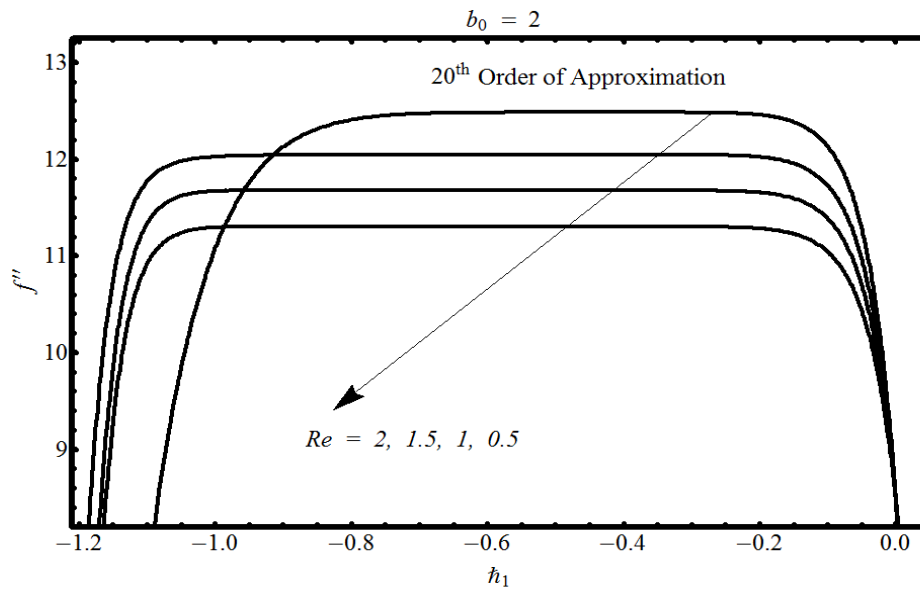
$Fig.(1.2)$. $\hbar$-curves for the velocity profile f for different values of the Reynolds number Re
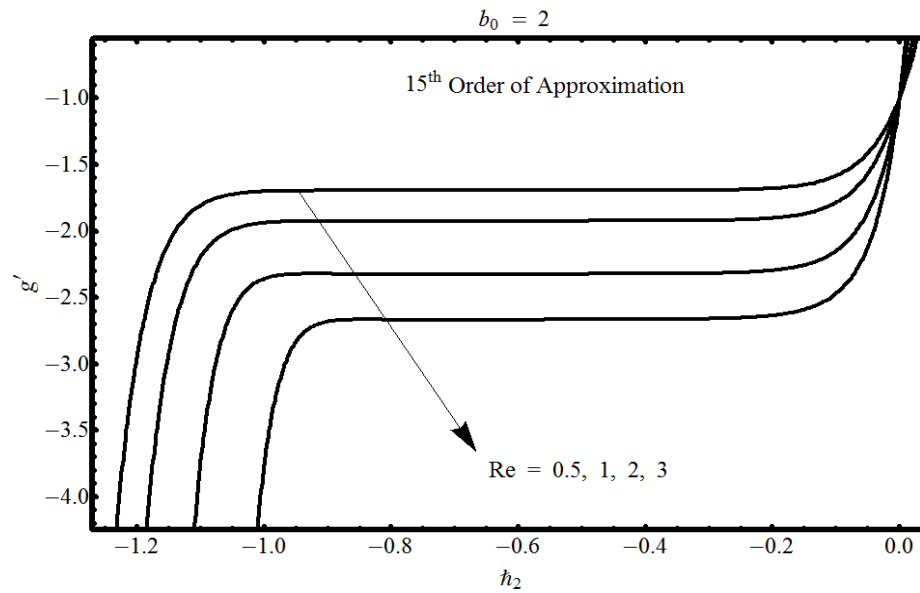
$Fig.(1.3)$. $\hbar$-curves for the velocity profile g for different values of the Reynolds number Re
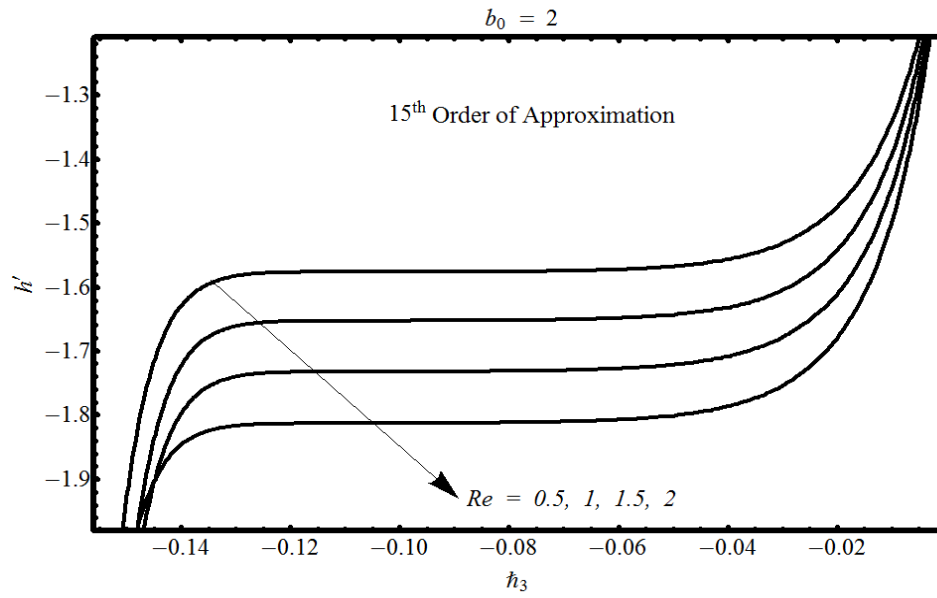
$Fig.(1.4)$. $\hbar$-curves for the velocity profile h for different values of the
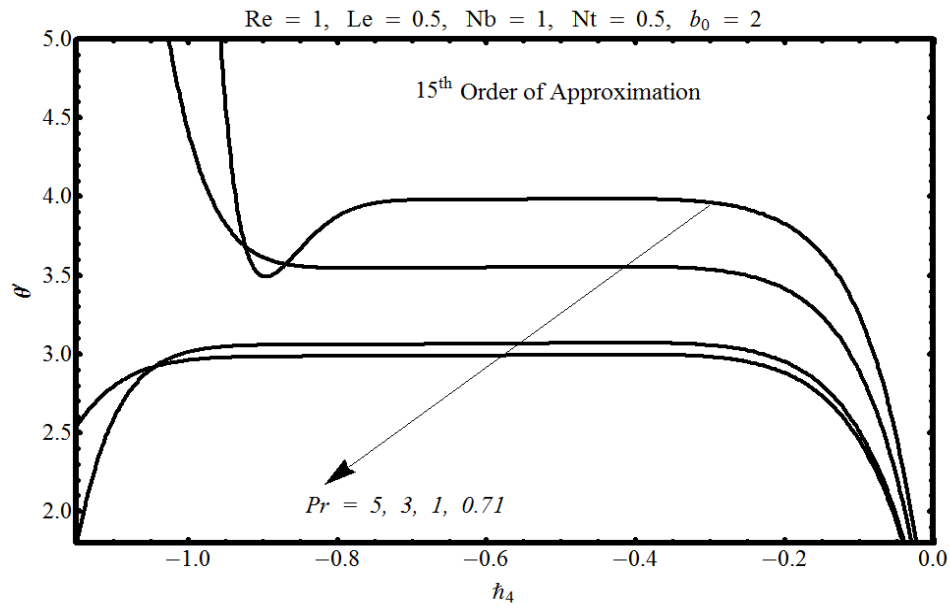
Reynolds number Re

$Fig.(1.5)$. $\hbar$-curves for the temperature profile θ for different values of the

Prandtl number Pr

$b_0 = 2$

$f'(\eta)$
$Re = 5, 2, 0.5$

$f(\eta)$
$Re = 5, 2, 0.5$
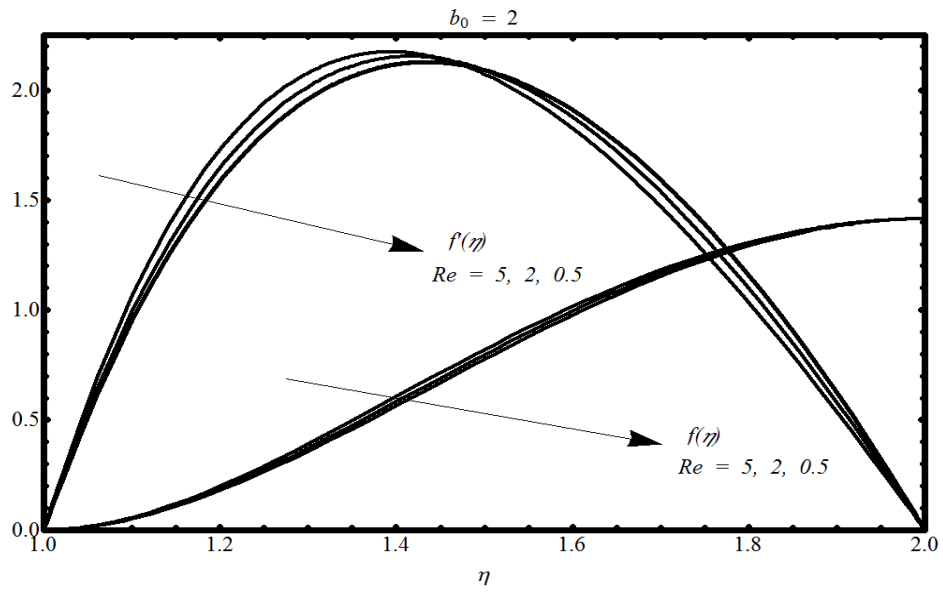
$Fig.(1.6)$. Influence of the Reynolds number Re over the velocity profile f
and the velocity gradient f'

$b_0 = 2$

$Re = 8, 4, 2, 0.5$
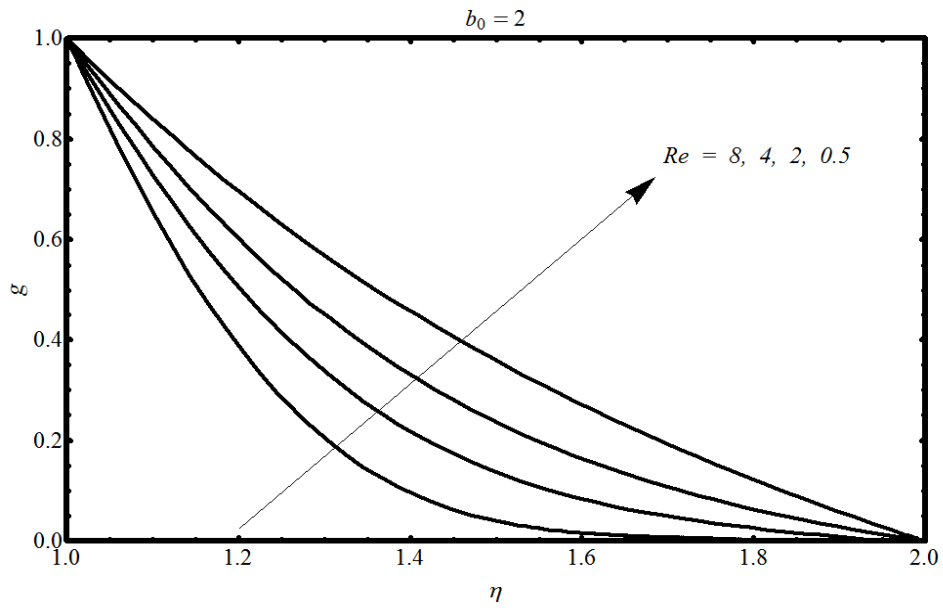
$Fig.(1.7)$. Influence of the Reynolds number Re over the velocity profile g

23
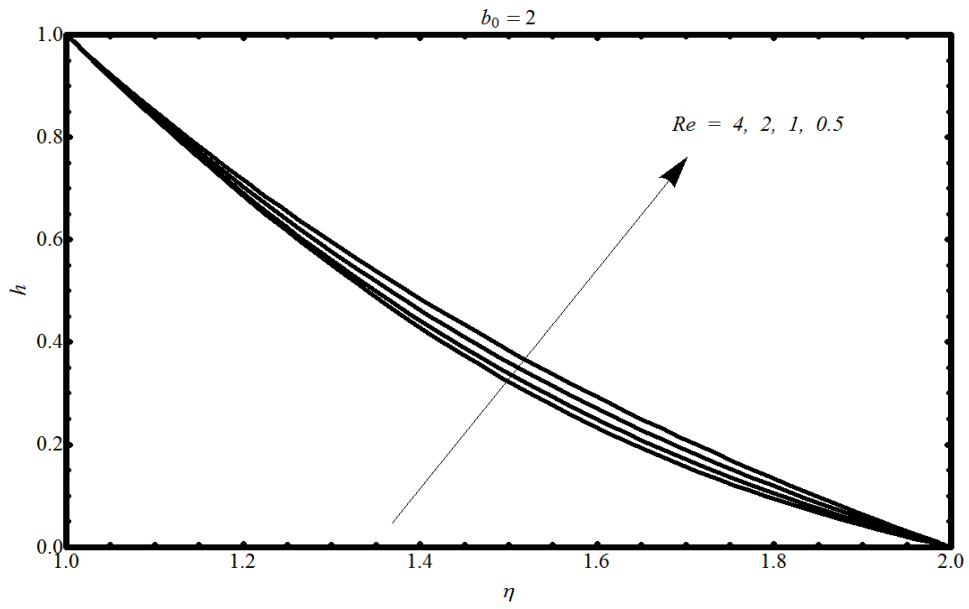
$Fig.(1.8)$. Influence of the Reynolds number Re over the velocity profile h
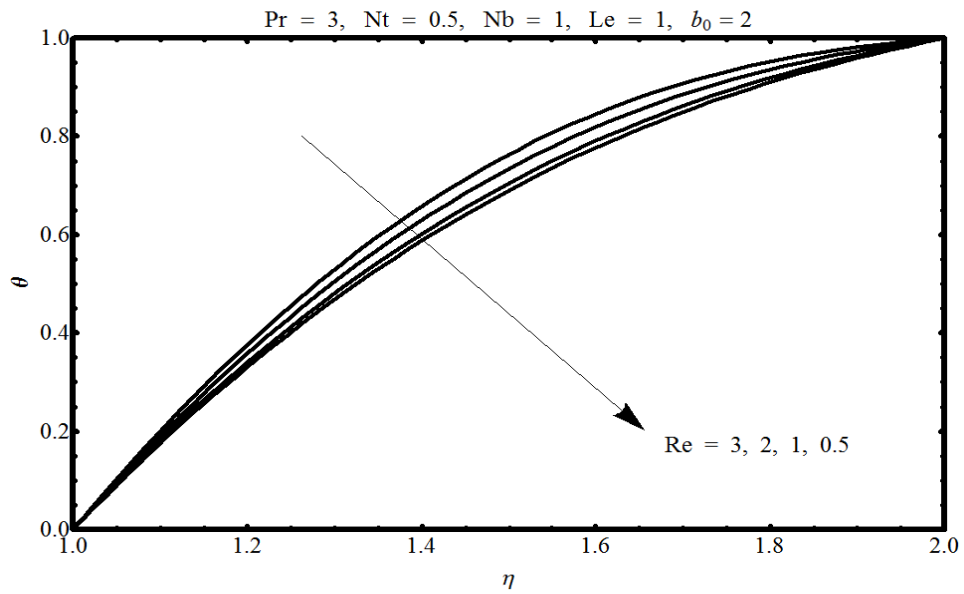
$Fig.(1.9)$. Influence of the Reynolds number Re over the temperature profile θ
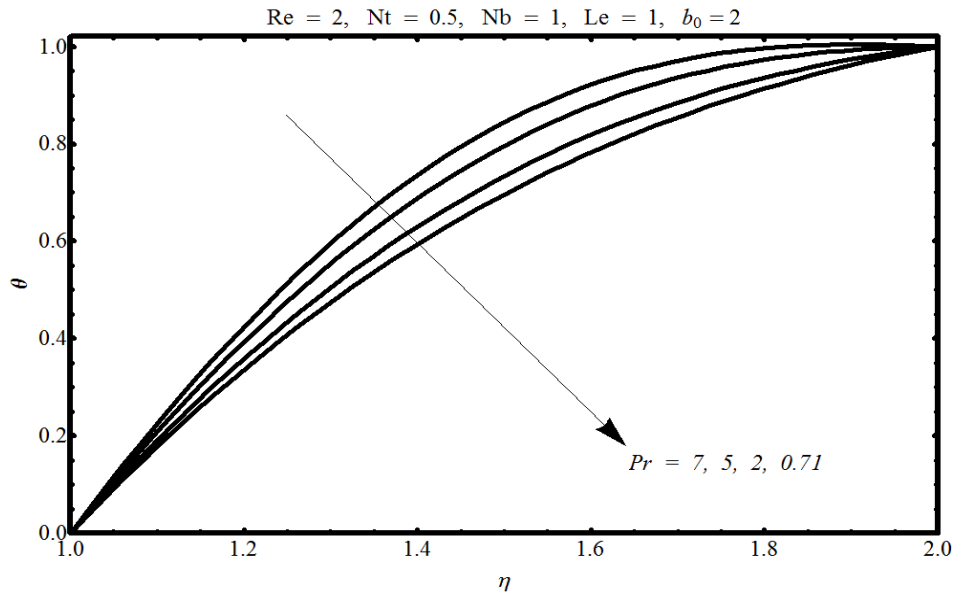
$Fig.(1.10)$. Influence of the Prandtl number Pr over the temperature profile
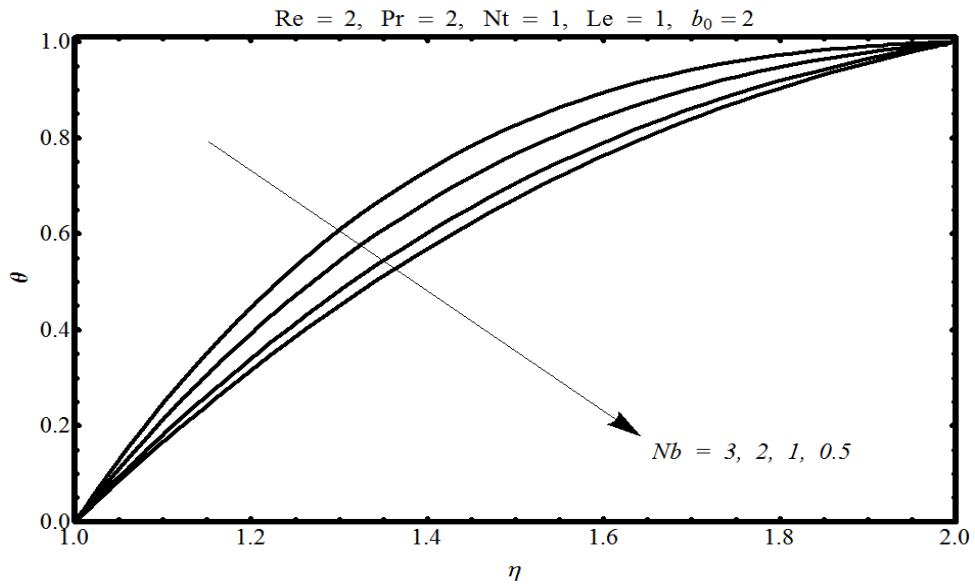
θ

$Fig.(1.11)$. Influence of the Brownian motion parameter Nb over the
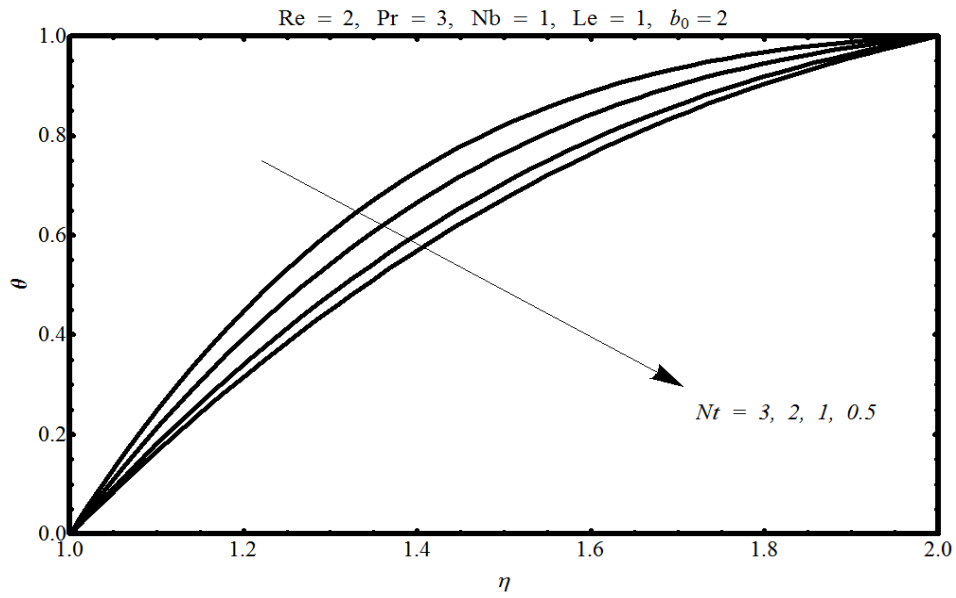
temperature profile θ

Re = 2, Pr = 3, Nb = 1, Le = 1, $b_0 = 2$

$Nt = 3, 2, 1, 0.5$

$Fig.$(1.12). Influence of the thermophoresis parameter Nt over the

temperature profile θ

Pr = 3, Nt = 0.5, Nb = 1, Le = 1, $b_0 = 2$

$Re = 0.5, 2, 4, 8$
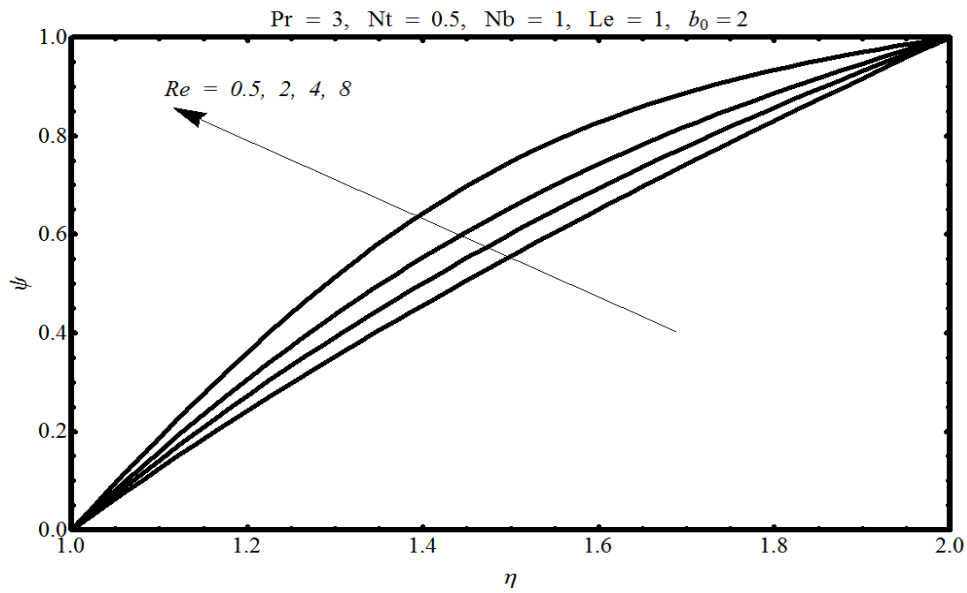
$Fig.$(1.13). Influence of the Reynolds number Re over the nanoparticle

concentration profile ψ

26
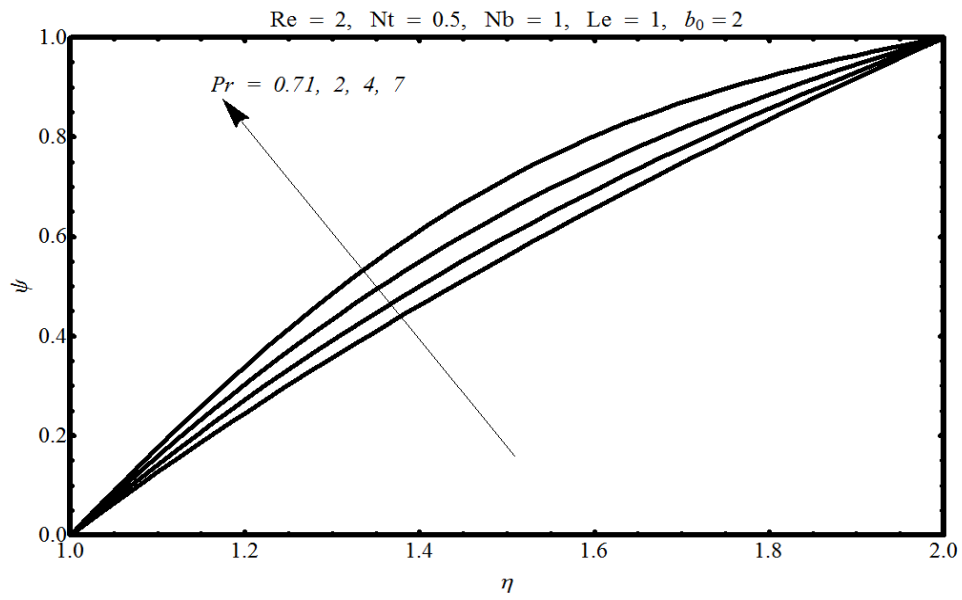
$Fig.$(1.14). Influence of the Prandtl number Pr over the nanoparticle
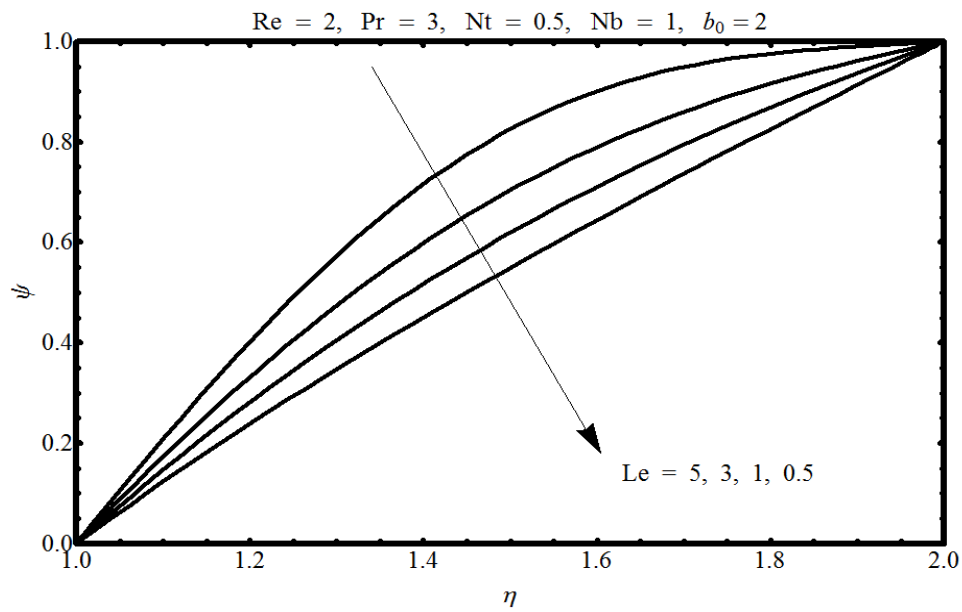
concentration ψ

$Fig.$(1.15). Influence of the Lewis number Le over the nanoparticle

concentration profile ψ
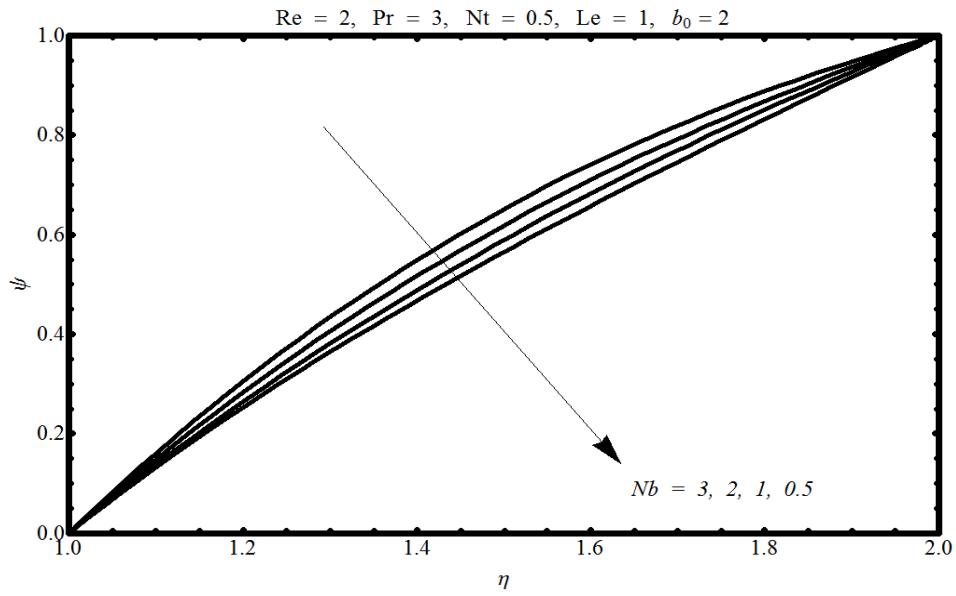
$Fig.(1.16)$. Influence of the Brownian motion parameter Nb over the nanoparticle concentration profile ψ
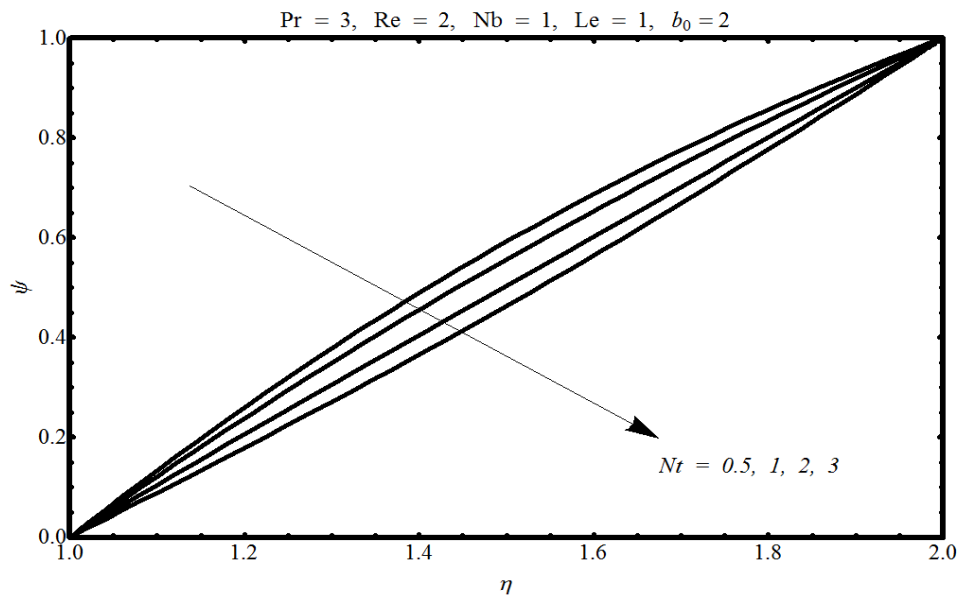
$Fig.(1.17)$. Influence of the thermophoresis parameter Nt over the nanoparticle concentration profile ψ

	$f''(1)$		$-f'''(1)$		$-g'(1)$		$-h'(1)$	
Re	Present	[34]	Present	[34]	Present	[34]	Present	[34]
0.5	11.3031		38.3226		1.6992		1.5766	
1	11.6772	11.6772	41.0797	41.0797	1.9309	1.9309	1.6554	1.6554
2	12.4123		46.6925		2.3373		1.8179	
3	13.1278		52.4104		2.6873		19837	
5	14.4942		64.0538		3.2745		2.3132	
10	17.5348	17.5348	93.5670	93.5670	4.3856	4.3856	3.0517	3.0517

$Table.(1.1)$. Behavior of Reynolds number Re over velocity profiles and comparison with wang [34] when $b_0 = 2$

	$\theta'(1)$				
$Pr\backslash Nb$	0.5	1	1.5	2	3
0.2	2.5329	3.0719	3.6597	4.2890	5.6425
0.71	3.1199	3.7435	4.4192	5.1396	6.6845
2	4.2742	5.0851	5.9606	6.8921	8.8889
5	5.9432	7.0670	8.2805	9.5720	12.3415
7	6.7049	7.9755	9.3479	10.8086	13.9413
10	7.6072	9.0515	10.6118	12.2726	15.8349

$Table.(1.2)$. Behavior of Prandtl number Pr and Brownian motion parameter Nb over the temperature profile θ when $Re = 5$, $Nt = 0.5$, $Le = 0.5$ and $b_0 = 2$

	$\psi'(1)$				
$Le\backslash Nt$	0	0.5	1	1.5	2
0.25	2.1439	0.3402	-2.1188	-5.3095	-9.3019
0.5	2.7029	0.8312	-1.8413	-5.4380	-10.0707
1	3.4842	1.5279	-1.4369	-5.6110	-11.1754
1.5	4.0336	2.0224	-1.1345	-5.7001	-11.9128
2	4.4683	2.4169	-0.8811	-5.7420	-12.4548
5	6.1551	3.9772	0.2303		
10	7.8124	5.5507			

$Table.(1.3)$. Behavior of Lewis number Le and thermophoresis parameter Nt over the temperature profile ψ when $Re = 5$, $Pr = 3$, $Nb = 1$ and $b_0 = 2$

1.5   Conclusion

The main conclusions obtained from the above study are

- With increase in the Reynolds number Re, the velocity profile f increases.

- With increase in the Reynolds number Re, the velocity profile g decreases.

- With increase in the Reynolds number Re, the velocity profile h decreases.

- The nondimensional temperature profile θ increases with the increase in the Reynolds number Re, the Prandtl number Pr, the Brownian motion parameter Nb and the thermophoresis parameter Nt.

- The nondimensional nanoparticle concentration profile ψ increases with the increase in the Reynolds number Re, the Prandtl number Pr, the Lewis number Le and the Brownian motion parameter Nb.

- The nanoparticle concentration profile ψ decreases with the increase in the thermophoresis parameter Nt.

- The shear stress at the surface of the inner cylinder increases with increase in the Reynolds number Re .

- The heat flux at the surface of the inner cylinder increases with increase in the Prandtl number Pr .

- The Sherwood number at the surface of the inner cylinder increases with increase in the Lewis number Le.

Chapter 2

Boundary layer stagnation flow and heat transfer of a nanofluid over a vertical slender cylinder

2.1 Introduction

In this chapter a study of the boundary layer stagnation flow and heat transfer of a nanofluid over a vertical slender cylinder is presented. The governing equations of motion, energy and nanoparticles are simplified by applying appropriate boundary layer approximations and then the system is converted to a nondimensional one by using suitable similarity transformations. The resulting system of three nondimensional coupled ordinary differential equations is solved by using the homotopy analysis method (HAM). At the end the physical behavior of different parameters involved in the system are discussed.

2.2 Formulation

Consider an incompressible flow of a nanofluid along a vertical permeable slender cylinder of radius r_0 having uniform ambient temperature T_∞. The coordinates (x, r) are used such that x is along the surface of the cylinder while r is in the radial direction. The velocity, temperature

and the nanoparticle concentration profiles are of the form

$$\mathbf{V}(x,r) = (w(x,r),0,u(x,r)), \quad T = T(x,r), \tag{2.1}$$

$$\phi = \phi(x,r), \tag{2.2}$$

where (w,u) are the velocity components along the (r,x) axes. The related boundary conditions are

$$\text{at } r = r_0, \quad u = 0, \quad \text{for } r \to \infty, \quad u = U_\infty(x/l), \tag{2.3}$$

$$\text{at } r = r_0, \; T = T_w(x), \quad \text{for } r \to \infty, \; T \to T_\infty, \tag{2.4}$$

$$\text{at } r = r_0, \; \phi = \phi_w(x), \quad \text{for } r \to \infty, \; \phi \to \phi_\infty, \tag{2.5}$$

where $U_\infty(x/l)$ is the mainstream velocity, T_w and T_∞ are the surface temperatures and the fluid temperature at infinity, while ϕ_w and ϕ_∞ are the nanoparticle concentration at the surface of the cylinder and the nanoparticle concentration of the fluid at infinity, respectively. The characteristic temperature ΔT and the characteristic nanoparticle concentration $\Delta\phi$ are calculated from the relations $T_w - T_\infty = (x/l)\,\Delta T$ and $\phi_w - \phi_\infty = (x/l)\,\Delta\phi$, where l is the reference length.

The governing equations of conservation of mass, momentum, energy and nanoparticle concentration are

$$\text{div}\,\mathbf{V} = \mathbf{0}, \tag{2.6}$$

$$\rho\frac{d\mathbf{V}}{dt} = \text{div}\,\mathbf{S} + \rho\tilde{\mathbf{g}}, \tag{2.7}$$

$$\rho c_p\frac{dT}{dt} = -\,\text{div}\,\mathbf{q} + \rho^*c_p^*\left(D_B\boldsymbol{\nabla}\phi\cdot\boldsymbol{\nabla}T + \frac{D_T}{T_\infty}\boldsymbol{\nabla}T\cdot\boldsymbol{\nabla}T\right), \tag{2.8}$$

$$\frac{d\phi}{dt} = D_B\boldsymbol{\nabla}^2\phi + \frac{D_T}{T_\infty}\boldsymbol{\nabla}^2T, \tag{2.9}$$

where $\tilde{\mathbf{g}}$ is the body force, c_p is the specific heat at constant pressure, T is the temperature, $\mathbf{q}$ is the heat flux, ρ^* is the nanoparticle mass density, c_p^* is the effective heat of the nanoparticle material, ϕ is the nanoparticle volume fraction, D_B is the Brownian diffusion coefficient and D_T is the thermophretic diffusion coefficient, while the Cauchy stress tensor $\mathbf{S}$ is defined in

Eq. (1.11).

The boundary layer equations of conservation of mass, momentum, heat transfer and the nanoparticle concentration profiles are

$$(rw)_r + ru_x = 0, \tag{2.10}$$

$$uu_x + wu_r = -\frac{1}{\rho}\frac{\partial p}{\partial x} + \nu(u_{rr} + \frac{1}{r}u_r) + [\frac{(\rho^* - \rho)(\phi - \phi_\infty)}{\rho} + (1 - \phi_\infty)(T - T_\infty)\beta_{th}]g_{gr}, \tag{2.11}$$

$$wT_r + uT_x = \alpha(T_{rr} + \frac{1}{r}T_r) + \frac{\rho^* c_p^*}{\rho c_p}[D_B \phi_r T_r + \frac{D_T}{T_\infty}T_r^2], \tag{2.12}$$

$$w\phi_r + u\phi_x = D_B(\phi_{rr} + \frac{1}{r}\phi_r) + \frac{D_T}{T_\infty}(T_{rr} + \frac{1}{r}T_r), \tag{2.13}$$

where p is the pressure, ν is the kinematic viscosity, β_{th} is the coefficient of thermal expansion, g_{gr} is the gravitational acceleration and α is the thermal diffusivity. Defining the following similarity transformations and nondimensional variables [42]

$$u = U_\infty(x/l)F'(\eta), \quad w = -\frac{r_0}{r}(\frac{\nu U_\infty}{l})^{1/2}F(\eta), \tag{2.14}$$

$$\theta = \frac{T - T_\infty}{T_w - T_\infty}, \quad \eta = \frac{r^2 - r_0^2}{2r_0}(\frac{U_\infty}{\nu l})^{1/2}, \tag{2.15}$$

$$\Psi = \frac{\phi - \phi_\infty}{\phi_w - \phi_\infty}. \tag{2.16}$$

With the help of above transformations, *Eq.* (2.10) is identically satisfied and *Eqs.* (2.11) to (2.13) take the following form

$$(1 + 2\gamma_c\eta)F''' + 2\gamma_c F'' + 1 + FF'' - F'^2 + \lambda_N(1 - \phi_\infty)(\theta + N_r\Psi) = 0, \tag{2.17}$$

$$(1 + 2\gamma_c\eta)\theta'' + 2\gamma_c\theta' + \Pr(F\theta' - F'\theta) + (1 + 2\gamma_c\eta)(B_P\theta'\Psi' + T_P\theta'^2) = 0, \tag{2.18}$$

$$(1 + 2\gamma_c\eta)\Psi'' + 2\gamma_c\Psi' + Le\Pr(F\Psi' - F'\Psi) + \frac{T_P}{B_P}[(1 + 2\gamma_c\eta)\theta'' + 2\gamma_c\theta'] = 0, \tag{2.19}$$

in which $\Pr = \nu/\alpha$ is the Prandtl number, $\gamma_c = (\nu l/U_\infty a^2)^{1/2}$ is the curvature parameter, $\lambda_N = g_{gr}\beta_{th}l\Delta T/U_\infty^2$ is the natural convection parameter, $N_r = (\rho^* - \rho)(\phi_w - \phi_\infty)/\rho\beta_{th}(T_w - T_\infty)(1 - \phi_\infty)$ is the buoyancy ratio, $B_P = \rho^* c_p^* D_B(\phi_w - \phi_\infty)/\rho c_p\alpha$ is the Brownian motion parameter,

$T_P = \rho^* c_p^* D_T \left(T_w - T_\infty\right) / \rho c_p \alpha T_\infty$ is the thermophoresis parameter and $Le = \alpha / D_B$ is the Lewis number.

The boundary conditions in nondimensional form are

$$F(0) = c_0, \quad F'(0) = 0, \quad F' \longrightarrow 1, \text{ as } \eta \longrightarrow \infty, \tag{2.20}$$

$$\theta(0) = 1, \quad \Psi(0) = 1, \quad \theta \longrightarrow 0, \quad \Psi \longrightarrow 0, \text{ as } \eta \longrightarrow \infty, \tag{2.21}$$

where c_0 is any constant. The skinfriction coefficient and the Nusselt number are

$$\frac{1}{2} c_f \operatorname{Re}^{1/2} = F''(0), \qquad Nu/\operatorname{Re}^{1/2} = -\theta'(0). \tag{2.22}$$

where $\operatorname{Re} = r_0 U_\infty / 2\upsilon$ is the Reynolds number.

2.3 Solution of the problem

The solutions of $Eqs.$ (2.17) to (2.19) subject to the boundary conditions (2.20) and (2.21) are obtained with the help of the homotopy analysis method (HAM). For HAM solutions, we choose the initial guesses as

$$F_0(\eta) = c_0 - 1 + \eta + e^{-\eta}, \tag{2.23}$$

$$\theta_0(\eta) = e^{-\eta}, \quad \Psi_0(\eta) = e^{-\eta}. \tag{2.24}$$

The corresponding auxiliary linear operators are

$$L_F = \frac{d^3}{d\eta^3} + \frac{d^2}{d\eta^2}, \quad L_\theta = \frac{d^2}{d\eta^2} + \frac{d}{d\eta}, \quad L_\Psi = \frac{d^2}{d\eta^2} + \frac{d}{d\eta}. \tag{2.25}$$

The zeroth-order deformation equations are

$$(1-q) L_f[\hat{f}(\eta; q) - f_0(\eta)] = q H_F \hbar_1 N_f[\hat{f}(\eta; q)], \tag{2.26}$$

$$(1-q) L_\theta[\hat{\theta}(\eta; q) - \theta_0(\eta)] = q H_\theta \hbar_2 N_\theta[\hat{\theta}(\eta; q)], \tag{2.27}$$

$$(1-q) L_\Psi[\hat{\Psi}(\eta; q) - \Psi_0(\eta)] = q H_\Psi \hbar_3 N_\Psi[\hat{\Psi}(\eta; q)], \tag{2.28}$$

34

where $H_f = e^{-\eta}$, $H_\theta = e^{-\eta}$, and $H_\Psi = e^{-\eta}$ are the auxiliary functions and

$$N_f[\hat{F}(\eta;q)] = (1 + 2\gamma_c\eta)\,\hat{F}''' + 2\gamma_c''\hat{F} + 1 + \hat{F}\hat{F}'' - \hat{F}'^2 + \lambda_N\,(1 - \phi_\infty)\,(\hat{\theta} + N_r\hat{\Psi}), \qquad (2.29)$$

$$N_\theta[\hat{\theta}(\eta;q)] = (1 + 2\gamma_c\eta)\,\hat{\theta}'' + 2\gamma_c\hat{\theta}' + \mathrm{Pr}(\hat{F}\hat{\theta}' - \hat{F}'\hat{\theta}) + (1 + 2\gamma_c\eta)\left(B_P\hat{\theta}'\hat{\Psi}' + T_P\hat{\theta}'^2\right), \qquad (2.30)$$

$$N_\Psi[\hat{\Psi}(\eta;q)] = \eta\hat{\Psi}'' + \hat{\Psi}' + Le\,\mathrm{Pr}\left(\hat{F}\hat{\Psi}' - \hat{F}'\hat{\Psi}\right) + \frac{T_P}{B_P}\left[(1 + 2\gamma_c\eta)\,\hat{\theta}'' + 2\gamma_c\hat{\theta}'\right]. \qquad (2.31)$$

The boundary conditions for the zeroth order system are

$$\hat{F}(0;q) = c_0, \quad \hat{F}'(0;q) = 0, \quad \hat{F}'(\eta;q) \longrightarrow 1, \text{ as } \eta \longrightarrow \infty, \qquad (2.32)$$

$$\hat{\theta}(0;q) = 1, \quad \hat{\Psi}(0;q) = 1, \quad \hat{\theta}(\eta;q) \longrightarrow 0, \quad \hat{\Psi}(\eta;q) \longrightarrow 0 \text{ as } \eta \longrightarrow \infty. \qquad (2.33)$$

The solutions are obtained with the help of MATHEMATICA and are discussed in the next section

2.4 Results and discussion

The solutions of the problem of nanofluid flow through a vertical slender cylinder are obtained through the homotopy analysis method. Due to the high dependence of the HAM solutions over the auxiliary parameters $\hbar's$ the convergence region for the nondimensional velocity, temperature and nanoparticle concentration profiles F', θ and ψ are graphed in $Figs.\,(2.1)$ to (2.3). $Fig.(2.1)$ shows the convergence curves for the nondimensional velocity profile F' plotted at the 0.05% level of nanoparticle concentration, when the curvature parameter $\gamma_c = 0.5$. From $Fig.\,(2.1)$ the acceptable convergence region for the auxiliary parameter $\hbar_1$ is $-1.2 \leq \hbar_1 \leq -0.5$. $Fig.\,(2.2)$ displays the $\hbar$ curve for the auxiliary parameter $\hbar_2$ associated with the nondimensional temperature profile θ. From the graph it is observed that the acceptable convergence region for the auxiliary parameter $\hbar_2$ is $-1.5 \leq \hbar_2 \leq -0.5$. $Fig.\,(2.3)$ presents the convergence region for the auxiliary parameter $\hbar_3$ related with the nanoparticle concentration profile ψ sketched for the Lewis number $Le = 0.2$.

The behavior of nondimensional velocity temperature and nanoparticle concentration profiles for different parameters is presented through $Figs.\,(2.4)$ to (2.19). $Fig.\,(2.4)$ shows the behavior of nondimensional velocity profile F' for different values of the Prandtl numbers $\Pr$. From the plot it is clear that with increase in the Prandtl number $\Pr$ the nondimensional velocity profile F' decreases. $Fig.\,(2.5)$ indicates the behavior of the nondimensional velocity profile F' for different values of the curvature parameter γ_c. From the plot it is obtained that with the increase in the curvature parameter γ_c the nondimensional velocity profile F' decreases. $Fig.\,(2.6)$ is included to analyze the influence of the natural convection parameter λ_N over the nondimensional velocity profile F'. From the sketch it is evident that with the increase in the natural convection parameter λ_N the nondimensional velocity profile F' increases. $Fig.\,(2.7)$ provides the impact of the buoyancy ratio N_r over the nondimensional velocity profile F'. From the graph it is noted that with the increase in the buoyancy ratio N_r the velocity profile F' increases. $Fig.\,(2.8)$ shows the influence of the thermophoresis parameter T_P over the nondimensional velocity profile F'. From the figure it is clear that with the increase in the thermophoresis parameter T_P the nondimensional velocity profile F' decreases. $Fig.\,(2.9)$ inculcates the pattern adopted by the nondimensional temperature profile θ with respect to the different values of the Prandtl number $\Pr$. From the plot it is obvious that with the increase in the Prandtl number $\Pr$ the nondimensional temperature profile θ and the thermal boundary layer thickness decreases. $Fig.\,(2.10)$ is schemed to observe the impact of the curvature parameter γ_c over the nondimensional temperature profile θ. From the graph it is noted that with the increase in the curvature parameter γ_c the nondimensional temperature profile θ increases. $Fig.\,(2.11)$ displays the impact of the natural convection parameter λ_N over the temperature function θ. From the graph it is observed that with the increase in the natural convection parameter λ_N the temperature flow rate θ decreases. $Fig.\,(2.12)$ indicates the impact of the buoyancy ratio N_r over the temperature profile θ. From the sketch it is evident that with increase in the buoyancy ratio N_r the nondimensional temperature profile θ decreases. $Fig.\,(2.13)$ provides an insight in the behavior of the temperature profile θ with respect to the Brownian motion parameter B_P. From $Fig.\,(2.13)$ it is revealed that with an increase in the Brownian motion parameter B_P the nondimensional temperature profile θ increases. $Fig.\,(2.14)$ displays the influence of the thermophoresis parameter T_P over the nondimensional temperature profile θ. From the plot it is

noted that with increase in the thermophoresis parameter T_P the nondimensional temperature flow rate θ increases. The influence of the Prandtl number Pr over the nanoparticle concentration profile ψ is presented in $Fig.\,(2.15)$. From the graph it is observed that the nanoparticle concentration profile ψ decreases with increase in the Prandtl number Pr. $Fig.(2.16)$ gives the behavior of buoyancy ratio N_r over the nanoparticle concentration function ψ. From $Fig.\,(2.16)$ it is observed that with increase in the buoyancy ratio N_r the nanoparticle concentration profile ψ decreases. The variation of the nanoparticle concentration function ψ with respect to the Brownian motion parameter B_P is sketched in $Fig.\,(2.17)$. It is noted from the plot that with an increase in the Brownian motion parameter B_P the nanoparicle concentration profile ψ decreases. $Fig.\,(2.18)$ provides an insight in the behavior of the nanoparticle concentration profile ψ for different values of the thermophoresis parameter T_P. From the graph it is observed that by increasing the thermophoresis parameter T_P the nanoparticle concentration profile ψ also enhances. $Fig.\,(2.19)$ is schemed to observe the impact of the Lewis number Le over the nanoparticle concentration profile ψ. From the graph it is noted that with an increase in the Lewis number Le the nanoparticle concentration profile decreases.

The associated important physical quantities, the shear stress, the skinfriction coefficient, the heat flux and the local Nusselt numbers are analyzed through tables. $Table.\,(2.1)$ contains the boundary derivatives for the nondimensional velocity profile computed at the surface of the cylinder that also corresponds to the shear stress at the surface and the skinfriction coefficient. Entries in $Table.\,(2.1)$ are tabulated for different values of the curvature parameter γ_c and the natural convection parameter λ_N. From $Table.\,(2.1)$ it is noted that with an increase in both the curvature parameter γ_c and the natural convection parameter λ_N the shear stress at the surface of the cylinder increases. $Table.\,(2.2)$ gives the influence of heat flux at the surface of the cylinder calculated for different values of the curvature parameter γ_c and the natural convection parameter λ_N. From data in $Table.\,(2.2)$ it is noted that with an increase in both the curvature parameter γ_c and the natural convection parameter λ_N, heat flux at the surface of the cylinder and the corresponding local Nusselt numbers increases.

37

15$^{\text{th}}$ Order of Approximation

Fig.(2.1). $\hbar$-curve for velocity profile F'

$\gamma_c = 0.5$, $\lambda_N = 1$, $Pr = 0.71$, $T_P = 0.5$, $N_r = 0.2$,
$B_P = 0.5$, $Le = 0.25$, $c_0 = 1$, $\phi_\infty = 0.5$,

15$^{\text{th}}$ Order of Approximation
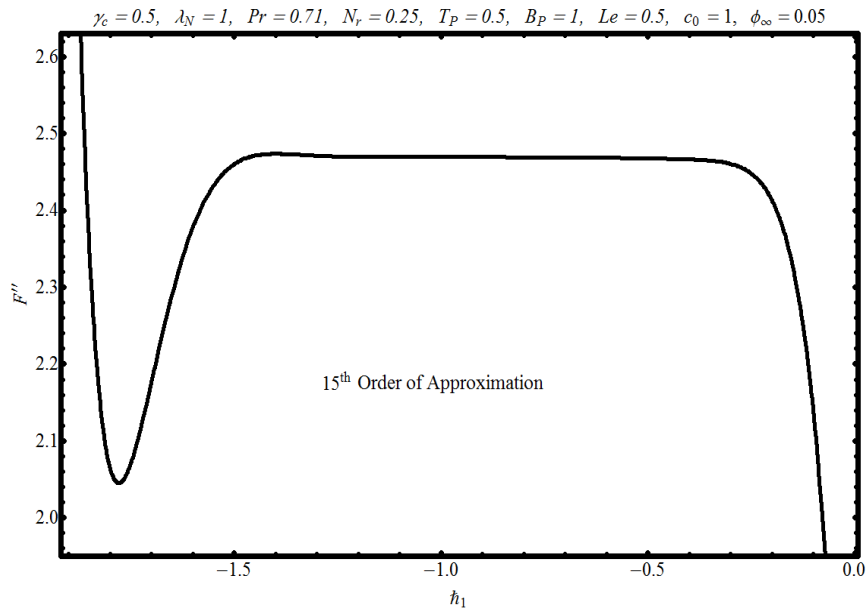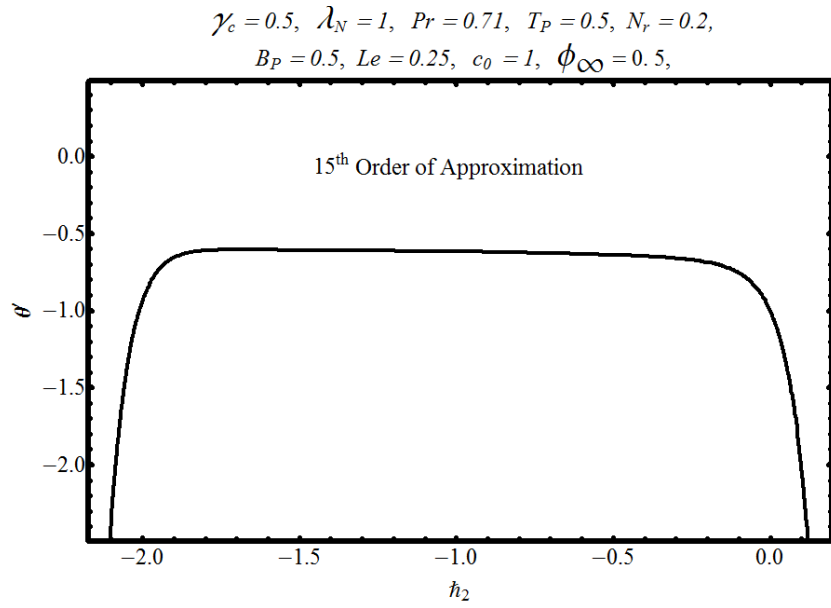
Fig.(2.2). $\hbar$-curve for temperature function θ

38

15$^{\text{th}}$ Order of Approximation
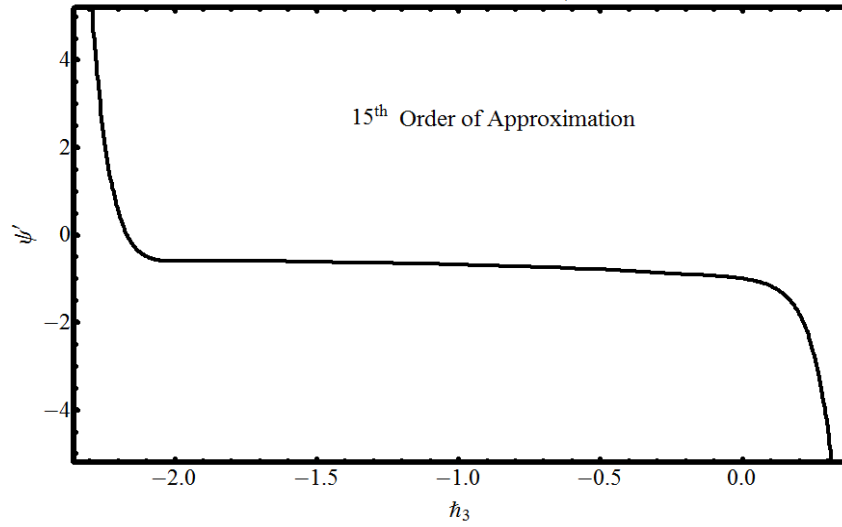
$Fig.(2.3)$. $\hbar$-curve for nanoparticle concentration profile ψ

$\gamma_c = 1, \quad \lambda_N = 0.5, \quad N_r = 0.5, \quad B_P = 1,$

$T_P = 1, \quad \text{Le} = 1, \quad \phi_\infty = 0.05, \quad c_0 = 1$

Pr = 0.71, 2, 4
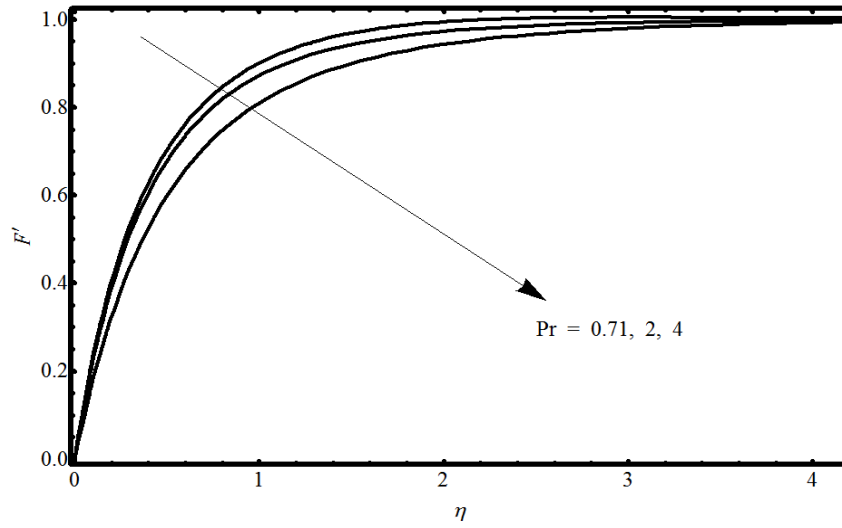
$Fig.(2.4)$. Influence of the Prandtl number Pr over the velocity
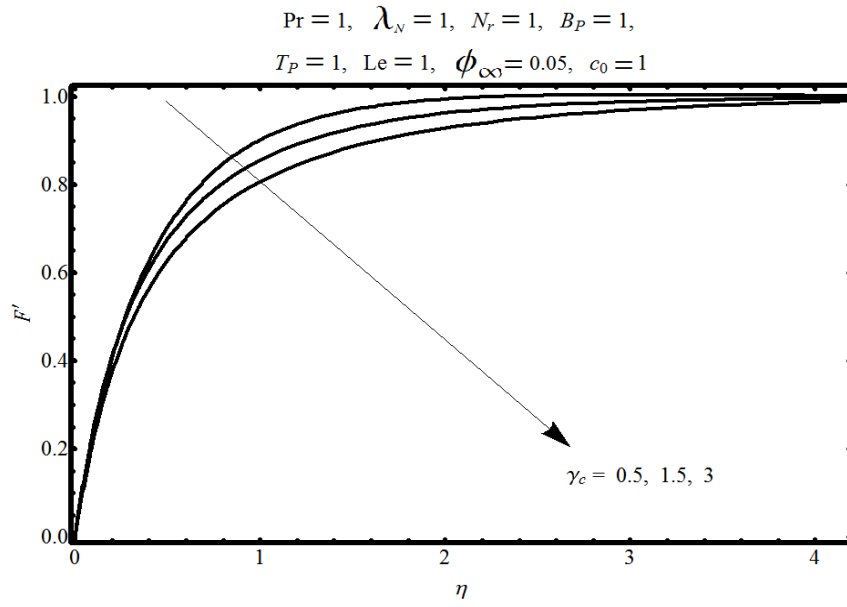
profile F'

$Fig.(2.5)$. Influence of the curvature parameter γ_c over the velocity profile F'
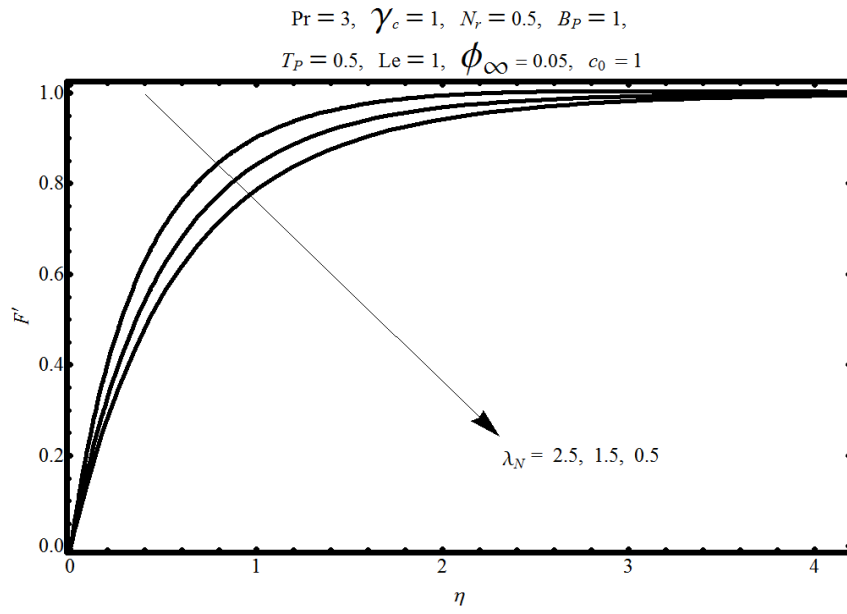
$Fig.(2.6)$. Influence of the natural convction parameter λ_N over the velocity profile F'

40

$Pr = 7, \quad \gamma_e = 0.5, \quad \lambda_N = 1, \quad B_P = 1,$

$T_P = 0.5, \quad Le = 1, \quad \phi_\infty = 0.05, \quad c_0 = 1$

$N_r = 0.5, \ 1.5, \ 2.5$

$Fig.(2.7)$. Influence of the buoyancy ratio N_r over the velocity profile F'

$Pr = 5, \quad \gamma_e = 0.5, \quad \lambda_N = 0.5, \quad N_r = 1,$

$B_T = 1, \quad Le = 0.5, \quad \phi_\infty = 0.05, \quad c_0 = 1$

$T_P = 0.5, \ 1, \ 2$
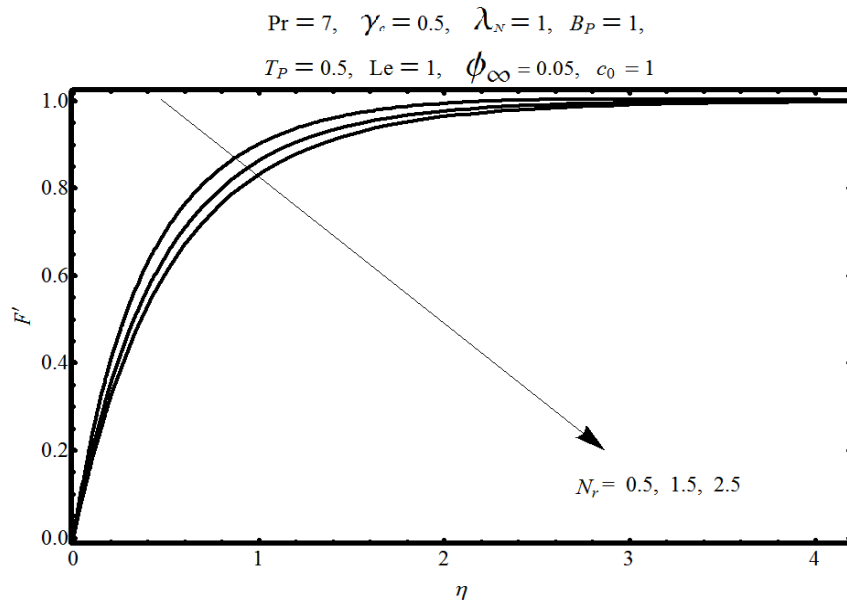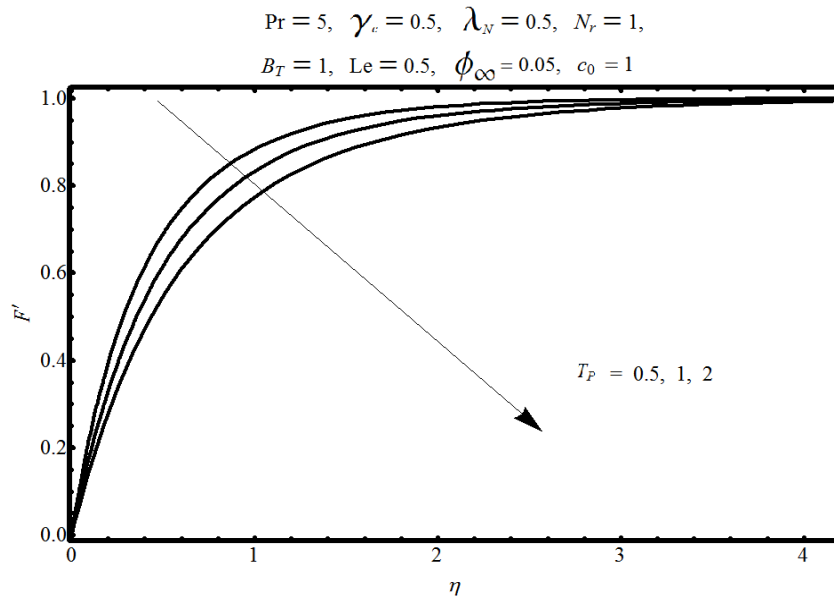
$Fig.(2.8)$. Influence of the thermophoresis parameter Nt over the velocity profile F'

$\gamma_c = 0.5,\ \lambda_N = 1,\ N_r = 0.5,\ B_P = 1,$
$T_P = 0.5,\ \text{Le} = 2,\ \phi_\infty = 0.05,\ c_0 = 1$

$\text{Pr} = 0.71,\ 2,\ 5,\ 7$

$Fig.$(2.9). Influence of the Prandtl number Pr over the temperature profile θ

$\text{Pr} = 3,\ \lambda_N = 1,\ N_r = 0.5,\ B_P = 1,$
$T_P = 0.5,\ \text{Le} = 1,\ \phi_\infty = 0.05,\ c_0 = 1$

$\gamma_c = 0.5,\ 1,\ 2$
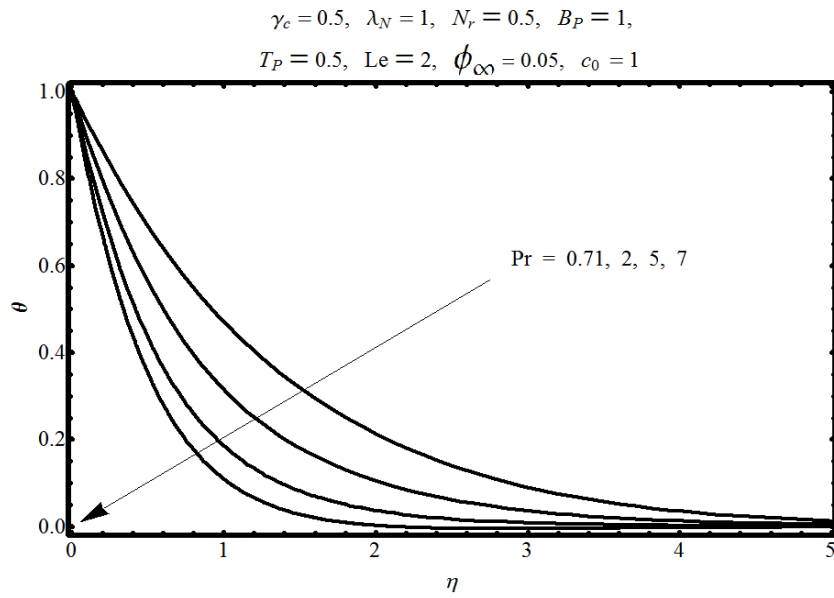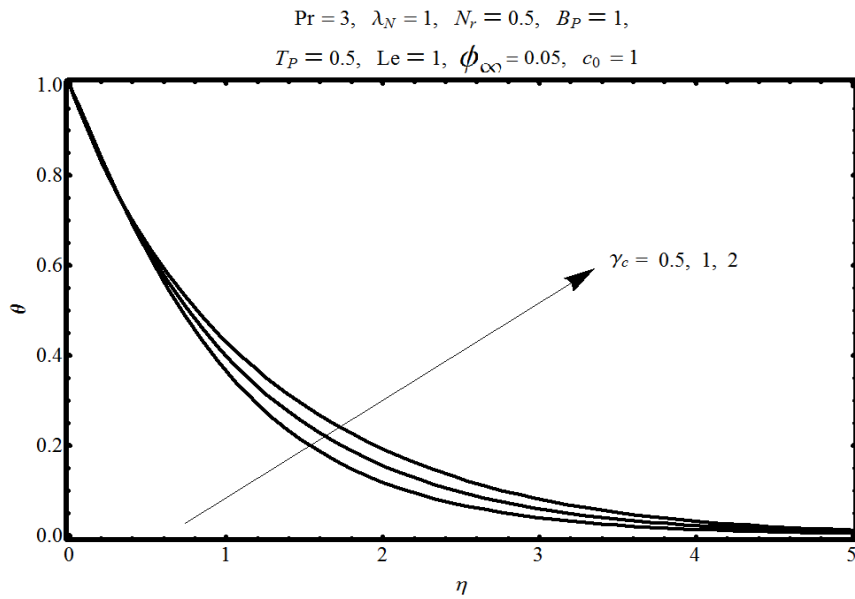
$Fig.$(2.10). Influence of the curvature parameter γ_c over the temperature profile θ

42
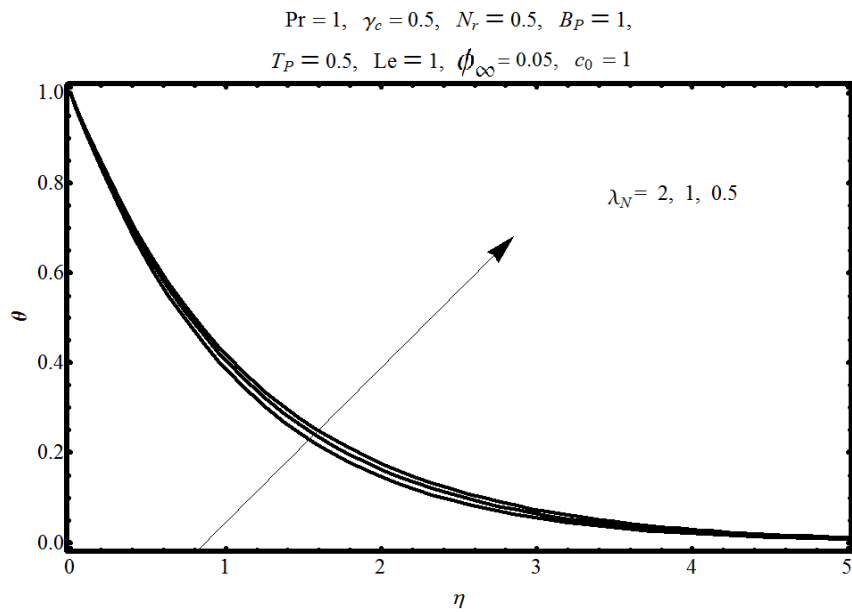
$Fig.(2.11)$. Influence of the natural convection parameter λ_N over the temperature profile θ
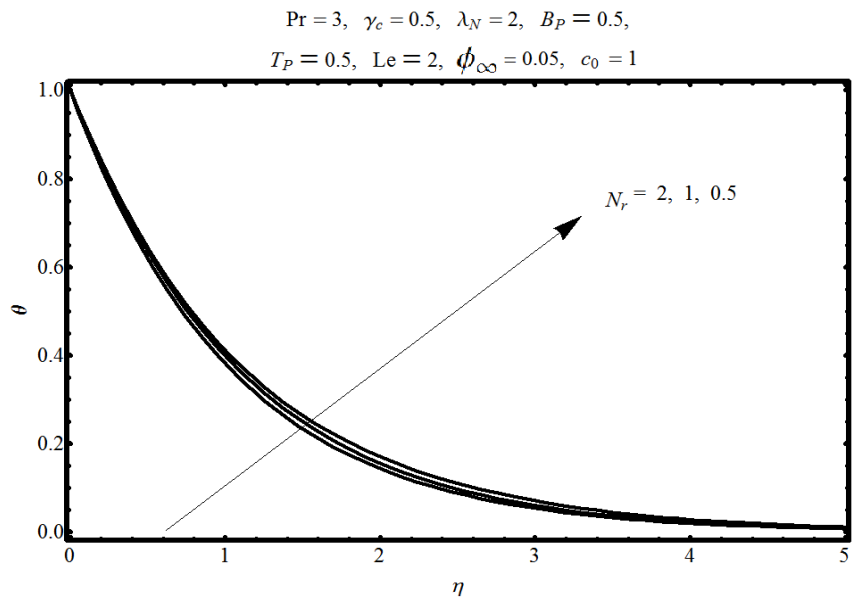
$Fig.(2.12)$. Influence of the buoyancy ratio N_r over the temperature profile θ
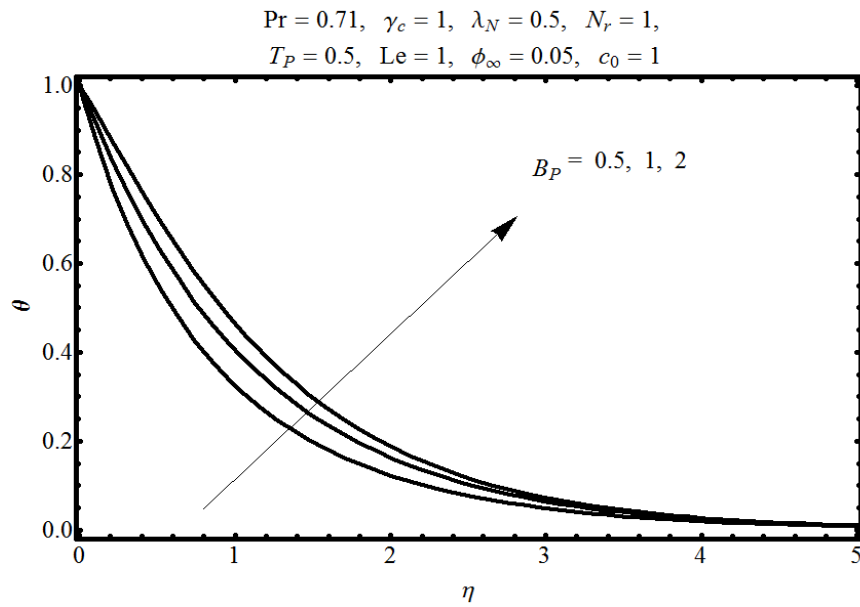
Pr = 0.71, γ_c = 1, λ_N = 0.5, N_r = 1,
T_P = 0.5, Le = 1, ϕ_∞ = 0.05, c_0 = 1

B_P = 0.5, 1, 2

$Fig.$(2.13). Influence of the Brownian motion parameter B_P over the
temperature profile θ

Pr = 0.71, γ_c = 2, λ_N = 0.5, N_r = 0.5,
B_P = 0.5, Le = 1, ϕ_∞ = 0.05, c_0 = 1

T_P = 0.5, 1, 2
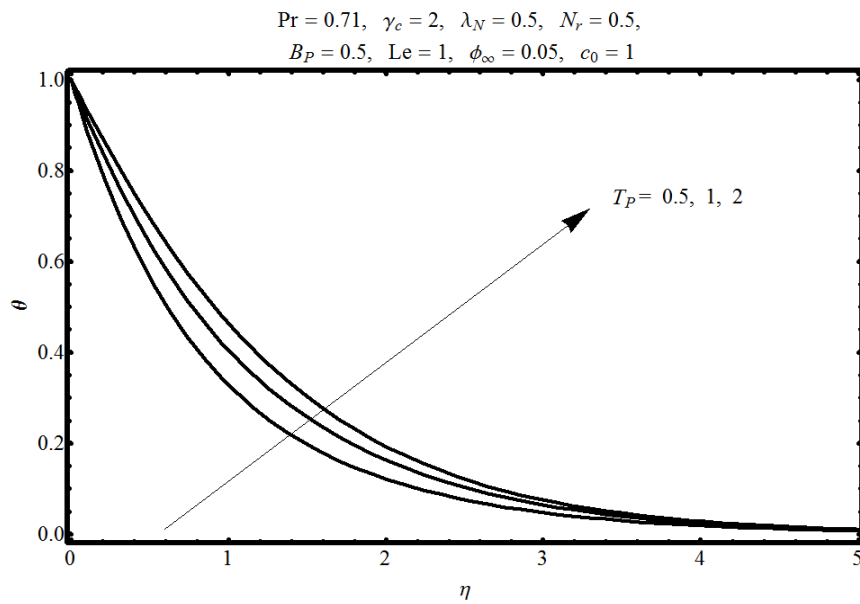
$Fig.$(2.14). Influence of the thermophoresis parameter T_P over the
temperature profile θ
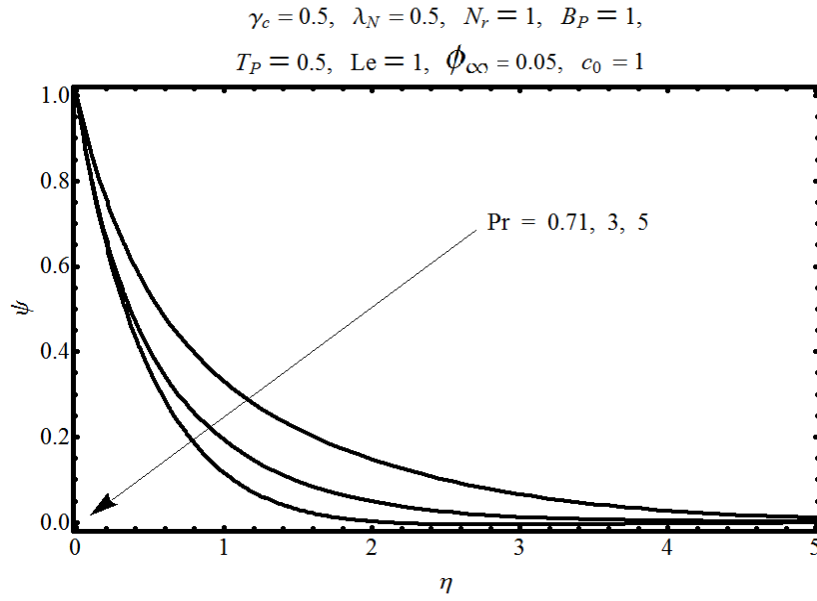
$\gamma_c = 0.5, \quad \lambda_N = 0.5, \quad N_r = 1, \quad B_P = 1,$
$T_P = 0.5, \quad Le = 1, \quad \phi_\infty = 0.05, \quad c_0 = 1$

Pr = 0.71, 3, 5

$Fig.(2.15)$. Influence of the Prandtl number Pr over the
nanoparticle concentration profile ψ

$Pr = 3, \quad \gamma_c = 0.5, \quad \lambda_N = 0.5, \quad B_P = 1,$
$T_P = 0.5, \quad Le = 1, \quad \phi_\infty = 0.05, \quad c_0 = 1$

$N_r = 0.5, \; 1.5, \; 2.5$
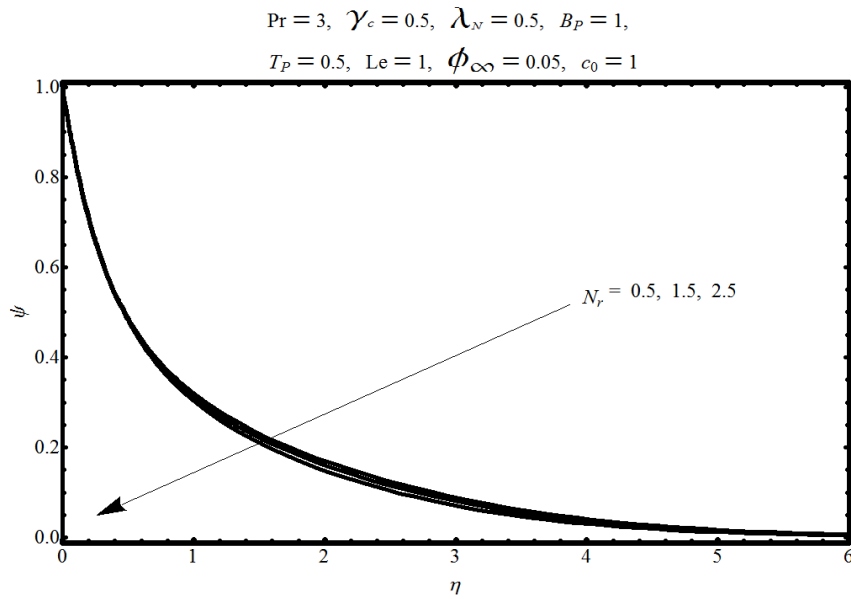
$Fig.(2.16)$. Influence of the buoyancy ratio N_r over the nanoparticle
concentration profile ψ

B_P = 2, 1, 0.5
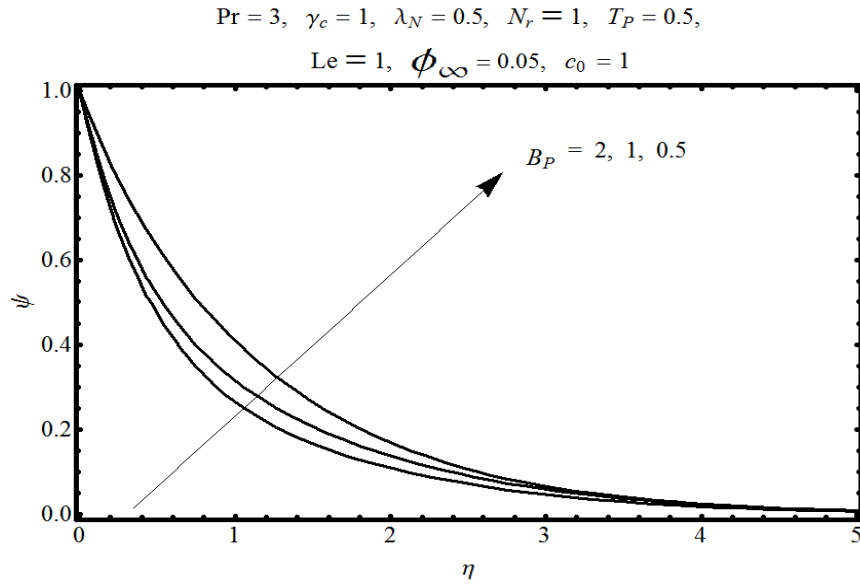
$Fig.$(2.17). Influence of the Brownian motion parameter B_P over the nanoparticle concentration profile ψ

T_P = 0.5, 1, 2

$Fig.$(2.18). Influence of the thermophoresis parameter T_P over the nanoparticle concentration profile ψ

$$Pr = 5, \quad \gamma_c = 1, \quad \lambda_N = 0.5, \quad N_r = 1,$$
$$B_P = 1, \quad T_P = 1, \quad \phi_\infty = 0.05, \quad c_0 = 1$$
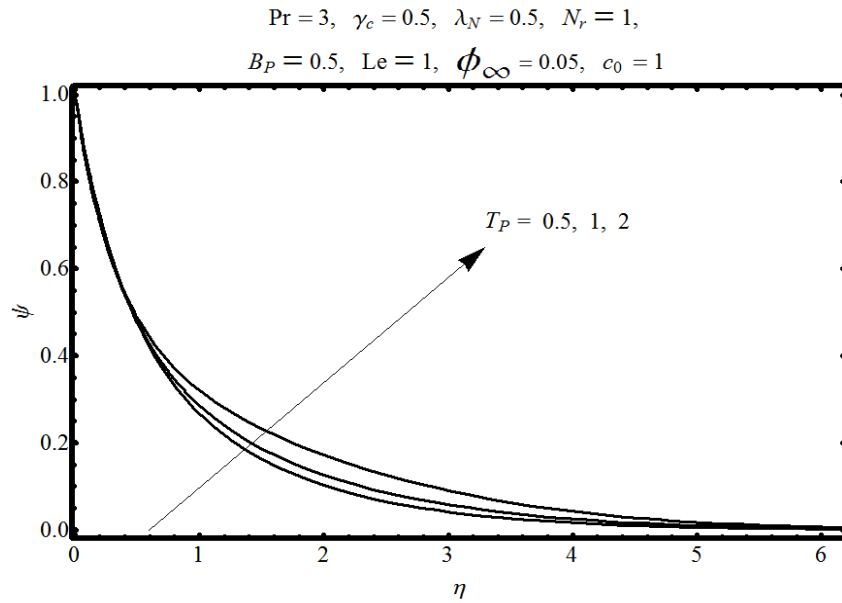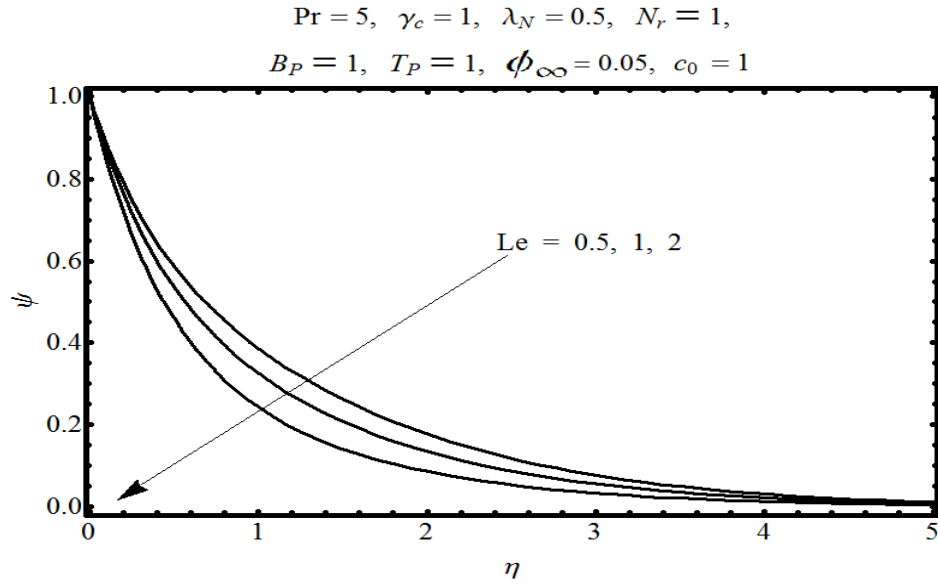
$Fig.$(2.19). Influence of the Lewis number Le over the nanoparticle concentration profile ψ

$\gamma_c \backslash \lambda_N$	$f''(0)$					
	0.0	0.25	0.5	1	1.5	2.0
0.25	1.9341	1.9478	1.9614	1.9887	2.0159	2.0431
0.50	2.0397	2.0523	2.0658	2.0927	2.1196	2.1464
7.50	2.1048	2.1178	2.1307	2.1566	2.1824	2.0281
1.00	2.1751	2.1821	2.1945	2.2194	2.2442	2.2690
1.25	2.2206	2.2324	2.2443	2.2681	2.2918	2.3154
1.50	2.2982	2.3096	2.3212	2.3302	2.3532	2.3761
2.00	2.4099	2.4186	2.4295	2.4512	2.4730	2.4945

$Table.$(2.1). Variation of boundary derivative for velocity profile F' for different values of the natural convection parameter λ_N and the vurvature parameter γ_c when $Pr = 0.72$, and $\phi_\infty = 0.05$

$\gamma_c \backslash \lambda_N$	-θ′(0)					
	0.0	0.25	0.5	1	1.5	2.0
0.25	0.5896	0.5901	0.5907	0.5920	0.5930	0.5941
0.50	0.6151	0.6156	0.6162	0.6173	0.6183	0.6196
0.75	0.6503	0.6508	0.6513	0.6522	0.6532	0.6541
1.00	0.6840	0.6845	0.6849	0.6858	0.6867	0.6875
1.50	0.7485	0.7488	0.7492	0.7500	0.7507	0.7515
2.00	0.8064	0.8067	0.8071	0.8077	0.8083	0.8090

$Table.$(2.2). Variation of boundary derivatives for
temperature profile θ for different values of the natural
convection parameter λ_N and the curvature parameter γ_c
when $Pr = 0.72$, and $\phi_\infty = 0.05$

2.5   Conclusion

The main finding of this chapter are summarized as

- The nondimensional velocity profile F' decreases with the increase in the Prandtl number Pr, the curvature parameter γ_c and the thermophoresis parameter T_p.

- The nondimensional velocity profile F' increases with increase in the natural convection parameter λ_N and the buoyancy ratio N_r

- The nondimensional temperature profile θ decreases with the increase in the Prandtl number Pr, the natural convection parameter λ_N, the buoyancy ratio N_r and the Brownian motion parameter B_p.

- The nondimensional temperature profile θ increases with the increase in the curvature parameter γ_c and the thermophoresis parameter T_p.

48

- The nondimensional nanoparticle concentration profile ψ decreases with the increase in the Prandtl number Pr, the buoyancy parameter N_r, the Lewis number Le and the Brownian motion parameter B_p.

- The nanoparticle concentration profile ψ increases with the increase in the thermophoresis parameter T_p.

- The shear stress at the surface of the cylinder increases with increase in the curvature parameter γ_c and the natural convection parameter λ_N.

- The heat flux at the surface of the cylinder increases with increase in the curvature parameter γ_c and the natural convection parameter λ_N.

Chapter 3

Boundary layer stagnation flow over an exponentially stretching cylinder

3.1   Introduction

The present chapter offers an analysis for the problem of steady, incompressible stagnation point boundary layer flow and heat transfer of a viscous fluid flowing through a vertical cylinder that is stretched exponentially along its surface. The governing partial differential equations of conservation of mass, momentum and energy along with the boundary conditions of exponentially stretching cylinder are reduced to a system of nonlinear ordinary differential equations by using the boundary layer approach and a suitable similarity transformation. The resulting coupled system of differential equations along with the appropriate boundary conditions is solved with the help of numerical technique, the Keller-box method. The effects of the involved parameters such as Reynolds numbers, Prandtl numbers and the natural convection parameter are presented through sketches. The associated physical properties on flow and heat transfer characteristics that are the skinfriction coefficient and Nusselt numbers are presented for different parameters.

3.2 Formulation

Consider the boundary layer stagnation flow of viscous fluid flowing over a vertical exponentially stretched circular cylinder. The cylinder of radius a is assumed to be stretched exponentially along its axial direction with a surface stretching velocity $V_w = 2ak^*e^{z/b}$. The surface temperature T_w and the ambient temperature T_∞ are such that for assisting flows $T_w - T_\infty > 0$ while for opposing flows $T_w - T_\infty < 0$. The velocity field and temperature profile are

$$\mathbf{V}\left(r,z\right) = \left(u\left(r,z\right), 0, w\left(r,z\right)\right), \quad T = T\left(r,z\right), \tag{3.1}$$

where (u, w) are the velocity components along the (r, z) axes. The related boundary conditions are

$$\text{at } r = a, \quad u = 0, \quad w = V_w, \quad \text{for } r \to \infty, \quad w = V_\infty, \tag{3.2}$$

$$\text{at } r = a, \quad T = T_w, \quad \text{for } r \to \infty, \quad T \to T_\infty. \tag{3.3}$$
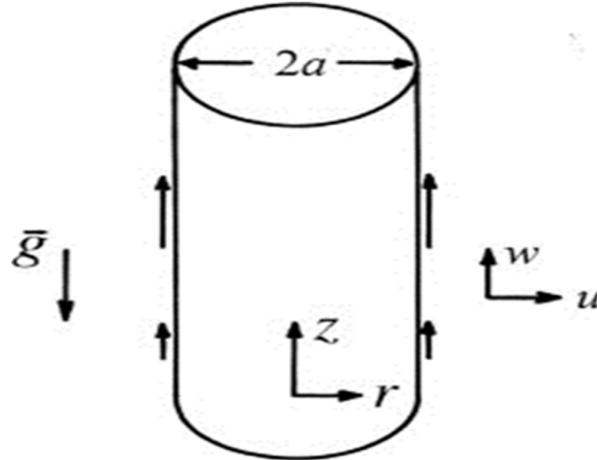
where $V_\infty = 2bk^*e^{z/b}$.

*Fig.*3.1. *Fluid is flowing over a vertical cylinder of radius a that is stretched axially with an exponential surface stretching velocity V_w.*

The governing equations of conservation of mass and momentum are stated in $Eqs. (2.6)$ and (2.7), while the energy equation for the present problem is of the form

$$\rho c_p \frac{dT}{dt} = \mathbf{S} \cdot \boldsymbol{\nabla} \mathbf{V} - \text{div } \mathbf{q}, \tag{3.4}$$

For the velocity field $Eq. (3.1)$ the concerned boundary layer equations of motion and heat transfer in presence of heat dissipation are

$$u_r + \frac{u}{r} + w_z = 0, \tag{3.5}$$

$$uw_r + ww_z = V_\infty \frac{dV_\infty}{dz} + \nu(w_{rr} + \frac{1}{r}w_r) + g_{gr}\beta_{th}(T - T_\infty), \tag{3.6}$$

$$uT_r + wT_x = \alpha(T_{rr} + \frac{1}{r}T_r) + \frac{\nu}{c_p}w_r^2, \tag{3.7}$$

where ν is the kinematic viscosity, g_{gr} is the gravitational acceleration, β_{th} is the coefficient of thermal expansion and α is the thermal diffusivity.

3.3 Solution of the problem

The system of partial differential equations along with the boundary conditions is simplified with the aid of following similarity transformations:

$$u = -\frac{1}{2}V_\infty \frac{G(\eta)}{\sqrt{\eta}}, \qquad w = V_\infty G'(\eta), \tag{3.8}$$

$$\theta = \frac{(T - T_\infty)}{(T_w - T_\infty)}, \qquad \eta = \frac{r^2}{b^2}, \tag{3.9}$$

where $T_w - T_\infty = ce^{z/b}$. With the help of the above transformations, $Eqs.$ (3.5) to (3.7) become

$$\eta f''' + f'' + \text{Re}(ff'' - f'^2 + 1) + \text{Re } \lambda\theta = 0, \tag{3.10}$$

$$\eta\theta'' + \theta' + \text{Re Pr}(f\theta' - f'\theta) + \text{Pr } Ec\eta f''^2 = 0, \tag{3.11}$$

in which $\text{Re}_z = aV_\infty/4\nu$ is the Reynolds number, $\lambda = g_{gr}\beta_{th}a(T_w - T_\infty)/V_\infty^2$ is the natural convection parameter, $\text{Pr} = v/\alpha$ is the Prandtl number and $Ec = V_\infty^2/c_p(T_w - T_\infty)$ is the

Eckert number. The associated boundary conditions now take the form

$$G(1) = 0, \quad G'(1) = \varepsilon, \quad G' \longrightarrow 1, \text{ as } \eta \longrightarrow \infty, \tag{3.12}$$

$$\theta(1) = 1, \quad \theta \longrightarrow 0, \text{ as } \eta \longrightarrow \infty, \tag{3.13}$$

where $\varepsilon = a/b$. The skinfriction coefficient c_f and the local Nusselt number Nu are

$$c_f \operatorname{Re}_z^{1/2} = \frac{1}{\frac{1}{2}\rho V_\infty^2} \tau_{rz}|_{r \to a}, \quad Nu/\operatorname{Re}_z^{1/2} = -\theta'(1). \tag{3.14}$$

3.4 Numerical Scheme

The solution of the present problem is obtained using the Keller-box method. To develop the technique the system of differential equations (3.10) and (3.11) along with the boundary conditions (3.12) and (3.13) are converted into a first order differential system. The resulting system is then solved using the block elimination method. To develop a first order differential system, we consider

$$G_1 = G', \quad G_2 = G_1', \quad G_3 = \theta'. \tag{3.15}$$

Then the resulting system is

$$\eta G_2' + G_2 + \operatorname{Re}_z(GG_2 - G_1^2 + 1) + \operatorname{Re}_z \lambda\theta = 0, \tag{3.16}$$

$$\eta G_3' + G_3 + \operatorname{Re}_z \operatorname{Pr}(GG_3 - G_1\theta) + \operatorname{Pr} Ec\eta G_2^2 = 0, \tag{3.17}$$

with the boundary conditions

$$G(1) = 0, \quad G_1(1) = \varepsilon, \quad G_1 \longrightarrow 1, \text{ as } \eta \longrightarrow \infty, \tag{3.18}$$

$$\theta(1) = 1, \quad \theta \longrightarrow 0, \text{ as } \eta \longrightarrow \infty. \tag{3.19}$$

The first order derivatives are approximated about $\eta_{j-(1/2)}$ using the central difference, that yield

$$G_j^{(i)} - G_{j-1}^{(i)} = h_j(G_1)_{j-(1/2)}^{(i)}, \tag{3.20}$$

53

$$(G_1)_j^{(i)} - (G_1)_{j-1}^{(i)} = h_j(G_2)_{j-(1/2)}^{(i)}, \qquad (3.21)$$

$$\theta_j^{(i)} - \theta_{j-1}^{(i)} = h_j(G_3)_{j-(1/2)}^{(i)}, \qquad (3.22)$$

$$\eta_{j-(1/2)}((G_2)_j^{(i)} - (G_2)_{j-1}^{(i)}) + h_j(G_2)_{j-(1/2)}^{(i)} + h_j \operatorname{Re}_z \lambda \theta_{j-(1/2)}^{(i)}$$

$$+ h_j \operatorname{Re}_z (G_{j-(1/2)}^{(i)}(G_2)_{j-(1/2)}^{(i)} - ((G_1)_{j-(1/2)}^{(i)})^2 + 1) = (R_f)_{j-(1/2)}^{(i-1)}, \qquad (3.23)$$

$$\eta_{j-(1/2)}((G_3)_j^{(i)} - (G_3)_{j-1}^{(i)}) + h_j(G_3)_{j-(1/2)}^{(i)} + h_j \operatorname{Pr} Ec\eta(G_2)_{j-(1/2)}^{(i)2}$$

$$+ h_j \operatorname{Re}_z \operatorname{Pr}(G_{j-(1/2)}^{(i)}(G_3)_{j-(1/2)}^{(i)} - (G_1)_{j-(1/2)}^{(i)}\theta_{j-(1/2)}^{(i)}) = (R_\theta)_{j-(1/2)}^{(i-1)}, \qquad (3.24)$$

where, $h_j = \eta_j - \eta_{j-1}$, and

$$(R_f)_{j-(1/2)}^{(i-1)} = \eta_{j-(1/2)}((G_2)_{j-1}^{(i-1)} - (G_2)_j^{(i-1)}) + h_j(G_2)_{j-(1/2)}^{(i-1)}$$

$$+ h_j \operatorname{Re}_z(G_{j-(1/2)}^{(i-1)}(G_2)_{j-(1/2)}^{(i-1)} - ((G_1)_{j-(1/2)}^{(i-1)})^2) + h_j \operatorname{Re}_z \lambda \theta_{j-(1/2)}^{(i-1)}, \qquad (3.25)$$

$$(R_\theta)_{j-(1/2)}^{(i-1)} = \eta_{j-(1/2)}((G_3)_{j-1}^{(i-1)} - (G_3)_j^{(i-1)}) + h_j(G_3)_{j-(1/2)}^{(i-1)}$$

$$+ h_j \operatorname{Re}_z \operatorname{Pr}(G_{j-(1/2)}^{(i-1)}(G_3)_{j-(1/2)}^{(i-1)} - (G_1)_{j-(1/2)}^{(i-1)}\theta_{j-(1/2)}^{(i-1)}) + h_j \operatorname{Pr} Ec\eta(G_2)_{j-(1/2)}^{(i-1)2}. \qquad (3.26)$$

Further, these difference equations are linearized by Newton's method. The resulting tridiagonal system is then solved using block-elimination technique. Further details of the procedure can be found in [94].

3.5 Results and discussion

The present investigation is carried for the problem of natural convection boundary layer stagnation point flow of a viscous fluid that is flowing over a vertical cylinder. The cylinder is assumed to be stretching exponentially along its axial direction with a surface stretching velocity $V_w = 2ak^*e^{z/b}$ while the free stream velocity is $V_\infty = 2bk^*e^{z/b}$. The solutions of the problem are computed using the numerical scheme, the Keller-box technique. The impact of the involved parameters Reynolds number Re_z, the natural convection parameter λ, the stretching ratio ε, the Prandtl number Pr and the Eckert number Ec over the non-dimensional velocity and temperature profiles G' and θ are presented graphically in $Figs.(3.1) - (3.10)$. $Fig.1$ dis-

54

plays the influence of Reynolds number Re_z over the velocity profile G' for different values of the stretching ratio ε. From $Fig.(3.1)$ it is observed that for $\varepsilon < 1$, increase in Reynolds number Re_z increases the velocity profile G', while for $\varepsilon > 1$, increase in the Reynolds number Re_z decreases the velocity profile G'. $Fig.(3.2)$ shows the behavior of velocity function G' computed for different values of the natural convection parameter λ and the stretching ratio ε. From the sketch it is noted that for both $\varepsilon = 0.5$ and 1.5, increase in the natural convection parameter λ increases the velocity profile G' because higher natural convection parameter λ is associated with the higher density difference in the fluid which produces increase in the velocity profile G'. $Fig.(3.3)$ indicates the convergence pattern for the velocity profile G' for different values of the stretching ratio ε. The influence of Prandtl numbers Pr over the non-dimensional velocity profile G' for different values of the stretching ratio ε is sketched in $Fig.(3.4)$ when $\mathrm{Re}_z = 5$, $\lambda = 0.5$ and $Ec = 0.5$. From the graph it is observed that increase in the Prandtl numbers Pr reduces the velocity profile G' for any choice of ε. $Fig.(3.5)$ gives the impact of Eckert numbers Ec over the velocity profile G' for $\varepsilon = 0$ and 2. From the figure it is evident that increase in the Eckert numbers Ec enhances the velocity profile G'. $Fig.(3.6)$ inculcates the influence of Prandtl numbers Pr over the temperature function θ. From $Fig.(3.6)$ it is observed that increase in the Prandtl number Pr decreases the temperature profile θ. This observation is consistent with the fact that increase in the Prandtl numbers Pr reduces the thermal diffusion rate and hence decreases the temperature function θ. $Fig.(3.7)$ shows the behavior of temperature profile θ for different values of the Reynolds numbers Re_z that depicts that increase in the Reynolds numbers Re_z decreases the temperature flow. This observation corresponds to the fact that high Reynolds numbers Re_z are associated with more dense fluids that tend to reduce the temperature flow rate θ. $Fig.(3.8)$ gives the influence of Eckert numbers Ec over the temperature function θ that indicates that with increase in the Eckert numbers Ec increases the temperature profile θ. This observation reveals the fact that higher Eckert numbers Ec corresponds to the excess in thermal energy due to frictional heating stored in the fluid. $Fig.(3.9)$ indicates the behavior of temperature profile θ computed for different values of the natural convection parameter λ. From the observed sketch it is clear that with the increase in natural convection parameter λ, the temperature profile θ decreases. $Fig.(3.10)$ depicts the impact of Reynolds numbers Re computed for the case of shrinking cylinder with $\varepsilon = -0.5$ and -1.5. From the plot

it is noticed that with the increase in Reynolds numbers Re_z the velocity function increases.

$Table.$(3.1) contains values for the boundary derivatives for velocity profile G' corresponding to the skinfriction coefficient calculated for different choices of Reynolds numbers Re_z and the natural convection parameter λ. From the table it is noticeable that the skinfriction coefficient increases with increase in both the Reynolds number Re_z and the natural convection parameter λ. $Table.$(3.2) shows the behavior of boundary derivatives for the temperature function θ corresponding to the local Nusselt numbers computed for different values of Prandl numbers Pr and Reynolds numbers Re_z. From $Table.$(3.2) it is observed that the local Nusselt numbers increases with increase in both the Prandtl numbers Pr and Reynolds numbers Re_z.
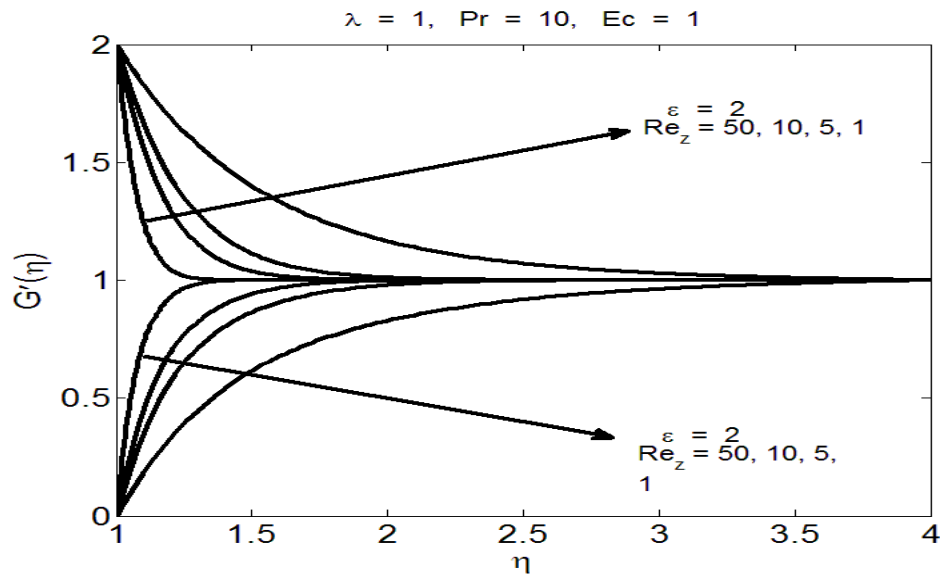
$Fig.$(3.2). Behavior of the velocity profile G' for different values of the stretching ratio ε and the Reynolds number Re_z
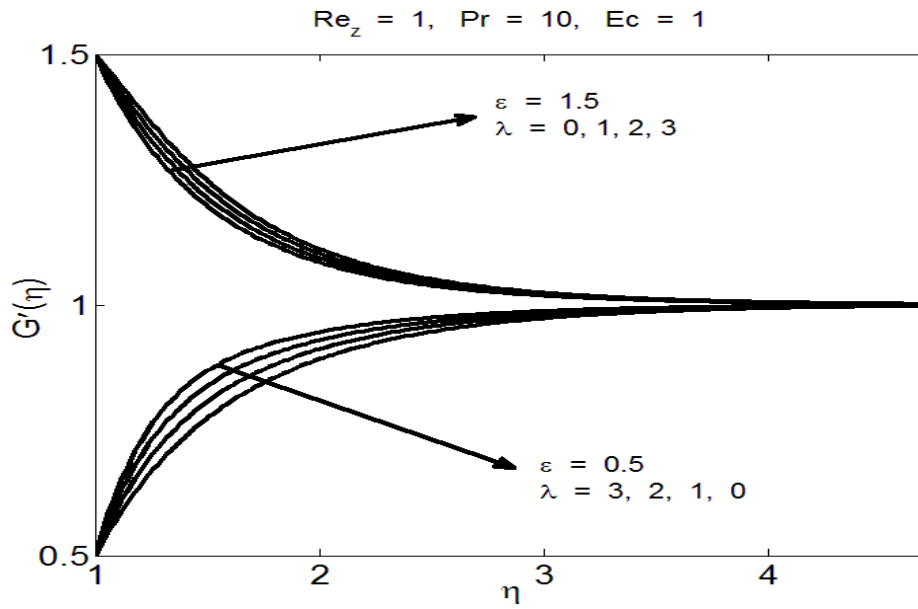
Fig.(3.3). Behavior of the velocity profile G' for different values of the stretching ratio ε and the natural convection parameter λ
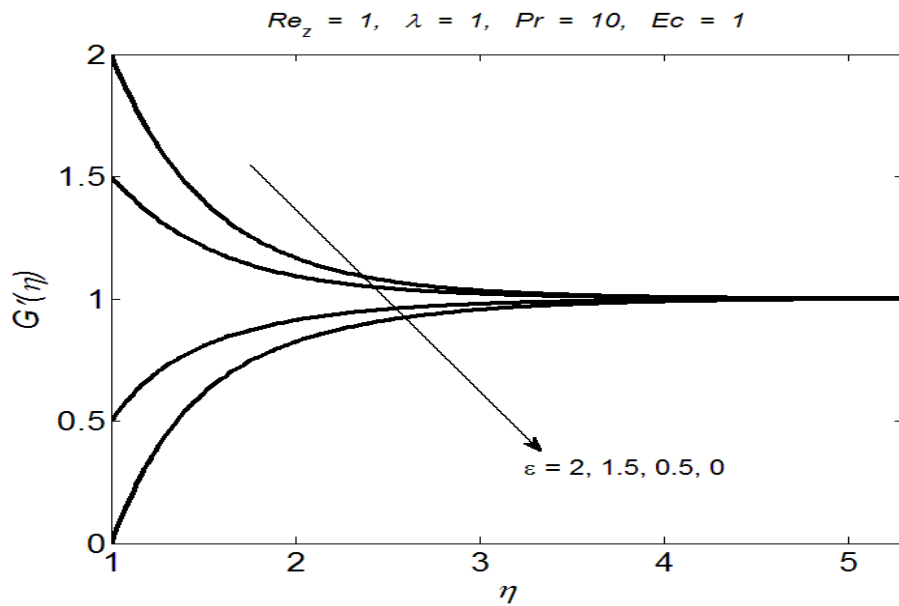
Fig.(3.4). Behavior of the velocity profile G' for different values of the stretching ratio ε
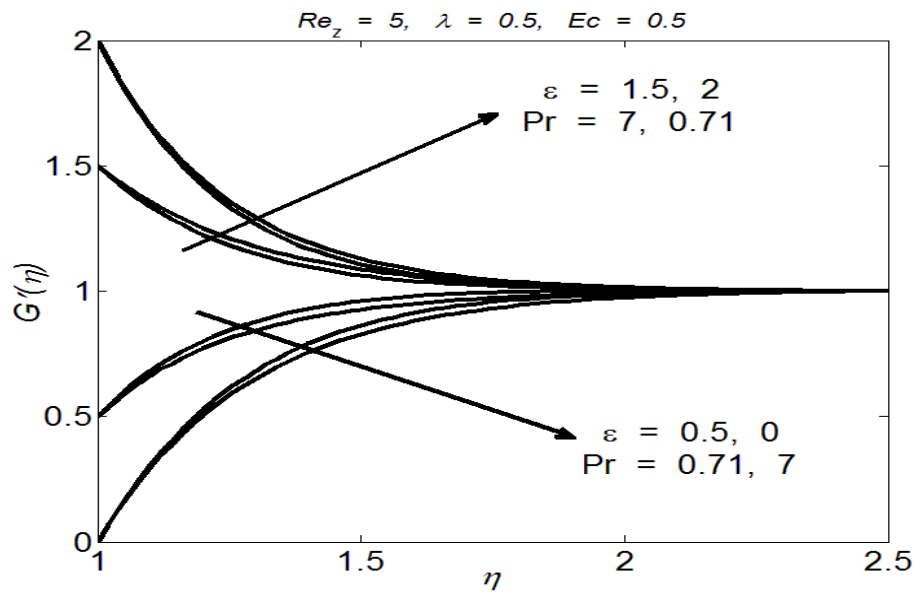
$Fig.(3.5)$. Behavior of the velocity profile G' for different choices of the stretching ratio ε and the Prandtl number Pr
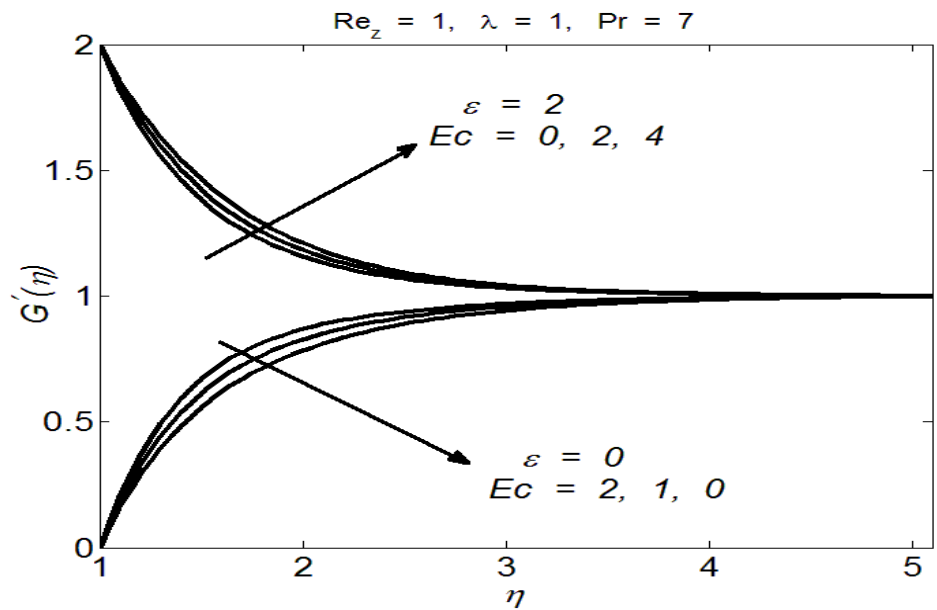
$Fig.(3.6)$. Behavior of the velocity profile G' for different values of the stretching ratio ε and the Eckert number Ec

$Re_z = 5, \quad \lambda = 0.5, \quad \varepsilon = 1, \quad Ec = 0.5$

$Pr = 70, 20, 7, 0.71$

$Fig.(3.7)$. Behavior of the temperature profile θ for different choices of the Prandtl number Pr

$\lambda = 0.5, \quad Pr = 10, \quad Ec = 0.5, \quad \varepsilon = 0.5$

$Re_z = 20, 10, 5, 1$
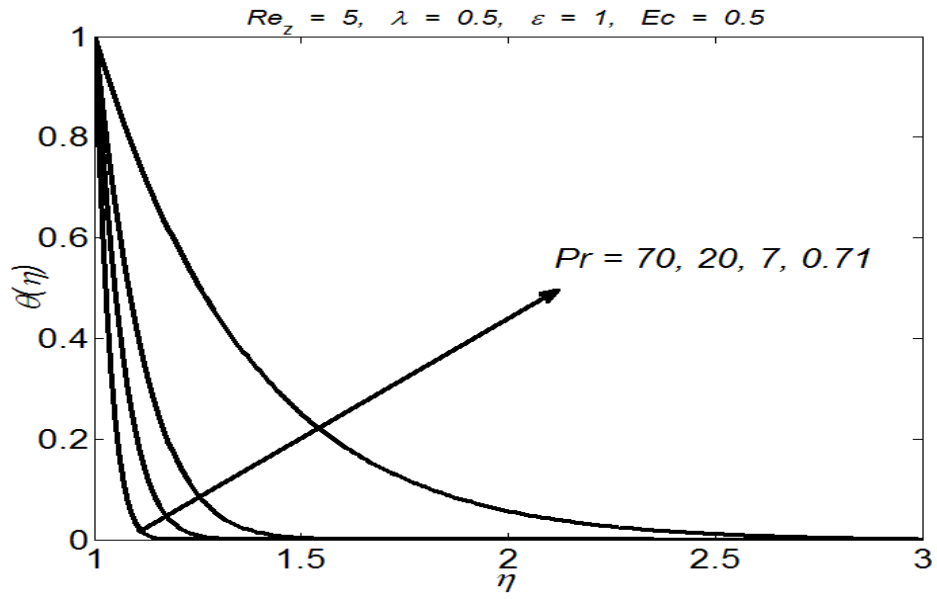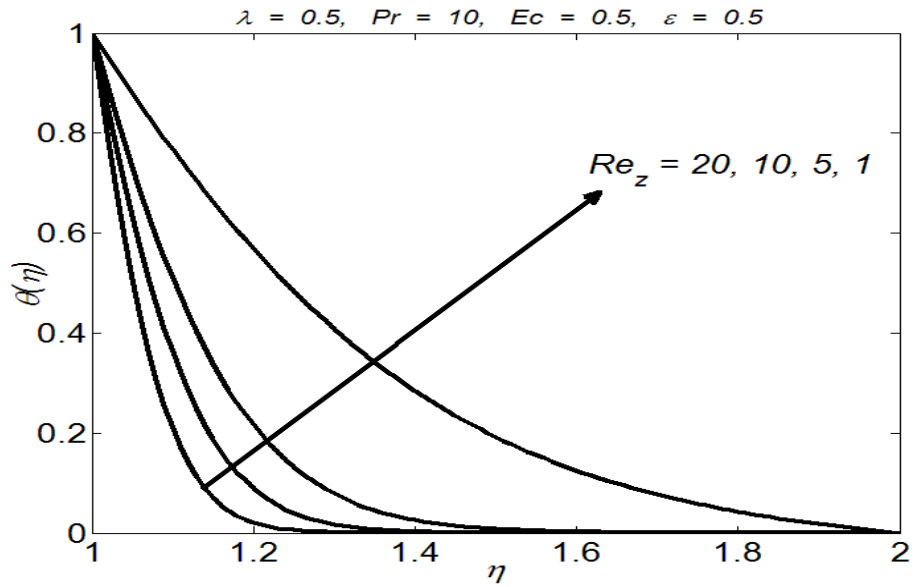
$Fig.(3.8)$. Behavior of the temperature profile θ for different values of the Reynolds number Re_z

59
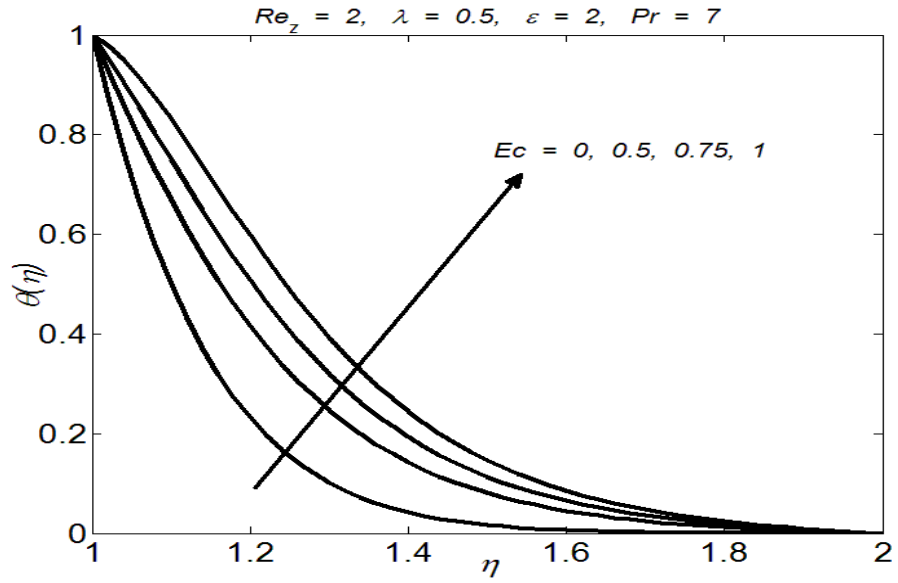
$Fig.(3.9)$. Behavior of the temperature profile θ for different values of the Eckert number Ec
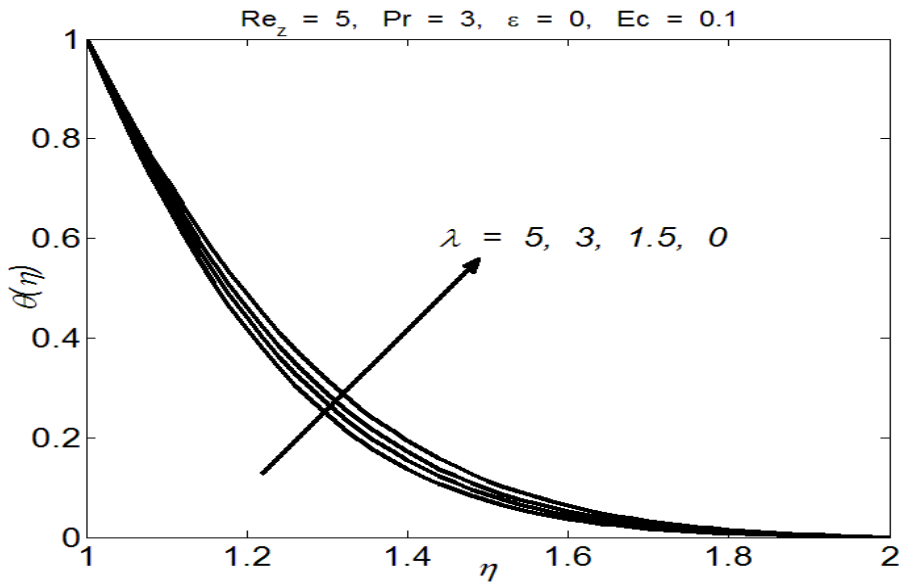
$Fig.(3.10)$. Behavior of the temperature profile θ for different choices of the natural convection parameter λ
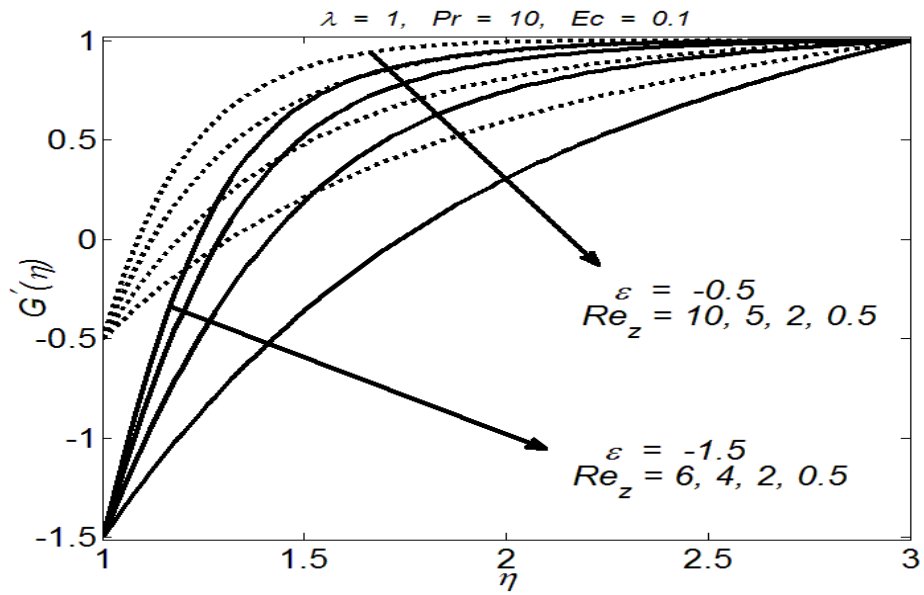
$Fig.$(3.11). Behavior of the velocity profile G' for different values of the Reynolds number Re_z in case of the shrinking cylinder when $\varepsilon = -0.5, \, -1.5$

	$G''(1)$					
$\mathrm{Re}_z\backslash\lambda$	0	0.25	0.5	0.75	1	2
0.5	0.6728	0.7089	0.7449	0.7807	0.8163	0.9573
1	0.8509	0.9047	0.9582	1.0114	1.0643	1.2729
5	1.7187	1.8410	1.9624	2.0831	2.2029	2.6747
10	2.3804	2.5533	2.7250	2.8956	3.0649	3.7318
100	7.2597	7.8065	8.3494	8.8885	9.4239	11.5310
1000	22.6838	24.4132	26.1300	27.8347	29.5276	36.1898

$Table.$(3.1). Behavior of the shear stress at the surface of the cylinder for different values of the involved parameters

61

$Pr\backslash Re_z$				$-\theta'(1)$		
	0.5	1	5	10	50	100
0.7	1.0822	1.2520	2.2838	3.1297	6.7036	9.3797
1	1.1501	1.3768	2.6405	3.6354	7.8302	10.9717
7	2.1083	2.8599	6.0729	8.4816	18.6426	26.2554
10	2.4406	3.3316	7.1223	9.9641	21.9535	30.9365
20	3.2813	4.5168	9.7621	13.6947	30.2880	42.7207
70	5.7514	8.0022	17.5401	24.6905	54.8638	77.4726
100	6.7815	9.4572	20.7900	29.2856	65.1363	91.9993

$Table.$(3.2). Behavior of the heat flux at the surface of the cylinder
for different values of the involved parameters

3.6   Conclusion

Noticeable conclusions obtained from the above study are

- The nondimensional velocity profile G' decreases with the increase in the Reynolds number Re_z, when the stretching ratio $\varepsilon > 1$.

- The nondimensional velocity profile G' increaeses with the increase in the Reynolds number Re_z, when the stretching ratio $\varepsilon < 1$.

- The velocity profile G' increases with increase in the natural convection parameter λ.

- The nondimensional temperature profile θ decreases with the increase in the Prandtl number Pr, the Reynolds number Re_z and the natural convection parameter λ.

- The temperature profile θ increases with increase in the Eckert number Ec.

- The shear stress at the surface increases with increase in the Reynolds number Re_z.

- The heat flux at the surface increases with increase in the Prandtl number Pr.

- The skinfriction coefficient c_f increases with increase in the natural convection parameter λ.

- The local Nusselt number Nu increases with increase in the Reynolds number Re_z.

Chapter 4

Annular axisymmetric stagnation flow of a Casson fluid through porous media in a moving cylinder

4.1 Introduction

The present chapter provides an investigation for the flow of a non-Newtonian Casson fluid flowing through porous medium. The fluid is assumed to be flowing through the annular region between the two concentric cylinders. The infinite inner cylinder is rotating as well as translating along the axial direction while the finite outer cylinder is kept fixed. For solution of the problem, the governing equations are nondimensionalized using a similarity transformation; the obtained system of ordinary differential equations is then solved numerically using the 5^{th}order Runge-Kutta Fehlberg method. The behavior of velocity and temperature profiles is discussed in detail for the parameters involved.

4.2 Formulation

Consider an incompressible flow of a Casson fluid between two cylinders flowing through porous medium. The flow is assumed to be axisymmetric about z-axis. The inner cylinder is of radius R rotating with an angular velocity Ω and moving with velocity W in the axial z-direction. The

inner cylinder is enclosed by an outer cylinder of radius b_0R. The fluid is injected radially with velocity U from the outer cylinder towards the inner cylinder. The geometry of the problem is shown in $Fig.\,(1.1)$, whereas the velocity and temperature profiles are stated in $Eqs.\,(1.1)$ and (1.2). The governing equations of conservation of mass, momentum, and energy are

$$\text{div } \mathbf{V} = \mathbf{0}, \tag{4.1}$$

$$\rho\frac{d\mathbf{V}}{dt} = \text{div } \mathbf{S} - \frac{\nu\phi_p}{k_0}\mathbf{V}, \tag{4.2}$$

$$\rho c_p\frac{dT}{dt} = -\text{div } \mathbf{q}, \tag{4.3}$$

where ν is the kinematic viscosity, ϕ_p is porosity of porous space and k_0 is permeability of porous space. The Cauchy stress tensor $\mathbf{S}$ for Casson fluid in simplified form can be defined as

$$\mathbf{S} = -p\mathbf{I} + \mu(1 + 1/\beta_c)\mathbf{A}_1, \tag{4.4}$$

where β_c is the Casson fluid parameter. The governing boundary layer equations of motion and heat transfer are

$$r\frac{\partial V_z}{\partial z} + \frac{\partial(rV_r)}{\partial r} = 0, \tag{4.5}$$

$$V_r\frac{\partial V_r}{\partial r} + V_z\frac{\partial V_r}{\partial z} - \frac{V_\theta^2}{r} = -\frac{1}{\rho}\frac{\partial p}{\partial r} + \nu(1 + \frac{1}{\beta_c})(\frac{\partial^2 V_r}{\partial r^2} + \frac{1}{r}\frac{\partial V_r}{\partial r} + \frac{\partial^2 V_r}{\partial z^2} - \frac{V_r}{r^2}) - \frac{\nu\phi_p}{k_0}V_r, \tag{4.6}$$

$$V_r\frac{\partial V_\theta}{\partial r} + V_z\frac{\partial V_\theta}{\partial z} + \frac{V_rV_\theta}{r} = \nu(1 + \frac{1}{\beta_c})(\frac{\partial^2 V_\theta}{\partial r^2} + \frac{1}{r}\frac{\partial V_\theta}{\partial r} + \frac{\partial^2 V_\theta}{\partial z^2} - \frac{V_\theta}{r^2}) - \frac{\nu\phi_p}{k_0}V_\theta, \tag{4.7}$$

$$V_r\frac{\partial V_z}{\partial r} + V_z\frac{\partial V_z}{\partial z} = -\frac{1}{\rho}\frac{\partial p}{\partial z} + \nu(1 + \frac{1}{\beta_c})(\frac{\partial^2 V_z}{\partial r^2} + \frac{1}{r}\frac{\partial V_z}{\partial r} + \frac{\partial^2 V_z}{\partial z^2}) - \frac{\nu\phi_p}{k_0}V_z, \tag{4.8}$$

$$V_r\frac{\partial T}{\partial r} + V_z\frac{\partial T}{\partial z} = \alpha(\frac{\partial^2 T}{\partial r^2} + \frac{1}{r}\frac{\partial T}{\partial r} + \frac{\partial^2 T}{\partial z^2}), \tag{4.9}$$

where (V_r, V_θ, V_z) are the velocity components along (r, θ, z) axes and α is the thermal diffusivity. The corresponding boundary conditions are

$$V_r(R, z) = 0, \quad V_\theta(R, z) = \Omega l_0, \quad V_z(R, z) = W, \quad T(R, z) = T_{in}, \tag{4.10}$$

$$V_r(b_0R, z) = -U, \quad V_\theta(b_0R, z) = 0, \quad V_z(b_0R, z) = 0, \quad T(b_0R, z) = T_{out}, \tag{4.11}$$

where T_{in} is the fluid temperature at the surface of the inner cylinder, T_{out} is the fluid temperature at the surface of the outer cylinder and l_0 is the reference length.

4.3 Solution of the problem

The system of nonlinear partial differential equations (4.5) to (4.9) subject to the boundary conditions (4.10) and (4.11) are simplified by invoking the similarity transformations defined in *Eqs.* (1.19) to (1.21). The resulting system of ordinary differential equations is of the form

$$(1 + 1/\beta_c)(\eta f^{(IV)} + 2f''') + \text{Re}(ff''' - f'f'') - kpf'' = 0, \tag{4.12}$$

$$(1 + 1/\beta_c)(\eta g'' + g') + \text{Re}\left(fg' - f'g\right) - kpg = 0, \tag{4.13}$$

$$(1 + 1/\beta_c)(\eta h'' + h' - \frac{h}{4\eta}) + \text{Re}\left(2fh' + \frac{fh}{\eta}\right) - kph = 0, \tag{4.14}$$

$$\eta\theta'' + \theta' + \text{Pr}\,\text{Re}\,f\theta' = 0, \tag{4.15}$$

in which $Re = UR/2\nu$ is the Reynolds number, $kp = R^2\phi_p/4k_0$ is the porosity parameter and $\text{Pr} = \nu/\alpha$ is the Prandtl number. The nondimensional boundary conditions are stated in *Eqs.* (1.28) to (1.30). For numerical solution of the problem, we consider

$$F_1 = f', \quad F_2 = F_1', \quad F_3 = F_2', \quad F_4 = g', \quad F_5 = h' \text{ and } F_6 = \theta' \tag{4.16}$$

then the resulting system is

$$(1 + 1/\beta_c)(\eta F_3' + 2F_3) + \text{Re}(fF_3 - F_1F_2) - kpF_2 = 0, \tag{4.17}$$

$$(1 + 1/\beta_c)(\eta F_4' + F_4) + \text{Re}\left(fF_4 - F_1g\right) - kpg = 0, \tag{4.18}$$

$$(1 + 1/\beta_c)(\eta F_5' + F_5 - \frac{h}{4\eta}) + \text{Re}\left(2fF_5 + \frac{fh}{\eta}\right) - kph = 0, \tag{4.19}$$

$$\eta F_6' + F_6 + \text{Pr}\,\text{Re}\,fF_6 = 0, \tag{4.20}$$

with the boundary conditions

$$f(1) = 0, \quad F_1(1) = 0, \quad g(1) = 1, \quad h(1) = 1, \quad \theta(1) = 0, \tag{4.21}$$

$$f(b_0) = \sqrt{b_0}, \quad F_1(b_0) = 0, \quad g(b_0) = 0, \quad h(b_0) = 0, \quad \theta(b_0) = 1. \tag{4.22}$$

The above system of first order ordinary differential equations is solved numerically with the help of 5^{th}order Runge-Kutta Fehlberg method and the obtained results are discussed in the next section.

4.4   Results and discussion

The numerical solutions of the problem of steady, incompressible, non-Newtonian Casson fluid flowing through the annular region between the concentric cylinders are obtained through the 5th order Runge-Kutta Fehlberg method. The outer cylinder is assumed to be fixed while the inner cylinder is translating with a constant axial velocity and is also rotating axisymmetrically about the axial direction through some porous medium. The behavior of non-dimensional velocity profiles for the involved parameters is plotted in $Figs.(4.1)$ to (4.12) when $b_0 = 2$. In these figures f is associated with the fluid flow in radial direction, g is concerned with the fluid flow in axial direction while h represents the rotation effects in the fluid flow caused due to the rotation of the inner cylinder. $Figs.(4.1)$ to (4.3) show the behavior of radial velocity with respect to the Reynolds numbers Re, Casson fluid parameter β_c and the porosity parameter kp respectively. From $Fig.(4.1)$ it is noted that with the increase in the Reynolds numbers Re the non-dimensional radial velocity increases. This happen because higher radial velocity is concerned with a higher injunction velocity (also a higher Reynolds number) from outer cylinder towards the inner cylinder. $Fig.(4.2)$ shows that with increase in the Casson fluid parameter β_c increases the radial velocity f. $Fig.(4.3)$ indicates that by increasing the porosity parameter kp the radial velocity decreases because higher kp corresponds to porous medium with lesser permeability and thus fluid flow encounters more resistance. The influence of Reynolds number Re over the velocity gradient f' is sketched in $Fig.(4.4)$ that indicates that near the surface of inner cylinder, velocity gradient increases with the increase in the Reynolds number Re while near the surface of the outer cylinder, increase in Re decreases the velocity gradient. $Figs.(4.5)$ and (4.6) give the impact of Casson fluid parameter β_c and the porosity parameter kp over the velocity gradient f'. From these graphs it is observed that near the surface of inner cylinder increase in the Casson fluid parameter β_c increases the velocity gradient f' while increase in the porosity parameter kp decreases the velocity gradient f', whereas near the surface of

66

outer cylinder, increase in the Casson fluid parameter β_c decreases the velocity gradient f' while increase in the porosity parameter kp increases the velocity gradient f'. $Figs.$(4.7) to (4.9) show the behavior of axial velocity profile g for the Reynolds number Re, the Casson fluid parameter β_c and the porosity parameter kp. From these plots it is noticed that the axial velocity g decreases with increase in all the parameters the Reynolds numer Re, the Casson fluid parameter β_c and the porosity paramter kp. $Figs.$(4.10) to (4.12) show the pattern adopted by the non-dimensional rotation velocity h for the involved parameters the Reynolds number Re, the Casson fluid parameter β_c and the porosity parameter kp respectively. From these figures it is evident that with the increase in all the three parameters the angular velocity profile h decreases. The variation in temperature flow θ for different values of the Prandtl number Pr and the Reynolds number Re is presented in $Figs.$(4.13) and (4.14). From these sketches it is noted that with the increase in both the Prandtl number Pr and the Reynolds number Re the non-dimensional temperature profile increases.

To validate the accuracy of the current numerical results the present Fehlberg solutions are compared as a special case with the existing work of Hong and Wang [34] in $Table.$(4.1). The boundary derivatives obtained for the velocity profiles are in excellent agreement. $Table.$(4.2) predicts the behavior of boundary derivatives for the velocity profiles f and g computed at the surface of the inner cylinder that proportional to the skinfriction at the surface of the inner cylinder computed for different values of the Casson fluid parameter β_c and the porosity parameter kp. From $Table.$(4.2) it is evident that increasing the Casson fluid parameter β_c and the porosity parameter kp also increases the skinfriction coefficient. $Table.$(4.3) contains the values for the boundary derivative of the angular velocity profile that are computed for different Reynolds number Re and Prandtl number Pr and that corresponds to the azimuthal shear stress at the surface of the inner cylinder. From $Table.$(4.3) it is observed that increase in both the Reynolds number Re and the Prandtl number Pr increases the azimuthal shear stress. $Table.$(4.4) shows the numerical values of the boundary derivative of the temperature flow function θ that predicts the behavior of Nusselt numbers Nu against Prandtl number Pr and Reynolds number Re. From $Table.$(4.4) it is observed that the Nusselt numbers increases with the increase in both the Prandtl number Pr and the Reynolds number Re.
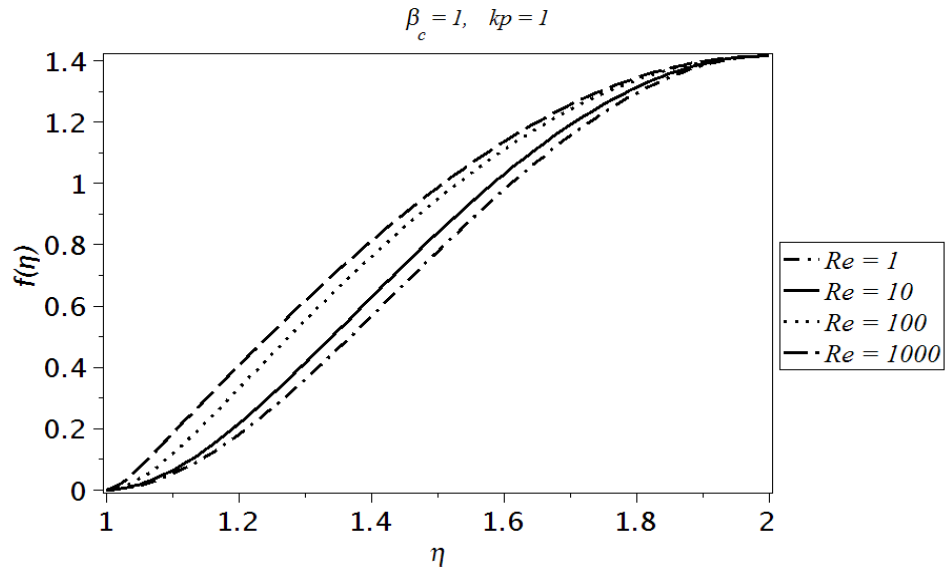
$Fig.(4.1)$. Influence of the Reynolds number Re over the velocity profile f
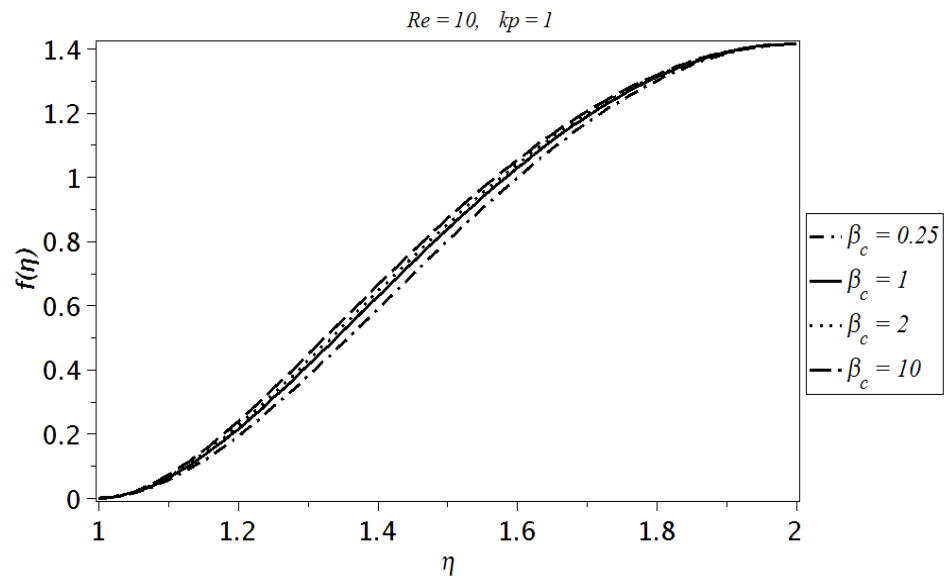
$Fig.(4.2)$. Influence of the Casson fluid parameter β_c over the velocity profile f
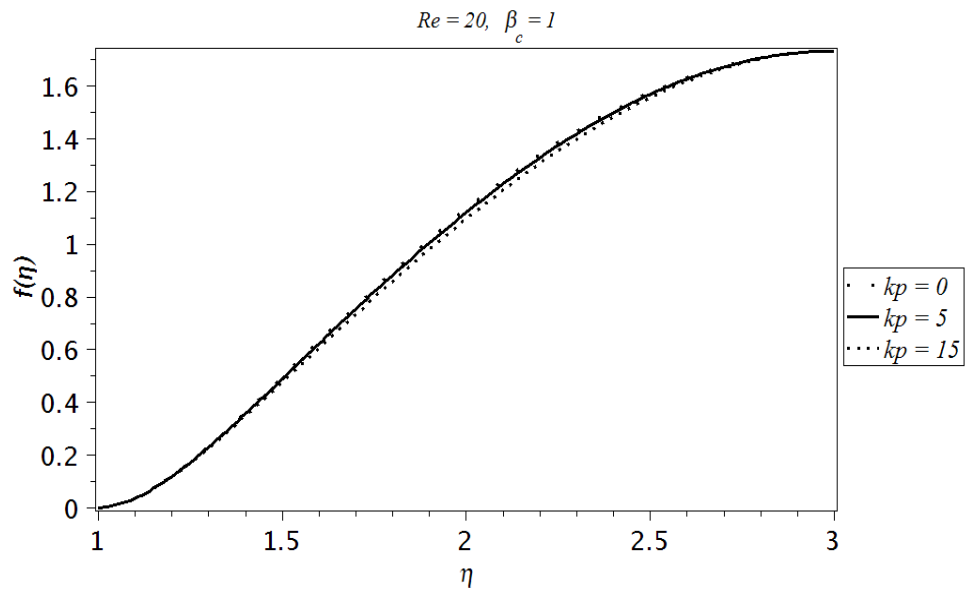
$Fig.(4.3)$. Influence of the porosity parameter k_p over the velocity profile f
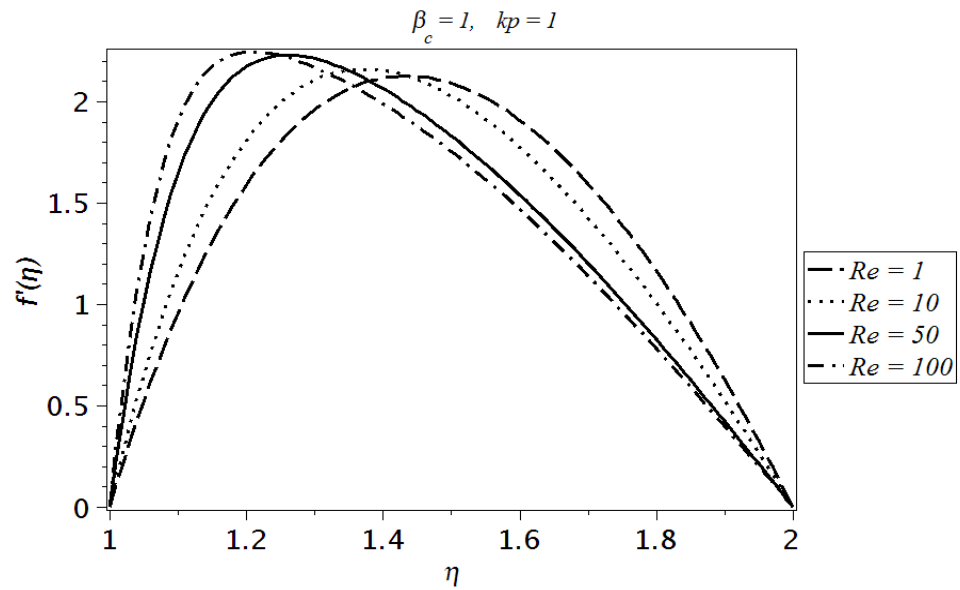
$Fig.(4.4)$. Influence of the Reynolds number Re over the velocity profile f'
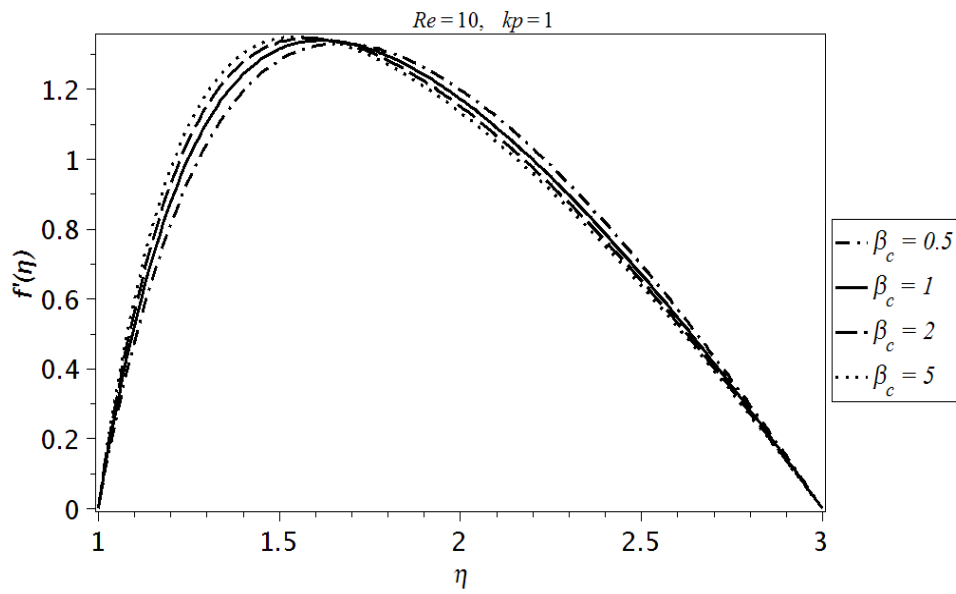
Fig.(4.5). Influence of the Casson fluid parameter β_c over the velocity gradient f'
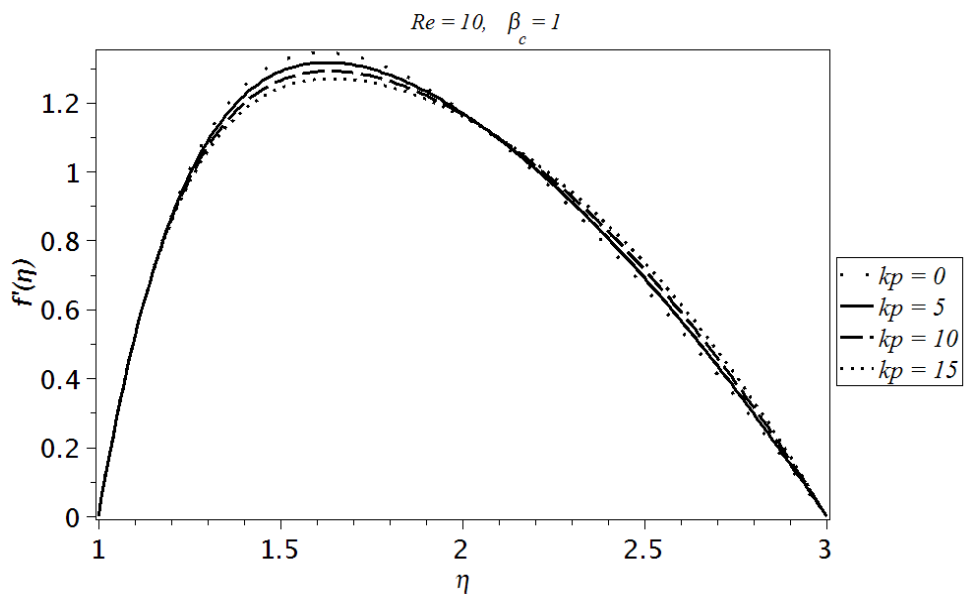
Fig.(4.6). Influence of the porosity parameter k_p over the velocity gradient f'

$Fig.(4.7)$. Influence of the Reynolds number Re over the velocity profile g

$Fig.(4.8)$. Influence of the Casson fluid parameter β_c over the velocity profile g

71
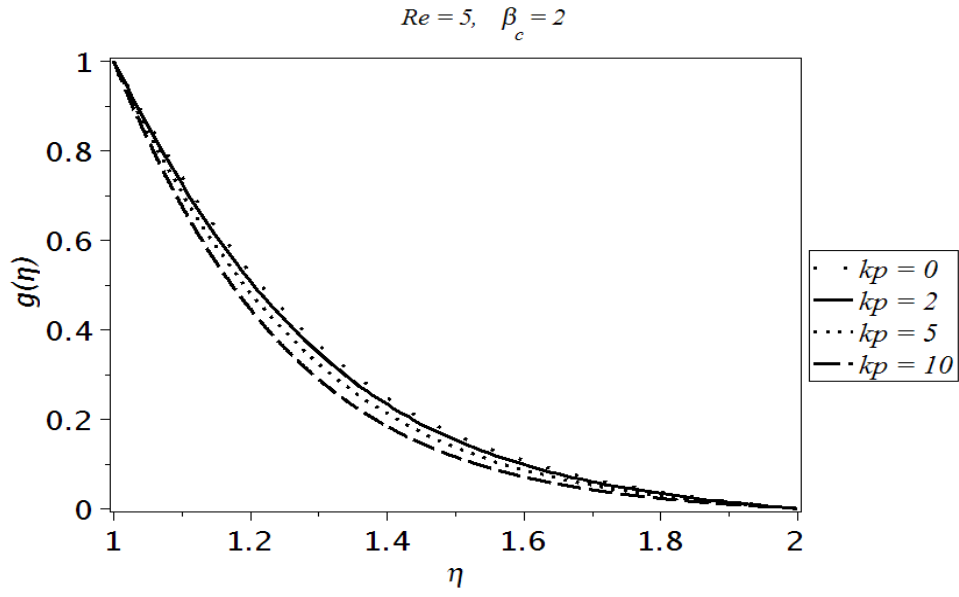
$Fig.(4.9)$. Influence of the porosity parameter k_p over the velocity profile g
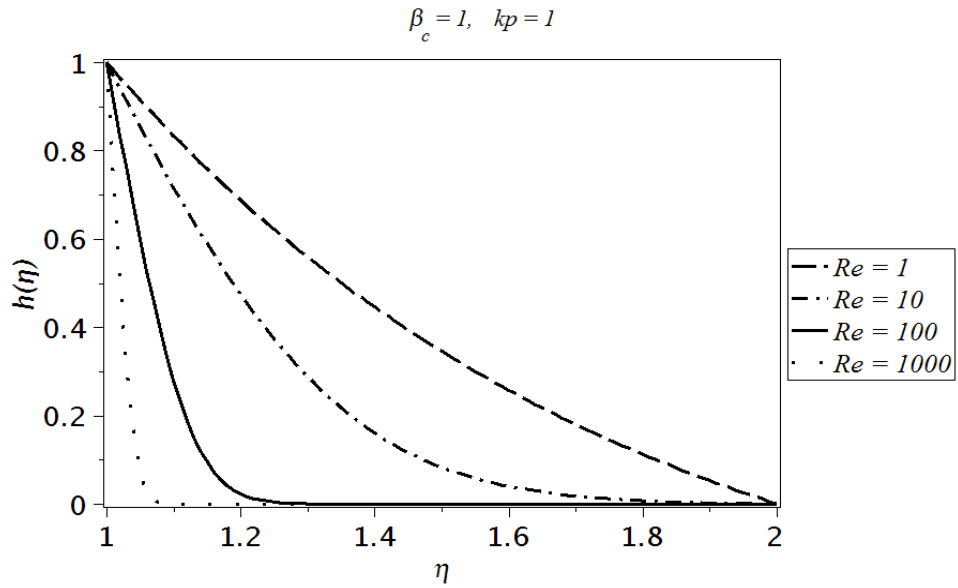
$Fig.(4.10)$. Influence of the Reynolds number Re over the velocity profile h

72
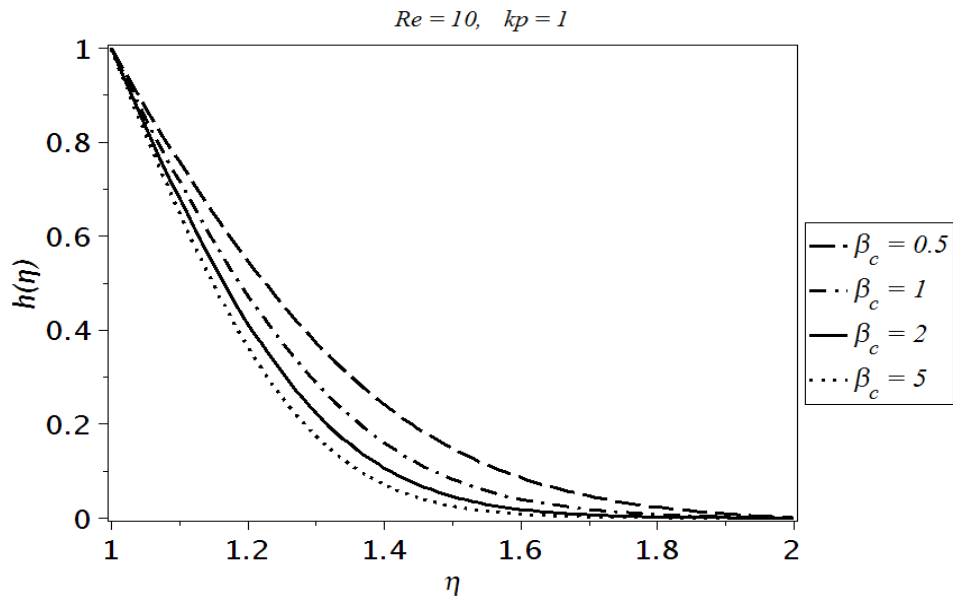
Fig.(4.11). Influence of the Casson fluid parameter β_c over the velocity profile h
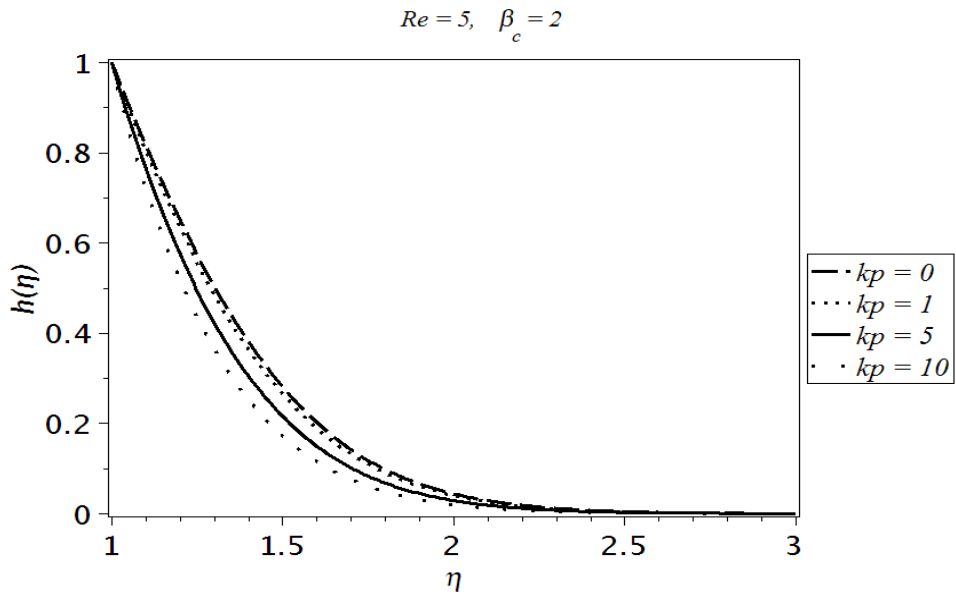
Fig.(4.12). Influence of the porosity parameter k_p over the velocity profile h

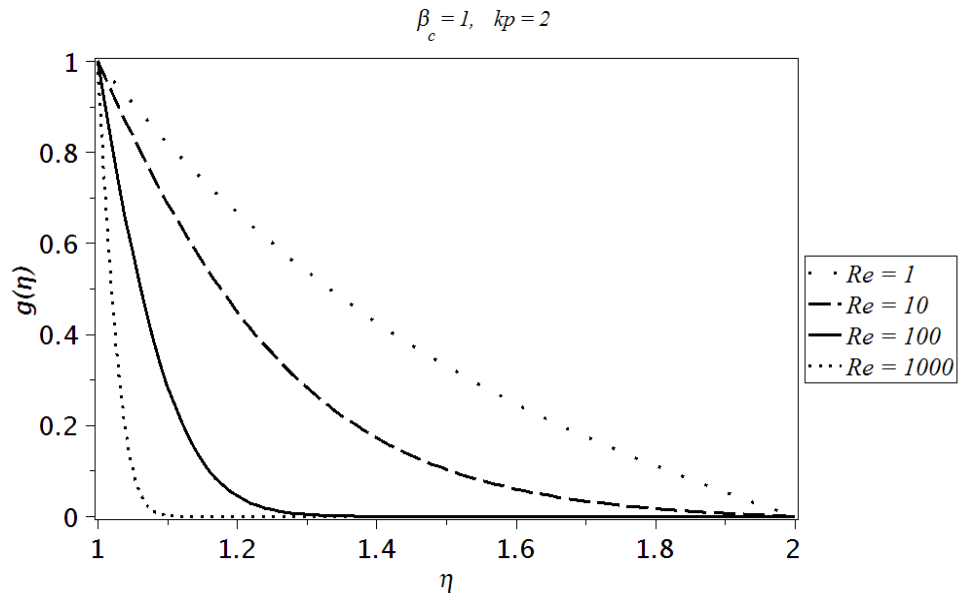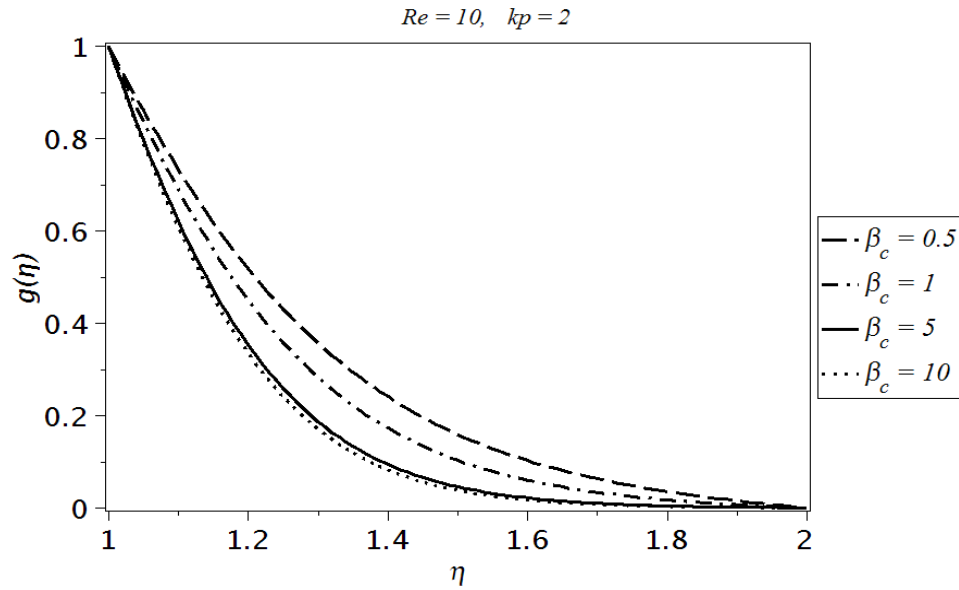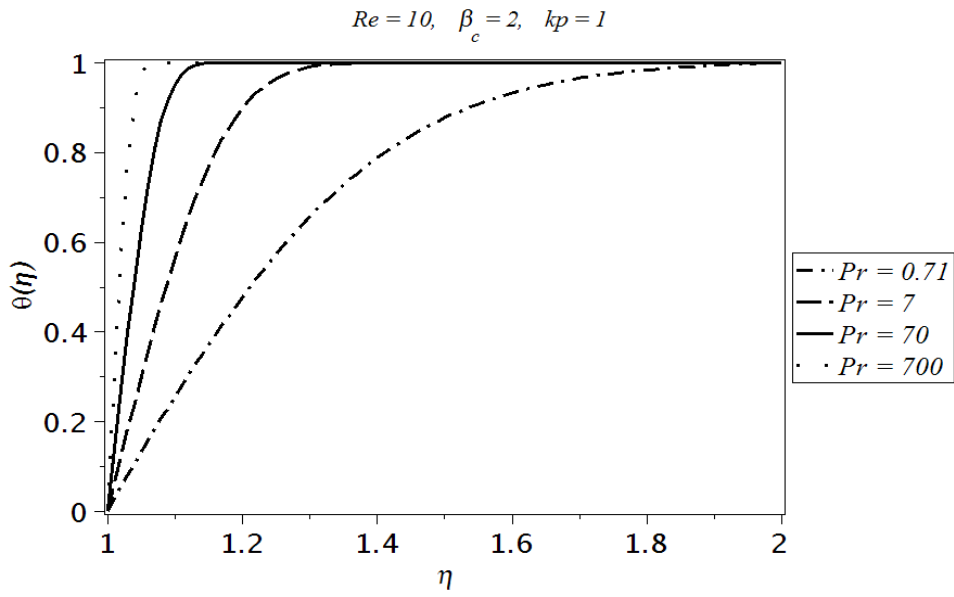*Fig.*(4.13). Influence of the Prandtl number Pr over the temperature profile

θ
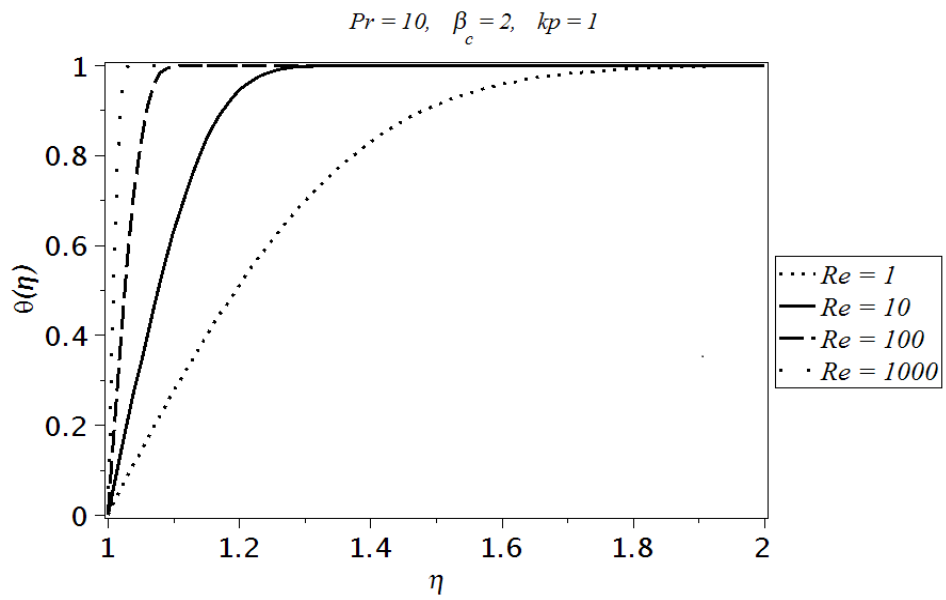
Fig.(4.14). Influence of the Reynolds number Re over the temperature

profile θ

	$f''(l)$		$-f'''(l)$		$-g'(l)$		$-h'(l)$	
Re	Present	[34]	Present	[34]	Present	[34]	Present	[34]
0.1	11.001	11.0010	36.1443	36.1443	1.4963	1.4963	10.5151	10.5151
1	11.677	11.6772	41.0795	41.0797	1.9309	1.9309	10.6511	10.6511
10	17.5345	17.5348	93.565	93.5670	4.3856	4.3856	12.0407	12.0407
100	44.449	44.4492	790.731	590.738	12.6450	12.6450	24.8226	24.8226
1000	132.436	132.436	8511.80	5211.80	38.7853	38.7853	75.1076	75.1076

$Table.(4.1)$. Comparison of the boundary derivatives of the present results with the work [34] when $\beta_c = 20000$ and $kp = 0$

	$f'(l)$				
β_c/kp	0.2	0.5	1	2	5
0.5	13.3664	13.3736	13.3855	13.4094	13.4813
1	14.4999	14.5085	14.5229	14.5517	14.6393
5	16.5834	16.5927	16.6084	16.6401	16.7389
50	17.4308	17.4399	17.4552	17.4866	17.5859
500	17.5296	17.5387	17.5539	17.5852	17.6845
5000	17.5396	17.5487	17.5640	17.5953	17.6945
	$-g'(l)$				
0.5	2.8048	2.8207	2.8470	2.8991	3.0514
1	3.2879	3.3079	3.3410	3.4066	3.5983
5	4.0711	4.0972	4.1405	4.2261	4.4765
50	4.3670	4.3953	4.4422	4.5352	4.8070
500	4.4009	4.4295	4.4768	4.5706	4.8448
5000	4.4044	4.4329	4.4803	4.5742	4.8487

$Table.(4.2)$. Behavior of boundary derivatives for velocity profiles computed for different β_c and kp when Re $= 10$

	$-h'(l)$				
Re/kp	0.2	0.5	1	2	5
0.5	1.6705	1.7335	1.8358	2.0309	2.5534
1	1.7987	1.8584	1.9555	2.1412	2.6422
5	2.7703	2.8095	2.8740	3.0003	3.3588
10	3.6861	3.7142	3.7608	3.8529	4.1216
100	10.5678	10.5766	10.5912	10.6203	10.7076
1000	32.4320	32.4348	32.4394	32.4486	32.4763

$Table.(4.3)$. Behavior of boundary derivatives for angular velocity profiles computed for different Pr and Re when $\beta_c = 5$

	$\Theta'(1)$				
Re/Pr	0.7	7	20	70	700
0.5	1.5063	2.0426	2.8658	4.4448	9.7080
1	1.5707	2.5416	3.6821	5.6738	12.3513
5	2.0910	4.6744	6.7300	10.3204	22.4300
10	2.6897	6.2203	8.9540	13.7367	29.8783
100	7.6624	17.8594	25.7870	39.6852	
1000	23.3458	54.8459	79.3885		

Table.(4.4). Behavior of boundary derivatives for

temperature profile computed for different Pr and Re

when $\beta_c = 5, kp = 2$

4.5   Conclusion

Brief conclusions obtained from the above study are stated as

- With increase in the Reynolds number Re and the Casson fluid parameter β, the velocity profile f increases.

- With increase in the porosity parameter kp the velocity profile f decreases.

- With increase in the Reynolds number Re and the Casson fluid parameter β, the velocity profile g decreases.

- With increase in the Reynolds number Re and the Casson fluid parameter β, the velocity profile h decreases.

- With increase in the porosity parameter kp the nondimensional velocity profiles g and h decreases.

- The nondimensional temperature profile θ increases with the increase in the Reynolds number Re, the Prandtl number Pr.

- The shear stress at the surface of the inner cylinder increases with increase in the Casson fluid parameter β_c.

- The heat flux at the surface of the inner cylinder increases with increase in the Prandtl number Pr.

76

Chapter 5

Axisymetric stagnation flow of a micropolar nanofluid in a moving cylinder

5.1 Introduction

In this chapter, an analysis is carried out for the axisymmetric stagnation flow of a micropolar fluid containing nanoparticles in a moving cylinder. The coupled nonlinear partial differential equations of the problem are simplified with the help of similarity transformations and the resulting coupled nonlinear differential equations are solved numerically by means of the 5th order Runge-Kutta Shooting method. The features of the flow phenomena, inertia, heat transfer and nanoparticles are analyzed and discussed.

5.2 Formulation

Let us consider an incompressible flow of a micropolar nanofluid between two cylinders such that the flow is axisymmetric about z-axis. The inner cylinder is of radius R rotating with angular velocity Ω and moving with velocity W in the axial z-direction. The inner cylinder is enclosed by an outer cylinder of radius $b_0 R$. Further, the fluid is injected radially with velocity U from the outer cylinder towards the inner cylinder. The geometry of the problem is

shown in $Fig.(1.1)$. The governing equations of conservation of mass, energy and nanoparticle concentration are staded in $Eqs.(1.7), (1.9)$ and (1.10) respectively, while the linear and angular momentum equations are

$$\rho \frac{d\mathbf{V}}{dt} = -\boldsymbol{\nabla}p + k\boldsymbol{\nabla} \times \mathbf{W} + (\mu + k)\boldsymbol{\nabla}^2\mathbf{V}, \tag{5.1}$$

$$\rho j \frac{d\mathbf{W}}{dt} = -2k\mathbf{W} + k\boldsymbol{\nabla} \times \mathbf{V} - \boldsymbol{\gamma}_m(\boldsymbol{\nabla} \times \boldsymbol{\nabla} \times \mathbf{W}) + (\alpha_m + \beta_m + \gamma_m)\boldsymbol{\nabla}(\boldsymbol{\nabla} \times \mathbf{W}), \tag{5.2}$$

where μ is the dynamic viscosity, k is the vertex viscosity, j is the microrotation density, $\mathbf{W}(r,z)$ is the angular microrotation momentum and $\alpha_m, \beta_m, \gamma_m$ are the micropolar constants.

For the velocity field $\mathbf{V}(r,z) = (V_r(r,z), V_\theta(r,z), V_z(r,z))$, angular velocity $\mathbf{W}(r,z) = (0, N^*(r,z), 0)$, heat transfer profile $T = T(r,z)$ and the nanoparticle concentration function $\phi = \phi(r,z)$ the equations of conservation of mass, momentum, angular momentum, heat transfer and the nanoparticle concentration can be expressed as

$$r\frac{\partial V_z}{\partial z} + \frac{\partial(rV_r)}{\partial r} = 0, \tag{5.3}$$

$$V_r\frac{\partial V_r}{\partial r} + V_z\frac{\partial V_r}{\partial z} - \frac{V_\theta^2}{r} = --\frac{1}{\rho}\frac{\partial p}{\partial r} + (\mu + k)(\frac{\partial^2 V_r}{\partial r^2} + \frac{1}{r}\frac{\partial V_r}{\partial r} + \frac{\partial^2 V_r}{\partial z^2} - \frac{V_r}{r^2}) - k\frac{\partial N^*}{\partial z}, \tag{5.4}$$

$$V_r\frac{\partial V_\theta}{\partial r} + V_z\frac{\partial V_\theta}{\partial z} + \frac{V_r V_\theta}{r} = (\mu + k)(\frac{\partial^2 V_\theta}{\partial r^2} + \frac{1}{r}\frac{\partial V_\theta}{\partial r} + \frac{\partial^2 V_\theta}{\partial z^2} - \frac{V_\theta}{r^2}), \tag{5.5}$$

$$V_r\frac{\partial V_z}{\partial r} + V_z\frac{\partial V_z}{\partial z} = --\frac{1}{\rho}\frac{\partial p}{\partial z} + (\mu + k)(\frac{\partial^2 V_z}{\partial r^2} + \frac{1}{r}\frac{\partial V_z}{\partial r} + \frac{\partial^2 V_z}{\partial z^2}) + k\left(\frac{\partial N^*}{\partial r} + \frac{1}{r}N^*\right), \tag{5.6}$$

$$\rho j\left(V_r\frac{\partial N^*}{\partial r} + V_z\frac{\partial N^*}{\partial z}\right) = -2kN^* + k\left(\frac{\partial V_r}{\partial z} - \frac{\partial V_z}{\partial r}\right) + \gamma_m\left(\frac{\partial^2 N^*}{\partial r^2} + \frac{1}{r}\frac{\partial N^*}{\partial r} + \frac{\partial^2 N^*}{\partial z^2} - \frac{1}{r^2}N^*\right), \tag{5.7}$$

$$V_r\frac{\partial T}{\partial r} + V_z\frac{\partial T}{\partial z} = \alpha(\frac{\partial^2 T}{\partial r^2} + \frac{1}{r}\frac{\partial T}{\partial r} + \frac{\partial^2 T}{\partial z^2}) + \frac{\rho^* c_p^*}{\rho c_p}[D_B\left(\frac{\partial \phi}{\partial r}\frac{\partial T}{\partial r} + \frac{\partial \phi}{\partial z}\frac{\partial T}{\partial z}\right)$$
$$+ \frac{D_T}{T_{in}}\left((\frac{\partial T}{\partial r})^2 + (\frac{\partial T}{\partial z})^2\right)], \tag{5.8}$$

$$V_r\frac{\partial \phi}{\partial r} + V_z\frac{\partial \phi}{\partial z} = D_B\left(\frac{\partial^2 \phi}{\partial r^2} + \frac{1}{r}\frac{\partial \phi}{\partial r} + \frac{\partial^2 \phi}{\partial z^2}\right) + \frac{D_T}{T_{in}}(\frac{\partial^2 T}{\partial r^2} + \frac{1}{r}\frac{\partial T}{\partial r} + \frac{\partial^2 T}{\partial z^2}), \tag{5.9}$$

where $Eq.(5.3)$ is the continuity equation, $Eqs.(5.4)$ to (5.6) are the r, θ and z components of momentum equation, $Eqs.(5.7)$ to (5.9) are the angular momentum, temperature and nanoparticle concentration equations, respectively.

5.3 Solution of the problem

To simplify the above system of nonlinear coupled partial differential equations the similarity transformations defined in $Eqs.\,(1.19)$ to (1.22) are used along with the following relation for the angular momentum velocity profile N^*

$$N^* = 2\frac{U}{R}M\left(\eta\right)\xi + \frac{W}{R}P(\eta). \tag{5.10}$$

With the help of these transformations, $Eq.\,(5.3)$ is identically satisfied and $Eqs.\,(5.4)$ to (5.9) take the following forms

$$\eta f^{(IV)} + 2f''' + \frac{\mathrm{Re}}{(1+K)}(ff''' - f'f'') + \frac{K}{8\,(1+K)\,\sqrt{\eta}}\left(4\eta M'' + 4M' - \frac{M}{\eta}\right) = 0, \tag{5.11}$$

$$\eta g'' + g' + \frac{\mathrm{Re}}{(1+K)}\left(fg' - f'g\right) + \frac{K}{(1+K)}\sqrt{\eta}\left(4P' + \frac{2P}{\eta}\right) = 0, \tag{5.12}$$

$$4\eta h'' + 4h' - \frac{h}{\eta} + \frac{\mathrm{Re}}{(1+K)}\left(4fh' + \frac{2fh}{\eta}\right) = 0, \tag{5.13}$$

$$4\eta M'' + 4M' - \frac{M}{\eta} - \frac{4\,\mathrm{Re}}{\Lambda}(fM' + f'M) - \frac{2K\delta}{\Lambda}\left(M + \sqrt{\eta}f''\right) = 0, \tag{5.14}$$

$$4\eta P'' + 4P' - \frac{P}{\eta} - \frac{2K\delta}{\Lambda}\left(P + \sqrt{\eta}g'\right) - \frac{4\,\mathrm{Re}}{\Lambda}\left(fP' + Mg\right) = 0, \tag{5.15}$$

$$\eta\theta'' + \theta' + \mathrm{Pr}\,\mathrm{Re}\,f\theta' + Nb\eta\theta'\Psi' + Nt\eta\theta'^2 = 0, \tag{5.16}$$

$$\eta\Psi'' + \Psi' + Le\,\mathrm{Pr}\,\mathrm{Re}\,f\Psi' + \frac{Nt}{Nb}\left(\eta\theta'' + \theta'\right) = 0, \tag{5.17}$$

where $\mathrm{Re} = UR/2\nu$ is the cross-flow Reynolds number, $\mathrm{Pr} = v/\alpha$ is the Prandtl number, $\Lambda = \gamma_m/\mu j$ is the micropolar coefficient, $\delta = R^2/j$ and $K = k/\mu$ are the micropolar parameters, $Le = \alpha/D_B$ is the Lewis number, $Nb = \rho^* c_p^* D_B\left(\phi_{out} - \phi_{in}\right)/\rho c_p\alpha$ is the Brownian motion parameter and $Nt = \rho^* c_p^* D_T\left(T_{out} - T_{in}\right)/\rho c_p\alpha T_{in}$ is the thermophoresis parameter. The boundary conditions in nondimensional form the linear velocities, temperature are nanoparticle concentration profiles are listed in $Eqs.\,(1.28)$ to (1.31) while the boundary conditions associated with the nondimensional angular momentum profile are of the form

$$M\left(1\right) = -2nf''\left(1\right), \quad M\left(b_0\right) = 0, \quad P\left(1\right) = -2ng'\left(1\right), \quad P\left(b_0\right) = 0. \tag{5.18}$$

The solution of the above boundary value problem is obtained with the help of the 5th order shooting method and is discussed in the next section.

5.4   Results and discussion

The governing nonlinear partial differential equations of the axisymmetric stagnation flow of micropolar nanofluid in a moving cylinder are simplified by using similarity transformation and then the reduced highly nonlinear coupled differential equations are solved numerically with the help of 5th order shooting method. The velocity field for different values of the Reynolds number Re and the micropolar parameter K are plotted in $Figs.$ (5.1) to (5.7). $Fig.$ (5.1) shows the behavior of Reynolds number Re over the radial velocity profile $f(\eta)$. From the figure it is observed that with the increase in the Reynolds number Re, the radial velocity profile $f(\eta)$ increases. $Fig.$ (5.2) provides the impact of micropolar parameter K over the radial velocity profile $f(\eta)$. From $Fig.$ (5.2) it is noted that with the increase in the micropolar parameter K, the velocity profile $f(\eta)$ decreases. $Figs.$ (5.3) and (5.4) are plotted to observe the influence of Reynolds number Re and the micropolar parameter K over the velocity gradient $f'(\eta)$. From these graphs it is noted that with increase in the Reynolds number Re and the micropolar parameter K, the velocity gradient $f'(\eta)$ has a dual behavior. That is with the increase/decrease in the Reynolds number Re /micropolar parameter K, the velocity gradient $f'(\eta)$ increases near the surface of the inner cylinder, while the velocity gradient $f'(\eta)$ decreases near the surface of the outer cylinder. $Fig.$ (5.5) predicts the influence of Reynolds number Re over the velocity profile $g(\eta)$. From the sketch it is observed that with the increase in the Reynolds number Re, the velocity profile $g(\eta)$ decreases. The impact of micropolar parameter K over the velocity profile $g(\eta)$ is sketched in $Fig.$ (5.6). It is observed that the nondimensional velocity profile $g(\eta)$ increases with the increase in the micropolar parameter K. The nondimensional angular velocity profile $h(\eta)$ for different values of the Reynolds number Re is plotted in $Fig.$ (5.7). From the figure it is depicted that the angular velocity field $h(\eta)$ decreases with the increase in Reynolds number Re. The variation of microrotation functions M and P for different values of the involved parameters are plotted in $Figs.$ (5.8) to (5.12). $Fig.$ (5.8) shows the influence of micropolar parameter K over the microrotation velocity profile $M(\eta)$. From the plot it is

noticed that with the increase in the micropolar parameter K, the microrotation velocity profile $M(\eta)$ has a dual behavior. That is near the surface of the inner cylinder, increase in the micropolar parameter K decreases the microrotation profile $M(\eta)$, while near the surface of the outer cylinder, increase in the micropolar parameter K increases the microrotation velocity profile $M(\eta)$. $Fig.\,(5.9)$ gives the impact of the Reynolds number Re over the microrotation velocity profile $M(\eta)$. $Fig.\,(5.10)$ inculcates the influence of micropolar parameter Λ over the microrotation parameter $M(\eta)$. From the sketch it is noted that with the increase in the micropolar parameter Λ, the microrotation velocity profile $M(\eta)$ decreases. $Figs.\,(5.11)$ and (5.12) show the impact of micropolar parameter K and the Reynolds number Re over the microrotation velocity profile $P(\eta)$. From these graphs it is seen that with the increase in both the micropolar parameter K and the Reynolds number Re, the microrotation velocity profile $P(\eta)$ increases. The variation of temperature function $\theta(\eta)$ is presented in $Figs.\,(5.13)$ to (5.16) for different involved parameters. $Figs.\,(5.13)$ and (5.14) show the influence of the Prandtl number Pr and the Reynolds number Re over the temperature profile $\theta(\eta)$. From these figures it is observed that with the increase in both the Prandtl number Pr and the Reynolds number Re, the temperature flow rate $\theta(\eta)$ increases. $Figs.\,(5.15)$ and (5.16) display the impact of the Brownian motion parameter Nb and the thermophoresis parameter Nt over the temperature function $\theta(\eta)$. From these plots it is noted that with the increase in both the Brownian motion parameter Nb and the thermophoresis parameter Nt, the temperature profile $\theta(\eta)$ increases. The variation of the nanoparticle concentration function $\psi(\eta)$ for different parameters is plotted in $Figs.\,(5.17)$ to (5.20). $Figs.\,(5.17)$, (5.18) and (5.19) are graphed to observe the impact of the Lewis number Le, the Prandtl number Pr and the Reynolds number Re over the nanoparticle concentration profile $\psi(\eta)$, respectively. From these plots it is noted that with the increase in Lewis number Le, Prandtl number Pr and the Reynolds number Re, the nanoparticle concentration function $\psi(\eta)$ also increases. $Fig.\,(5.20)$ gives the behavior of the thermophoresis parameter Nt over the nanopaticle concentration profile $\psi(\eta)$. From the plot it is observed that with the increase in the thermophoresis parameter Nt, the nanoparticle concentration profile $\psi(\eta)$ decreases.

$Table.\,(5.1)$ shows the behavior of boundary derivatives of the radial velocity profile $f(\eta)$ computed at the surface of the inner cylinder for different values of the Reynolds number Re and the microplar parameter K. From the table it is observed that with increase in the Reynolds

number Re the boundary derivative of the velocity profile and the associated skinfriction co-efficient at the surface of the inner cylinder increases, while with increase in the micropolar parameter K the boundary derivative and the skinfriction coefficient at the surface of the inner cylinder decreases. $Table.\,(5.2)$ is tabulated to observe the behavior of the boundary derivatives of the velocity profile $g(\eta)$ computed for different pairs of the Reynolds number Re and the micropolar parameter K. From the table it is noted that with increase in the Reynolds number Re the boundary derivatives show an oscillatory behavior. $Table.\,(5.3)$ provides the behavior of the boundary derivative of the velocity profile $h(\eta)$ calculated for different values of the Reynolds number Re and the micropolar parameter K at the surface of the inner cylinder. From $Table.(5.3)$ it is observed that with increase in the Reynolds number Re, the boundary derivative and the associated azimuthal shear stress at the surface of the inner cylinder increases, while with increase in the micropolar parameter K the boundary derivative and the azimuthal shear stress decreases. $Table.\,(5.4)$ shows the boundary derivatives for the micro-rotation profile $M(\eta)$ tabulated for different values of the micropolar parameters K and Λ. From the data in $Table.\,(5.4)$ it is noticed that with increase in the micropolar parameter Λ/K the boundary derivatives of the microrotation profile decreases/decreases. $Table.\,(5.5)$ shows the comparison of the microrotation profile $P(\eta)$ for different combinations of the micropolar parameters K and Λ. From entries in $Table.\,(5.5)$ it is observed that with increase in the micropolar parameter Λ the microrotation profile decreases. $Table.\,(5.6)$ shows the behavior of the boundary derivatives of the temperature profile $\theta(\eta)$ corresponding to the Nusselt number Nu at the surface of the inner cylinder calculated for different values of the Prandtl number Pr and the Reynolds number Re . From $Table.\,(5.6)$ it is noted that with increase in both Prandtl number Pr and the Reynolds number Re, the boundary derivative at the surface of the inner cylinder and the Nusselt numbers increase. $Table.\,(5.7)$ predicts the influence of the Lewis number Le and the thermophoresis parameter Nt over the boundary derivatives of the nanoparticle concentration profile $\psi(\eta)$ corresponding to the sherwood number at the surface of the inner cylinder. From the table it is observed that with increase in the Lewis number Le increases the sherwood number, while increase in the thermophoresis parameter Nt the boundary derivatives of the nanoparticle concentration profile and the associated sherwood number decreases. $Tables.\,(5.8)$ and (5.9) give a comparison of a special case of the present results to that obtained

in $Ch.4$ and $Ch.1$, respectively. Results in $Ch.1$ were computed through the homotopy analysis method, while solutions in $Ch.4$ were calculated through the Runge-Kutta Fehlberg method. From these tables it is observed that the obtained solutions are in excellent agreement.
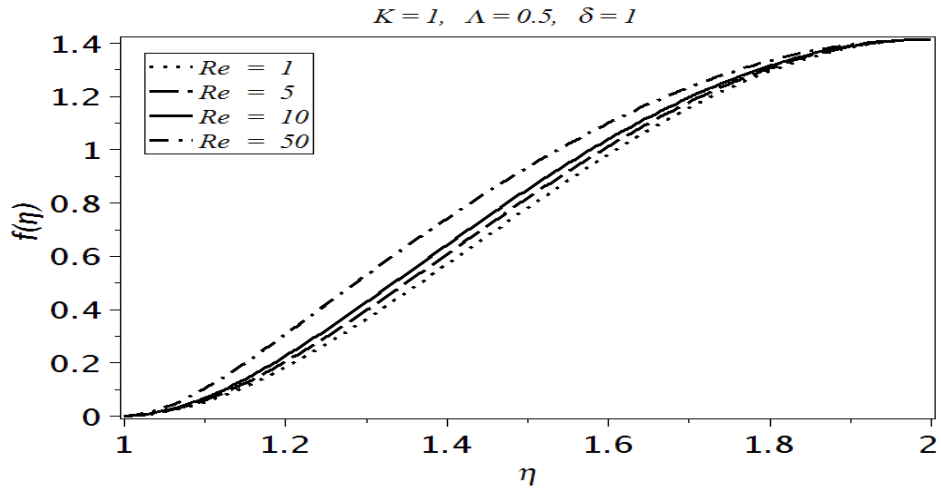
$Fig.$(5.1). Influence of the Reynolds numbe Re over the radial velocity profile $f(\eta)$
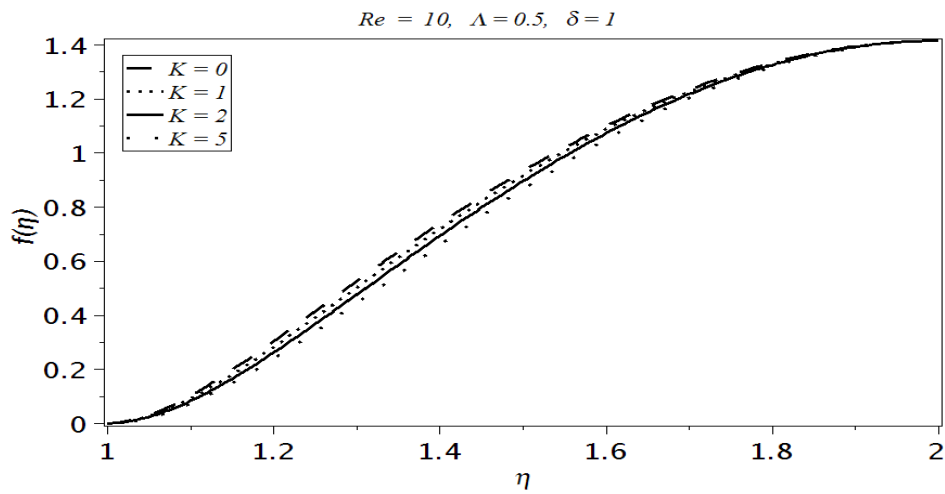
$Fig.$(5.2). Influence of the micropolar parameter K over the radial velocity profile $f(\eta)$
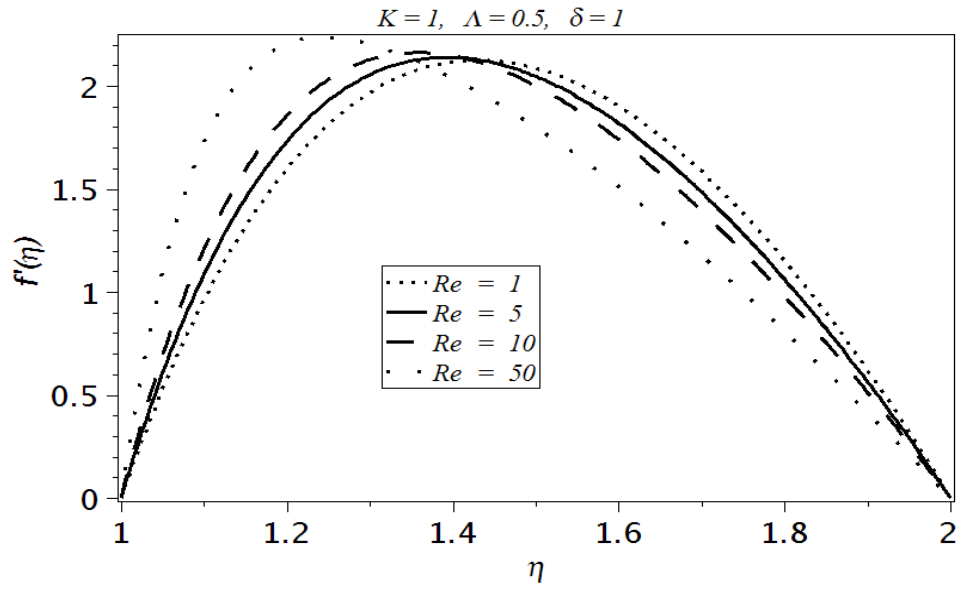
$Fig.(5.3)$. Influence of the Reynolds number Re over the radial velocity gradient $f'(\eta)$
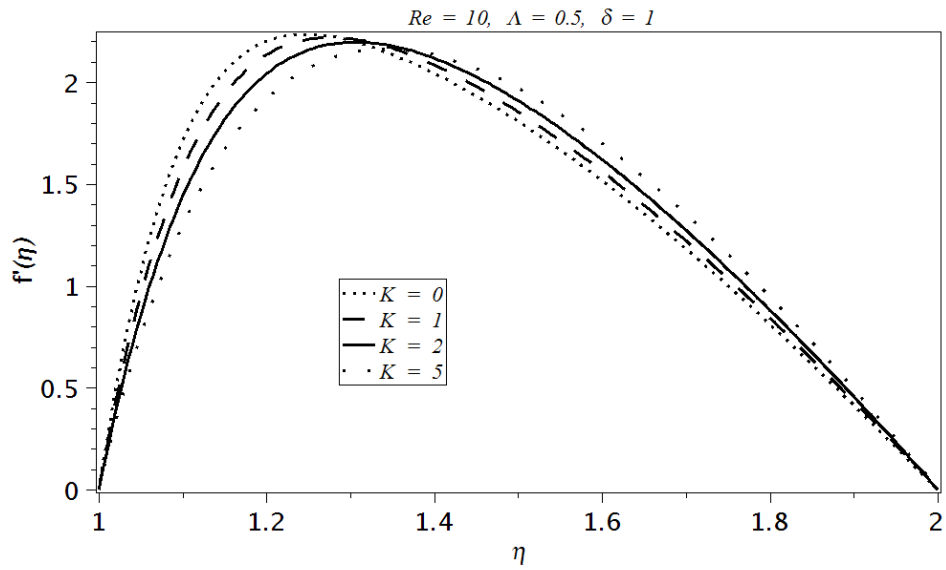
$Fig.(5.4)$. Influence of the micropolar parameter K over the radial velocity gradient $f'(\eta)$

$K = 0.1, \quad \Lambda = 0.5, \quad \delta = 1$
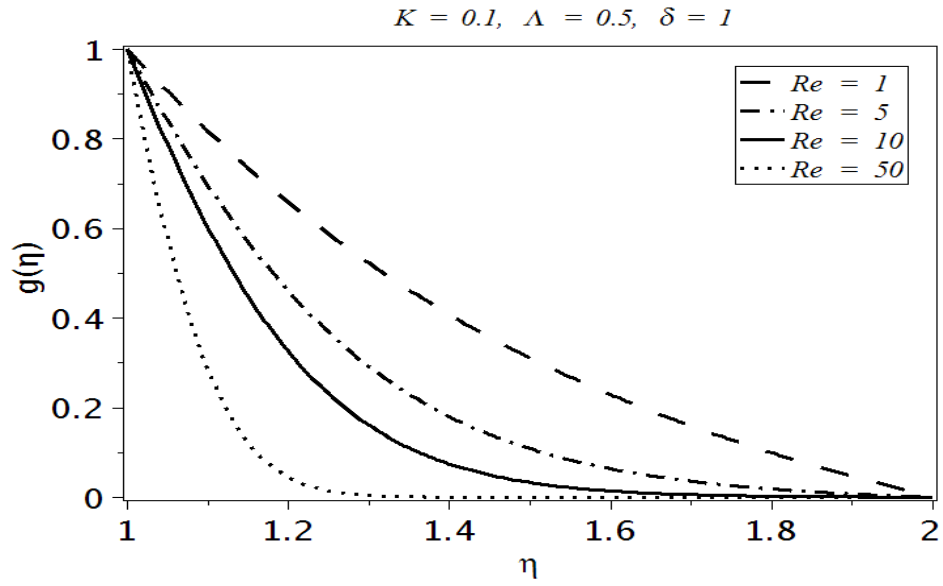
Fig.(5.5). Influence of the Reynolds number Re over the velocity profile $g(\eta)$

$Re = 10, \quad \Lambda = 0.1, \quad \delta = 1, \quad n = 0$
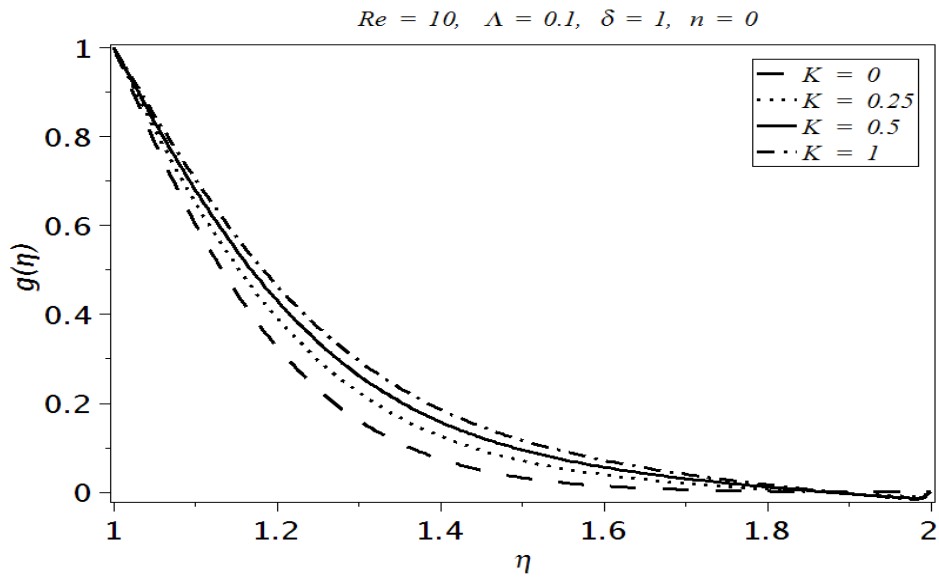
Fig.(5.6). Influence of the micropolar parameter K over the velocity profile

$g(\eta)$
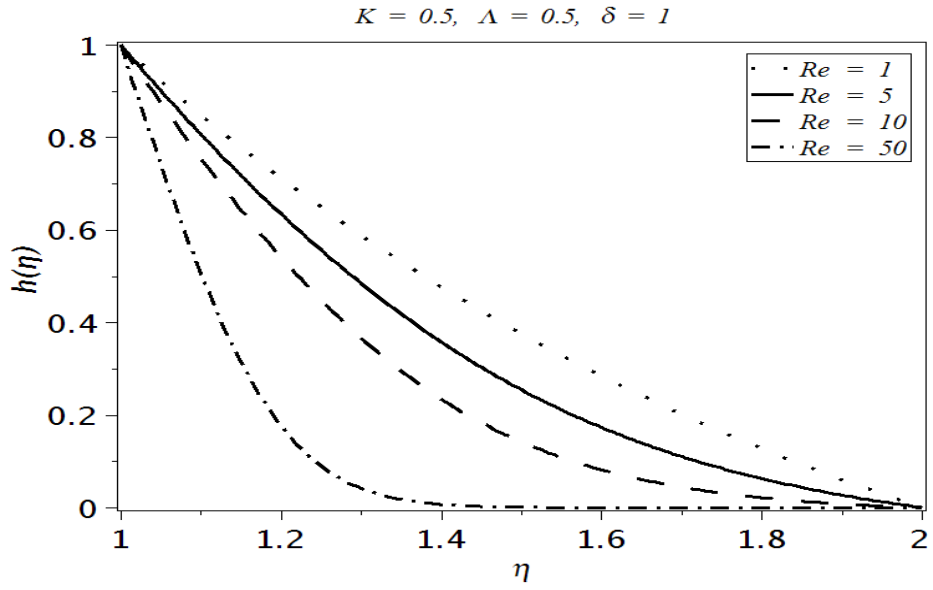
$Fig.(5.7)$. Influence of the Reynolds number Re over the angular velocity
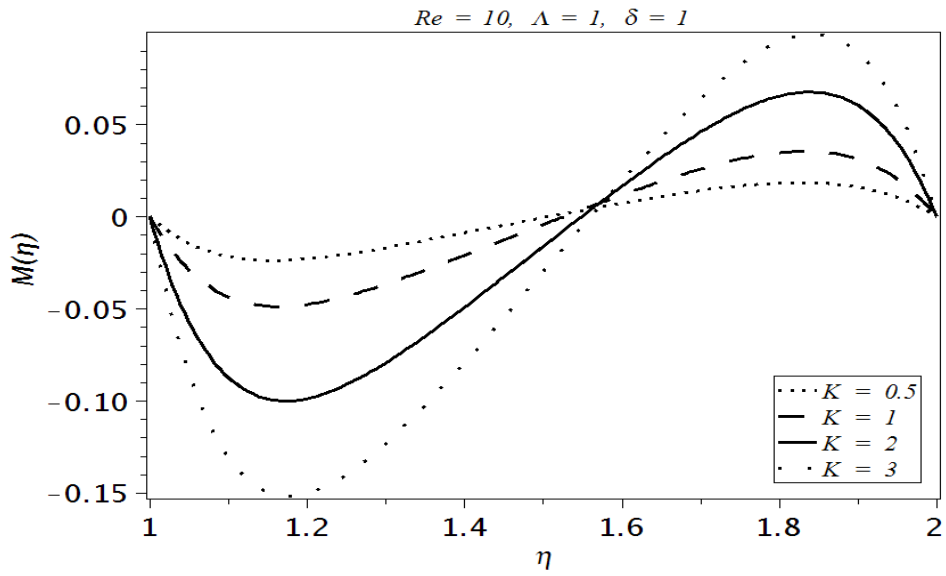
profile $h(\eta)$

$Fig.(5.8)$. Influence of the micropolar parameter K over the microrotation

velocity profile $M(\eta)$ when $n = 0$
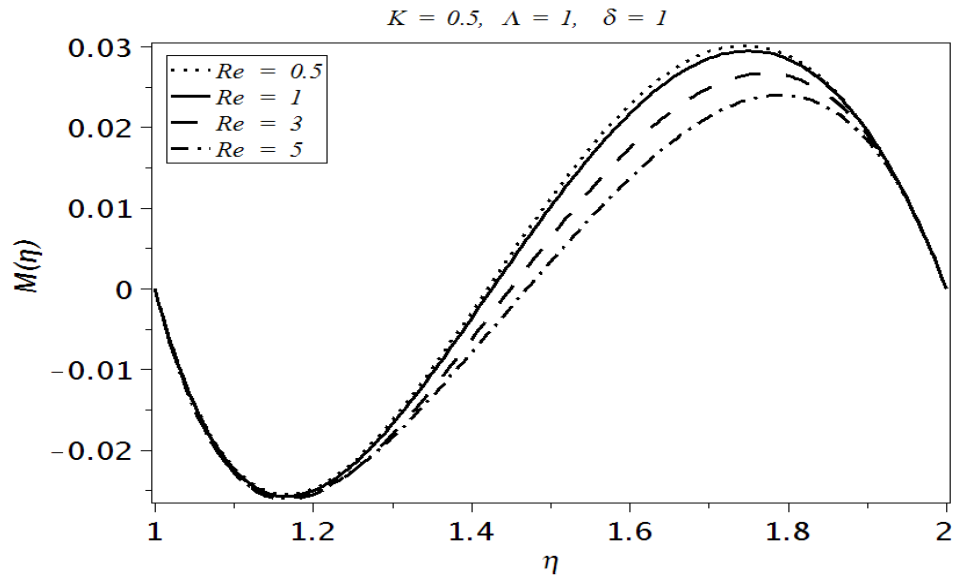
$Fig.$(5.9). Influence of the Reynolds number Re over the microrotation
velocity profile $M(\eta)$ when $n = 0$
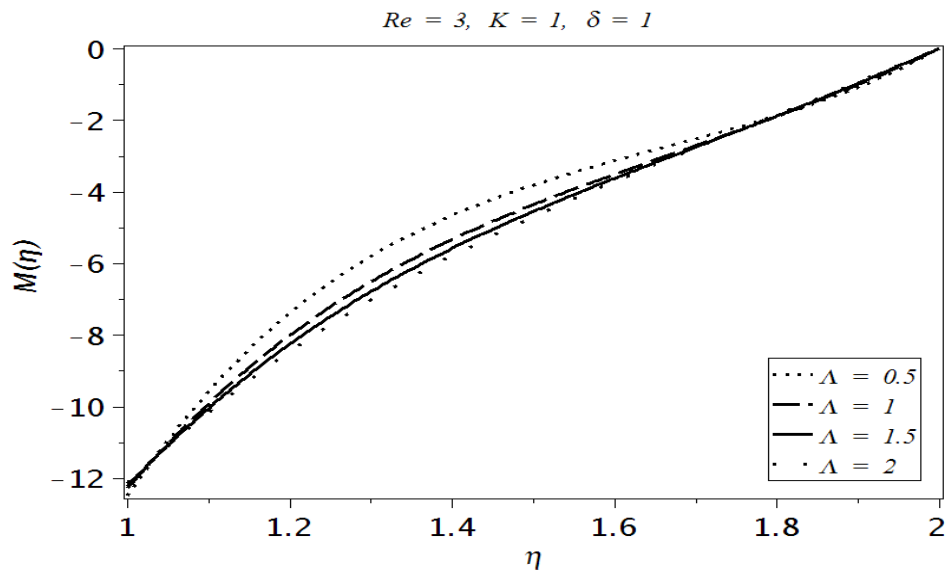
$Fig.$(5.10). Influence of the micropolar parameter Λ over the microrotation
velocity profile $M(\eta)$ when $n = 0.5$
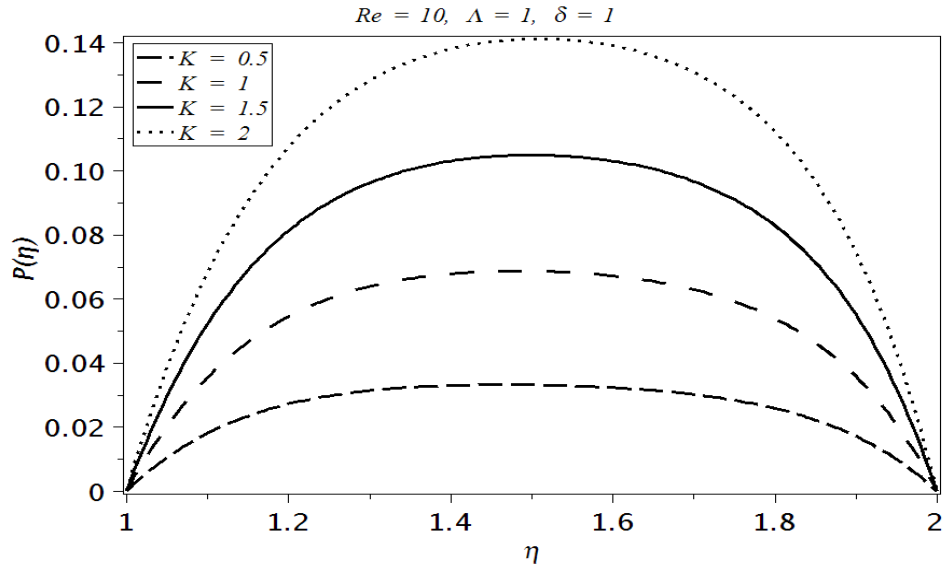
$Fig.$(5.11). Influence of the micropolar parameter K over the microrotation velocity profile $P(\eta)$ when $n = 0$
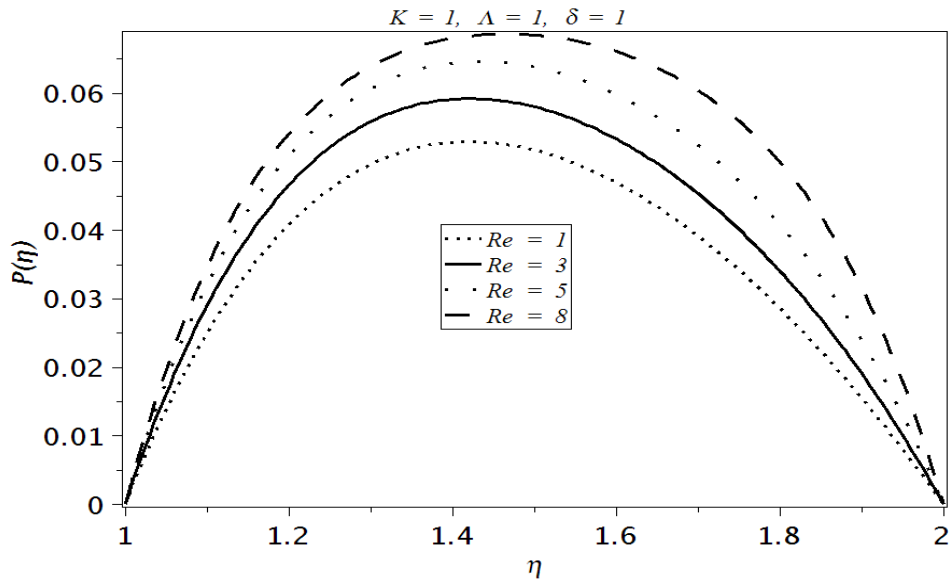
$Fig.$(5.12). Influence of the Reynolds number Re over the microrotation velocity profile $P(\eta)$ when $n = 0$
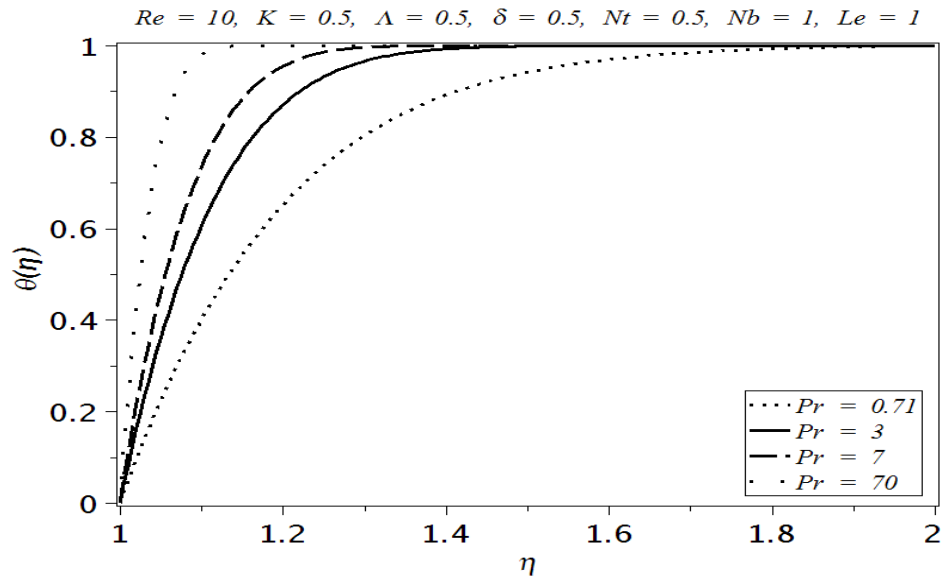
$Fig.(5.13)$. Influence of the Prandtl number Pr over the temperature profile

$\theta(\eta)$
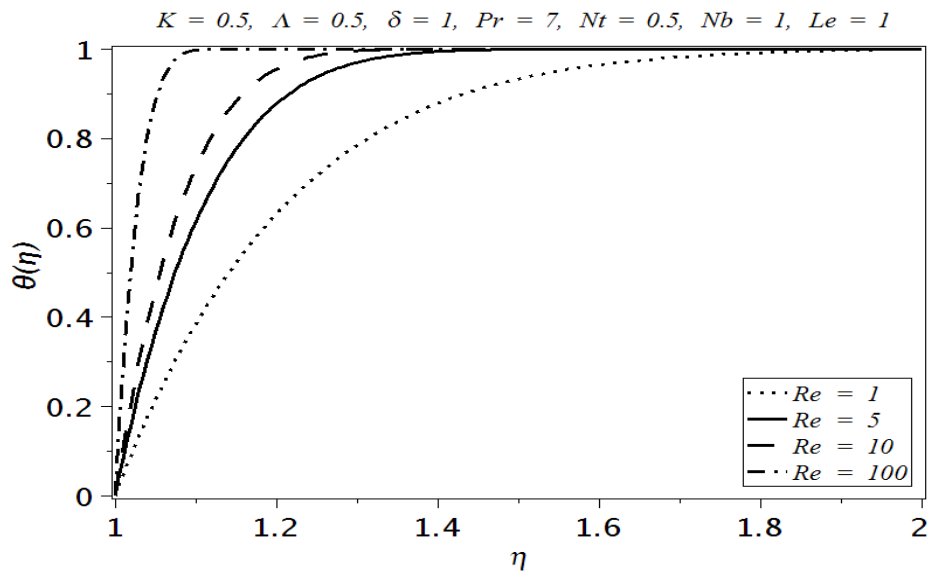
$Fig.(5.14)$. Influence of the Reynolds number Re over the temperature
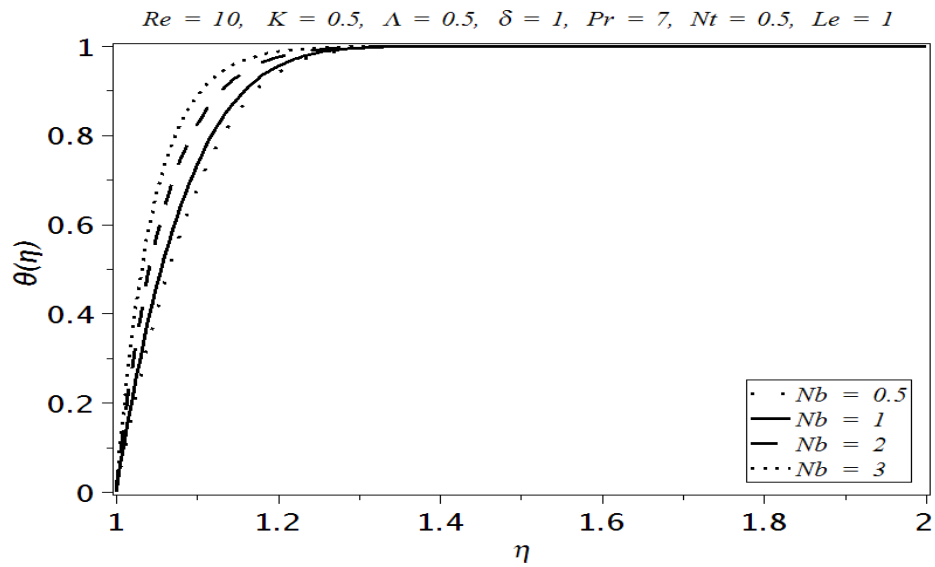
profile $\theta(\eta)$

Fig.(5.15). Influence of the Brownian motion parameter Nb over the temperature profile $\theta(\eta)$
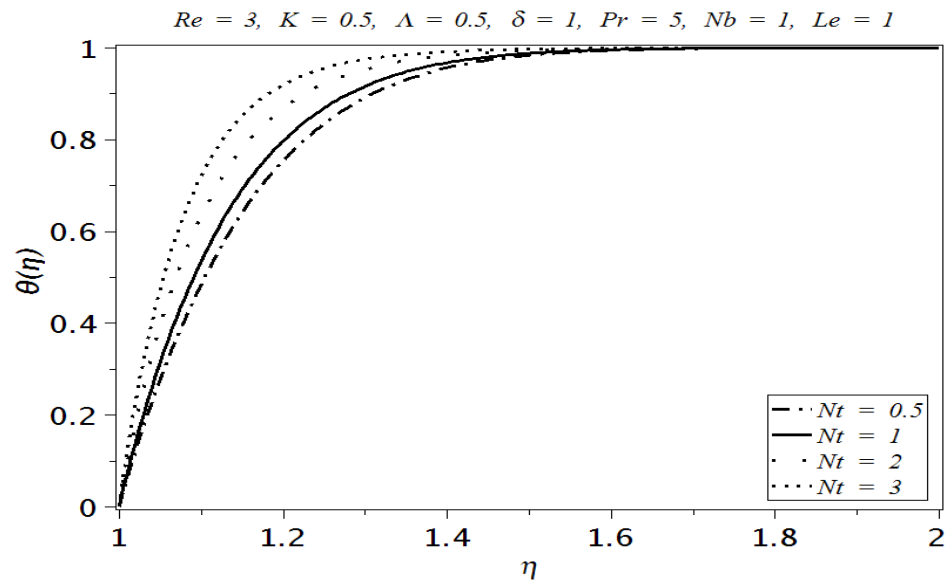
Fig.(5.16). Influence of the thermophorises parameter Nt over the temperature profile $\theta(\eta)$
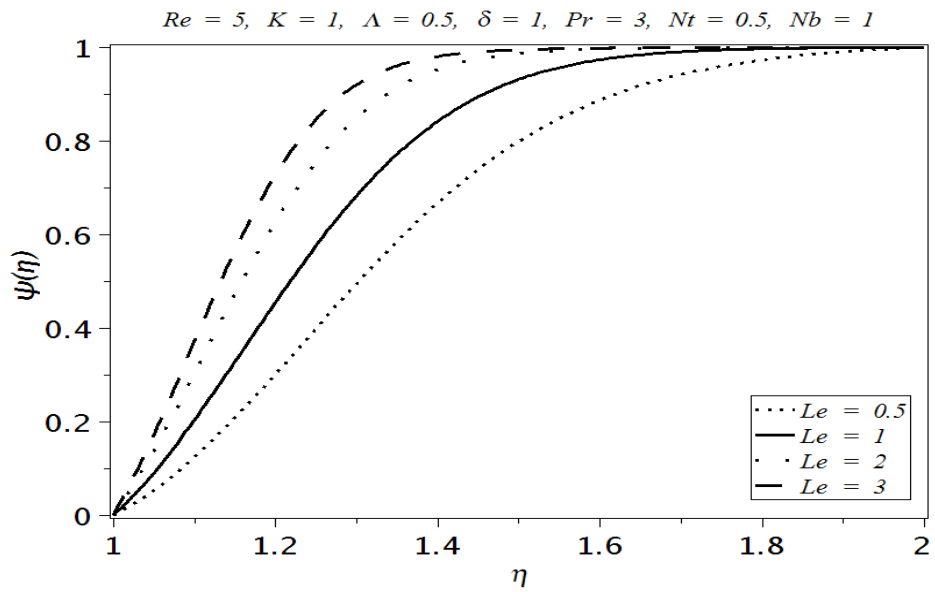
$Fig.(5.17)$. Influence of the Lewis number Le over the nanoparticle
concentration profile $\psi(\eta)$
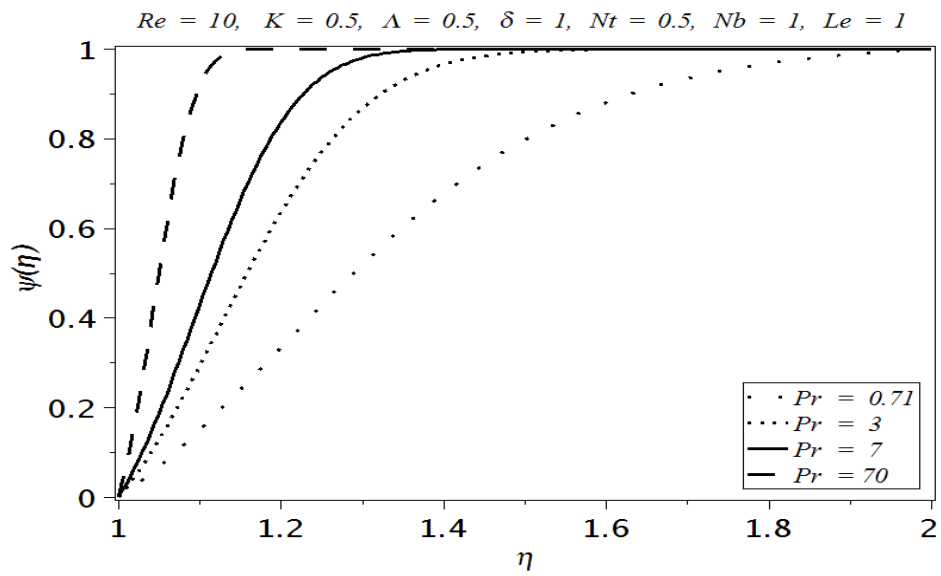
$Fig.(5.18)$. Influence of the Prandtl number Pr over the nanoparticle
concentration profile $\psi(\eta)$
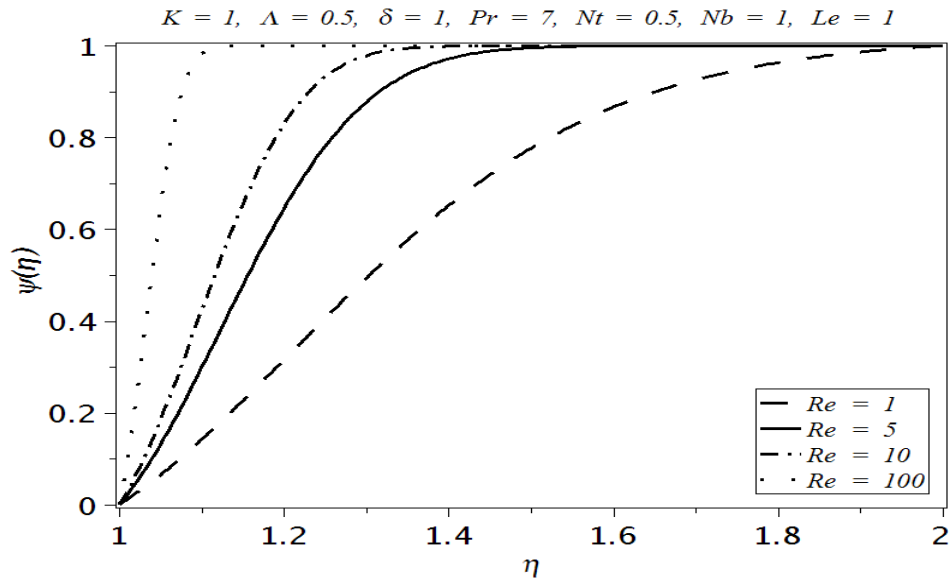
$Fig.(5.19)$. Influence of the Reynolds number Re over the nanoparticle
concentration profile $\psi(\eta)$
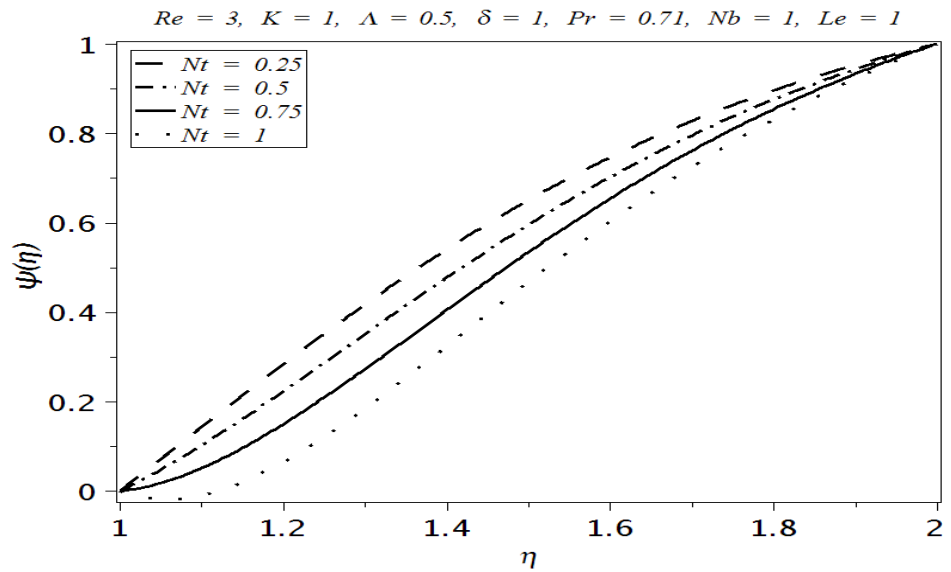
$Fig.(5.20)$. Influence of the thermophorises parameter Nt over the
nanoparticle concentration profile $\psi(\eta)$

Re\K	f''(1)					-f'''(1)				
	0.25	0.5	1	1.5	2	0.25	0.5	1	1.5	2
0.5	11.2614	11.2424	11.2374	11.2530	11.2777	38.074	37.962	37.938	38.037	38.190
1	11.5897	11.5384	11.4898	11.4762	11.4793	40.538	40.221	39.920	39.834	39.850
3	12.8727	12.7003	12.4858	12.3610	12.2822	50.624	49.427	47.944	47.082	46.534
5	14.0893	13.8047	13.4325	13.2014	13.0450	60.916	58.747	55.955	54.243	53.092
10	16.8269	16.3023	15.5763	15.0981	14.7594	86.929	82.174	75.811	71.750	68.933
20	21.3000	20.4436	19.1975	18.3292	17.6877	138.58	128.79	115.25	106.28	99.901
50	30.8292	29.3851	27.2173	25.6423	24.4319	288.10	264.19	230.51	207.63	190.93
70	35.6825	33.9581	32.3560	29.4527	27.9804	385.10	352.05	305.37	273.55	250.23
100	41.8399	39.7662	36.6252	34.3168	32.5230	528.45	481.85	415.90	415.90	337.78

$Table.(5.1)$. Behavior of the boundary derivatives of the radial velocity profile $f(\eta)$ at the surface of the inner cylinder, computed for different values of the Reynolds number Re and the micropolar parameter K, when $\Lambda = 0.5$, $\delta = 1$ and $n = 0.5$

Re\K	g'(1)						
	0.25	0.5	0.75	1	1.25	1.5	2
0.25	-2.2167	-3.3149	-5.7969	-18.3329	17.0898	5.8285	2.4096
0.5	-2.1962	-3.0660	-5.0086	-13.8641	16.3933	4.8731	1.7943
1	-2.1391	-2.5917	-3.6252	-7.6265	15.2573	2.8400	0.56696
2	-1.9923	-1.7547	-1.5119	-1.0441	9.4755	2.7687	-2.0588
3	-1.8502	-1.0897	-0.0883	-1.8864	10.4733	18.8852	-5.4856
5	-1.6997	-0.2554	1.4594	4.0434	9.2579	28.5712	-21.742
10	-1.8930	0.3573	2.6564	5.2795	8.6044	13.3232	37.0041
20	-2.5317	0.5509	3.4778	6.3945	9.4341	12.7424	20.9855
30	-3.0714	0.6177	4.0584	7.3645	10.6256	13.9245	20.9922
50	-3.9567	0.6806	4.9750	9.0250	12.8982	16.6477	23.1315

$Table.(5.2)$. Behavior of the boundary derivatives of the velocity profile $g(\eta)$ at the surface of the inner cylinder, computed for different values of the Reynolds number Re and the micropolar parameter K, when $\Lambda = 0.5$, $\delta = 1$ and $n = 0.5$

93

	-h'(1)						
Re\K	0.25	0.5	0.75	1	1.25	1.5	2
0.25	1.5304	1.5253	1.5217	1.5190	1.5169	1.5152	1.5127
0.5	1.5612	1.5509	1.5436	1.5381	1.5334	1.5305	1.5254
1	1.6238	1.6029	1.5881	1.5770	1.5684	1.5615	1.5512
2	1.7529	1.7099	1.6793	1.6565	1.6389	1.6248	1.6038
3	1.8853	1.8198	1.7731	1.7383	1.7113	1.6897	1.6576
5	2.1531	2.0440	1.9654	1.9062	1.8601	1.8233	1.7683
10	2.7837	2.5897	2.4434	2.3299	2.2395	2.1660	2.0544
20	3.7834	3.4967	3.2719	3.0900	2.9397	2.8134	2.6135
30	4.5566	4.2083	3.9340	3.7107	3.5242	3.3657	3.1096
50	5.7806	5.3344	4.9831	4.6970	4.4580	4.2542	3.9231

$Table.(5.3)$. Behavior of the boundary derivatives of the angular velocity profile $h(\eta)$ at the surface of the inner cylinder, computed for different values of the Reynolds number Re and the micropolar parameter K, when $\Lambda = 0.5$, $\delta = 1$ and $n = 0.5$

	M'(1)					
Λ\Re	0.5	1	5	10	50	100
0.2	26.3637	30.1395	56.3959	83.1979	274.5605	498.1011
0.4	22.3237	24.6928	43.0974	63.2277	207.8854	381.2508
0.6	20.6443	22.4030	36.8322	53.7210	176.2865	323.1740
0.8	19.7243	21.1395	33.0704	47.8115	156.6602	287.1224
1	19.1436	20.3385	30.5545	43.6833	142.8615	261.7901
1.2	18.7438	19.7855	28.7567	40.6091	132.4344	242.6580
1.4	18.4518	19.3806	27.4134	38.2248	124.1729	227.5069
1.6	18.2291	19.0715	26.3659	36.3215	117.4039	215.0984
1.8	18.0537	18.8278	25.5329	34.7682	111.7174	204.6781
2.0	17.9120	18.6306	24.8535	33.4778	106.8467	195.7557

$Table.(5.4)$. Behavior of the boundary derivatives of the microrotation velocity profile $M(\eta)$ at the surface of the inner cylinder, computed for different values of the Reynolds number Re and the micropolar parameter Λ when $K = 2$, $\delta = 1$ and $n = 0.5$

K\Λ	P′(1)					
	0.25	0.5	0.75	1	1.5	2
0.1	21.931	10.4591	5.7802	3.3011	0.7546	-0.5366
0.5	28.1097	11.6202	5.4696	2.3461	-0.7623	-2.2984
1	52.8074	17.5462	5.1654	-0.5753	-5.6769	-7.9182
1.5	-117.4082	-30.9546	6.6277	52.0099	-1641.0883	-148.1705
2	-15.0975	-0.2506	5.4808	8.9288	13.6856	17.1908
2.5	-3.5101	2.8565	5.3799	6.8440	8.7498	10.0544
3	1.0861	4.0668	5.3480	6.0995	7.0994	7.7966
4	5.3014	5.1813	5.3507	5.4931	5.7706	6.0189
5	7.4852	5.7820	5.3955	5.2463	5.1988	5.2584

$Table.$(5.5). Behavior of the boundary derivatives of the microrotation velocity profile $P(\eta)$ at the surface of the inner cylinder, computed for different values of the micropolar parameters K and Λ when $\mathrm{Re} = 3$, $\delta = 1$ and $n = 0.5$

Pr\Re	θ′(1)						
	0.5	1	2	5	10	50	100
0.2	2.8173	2.8496	2.9160	3.1265	3.5000	6.2687	8.6813
0.71	2.8978	3.0117	3.2435	3.9487	5.0575	10.4229	14.4354
3	3.2537	3.7088	4.5470	6.4623	8.6398	17.8702	24.8065
7	3.8400	4.7462	6.1234	8.7555	11.6844	24.2169	33.6565
10	4.2419	5.3721	6.9536	9.9221	13.2394	27.4665	38.1891
70	8.2884	10.5871	13.6059	19.3516	25.8429	53.8547	75.0028
100	9.3670	11.9527	15.3545	21.8381	29.1696	60.8246	84.7272
150	10.7548	13.7126	17.6097	25.0464	33.4625	69.8197	97.2773
300	13.5997	17.3250	22.2417	31.6387	42.2846	88.3072	123.0717

$Table.$(5.6). Behavior of the boundary derivatives of the temperature profile $\theta(\eta)$ at the surface of the inner cylinder, computed for different values of the Prandtl number Pr and the Reynolds number Re when $K = 0.1$, $\Lambda = 0.5$, $\delta = 1$, $Nb = 1$, $Nt = 0.5$, $Le = 1$ and $n = 0$

Le\Nt	$\psi'(1)$						
	0.1	0.2	0.4	0.5	0.7	0.8	1
0.25	2.0037	1.6343	0.8157	0.3651	-0.6225	-1.1608	-2.3298
0.5	2.6465	2.2693	1.4172	0.9399	-0.1230	-0.7108	-2.0047
0.75	3.1158	2.7330	1.8571	1.3608	0.2441	-0.3794	-1.7638
1	3.4877	3.1005	2.2061	1.6953	0.5373	-0.1135	-1.5676
1.5	4.0724	3.6781	2.7562	2.2239	1.0048	0.3132	-1.2454
2	4.5355	4.1359	3.1939	2.6459	1.3821	0.6606	-0.9755
3	5.2662	4.8588	3.8883	3.3183	1.9912	1.2270	-0.5205
4	7.3556	5.4338	4.4436	3.8583	2.4873	1.6931	-0.1336
5	6.3363	5.9193	4.9143	4.3177	2.9136	2.0967	0.2095

$Table.(5.7)$. Behavior of the boundary derivatives of the nanoparticle concentration profile $\psi(\eta)$ at the surface of the inner cylinder, computed for different values of the Lewis number Le and the thermophoresis parameter Nt when $\mathrm{Re} = 3$, $K = 0.1$, $\Lambda = 0.5$, $\delta = 1$, $\mathrm{Pr} = 7$, $Nb = 1$ and $n = 0$

	$f''(1)$		$-g'(1)$		$-h'(1)$	
Re	Present	Ch. 4	Present	Ch. 4	Present	Ch. 4
0.1	11.001	11.0010	1.4963	1.4963	10.5151	10.5151
1	11.677	11.6772	1.9309	1.9309	10.6511	10.6511
10	17.5345	17.5348	4.3856	4.3856	12.0407	12.0407
100	44.449	44.4492	12.6450	12.6450	24.8226	24.8226

$Table.(5.8)$. Comperison of a special case of the present results with the results obtained in $Ch.4$ for $K = 0$, $kp = 0$ and $\beta = 20000$

	Pr\Nb	0.5		1		1.5		2	
		Present	Ch. 1	Present	Ch. 1	Present	Ch. 1	Present	Ch. 1
θ'(1)	2	4.2742	4.2742	5.0851	5.0851	5.9606	5.9606	6.8921	6.8921
	5	5.9432	5.9432	7.0670	7.0670	8.2805	8.2805	9.5720	9.5720
	7	6.7049	6.7049	7.9755	7.9755	9.3479	9.3479	10.8086	10.8086
	10	7.6072	7.6072	9.0515	9.0515	10.6118	10.6118	12.2726	12.2726
	Parameters: Re = 5, Le = 0.5, Nt = 0.5								
	Le\Nt	0.5		1		1.5		2	
		Present	Ch. 1	Present	Ch. 1	Present	Ch. 1	Present	Ch. 1
ψ'(1)	0.25	0.3402	0.3402	-2.1188	-2.1188	-5.3095	-5.3095	-9.3019	-9.3019
	0.5	0.8312	0.8312	-1.8413	-1.8413	-5.4380	-5.4380	-10.0707	-10.0707
	1	1.5279	1.5279	-1.4369	-1.4369	-5.6110	-5.6110	-11.1754	-11.1754
	1.5	2.0224	2.0224	-1.1345	-1.1345	-5.7001	-5.7001	-11.9128	-11.9128
	Parameters: Re = 5, Pr = 3, Nb = 1								

$Table$.(5.9). Comperison of a special case of the present results with the results obtained in Ch.1 for $K = 0$

5.5   Conclusion

The above discussion is summarized as

- With the increase in the Reynolds number Re and the micropolar parameter K, the velocity profile f increases.

- With the increase in the Reynolds number Re, the velocity profile g decrease.

- With the increase in the Reynolds number Re, the velocity profile h decrease.

- With the increase in the Reynolds number Re and the micropolar parameter K, the microrotation velocity profile M increases.

97

- With the increase in the Reynolds number Re and the micropolar parameter K, the microrotation velocity profile N increases.

- The nondimensional temperature profile θ increases with the increase in the Reynolds number Re, the micropolar parameter K, the Prandtl number Pr, the Brownian motion parameter Nb and the thermophoresis parameter Nt.

- The nondimensional nanoparticle concentration profile ψ increases with the increase in the Reynolds number Re, the micropolar parameter K, the Prandtl number Pr, the Lewis number Le and the Brownian motion parameter Nb.

- The nanoparticle concentration profile ψ decreases with the increase in the thermophoresis parameter Nt.

- The shear stress at the surface of the inner cylinder increases with increase in the Reyniolds number Re.

- The heat flux at the surface of the inner cylinder increases with increase in the Prandtl number Pr.

- The Sherwood number at the surface of the inner cylinder decreases with increase in the thermophoresis parameter Nt.

Chapter 6

Natural convection heat transfer in micropolar nanofluid over a vertical slender cylinder

6.1 Introduction

In this chapter, we have studied the boundary layer flow and heat transfer of a micropolar fluid containing nanoparticles and is flowing over a vertical cylinder. The governing partial differential equations of momentum, angular momentum, energy and nanoparticle concentration are reduced to nonlinear coupled ordinary differential equations by applying the boundary layer approximation and a suitable similarity transformation. The obtained nonlinear coupled ordinary differential equations along with the appropriate boundary conditions are solved by 5th order shooting method. The effects of the physical parameters on the flow and heat transfer characteristics of the model are presented through graphs and the salient features are discussed.

6.2 Formulation

Consider an incompressible flow of a non-Newtonian micropolar nanofluid along a vertical permeable slender cylinder of radius r_0 having uniform ambient temperature T_∞. The coordinates (x, r) are used such that x is along the surface of the cylinder while r is in the radial direction.

The governing equations of conservation of mass heat transfer and nanoparticle concentration profiles are listed in $Eqs.\,(2.6)\,,(2.8)$ and $(2.9)\,,$ while the angular momentum equation is stated in $Eq.\,(5.2)\,,$ whereas the linear momentum equation associated with the problem is

$$\rho\frac{d\mathbf{V}}{dt} = -\mathbf{\nabla}p + k\mathbf{\nabla} \times \mathbf{W} + (\mu + k)\,\mathbf{\nabla}^2\mathbf{V} + \rho\tilde{\mathbf{g}}. \tag{6.1}$$

For the velocity field $\mathbf{V}\,(x,r) = (w\,(x,r)\,,0,u\,(x,r))$, angular velocity $\mathbf{W}\,(r,z) = (0,\chi\,(x,r)\,,0)\,,$ heat transfer profile $T = T(x,r)$ and the nanoparticle concentration function $\phi = \phi\,(x,r)\,,$ the boundary layer equations of conservation of mass, momentum, angular momentum, heat transfer and the nanoparticle concentration are

$$(rw)_r + ru_x = 0, \tag{6.2}$$

$$uu_x + wu_r = U\frac{dU}{dx} + \frac{\mu + K}{\rho}(u_{rr} + \frac{1}{r}u_r) + \frac{K}{\rho}\left(\chi_r + \frac{\chi}{r}\right)$$
$$+[\frac{(\rho^* - \rho)\,(\phi - \phi_\infty)}{\rho} + (1 - \phi_\infty)\,(T - T_\infty)\,\beta_{th}]g_{gr}, \tag{6.3}$$

$$w\chi_r + u\chi_x = \frac{\gamma^*}{\rho j}\left(\chi_{rr} + \frac{\chi_r}{r} - \frac{\chi}{r^2}\right) - \frac{K}{\rho c_p}\,(u_r + 2\chi)\,, \tag{6.4}$$

$$wT_r + uT_x = \alpha(T_{rr} + \frac{1}{r}T_r) + \frac{\rho^* c_p^*}{\rho c_p}\left[D_B\phi_r T_r + \frac{D_T}{T_\infty}T_r^2\right], \tag{6.5}$$

$$w\phi_r + u\phi_x = D_B\left(\phi_{rr} + \frac{1}{r}\phi_r\right) + \frac{D_T}{T_\infty}(T_{rr} + \frac{1}{r}T_r), \tag{6.6}$$

where χ is the angular microrotation momentum and $U_\infty\,(x/l)$ is the mainstream velocity.

The corresponding boundary conditions for the problem are

$$u(x,r_0) = 0, \qquad u(x,r) \longrightarrow U_\infty\,(x/l) \text{ as } r \longrightarrow \infty, \tag{6.7}$$

$$\chi\,(x,r_0) = -n\left(\frac{U_\infty}{\nu l}\right)^{\frac{1}{2}}\frac{U_\infty x}{l}F''\,(0)\,, \qquad \chi \to 0, \text{ as } r \longrightarrow \infty, \tag{6.8}$$

$$T(x,r_0) = T_w\,(x)\,, \qquad T(x,r) \longrightarrow T_\infty \text{ as } r \longrightarrow \infty, \tag{6.9}$$

$$\phi(x,r_0) = \phi_w, \qquad \phi(x,r) \longrightarrow \phi_\infty, \text{ as } r \longrightarrow \infty. \tag{6.10}$$

100

6.3 Solution of the problem

We make use of the following similarity transformations:

$$u = U_\infty\,(x/l)\,F'(\eta), \qquad w = -\frac{r_0}{r}\left(\frac{\nu U_\infty}{l}\right)^{\frac{1}{2}}F(\eta), \tag{6.11}$$

$$\chi = \frac{xU_\infty}{r_0 l}J(\eta), \qquad \theta = \frac{T-T_\infty}{T_w-T_\infty}, \tag{6.12}$$

$$\Psi = \frac{\phi-\phi_\infty}{\phi_w-\phi_\infty}, \qquad \eta = \frac{r^2-r_0^2}{2r_0}\left(\frac{U_\infty}{\nu l}\right)^{\frac{1}{2}}, \tag{6.13}$$

in which the characteristic temperature and concentration friction ΔT and $\Delta\phi$ respectively are calculated from the relations $T_w - T_\infty = (x/l)\,\Delta T$ and $\phi_w - \phi_\infty = (x/l)\,\Delta\phi$. With the help of above transformations the governing equations can be written as

$$(1+2\gamma_c\eta)\,F''' + 2\gamma_c F'' + \frac{1}{1+K}(1+FF''-F'^2) + \frac{\lambda_N}{1+K}(1-\phi_\infty)(\theta+N_r\Psi) + \frac{K\gamma_c}{1+K}J' = 0, \tag{6.14}$$

$$(1+2\gamma_c\eta)\,J'' - \frac{4\gamma_c^2}{1+2\gamma_c\eta}J + \frac{1}{\Lambda}\left(FJ'-F'J\right) - \frac{\gamma_c}{\Lambda}FJ - \frac{Ka_0\gamma_c}{\Lambda}\left[(1+2\gamma_c\eta)\,F''-2\gamma_c J\right] = 0, \tag{6.15}$$

$$(1+2\gamma_c\eta)\,\theta'' + 2\gamma_c\theta' + \Pr(F\theta'-F'\theta) + (1+2\gamma_c\eta)\left(B_P\theta'\Psi'+T_P\theta'^2\right) = 0, \tag{6.16}$$

$$(1+2\gamma_c\eta)\,\Psi'' + 2\gamma_c\Psi' + Le\,\Pr\left(F\Psi'-F'\Psi\right) + \frac{T_P}{B_P}\left[(1+2\gamma_c\eta)\,\theta''+2\gamma_c\theta'\right] = 0, \tag{6.17}$$

in which $a_0 = l/r_0$, $K = k/\mu$ is the micropolar parameter, $\lambda_N = g_{gr}\beta_{th}l\Delta T/U_\infty^2$ is the natural convection parameter, $\Lambda = \gamma^*/\mu j$ is the micropolar coefficient, $Le = \alpha/D_B$ is the Lewis number, $N_r = (\rho^*-\rho)\,(\phi_w-\phi_\infty)\,/\rho\beta_{th}\,(T_w-T_\infty)\,(1-\phi_\infty)$ is the buoyancy ratio, $B_P = \rho^*c_p^*D_B\,(\phi_w-\phi_\infty)\,/\rho c_p\alpha$ is the Brownian motion parameter and $T_P = \rho^*c_p^*D_T\,(T_w-T_\infty)\,/\rho c_p\alpha T_\infty$ is the thermophoresis parameter.

The boundary conditions in nondimensional form are

$$F(0) \quad = \quad c_0, \quad F'(0) = 0, \quad\quad F' \longrightarrow 1, \text{ as } \eta \longrightarrow \infty, \tag{6.18}$$

$$J(0) \quad = \quad -\frac{n}{\gamma_c}F''(0), \quad \theta(0) = 1, \quad \Psi(0) = 1, \tag{6.19}$$

$$J \quad \longrightarrow \quad 0, \quad \theta \longrightarrow 0, \quad \Psi \longrightarrow 0, \quad \text{as } \eta \longrightarrow \infty, \tag{6.20}$$

where c_0 is any constant.

The skinfriction coefficient and the Nusselt number in dimensionless form are

$$\frac{1}{2}C_f \operatorname{Re}^{1/2} = (1 + (1-n)K)f''(0), \quad\quad Nu/\operatorname{Re}^{1/2} = -\theta'(0). \tag{6.21}$$

where $\operatorname{Re} = r_0 U_\infty/2v$ is the Reynolds number.

The solutions of $Eqs.(6.14)$ to (6.17) subject to the boundary conditions (6.18) to (6.20) have been computed numerically with the help of 5th order Runge-Kutta shooting method and the results are discussed in the next section.

6.4 Results and discussion

The problem of stagnation point boundary layer flow of a non-Newtonian micropolar fluid containing nanoparticles and flowing over a vertical cylinder is studied in the present chapter. The governing set of nonlinear partial differential equations is first simplified with the help of boundary layer approximations. The simplified version is then converted into a system of ordinary differential equations by applying a suitable similarity transformation. The resulting system of ordinary differential equations is then solved numerically with the help of 5th order Runge-Kutta shooting technique. The impact of pertinent parameters over the nondimensional velocity, microrotation, heat transfer and nanoparticle concentration profiles F', J, θ and ψ is presented in the $Figs.(6.1)$ to (6.20). $Fig.(6.1)$ shows the influence of the curvature parameter γ_c over the nondimensional velocity profile F'. From the graph it is observed that with an increase in the curvature parameter γ_c the nondimensional velocity profile F' decreases. $Fig.(6.2)$ provides the impact of the micropolar parameter K over the velocity profile F' computed for 0.05% level of the nanoparticles concentration when the natural convection parameter $\lambda_N = 1$.

From the sketch it is noted that with an increase in the micropolar parameter K the velocity function F' decreases. The behavior of the nondimensional velocity profile F' for different values of the natural convection parameter λ_N is presented in $Fig.\,(6.3)$. From the plot it is evident that with an increase in the natural convection parameter λ_N the velocity profile F' increases. This increase is consistent with the fact that by increasing the natural convection parameter λ_N the fluid density difference increases that in return enhances the fluid flow rate F'. $Fig.\,(6.4)$ represents the velocity curves for different values of the buoyancy ratio N_r. From the graph it is depicted that by increasing the buoyancy ratio N_r the nondimensional velocity profile F' also increases. $Fig.\,(6.5)$ shows the influence of the curvature parameter γ_c over the nondimensional microrotation profile J for the case when $n = 0.5$. It is observed from $Fig.\,(6.5)$ that with an increase in the curvature parameter γ_c the microrotation profile J also increases. $Fig.\,(6.6)$ displays the impact of the micropolar parameter K over the nondimensional microrotation profile J for the situation when $n = 0$. From the sketch it is noted that with an increase in the micropolar parameter K the nondimensional microrotation profile J decreases. $Fig.\,(6.7)$ is plotted to observe the behavior of microrotation velocity function J for different values of the micropolar parameter Λ graphed at the 0.05% level of nanoparticle concentration. From the sketch it is depicted that with an increase in the micropolar parameter Λ the nondimensional microrotation profile J has a dual behavior. That is near the surface of the stretching cylinder, increase in the micropolar parameter Λ increases the microrotation velocity profile J, while in the far field region, increase in the micropolar parameter Λ decreases the microrotation velocity profile J. $Fig.\,(6.8)$ shows the influence of the curvature parameter γ_c over the nondimensional microrotation profile J. From the plot it is observed that with an increase in the curvature parameter γ_c the microrotation function J also increases. $Fig.\,(6.9)$ indicates towards the behavior of the Prandtl number Pr over the nondimensional temperature profile θ when the curvature parameter $\gamma_c = 1$ and the thermophoresis parameter $T_P = 0.5$. From $Fig.\,(6.9)$ it is noted that with an increase in the Prandtl number Pr the temperature flow rate θ and the thermal boundary layer thickness both decreases. The influence of the Brownian motion parameter B_P over the nondimensional temperature profile θ is portrayed in $Fig.\,(6.10)$. From the sketch it is observed that with an increase in the Brownian motion parameter B_P the nondimensional temperature profile θ increases. $Fig.\,(6.11)$ displays the impact

of the thermophoresis parameter T_P over the nondimensional temperature profile θ. From the plot it is evident that with an increase in the thermophoresis parameter T_P the temperature function θ increases. $Fig.\,(6.12)$ indicates the influence of the curvature parameter γ_c over the nanoparticle concentration profile ψ. From the sketch it is noted that with an increase in the curvature parameter γ_c the nanoparticle concentration function ψ increases. $Fig.\,(6.13)$ displays the influence of the Prandtl number Pr over the nanoparticle concentration function ψ. From the graph it is observed that with an increase in the Prandtl number Pr the nanoparticle concentration profile ψ decreases. $Fig.\,(6.14)$ is included to examine the pattern adopted by the nanoparticle concentration profile ψ for different values of the thermophoresis parameter T_P. From the graph it is noted that the nanoparticle concentration profile ψ increases with an increase in the thermophoresis parameter T_P. Some $Fig.\,(6.15)$ predicts the impact of the Brownian motion parameter B_P over the nanoparticle concentration profile ψ. From the sketch it is observed that with an increase in the Brownian motion parameter B_P the nanoparticle concentration profile ψ decreases.

Some important physical quantities associated with the problem such as the shear stress, skinfriction coefficient, heat flux, local Nusselt numbers and the sherwood numbers are presented through tables. $Table.\,(6.1)$ shows the behavior of the boundary derivatives for the nondimensional velocity profile that corresponds to the shear stress at the surface and the skinfriction coefficient computed at the surface of the cylinder, computed for different pairs of the micropolar parameter K and the curvature parameter γ_c. From the table it is observed that the shear stress at the surface of the cylinder increases with an increase in the curvature parameter γ_c, while the shear stress at the surface of the cylinder decreases with an increase in the micropolar parameter K. $Table.\,(6.2)$ displays the entries for the boundary derivatives of the microrotation profile J computed at the surface of the vertical cylinder for different combinations of the natural convection parameter λ_N and the micropolar parameter K. The observed behavior in $Table.\,(6.2)$ is increasing/decreasing for increase in the natural convection parameter λ_N/ micropolar parameter K. $Table.\,(6.3)$ shows the boundary derivatives for the nondimensional temperature profile θ that corresponds to the heat flux at the surface of the cylinder and the local Nusselt numbers Nu tabulated for different pairs of the Prandtl numbers Pr and the micropolar parameter K. From $Table.\,(6.3)$ it is noted that the heat flux at the

surface of the cylinder increases with an increase in the Prandtl number Pr, while with an increase in the micropolar parameter K the heat flux at the surface of the vertical cylinder and the corresponding Nusselt numbers decrease. $Table.\,(6.4)$ provides values for the boundary derivatives of the nanoparticle concentration profile corresponding to the sherwood numbers, calculated for different choices of the Lewis numbers Le and the Prandtl numbers Pr. From $Table.\,(6.4)$ it is evident that with an increase in the Lewis number Le, the sherwood numbers increase, whereas with respect to the Prandtl numbers Pr the sherwood numbers show a dual behavior, that is for low Lewis numbers $(Le = 0.2)$ increase in the Prandtl numbers Pr decreases the sherwood numbers while for Lewis numbers $Le \geq 0.4$, increase in the Prandtl number Pr also increases the sherwood numbers. To examine the accuracy of the present solutions a comparison of the present results with the available works in [42] and [44] are also presented a special case. $Table.\,(6.5)$ shows a comparison of the present solutions or the special case when $K = 0$ with the work in [42], while $Table.\,(6.6)$ gives a comparison of the present solutions for the special case when and with the work in [44]. From these tables it is clear that the results are in good agreement.

$Fig.(6.1)$. Influence of the curvature parameter γ_c over the velocity profile
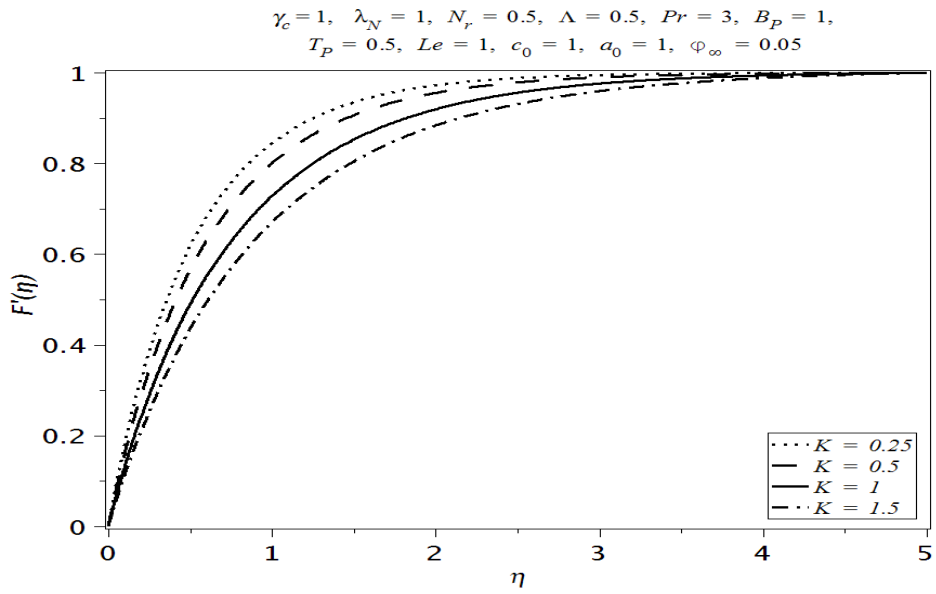
F'

$\gamma_c = 1, \quad \lambda_N = 1, \quad N_r = 0.5, \quad \Lambda = 0.5, \quad Pr = 3, \quad B_P = 1,$
$T_P = 0.5, \quad Le = 1, \quad c_0 = 1, \quad a_0 = 1, \quad \varphi_\infty = 0.05$

$Fig.$(6.2). Influence of the micropolar parameter K over the velocity profile F'

$\gamma_c = 0.5, \quad K = 0.5, \quad N_r = 0.5, \quad \Lambda = 0.5, \quad Pr = 3, \quad B_P = 1,$
$T_P = 0.5, \quad Le = 1, \quad c_0 = 1, \quad a_0 = 1, \quad \varphi_\infty = 0.05$

$Fig.$(6.3). Influence of the natural convection parameter λ_N over the velocity profile F'

106

$\gamma_c = 0.5$, $K = 0.5$, $\lambda_N = 1$, $\Lambda = 0.5$, $Pr = 3$, $B_P = 1$,
$T_P = 0.5$, $Le = 1$, $c_0 = 1$, $a_0 = 1$, $\varphi_\infty = 0.05$

Legend:
$\cdots N_r = 0.5$
$N_r = 2$
$N_r = 3$
$\cdots N_r = 5$

$Fig.(6.4)$. Influence of the buoyancy ratio N_r over the velocity profile F'

$K = 0.5$, $\lambda_N = 1$, $N_r = 0.5$, $\Lambda = 0.5$, $Pr = 3$, $B_P = 1$,
$T_P = 0.5$, $Le = 1$, $c_0 = 1$, $a_0 = 1$, $\varphi_\infty = 0.05$

Legend:
$\cdots \gamma_c = 0.2$
$\gamma_c = 0.3$
$\gamma_c = 0.5$
$\cdots \gamma_c = 0.7$

$Fig.(6.5)$. Influence of the curvature parameter γ_c over the microrotation

profile J

107

$\gamma_c = 0.25, \ \lambda_N = 1, \ N_r = 0.5, \ \Lambda = 0.5, \ Pr = 3, \ B_P = 1,$
$T_P = 0.5, \ Le = 1, \ c_0 = 1, \ a_0 = 1, \ \varphi_\infty = 0.05, \ n = 0$

$Fig.(6.6).$ Influence of micropolar parameter K over the microrotation profile J

$\gamma_c = 0.25, \ K = 0.5, \ \lambda_N = 1, \ N_r = 0.5, \ Pr = 3, \ B_P = 1,$
$T_P = 0.5, \ Le = 1, \ c_0 = 1, \ a_0 = 1, \ \varphi_\infty = 0.05, \ n = 0$
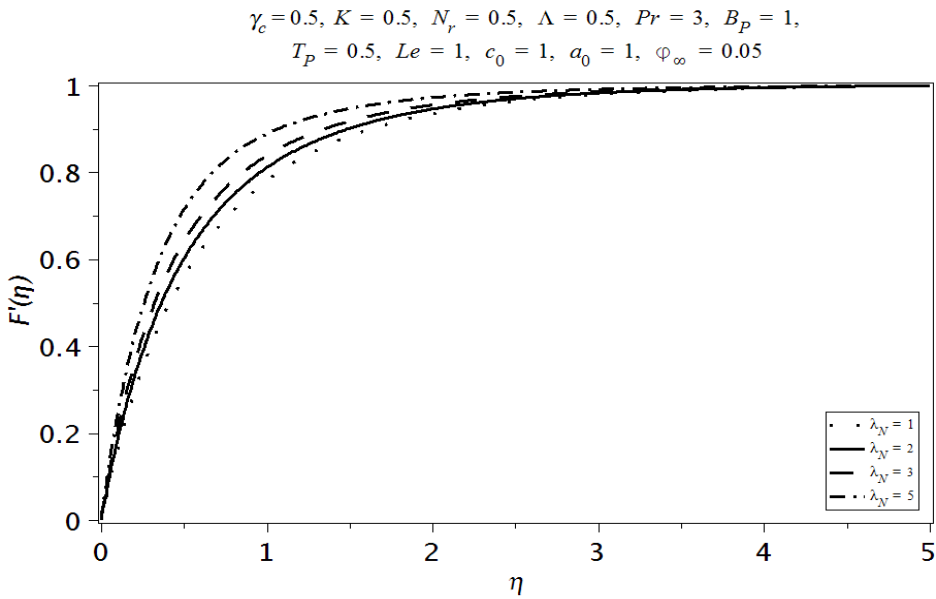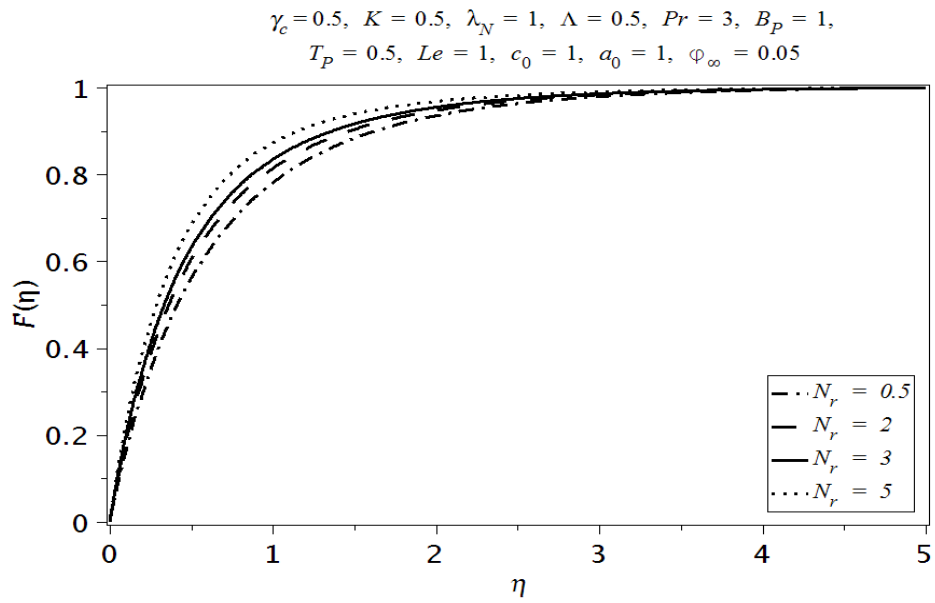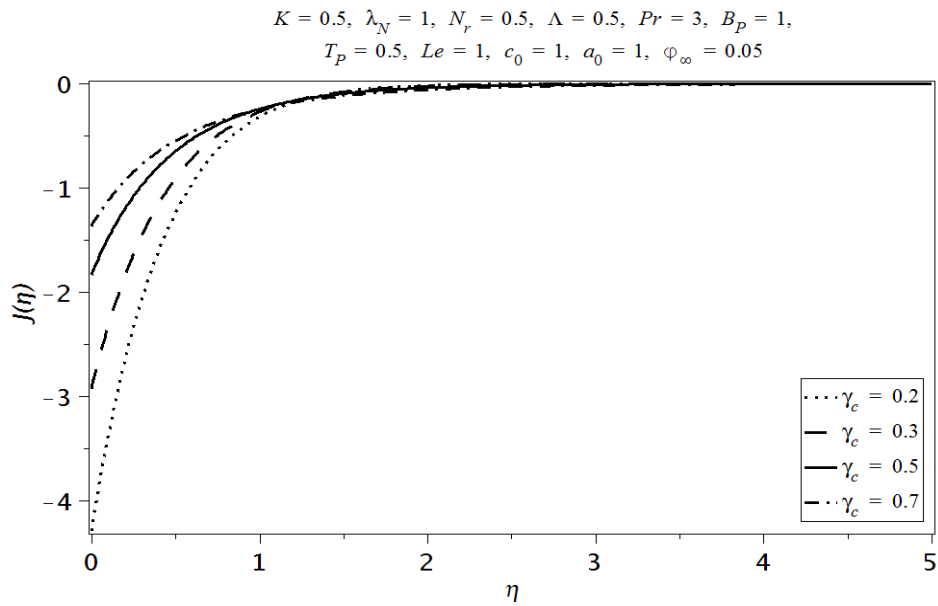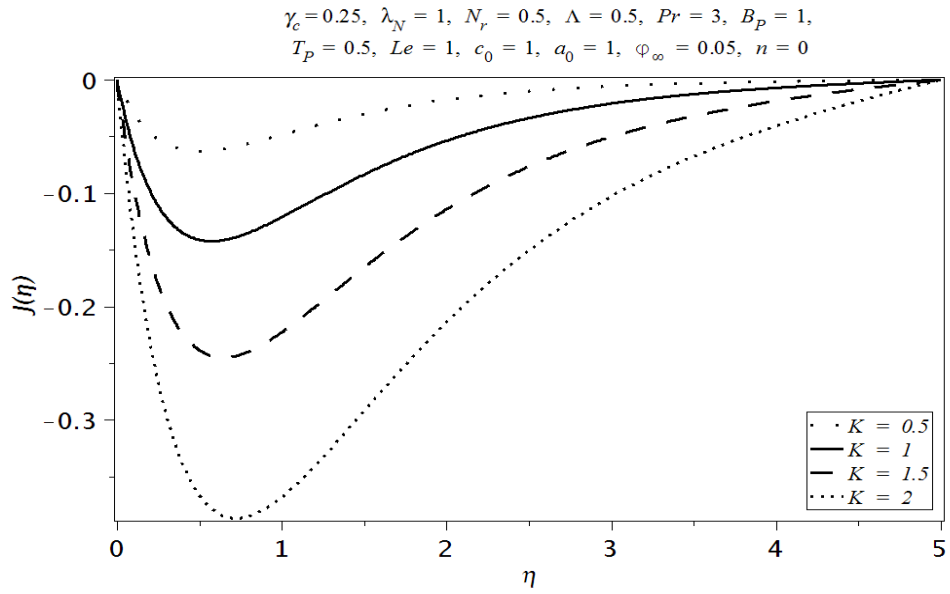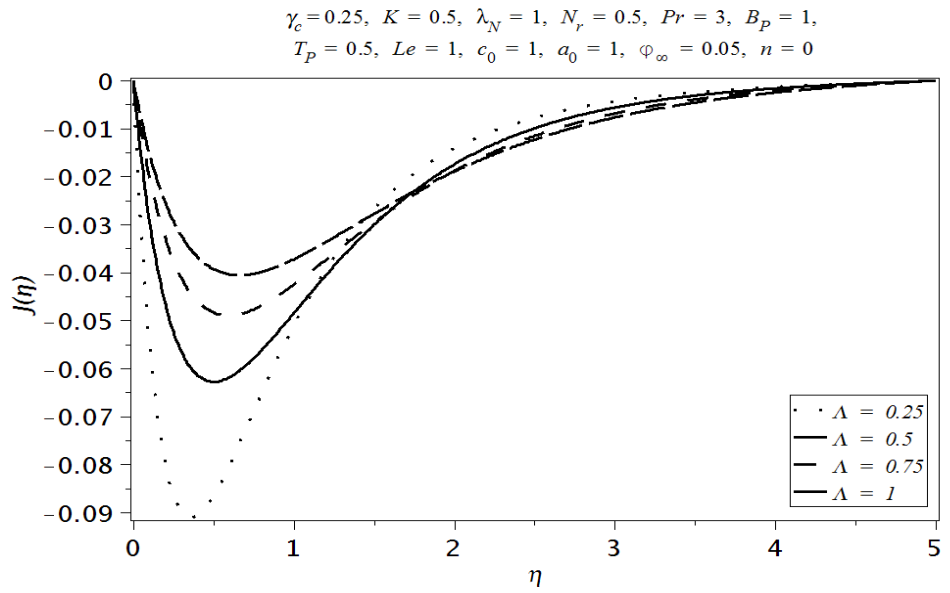
$Fig.(6.7).$ Influence of the micropolar parameter Λ over the microrotation profile J

108

$Fig.(6.8)$. Influence of curvature parameter γ_c over the tenperature profile θ

$\gamma_c = 1$, $K = 0.5$, $\lambda_N = 1$, $N_r = 0.5$, $\Lambda = 0.5$, $B_P = 1$,
$T_P = 0.5$, $Le = 1$, $c_0 = 1$, $a_0 = 1$, $\varphi_\infty = 0.05$
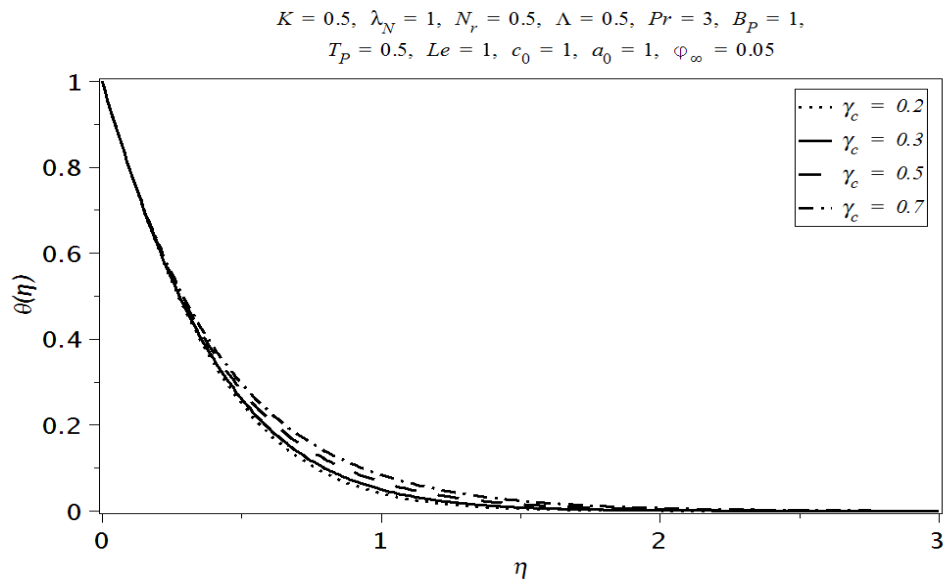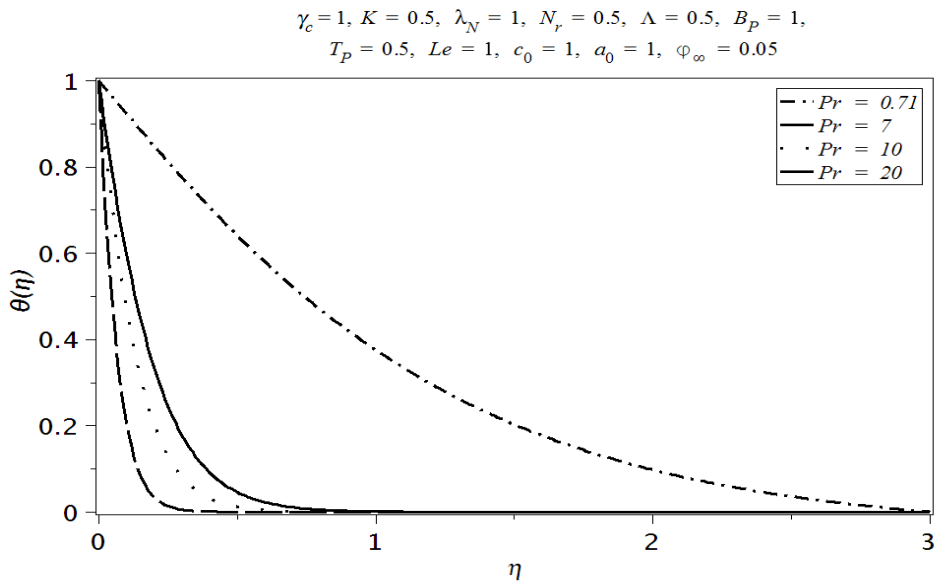
$Fig.(6.9)$. Influence of the Prandtl number Pr over the temperature profile θ
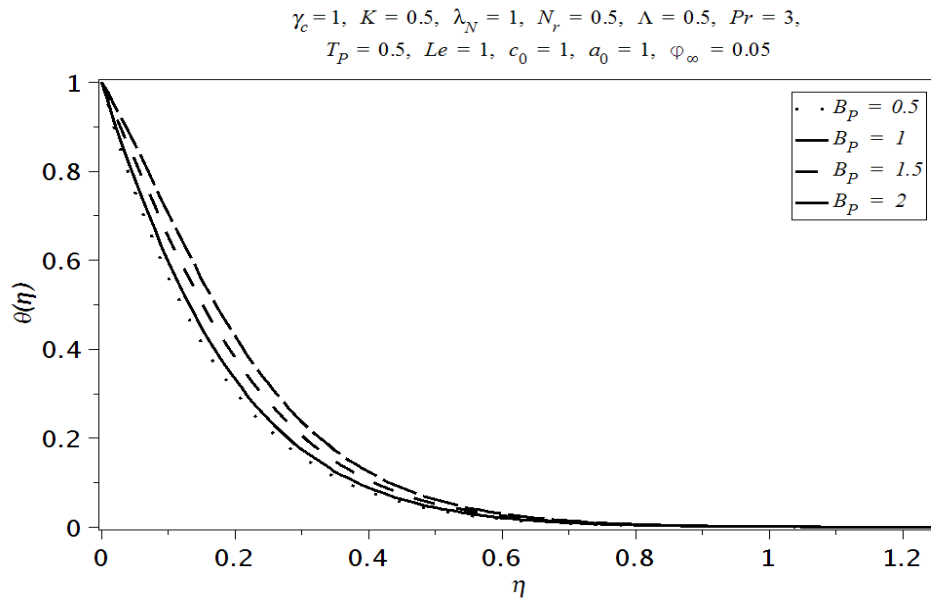
$Fig.$(6.10). Influence of the Brownian motion parameter B_P over the temperature profile θ
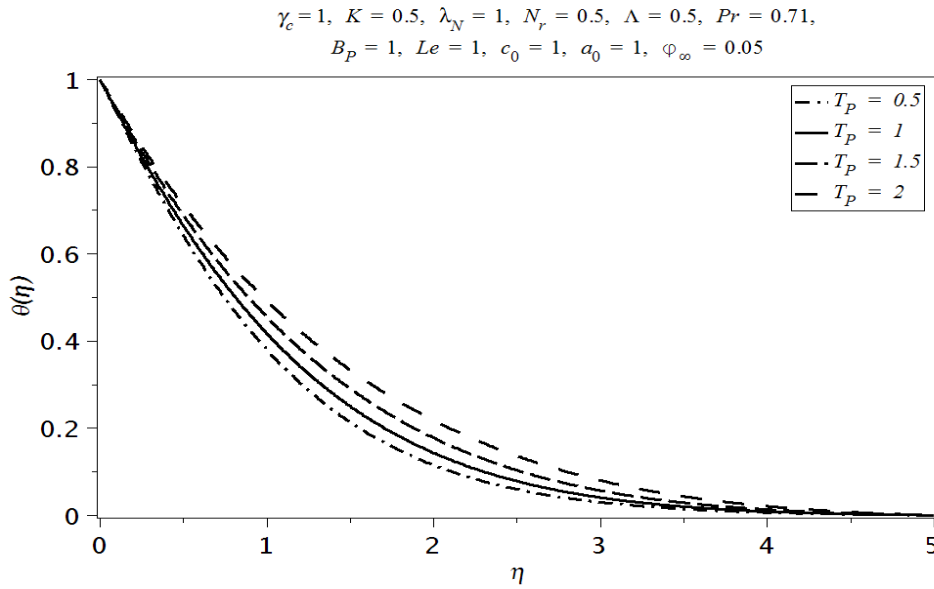
$Fig.$(6.11). Influence of the thermophoresis parameter T_P over the nanoparticle concentration profile ψ
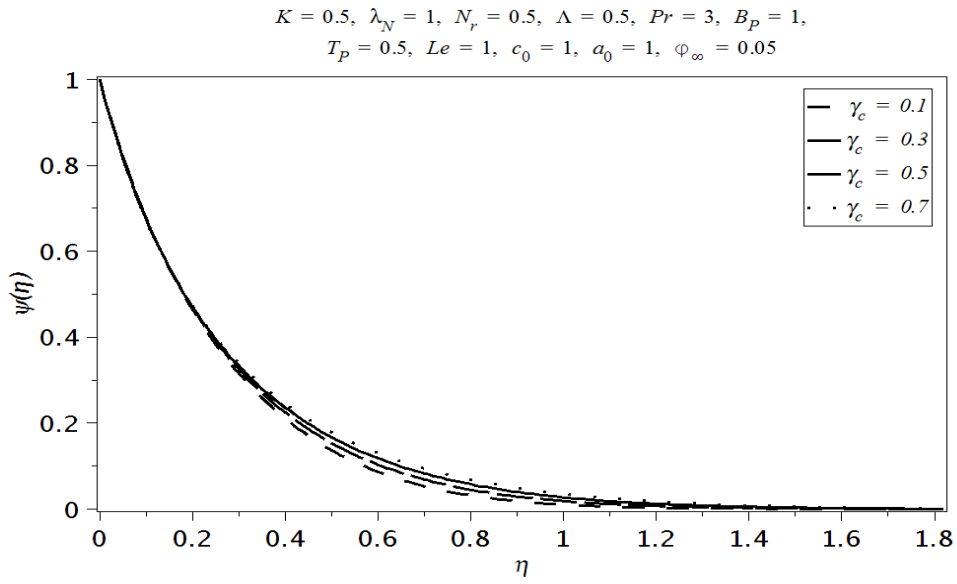
$Fig.$(6.12). Influence of curvature parameter γ_c over the nanoparticle concentration profile ψ

$\gamma_c = 0.25$, $K = 0.5$, $\lambda_N = 1$, $N_r = 0.5$, $\Lambda = 0.5$, $B_P = 1$,
$T_P = 0.5$, $Le = 1$, $c_0 = 1$, $a_0 = 1$, $\varphi_\infty = 0.05$
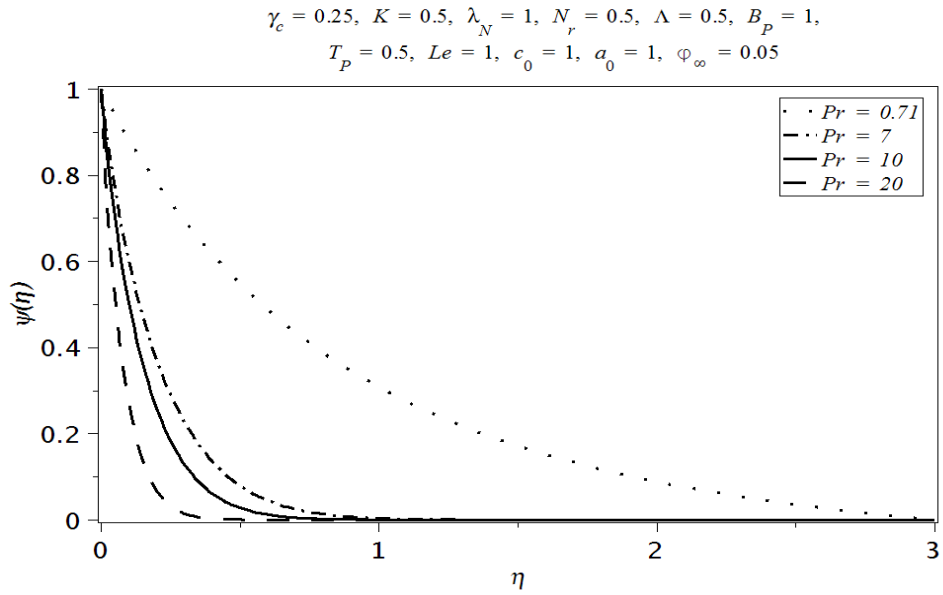
$Fig.$(6.13). Influence of the Prandtl number Pr over the nanoparticle concentration profile ψ

$Fig.$(6.14). Influence of the thermophoresis parameter T_P over the nanoparticle concentration profile ψ

$\gamma_c = 0.25$, $K = 0.5$, $\lambda_N = 1$, $N_r = 0.5$, $\Lambda = 0.5$, $Pr = 0.71$,
$T_P = 0.5$, $Le = 1$, $c_0 = 1$, $a_0 = 1$, $\varphi_\infty = 0.05$
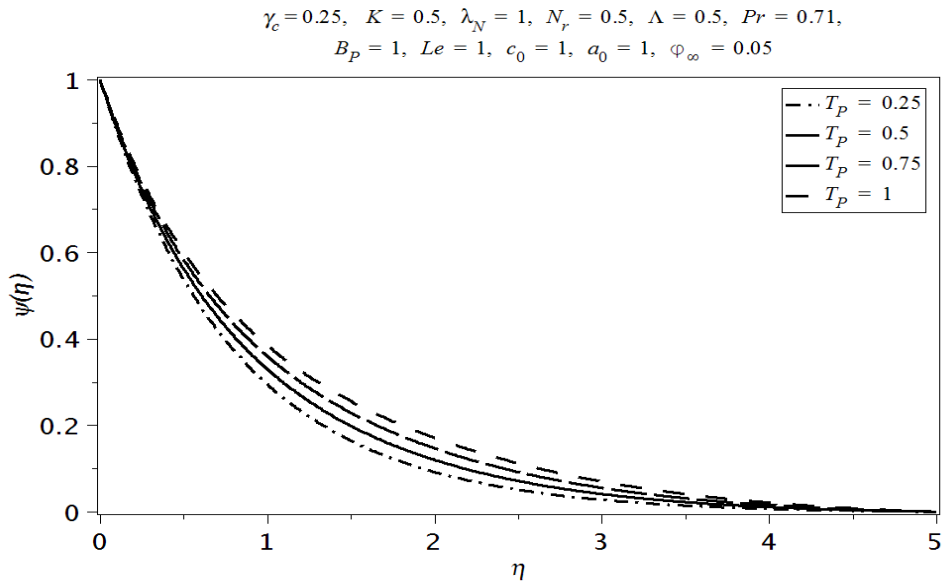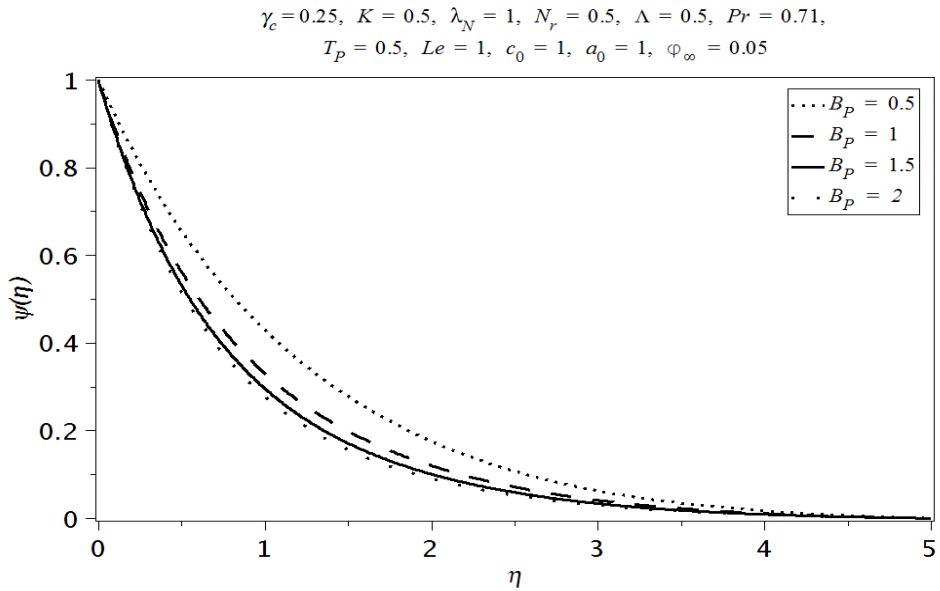
$Fig.$(6.15). Influence of the Brownian motion parameter B_P over the nanoparticle concentration profile ψ

	$F''(0)$					
$K\backslash\gamma_c$	0.1	0.2	0.3	0.4	0.5	0.6
0.25	1.9303	1.9765	2.0219	2.0666	2.1106	2.1540
0.5	1.6716	1.7154	1.7581	1.7994	1.8396	1.8791
0.75	1.4854	1.5272	1.5668	1.6042	1.6392	1.6740
1	1.3443	1.3840	1.4204	1.4530	1.4813	1.5019
1.25	1.2332	1.2708	1.3035	1.3305	1.3504	1.3610
1.5	1.1431	1.1785	1.2072	1.2274	1.2365	1.2473
1.75	1.0683	1.1015	1.1257	1.1380	1.1327	1.1459
2	1.0051	1.0359	1.0552	1.0579	1.0598	1.0605

$Table.(6.1)$. Behavior of the boundary derivatives of the velocity profile $F''(0)$ when $\lambda_N = 1$, $N_r = 0.5$, $\Lambda = 0.5$, $a_0 = 1$, $\text{Pr} = 3$, $B_P = 1$, $T_P = 0.5$, $Le = 1$, $\phi_\infty = 0.05$, $c_0 = 1$, $n = 1/2$

	$J'(0)$					
$\lambda_N \backslash K$	0.5	1	1.5	2	2.5	3
0.2	17.1324	13.5173	11.3004	9.7751	8.6459	7.7660
0.4	17.4042	13.7141	11.4539	9.9005	8.7517	7.8573
0.6	17.6761	13.9109	11.6074	10.0260	8.8575	7.9486
0.8	17.9481	14.1078	11.7610	10.1515	8.9633	8.0400
1	18.2201	14.3047	11.9146	10.2770	9.0692	8.1314
1.2	18.4922	14.5017	12.0684	10.1026	9.1751	8.2227
1.5	18.9005	14.7972	12.2988	10.5910	9.3340	8.3599
2	19.5813	15.2901	12.6833	10.9052	9.5990	8.5885

$Table.(6.2)$. Behavior of the boundary derivatives of the microrotation profile $J'(0)$ when $\gamma_c = 0.1$, $N_r = 0.5$, $\Lambda = 0.5$, $a_0 = 1$, $\text{Pr} = 3$, $B_P = 1$, $T_P = 0.5$, $Le = 1$, $\phi_\infty = 0.05$, $c_0 = 1$, $n = 1/2$

113

$\theta'(0)$						
$Pr\backslash K$	0.2	0.4	0.6	0.8	1	2
0.21	0.3602	0.3537	0.3481	0.3430	0.3385	0.3210
0.71	0.7465	0.7339	0.7232	0.7138	0.7055	0.6747
1	0.9357	0.9212	0.9089	0.8982	0.8888	0.8542
3	2.1590	2.1406	2.1253	2.1124	2.1013	2.0620
5	3.3891	3.3718	3.3578	3.3460	3.3360	3.3017
7	4.6415	4.6262	4.6139	4.6038	4.5952	4.5663
10	6.5469	6.5344	6.5245	6.5164	6.5096	6.4872

$Table.(6.3)$. Behavior of the boundary derivatives for the temperature profile $\theta'(0)$ when $\lambda_N = 0.5$, $\gamma_c = 0.1$, $N_r = 0.5$, $\Lambda = 0.5$, $a_0 = 1$, $B_P = 1$, $T_P = 0.5$, $Le = 1$, $\phi_\infty = 0.05$, $c_0 = 1$, $n = 0$

$\psi'(0)$						
$Le\backslash Pr$	0.21	0.71	1	3	7	10
0.2	0.3121	0.2326	0.1990			
0.4	0.4019	0.5043	0.5553	0.6948		
0.6	0.4836	0.7279	0.8446	1.4086	2.2234	
0.8	0.5590	0.9245	1.1003	2.0720	3.7711	5.0373
1	0.6292	1.1046	1.3369	2.7197	5.2750	7.2125
1.2	0.6954	1.2739	1.5615	3.3326	6.7518	9.3450
1.5	0.7885	1.5145	1.8842	4.2513	8.9352	12.4921

$Table.(6.4)$. Behavior of the boundary derivatives for the nanoparticle concentration profile $\psi'(0)$ when $\lambda_N = 0.5$, $\gamma_c = 0.1$, $N_r = 0.5$, $\Lambda = 0.5$, $a_0 = 1$, $K = 0.5$, $B_P = 1$, $T_P = 0.5$, $\phi_\infty = 0.05$, $c_0 = 1$, $n = 0$

	$F''(0)$					
	Present	[42]	Present	[42]	Present	[42]
$\lambda_N\backslash\gamma_c$	0.1		0.5		1	
0.1	3.1950	3.1950	3.4467	3.4467	3.7510	3.7510
0.5	3.4723	3.4723	3.7215	3.7215	4.0225	4.0225
1	3.8171	3.8171	4.0634	4.0634	4.3604	4.3604
2	4.5011	4.5011	4.7418	4.7418	5.0312	5.0312

$Table.$(6.5). Comparison of present results for

$F''(0)$ with [42] for $K = 0$

	$F''(0)$			
	Present	[44]	Present	[44]
$c_o\backslash\gamma_c$	0.5		1.5	
0	1.4886	1.4886	1.7954	1.7954
1	2.0397	2.0397	2.2982	2.2982
2	2.7332	2.7332	2.8746	2.8746

$Table.$(6.6). Comparison of present results for

$F''(0)$ with [44] for the special case when

$K = 0, \lambda_N = 0$

6.5 Conclusion

The main findings of the above discussion are

- The nondimensional velocity profile F' decreases with increase in the curvature parameter γ_c and the micropolar parameter K.

- The nondimensional velocity profile F' increases with increase in the natural convection parameter λ_N and the buoyancy ratio N_r.

- The nondimensional microrotation profile J increases with increase in the curvature parameter γ_c for the case when $n = 1/2$.

- The nondimensional microrotation profile J decreases with increase in the micropolar

115

parameter K for the case when $n = 0$.

- The nondimensional temperature profile θ decreases with increase in the Prandtl number Pr .

- The nondimensional temperature flow rate θ increases with increase in the curvature parameter γ_c, the Brownian motion parameter B_P and the thermophoresis parameter T_P.

- The nanoparticle concentration profile ψ decreases with increase in the curvature parameter γ_c, the Prandtl number Pr and the Brownian motion parameter B_p.

- The nanoparticle concentration profile ψ increases with increase in the thermophoresis parameter T_p.

- The shear stress at the surface of the cylinder decreases with increase in the microplar parameter K.

- The heat flux at the surface of the cylinder decreases with increase in the microplar parameter K.

- The sherwood number increases with increase in the Lewis number Le.

Chapter 7

Stagnation flow of couple stress nanofluid over an exponentially stretching sheet through a porous medium

7.1 Introduction

In this chapter an investigation is carried out for the problem of boundary layer stagnation point flow and heat transfer of a couple stress fluid containing nanoparticles and flowing over an exponentially stretching surface in a porous medium. The governing equations of couple stress fluid model for velocity, temperature and nanoparticle profiles are given under boundary layer approach. The nonlinear partial differential equations are simplified by using similar transformations. The analytical solutions of simplified equations are found with the help of homotopy analysis method. The convergence of the HAM solutions has been discussed by plotting $\hbar$-curves and also through homotopy pade approximation. The physical features of pertinent parameters have been discussed through graphs.

7.2 Formulation

Let us consider the boundary layer stagnation point flow of a steady incompressible couple stress fluid over an exponentially stretching sheet through a porous medium. The Cartesian coordinates (x, y) are used such that x is along the surface of the sheet, while y is taken normal to it. The governing equations of conservation of mass momentum, energy and the nanoparticle concentration are

$$\text{div } \mathbf{V} = 0, \tag{7.1}$$

$$\rho \frac{d\mathbf{V}}{dt} = \text{div } \mathbf{S} - \eta_0 \boldsymbol{\nabla}^4 \mathbf{V} - \frac{\mu \phi_p}{k_0} \mathbf{V}, \tag{7.2}$$

$$\rho c_p \frac{dT}{dt} = -\text{div } \mathbf{q} + \rho^* c_p^* \left(D_B \boldsymbol{\nabla} \phi \cdot \boldsymbol{\nabla} T + \frac{D_T}{T_\infty} \boldsymbol{\nabla} T \cdot \boldsymbol{\nabla} T \right), \tag{7.3}$$

$$\frac{d\phi}{dt} = D_B \boldsymbol{\nabla}^2 \phi + \frac{D_T}{T_\infty} \boldsymbol{\nabla}^2 T, \tag{7.4}$$

where η_0 is the material constant for the couple stress fluid, ϕ_p is the porosity of porous space, k_0 is the permeability of porous space and T_∞ is the fluid temperature lying far away from the sheet. The boundary layer equations of conservation of mass, momentum, heat transfer and nanoparticle concentration are

$$\frac{\partial v_x}{\partial x} + \frac{\partial v_y}{\partial y} = 0, \tag{7.5}$$

$$v_x \frac{\partial v_x}{\partial x} + v_y \frac{\partial v_x}{\partial y} = W_\infty \frac{dW_\infty}{dx} + \nu \frac{\partial^2 v_x}{\partial y^2} - \frac{\eta_0}{\rho} \frac{\partial^4 v_x}{\partial y^4} - \frac{\nu \phi_p}{k_0} v_x, \tag{7.6}$$

$$v_x \frac{\partial T}{\partial x} + v_y \frac{\partial T}{\partial y} = \alpha \frac{\partial^2 T}{\partial y^2} + \frac{\rho^* c_p^*}{\rho c_p} \left(D_B \frac{\partial T}{\partial y} \frac{\partial \phi}{\partial y} + \frac{D_T}{T_\infty} \left(\frac{\partial T}{\partial y} \right)^2 \right), \tag{7.7}$$

$$v_x \frac{\partial \phi}{\partial x} + v_y \frac{\partial \phi}{\partial y} = D_B \frac{\partial^2 \phi}{\partial y^2} + \frac{D_T}{T_\infty} \frac{\partial^2 T}{\partial y^2}, \tag{7.8}$$

here (v_x, v_y) are the velocity components along the (x, y) axes, ν is the kinematic viscosity, W_∞ is the free-stream velocity and α is the thermal diffusivity. The corresponding boundary conditions for the problem are

$$v_x = W_{sv}, \quad v_y = 0, \quad \text{at } y = 0, \quad v_y \longrightarrow W_\infty, \quad \text{as } y \longrightarrow \infty, \tag{7.9}$$

$$\frac{\partial^2 v_x}{\partial y^2} = 0, \quad \text{at } y = 0, \quad \text{and} \quad \frac{\partial v_x}{\partial y}, \quad \text{as } y \to \infty, \tag{7.10}$$

$$T = T_w, \quad \phi = \phi_w \quad \text{at } y = 0, \quad \text{and} \quad T \to T_\infty, \quad \phi \to \phi_\infty, \quad \text{as } y \to \infty, \tag{7.11}$$

where the free-stream velocity W_∞, the stretching velocity W_{sv} and the surface temperature T_w are defined as

$$W_\infty = Ae^{x/L}, \quad W_{sv} = Be^{x/L}, \quad T_w = T_\infty + ce^{x/L}, \tag{7.12}$$

where A, B and c are constants with appropriate dimensions while L is the reference length.

7.3 Solution of the problem

For solution of the problem we take the following similar similarity transformations [56]

$$v_x = Ae^{x/L}H'(\eta), \quad v_y = -(\frac{\nu A}{2L})^{1/2}e^{x/L}(H(\eta) + \eta H'(\eta)), \tag{7.13}$$

$$\theta = \frac{T - T_\infty}{T_w - T_\infty}, \tag{7.14}$$

$$\psi = \frac{\phi - \phi_\infty}{\phi_w - \phi_\infty}, \tag{7.15}$$

$$\eta = \left(\frac{A}{2\nu L}\right)^{1/2} e^{x/2L} y. \tag{7.16}$$

With the help of transformations in $Eqs.\,(7.13)$ to (7.16), $Eq.\,(7.5)$ is identically satisfied while $Eqs.\,(7.6)$ to (7.8) take the form

$$\lambda_c H^{(5)} - H''' - HH'' + 2H'^2 - 2 + k_p^* H' = 0, \tag{7.17}$$

$$\theta'' + \Pr(H\theta' - 2H'\theta) + B_P \theta' \psi' + T_P \theta'^2 = 0, \tag{7.18}$$

$$\psi'' + \Pr Le\left(H\psi' - 2H'\psi\right) + \frac{T_P}{B_P}\theta'' = 0, \tag{7.19}$$

where $\lambda_c = \eta_0 W_\infty / 2\mu\nu L$ is the couple stress fluid parameter, $k_p^* = 2\nu L\phi_p / W_\infty k_0$ is the porosity parameter, $\mathrm{Pr} = \nu/\alpha$ is the Prandtl number, $B_P = (\phi_w - \phi_\infty) D_B \rho^* c_p^* / \alpha\rho c_p$ is the Brownian motion parameter, $T_P = (T_w - T_\infty) D_T \rho^* c_p^* / \alpha\rho c_p T_\infty$ is the thermophoresis parameter and $Le = \alpha/D_B$ is the Lewis number. The boundary conditions in nondimensional form are

$$H(0) \quad = \quad 0, \quad H'(0) = \epsilon, \quad H'''(0) = 0, \tag{7.20}$$

$$H' \quad \longrightarrow \quad 1, \quad H'' \longrightarrow 0, \quad \text{as } \eta \longrightarrow \infty, \tag{7.21}$$

$$\theta(0) \quad = \quad 1, \quad \psi(0) = 1, \quad \theta \to 0, \quad \psi \to 0 \text{ as } \eta \to \infty, \tag{7.22}$$

where $\epsilon = B/A$ is the stretching ratio. To solve the problem with the help of homotopy analysis method (HAM), the initial guess chosen and the corresponding auxiliary linear operators are [86]

$$f_0 \quad = \quad (\epsilon - 1) + (\epsilon - 1)(\frac{\eta^2}{2} - 1)e^{-\eta} + \eta, \quad \theta_0 = e^{-\eta}, \quad \psi_0 = e^{-\eta}, \tag{7.23}$$

$$L_f \quad = \quad \frac{d^5}{d\eta^5} + 3\frac{d^4}{d\eta^4} + 3\frac{d^3}{d\eta^3} + \frac{d^2}{d\eta^2}, \tag{7.24}$$

$$L_\theta \quad = \quad \frac{d^2}{d\eta^2} + \frac{d}{d\eta}, \quad L_\psi = \frac{d^2}{d\eta^2} + \frac{d}{d\eta}. \tag{7.25}$$

Further details of the HAM solution are presented in the next section. The important physical quantities heat flux at the surface of the sheet q_w, the local Nusselt numbers Nu and the Sherwood number Sh associated with the present problem are

$$q_w = -k\frac{\partial T}{\partial y}|_{y=0}, \quad Nu_x = -\sqrt{\mathrm{Re}_x}\theta'(0), \quad Sh = -\sqrt{\mathrm{Re}_x}\psi'(0), \tag{7.26}$$

where $\mathrm{Re}_x = W_\infty x^2 / 2\nu L$.

7.4 Results and discussion

The problem of boundary layer stagnation flow and heat transfer of a couple stress nanofluid flowing over an exponentially stretching sheet through a porous medium is solved analytically with the help of homotopy analysis method (HAM). The reliability and convergence of HAM

solutions are examined by computing $\hbar$-curves for nondimensional velocity, temperature and nanoparticle concentration profiles H', θ and ψ. Further, the homotopy pade approximation is also applied to confirm the convergence of the solutions, while for another check, the system of differential equations is also solved numerically with the help of Runge-Kutta Fehlberg method and a comparison of both the solutions is presented through tables. $Figs.(7.1)$ to (7.3) are planted to observe the convergence regions of the auxiliary parameters $\hbar_1, \hbar_2$ and $\hbar_3$ for nondimensional velocity, temperature and nanoparticle concentration profiles for different combinations of the involved parameters. $Fig.(7.1)$ is sketched for the convergence regions of the velocity profile H' for different combinations of the couple stress fluid parameter λ_c and the porosity parameter k_p^* when the stretching parameter $\epsilon = 0.25$. It is noticed that increase in both the couple stress fluid parameter λ_c and the porosity parameter k_p^*, decreases the acceptable convergence region for the auxiliary parameter $\hbar_1$. From $Fig.(7.1)$ the convergence region for velocity profile H' when the couple stress fluid parameter $\lambda_c = 1.5$ and the porosity parameter $k_p^* = 0.5$ is $-1.1 \leq \hbar_1 \leq -0.3$. $Fig.(7.2)$ contains the $\hbar$-curves plotted against temperature gradient for different choices of the Prandtl number Pr and the Brownian motion parameter B_P, while $Fig.(7.3)$ gives the $\hbar$-curves for nanoparticle concentration profile ψ for different values of the Prandtl number Pr and the Lewis number Le. From $Figs.(7.2)$ and (7.3) increase in the Prandtl number Pr, the Brownian motion parameter B_P and the Lewis number Le, decreases the convergence region. From $Fig.(7.3)$ when the Lewis number $Le = 0.5$ and the Prandtl number Pr $= 5$, the acceptable convergence region for the auxiliary parameter $\hbar_3$ is $-1.2 \leq \hbar_3 \leq -0.2$. $Tables.(7.1)$ to (7.3) are presented to cement the convergence of the obtained solutions. $Table.(7.1)$ contains the homotopy pade approximation values for velocity, temperature and nanoparticle concentration profiles for certain values of the involved parameters. The pade approximates are calculated up to $[30/30]$ approximates and the obtained values guarantees the convergence of HAM solutions. In $Table.(7.1)$ pade approximations for velocity profile calculated are for stretching ratio $\epsilon = 0.5$, while pade accelerators for temperature and nanoparticle concentration profiles are computed for stretching ratio $\epsilon = 1$. It is also noticed that convergence for velocity and temperature profiles are achieved much before then the convergence for nanoparticle concentration profile. $Tables.(7.2)$ and (7.3) provide a comparison of both the HAM and numerical solutions of the velocity, temperature and nanoparticle concen-

tration profiles for different values of the associated parameters. From these tables it is obvious that the obtained values are in good agreement.

The behavior of velocity, temperature and nanoparticle concentration profiles for different values of the involved parameters are presented in $Figs.(7.4)$ to (7.13). $Fig.(7.4)$ refers to the influence of couple stress fluid parameter λ_c over velocity profile H' for different values of porosity parameter k_p^*, when the stretching ratio $\epsilon = 2$. From $Fig.(7.4)$ it is clear that velocity profile has a dual behavior with respect to couple stress fluid parameter λ_c, that is, near the surface of the sheet the velocity profile increases with increase in the couple stress fluid parameter λ_c, while the velocity profile H' changes its behavior after a certain interval and then becomes decreasing with increase in the couple stress fluid parameter λ_c. In $Fig.(7.4)$ the behavior of velocity profile is sketched when the fluid is flowing without porous medium $(k_p^* = 0)$ and fluid through porous medium with porosity parameter $k_p^* = 1$. It is also noted from $Fig.(7.4)$ that the turning points for velocity profile for different values of the porosity parameter k_p^* lies almost at the same η, while the convergence rate for velocity profile is much quicker for smaller porosity parameter k_p^*. $Fig.(7.5)$ reflects the influence of porosity parameter k_p^* plotted for different values of stretching ratio ϵ, when couple stress fluid parameter $\lambda_c = 1$. From $Fig.(7.5)$ it is noted that the velocity profile H' near the sheet surface decreases with increase in the porosity parameter k_p^*, while in the far field region the velocity profile changes its behavior and becomes increasing with increase in the porosity parameter k_p. The convergence rate for velocity profile with the stretching ratio $\epsilon = 0.5, 1.5$ is almost the same. $Figs.(7.6)$ and (7.7) give the pattern followed by the velocity gradient for different combinations of the involved parameters that guarantees the satisfaction of the boundary conditions for the velocity gradient H'' associated with the couple stress fluid model. $Fig.(7.6)$ gives the behavior of velocity gradient H'' for different values of couple stress fluid parameter λ_c for fluid flowing through porous medium with porosity parameter $k_p^* = 0, 1$. It is observed from $Fig.(7.6)$ that near the boundary of the sheet velocity gradient H'' decreases with increase in the couple stress fluid parameter λ_c while in the far field region, increase in the couple stress fluid parameter λ_c increases the velocity gradient. It is also evident from $Fig.(7.6)$ that increase in the porosity parameter k_p^* increases the deviation of velocity gradient from the mean position. $Fig.(7.7)$ is plotted to observe the behavior of the porosity parameter k_p^* for couple stress fluids with $\lambda_c = 1$,

computed for the flat plate case $(\epsilon = 0)$, and the stretching sheet problem with stretching ratio $\epsilon = 2$. The dual behavior is evident in the sketch. From $Fig.(7.7)$ it is predicted that near the boundary of the sheet the velocity gradient is decreasing with increase in the porosity parameter k_p^*, while in the far field area the velocity gradient becomes increasing with increase in the porosity parameter k_p^*. $Fig.(7.8)$ inculcates the influence of porosity parameter k_p^* over the temperature profile θ for different values of the Prandtl number Pr and for specified values of the other parameters. From $Fig.(7.8)$ it is depicted that the influence of porosity parameter k_p^* over θ is opposite to that of the Prandtl number Pr that is with increase in the Prandtl number Pr the temperature profile θ and the thermal boundary layer thickness decreases, whereas with increase in porosity parameter k_p^* the temperature profile θ increases. $Fig.(7.9)$ describes the influence of Brownian motion parameter B_p over temperature profile θ computed for different values of the thermophoresis parameter T_p. From $Fig.(7.9)$ it is observed that increase in both the Brownian motion parameter B_p and the thermophoresis parameter T_p, the temperature profile θ increases. This observation is consistent with the fact that nanoparticles have high thermal conductivity and so has higher heat transfer rate. $Fig.(7.10)$ shows the influence of couple stress fluid parameter λ_c over temperature profile θ for shrinking sheet with $\epsilon = -0.25$ and stretching sheet with $\epsilon = 0.25, 1.5$ for specified values of the other involved parameters. From $Fig.(7.10)$ it is clear that increase in the stretching ratio ϵ decreases the temperature profile θ and the thermal boundary layer thickness, while increase in the couple stress fluid parameter λ_c increases the temperature profile θ. $Fig.(7.11)$ indicates the behavior of nanoparticle concentration profile ψ for different values of the Lewis number Le computed for different choices of the Prandtl number Pr. From $Fig.(7.11)$ it is predictable that with increase in both the Lewis number Le and the Prandtl numbet Pr the nanoparticle concentration profile ψ and the nano boundary layer thickness decreases. $Fig.(7.12)$ gives the influence of the porosity parameter k_p^* over the nanoparticle concentration profile ψ calculated for different values of the Prandtl number Pr. From $Fig.(7.12)$ it is clear that increase in the porosity parameter k_p^* increases the nanoparticle concentration profile ψ. $Fig.(7.13)$ is prepared to analyze the behavior of the thermophoresis parameter T_p over the nanoparticle concentration profile ψ for different values of the Brownian motion parameter B_p. The sketch indicates that increase in the thermophoresis parameter T_p, increases the nanoparticle concentration profile ψ.

$Table.$(7.4) contains values for boundary derivatives for nondimensional temperature profile θ at the surface of the sheet which corresponds to the influence of heat flux at the surface of the sheet for different values of the porosity parameter k_p^*, the Prandtl number Pr and the Brownian motion parameter B_p. From $Table.$(7.4) it is noted that with increase in the Prandtl number Pr, heat flux at the surface increases, whereas with increase in the porosity parameter k_p^* and the Brownian motion parameter B_p, heat flux at the surface of the stretching sheet decreases. $Table.$(7.5) refers to the behavior of Sherwood number Sh for different combinations of the porosity parameter k_p^*, the Prandtl number Pr and the Lewis number Le that correspond to the mass transfer rate at the surface of the sheet. From $Table.$(7.5) it is noticed that with increase in both the Prandtl number Pr and the Lewis number Le, the Sherwood numbers increase.
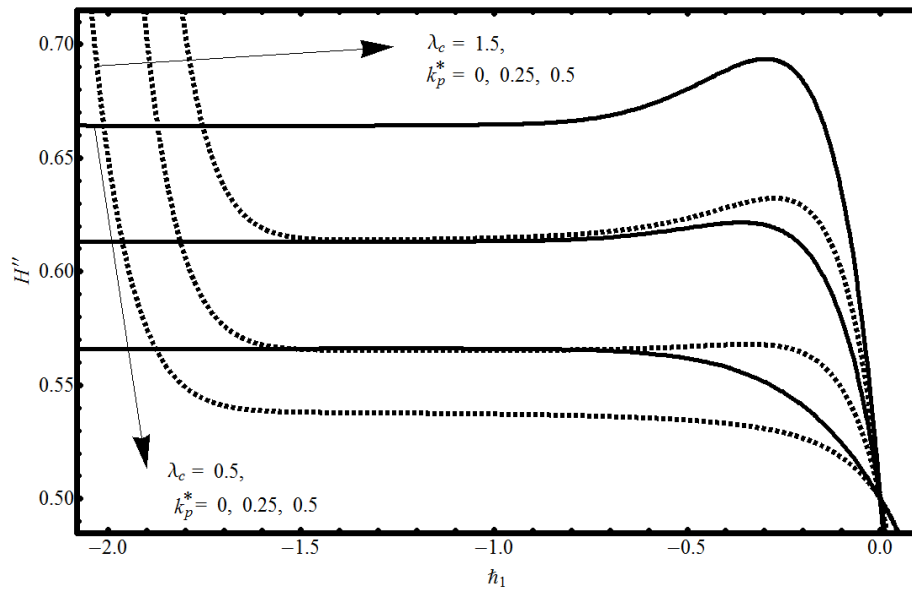

$Fig.$(7.1). $\hbar$-curve for H' for different values of λ_c and k_p^* plotted at 15th order of approximation, when $\epsilon = 0.25$
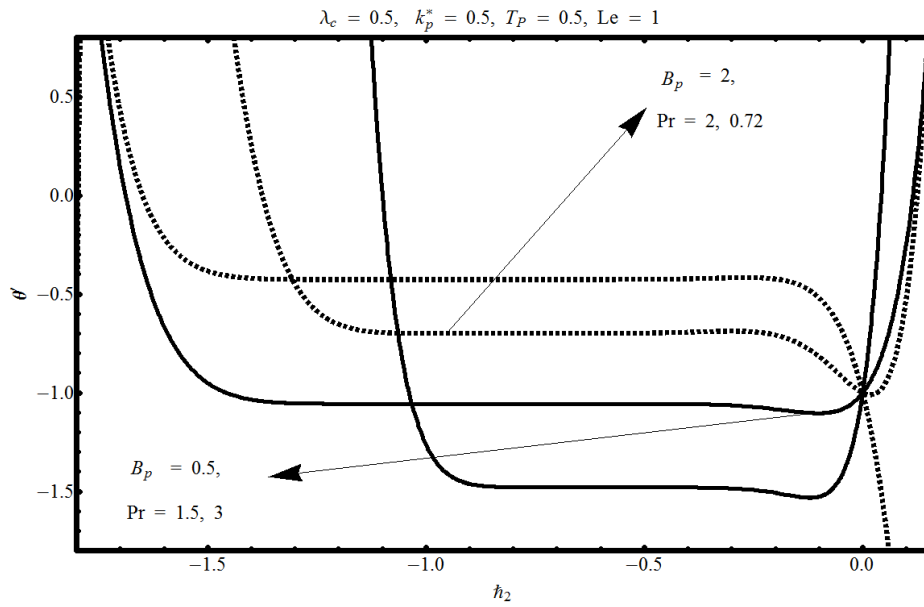
124

$Fig.(7.2)$. $\hbar$-curve for temperature profile θ for different values of B_p and Pr, plotted at 15th-Order of approximation, when $\epsilon = 0.5$
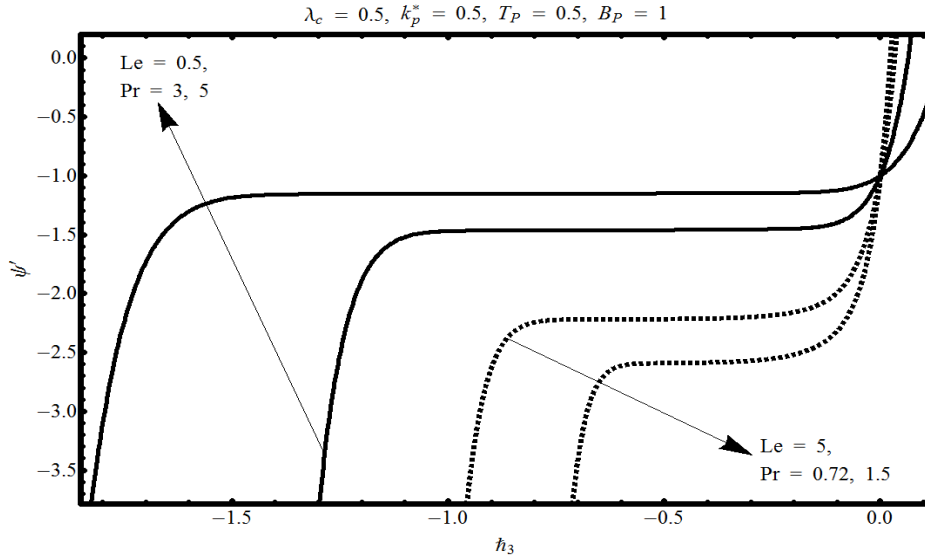

$Fig.(7.3)$. $\hbar$-curve for concentration profile ψ for different values of Le and Pr, plotted at 15th-Order of approximation, when $\epsilon = 0.5$
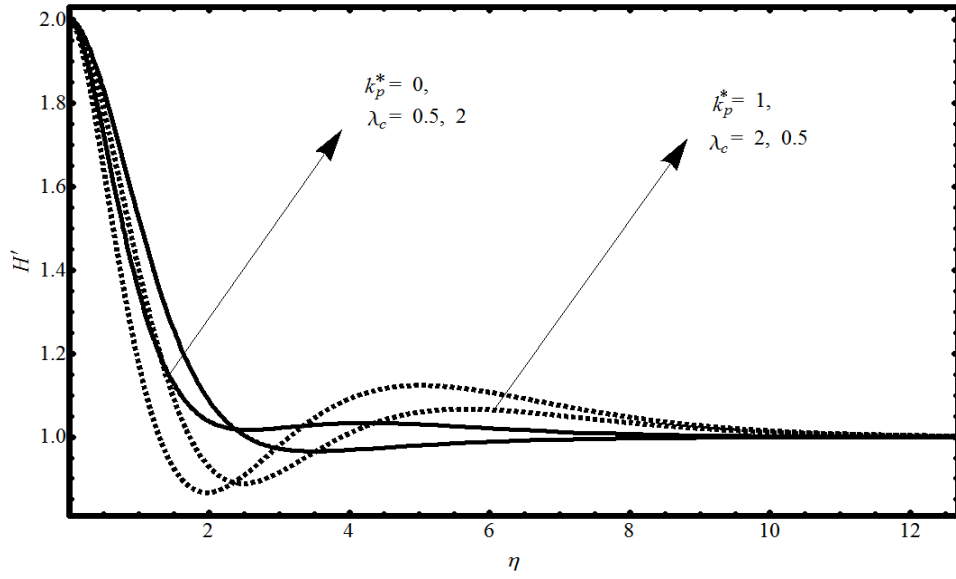
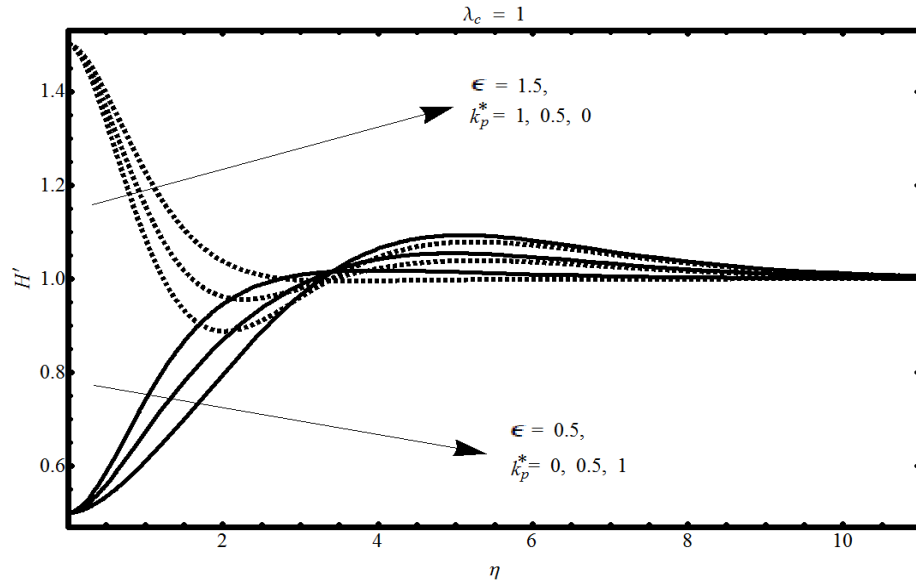$Fig.$(7.4). Influence of λ_c over H' for different k_p^*, when $\epsilon = 2$

$Fig.$(7.5). Influence of k_p^* over H' for different ϵ
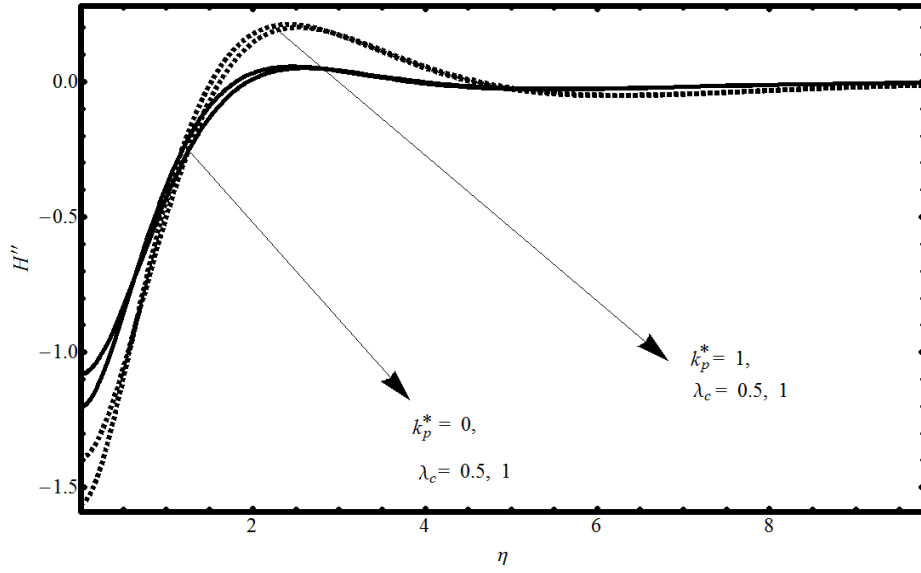
126

$Fig.(7.6)$. Influence of λ_c over H'' for different k_p^*, when $\epsilon = 2$
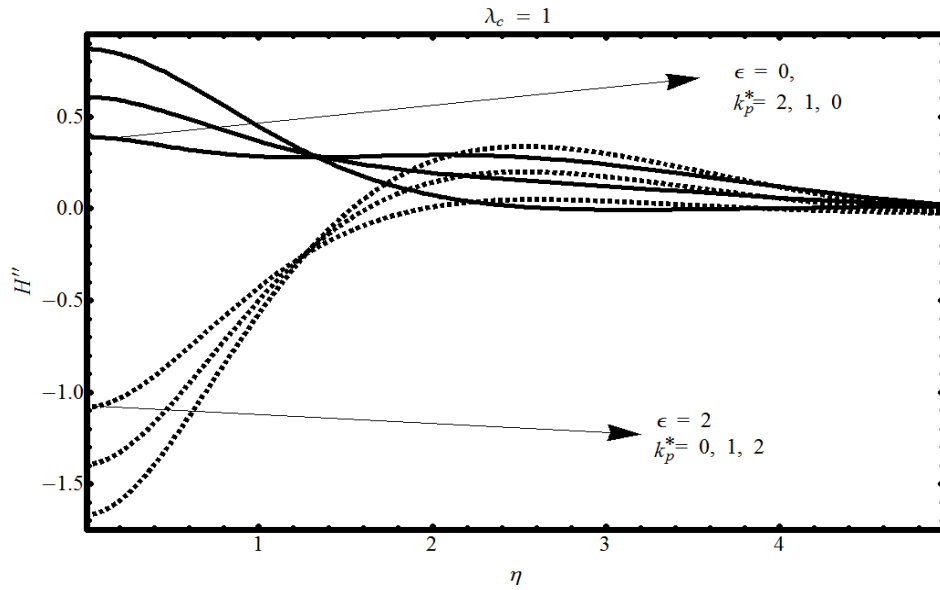
$Fig.(7.7)$. Influence of k_p^* over H'' for different ϵ
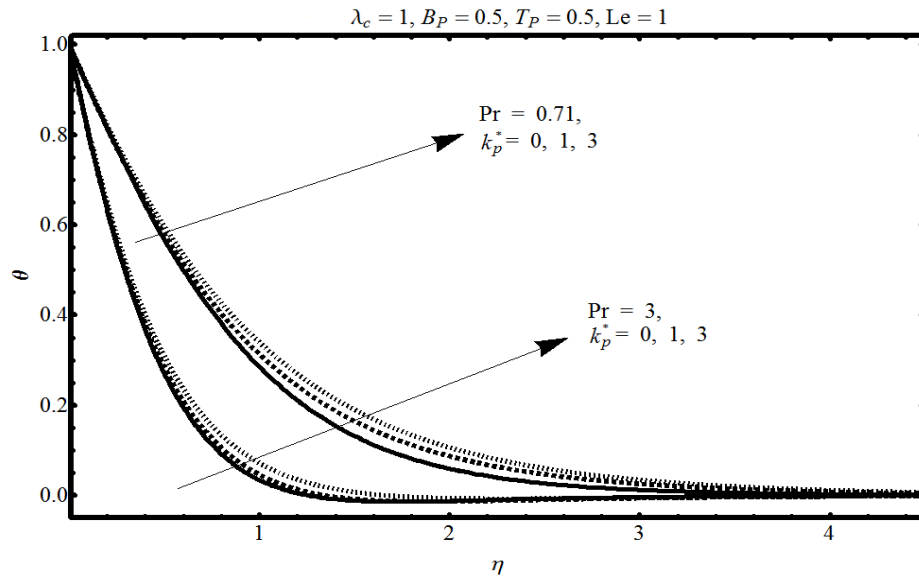
$Fig.(7.8)$. Influence of k_p^* over θ for different Pr, when $\epsilon = 1$
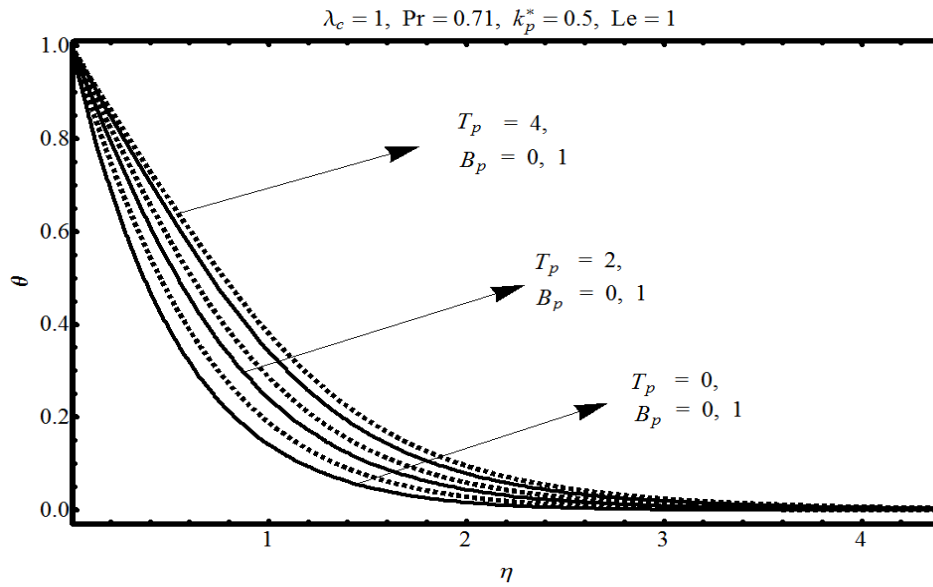
$Fig.(7.9)$. Influence of B_p over θ for different T_p, when $\epsilon = 2$
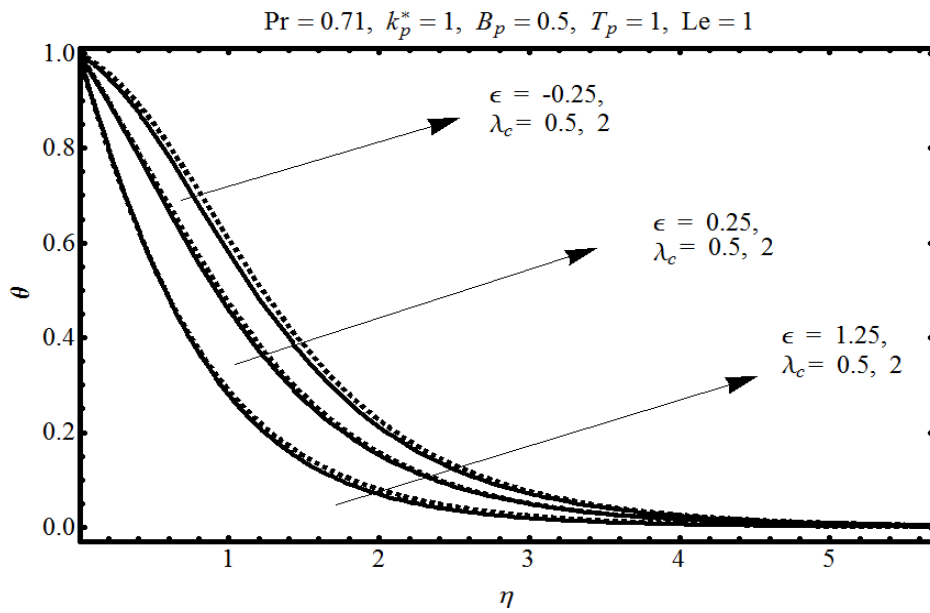
$Fig.(7.10)$. Influence of λ_c over θ for different ϵ
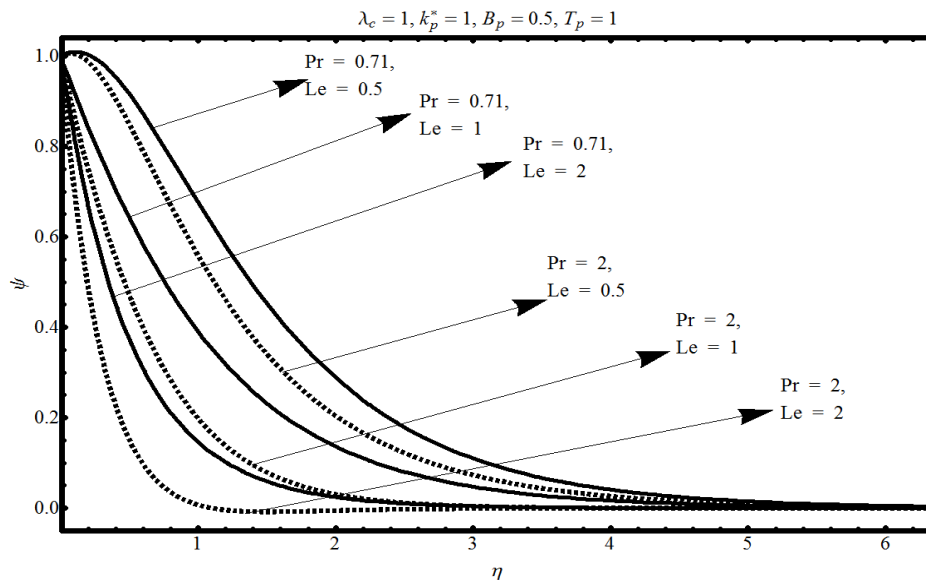
$Fig.(7.11)$. Influence of Le over θ for different Pr, when $\epsilon = 2$

129

$Fig.(7.12)$. Influence of Pr over ψ for different k_p^*, when $\epsilon = 2$

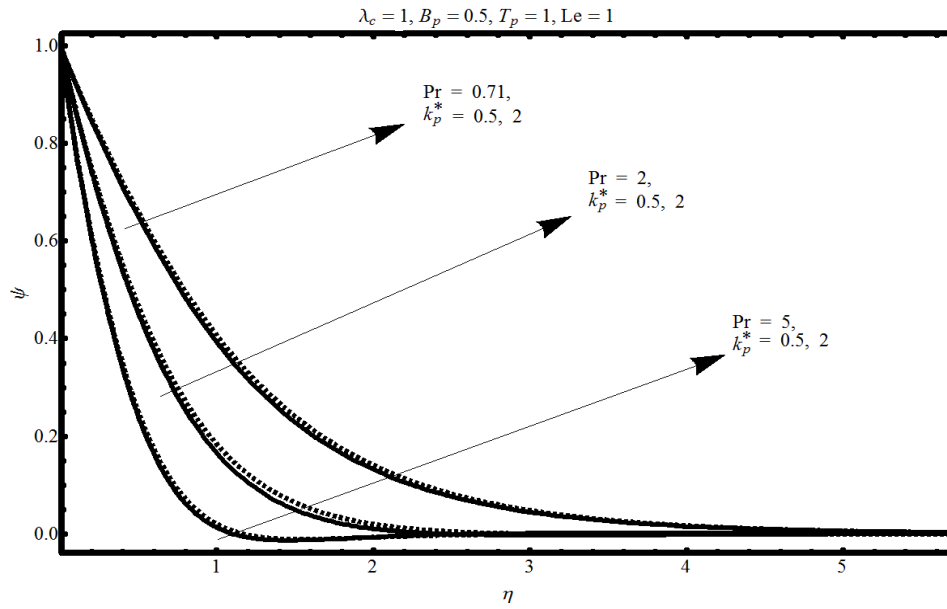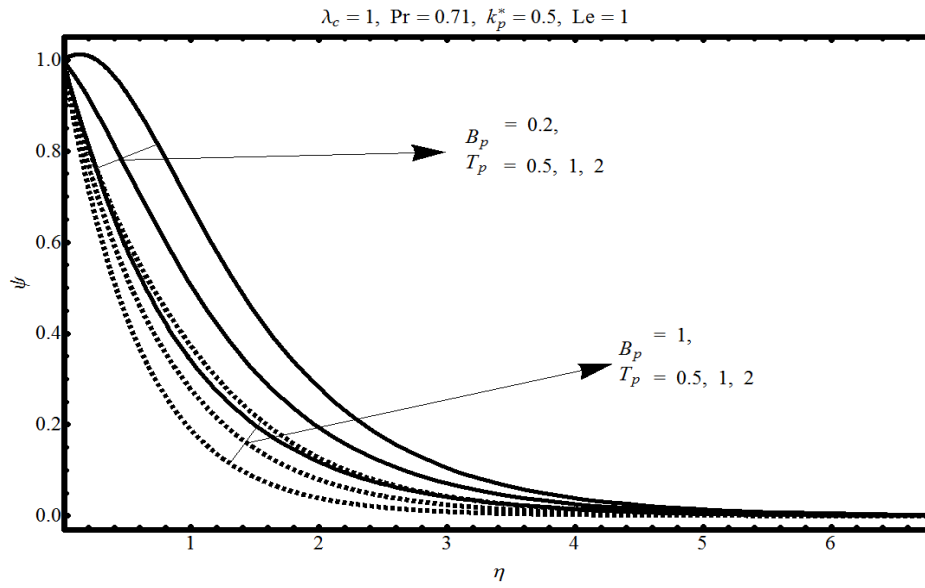$Fig.(7.13)$. Influence of B_p over ψ for different T_p, when $\epsilon = 2$

130

Order of App.	$H''(0)$	$\Theta'(0)$	$\psi'(0)$	Order of App.	$H''(0)$	$\Theta'(0)$	$\psi'(0)$
[1/1]	0.4883	-0.7601	-1.1705	[10/10]	0.4579	-0.7434	-1.1297
[2/2]	0.4814	-0.7449	-1.1274	[11/11]	0.4579	-0.7434	-1.1297
[4/4]	0.4611	-0.7438	-1.1282	[13/13]	0.4578	-0.7433	-1.1298
[5/5]	0.4591	-0.7436	-1.1288	[15/15]	0.4578	-0.7433	-1.1298
[7/7]	0.4582	-0.7435	-1.1294	[18/18]	0.4578	-0.7433	-1.1299
[8/8]	0.4580	-0.7434	-1.1295	[20/20]	0.4578	-0.7433	-1.1299

$Table.(7.1)$. Pade table showing the convergence of velocity, temperature and nanoparticle profiles for $\hbar_1 = \hbar_2 = \hbar_3 = -1$, $\mathrm{Pr} = 0.72$, $\lambda_c = 1$, $k_p^* = 0$, $B_p = 1$, $T_p = 1$, $Le = 1$

					$-H''(0)$			
	HAM	Fehlberg	HAM	Fehlberg	HAM	Fehlberg	HAM	Fehlberg
$\lambda_c \backslash k_p^*$	0		0.5		1		2	
0.5	1.2161	1.2161	1.3640	1.3640	1.4977	1.4977	1.7280	1.7280
1.0	1.0622	1.0622	1.1909	1.1909	1.3070	1.3070	1.5061	1.5061
1.5	0.9771	0.9771	1.0953	1.0953	1.2019	1.2019	1.3841	1.3841
2.0	0.9194	0.9194	1.0304	1.0304	1.1306	1.1306	1.3017	1.3017
5.0	0.7513	0.7513	0.8418	0.8418	0.9235	0.9235	1.0631	1.0631

$Table.(7.2)$. Comparison of Fehlberg and HAM solutions for velocity profile

		HAM	Fehlberg	HAM	Fehlberg	HAM	Fehlberg
	$\mathrm{Pr}\backslash k_p^*$	0		0.5		1.5	
$\Theta'(0)$	0.7	-1.1462	-1.1462	-1.1442	-1.1442	-1.1404	-1.1404
	2.0	-1.9541	-1.9541	-1.9528	-1.9528	-1.9506	-1.9506
	7.0	-3.6688	-3.6688	-3.6681	-3.6681	-3.6668	-3.6668
	10	-4.3870	-4.3870	-4.3864	-4.3864	-4.3853	-4.3853
$\psi'(0)$	0.7	-1.6285	-1.6285	-1.6170	-1.6170	-1.5955	-1.5955
	2.0	-2.8274	-2.8274	-2.8197	-2.8197	-2.8057	-2.8057
	7.0	-5.3600	-5.3600	-5.3550	-5.3550	-5.3474	-5.3474
	10	-6.4179	-6.4179	-6.4141	-6.4141	-6.4072	-6.4072

$Table.(7.3)$. Comparison of Fehlberg and HAM solutions for temperature and nanoparticle concentration profiles

131

		-Θ′(0)					
	Pr\B$_p$	0.1	0.2	0.5	1.0	1.5	2.0
Kp* = 0.5	0.7	0.85428	0.83051	0.78090	0.64500	0.53654	0.43632
	2.0	1.39052	1.36264	1.26977	1.09915	0.92758	0.76766
	7.0	2.45602	2.44693	2.29508	2.00517	1.71996	1.45353
	10	2.90465	2.86284	2.69916	2.38940	2.07920	1.75129
Kp* = 1.5	0.7	0.82850	0.80454	0.75276	0.61787	0.51049	0.41337
	2.0	1.35848	1.32958	1.23187	1.05344	0.87921	0.72209
	7.0	2.47591	2.43351	2.26806	1.95937	1.66174	1.39104
	10	2.91600	2.86969	2.68876	2.35143	2.02038	1.75103

Table.(7.4). Behavior of heat flux at the surface of the sheet when $\lambda_c = 1$, $\varepsilon = 0.5$, $k_p^* = 0.5$, $T_p = 0.5$, $Le = 1$

		-ψ′(0)					
	Pr\Le	0.0	0.25	0.5	1.0	2.0	5.0
Kp* = 0.5	0.7	0.19876	0.31113	0.41837	0.61863	0.96968	1.74583
	2.0	0.21738	0.35904	0.49709	0.89361	1.51097	2.69289
	5.0	0.24730	0.39879	0.73234	1.28213	2.08192	3.60141
	7.0	0.32979	0.62777	0.89534	1.35524	2.27060	3.87877
Kp* = 1.5	0.7	0.18537	0.29666	0.40283	0.30102	0.94843	1.70876
	2.0	0.20616	0.33923	0.48951	0.87404	1.47847	2.65723
	5.0	0.22471	0.35607	0.71728	1.25368	2.04430	3.56893
	7.0	0.29118	0.62260	0.88176	1.32951	2.23321	3.84671

Table.(7.5). Behavior of sherwood number when $\lambda_c = 1$, $\varepsilon = 0.5$, $k_p^* = 0.5$, $B_p = 0.5$, $T_p = 1$

7.5 Conclusion

Noticeable conclusions obtained from the above study are

- Near the surface of the sheet the nondimensional velocity profile H' decreases with the increase in the porosity parameter k_p^*.

- Near the surface of the sheet the velocity profile H' increases with increase in the couple

132

stress fluid parameter λ_c.

- The nondimensional temperature profile θ decreases with the increase in the Prandtl number Pr.

- The temperature function θ increases with increase in the porosity parameter k_p^*.

- The nanoparticle concentration profile ψ decreases with the increase in the Lewis number Le and the Prandtl number Pr.

- The skinfriction coefficient decreases with increase in the couple stress fluid parameter λ_c.

- The local Nusselt number increases with increase in the Prandtl number Pr.

- The sherwood number increases with increase in the Lewis number Le.

Chapter 8

Stagnation-point boundary layer flow of a Williamson fluid over an exponentially stretching cylinder

8.1 Introduction

The current chapter concerns with the problem of steady, incompressible boundary layer stagnation point flow and heat transfer of a non-Newtonian Williamson fluid flowing through a vertical exponentially stretched cylinder. The governing boundary layer partial differential equations along with the boundary conditions are reduced into a system of ordinary differential equations by using suitable similarity transformations. The nonlinear system is then solved with the aid of 5th order Runge-Kutta Fehlberg method. The influence of involved parameters is shown through graphs. The associated physical properties, skinfriction coefficient and local Nusselt number are also presented for different parameters.

8.2 Formulation

The boundary layer stagnation-point flow of a non-Newtonian Williamson fluid that flows over a vertical cylinder is considered for the case when the circular cylinder of radius a stretched exponentially along its axial direction with a surface stretching velocity $V_w = 2ak^*e^{z/b}$. The

equations of conservation of mass, momentum and heat transfer are

$$\text{div}\,\mathbf{V} = \mathbf{0}, \tag{8.1}$$

$$\rho\frac{d\mathbf{V}}{dt} = \text{div}\,\mathbf{S} + \rho\tilde{\mathbf{g}}, \tag{8.2}$$

$$\rho c_p\frac{dT}{dt} = -\text{div}\,\mathbf{q}, \tag{8.3}$$

where $\mathbf{S}$ is the Cauchy stress tensor for Williamson fluid and is defined as

$$\mathbf{S} = -p\mathbf{I} + \boldsymbol{\tau}, \tag{8.4}$$

$$\boldsymbol{\tau} = -\left[\mu_\infty + (\mu_0 + \mu_\infty)\left(1 - t_0\dot{\gamma}\right)^{-1}\right]\mathbf{A}_1, \tag{8.5}$$

where $-p\mathbf{I}$ is the spherical part of the stress due to constraint of incompressibility in which $\boldsymbol{\tau}$ is the extra stress tensor for Williamson fluid, μ_0 is the zero shear rate viscosity, μ_∞ is the infinite shear rate viscosity, t_0 is the time constant and $\dot{\gamma} = \sqrt{\Pi/2}$, where $\Pi = \sum_i\sum_j\dot{\gamma}_{ij}\dot{\gamma}_{ji}$ is the second invariant strain tensor.

At present we consider the case when $\mu_\infty = 0$, and $t_0\dot{\gamma} << 1$. The component of extra stress tensor becomes

$$\boldsymbol{\tau} = -\mu_0\left(1 + \Gamma_t\dot{\gamma}\right)\mathbf{A}_1. \tag{8.6}$$

With the help of $Eqs.$ (8.4) and (8.6) the boundary layer equations of motion and heat transfer obtained are

$$u_r + \frac{u}{r} + w_z = 0, \tag{8.7}$$

$$uw_r + ww_z = -\frac{1}{\rho}\frac{\partial p}{\partial z} + \nu(1 + 2\Gamma_t w_r)(w_{rr} + \frac{1}{r}w_r) + g_{gr}\beta_{th}(T - T_\infty), \tag{8.8}$$

$$uT_r + wT_x = \alpha(T_{rr} + \frac{1}{r}T_r), \tag{8.9}$$

where β_{th} is the coefficient of thermal expansion. The corresponding boundary conditions for the problem are

$$u(a, z) = 0, \quad w(a, z) = V_w \quad w(r, z) \longrightarrow V_\infty \text{ as } r \longrightarrow \infty, \tag{8.10}$$

$$T(a, z) = T_w(z), \quad T(r, z) \longrightarrow T_\infty \text{ as } r \longrightarrow \infty, \tag{8.11}$$

135

where $V_\infty = 2bk^*e^{z/b}$.

8.3   Solution of the problem

To simplify the partial differential equations (8.7) to (8.9) the similarity transformations defined in (3.8) and (3.9) are used. The resulting system is then of the form

$$\eta G''' + G'' + \mathrm{Re}(GG'' - G'^2 + 1) + W_s\sqrt{\eta}G''\left(\eta G''' + G''\right) + \mathrm{Re}\,\lambda\theta = 0, \qquad (8.12)$$

$$\eta\theta'' + \theta' + \mathrm{Re}\,\mathrm{Pr}(G\theta' - G'\theta) = 0, \qquad (8.13)$$

in which $\mathrm{Re}_z = aV_\infty/4\nu$ is the Reynolds number, $W_s = 4t_0V_\infty/b$ is the Williamson parameter, $\lambda = g_{gr}\beta_{th}a(T_w - T_\infty)/V_\infty^2$ is the natural convection parameter and $\mathrm{Pr} = v/\alpha$ is the Prandtl number. The associated nondimensional boundary conditions are defined in $Eqs.$ (3.12) and (3.13).

The skinfriction coefficient c_f and the local Nusselt number Nu are

$$c_f\,\mathrm{Re}_z^{1/2} = \frac{1}{\frac{1}{2}\rho V_\infty^2}\tau_{rz}|_{r\to a}, \quad Nu/\,\mathrm{Re}_z^{1/2} = -\theta'\left(1\right). \qquad (8.14)$$

The system of ordinary differential equations (8.12) and (8.13) subject to the boundary conditions (3.12) and (3.13) is first reduced to a system of first order equations using appropriate substitutions, then the resulting system is solved numerically with the help of 5th order Runge-Kutta Felhberg method. Further discussion about the obtained numerical solutions is presented in the next section.

8.4   Results and discussion

The problem of natural convection boundary layer stagnation-point flow of a non-Newtonian Williamson fluid flowing through a vertical stretching cylinder that is stretched along its axial direction with an exponential surface stretching velocity $V_w = 2ak^*e^{z/b}$ and a free-stream velocity $V_\infty = 2bk^*e^{z/b}$ is studied in the present chapter. The solution of the problem is obtained with the help of 5th order numerical scheme, the Runge-Kutta Felhberg technique.

The influence of important parameters, Reynolds number Re_z, Williamson parameter W_s, the natural convection parameter λ and the Prandtl number Pr over the non-dimensional velocity and temperature profiles G' and θ are presented in $Figs.\,(8.1)$ to (8.8). The convergence pattern of non-dimensional velocity profile G' is presented in $Fig.(8.1)$. From the sketch, it is observed that the different velocity curves achieved infinity condition almost simultaneously about $\eta \to 3$. The impact of Reynolds number Re over the velocity function G' for different values of ε is presented in $Fig.\,(8.2)$. From the figure it is noticed that for stretching sheet problem with $\varepsilon = 0.5$ and the shrinking sheet problem with $\varepsilon = -0.5$, increase in Reynolds number Re, the velocity profile G' increases, whereas for $\varepsilon > 1$, increase in Reynolds number Re_z decreases the velocity profile G'. $Fig.(8.3)$ displays the impact of Williamson parameter W_s over the velocity profile G' for different values of the stretching ratio ε. From $Fig.(8.3)$ it is observed that for any choice of stretching ratio ε, increase in Williamson parameter W_s decreases the velocity profile G'. The impact of natural convection parameter λ over the velocity function G' is presented in $Fig.(8.4)$ when $\varepsilon = 2$. From this plot, it is noted that with increase in the natural convection parameter λ, the velocity profile G' increases because higher natural convection parameter λ is associated with greater density difference in fluids that causes the increase in the fluid velocity. The effect of Prandtl number Pr over the non-dimensional velocity profile G' is portrayed in $Fig.(8.5)$. From the graph it is perceived that increase in the Prandtl number Pr the velocity function G' decreases. The influence of stretching ratio ε over the thermal flow θ is graphed in $Fig.(8.6)$. From the figure, it is observed that increase in the stretching ratio ε decreases the temperature flow θ. $Fig.(8.7)$ telecasts the influence of Prandtl number Pr over the temperature profile θ. It is noted that an increase in the Prandtl number Pr decreases the temperature profile θ. This behavior of the temperature profile θ is consistent with the observation that increase in the Prandtl number Pr, decreases the thermal diffusion rate and so the temperature function θ decreases. $Fig.(8.8)$ indicates the effects of Reynolds number Re_z over the temperature profile θ. From $Fig.(8.8)$, it is noticed that with the increase in the Reynolds number Re_z the temperature function decreases. This observation is consistent with the fact that high Reynolds number Re_z associates with more dense fluids which correspond to reduced temperature flow rate in the fluid and hence have low fluid temperature.

The behavior of skinfriction coefficient c_f and the local Nusselt number Nu are tabulated

in $Tables.$(8.1) and (8.2) for different values of the involved parameters. $Table.$(8.1) shows the values for boundary derivatives for velocity profile at the surface of the cylinder that corresponds to the skinfriction coefficient tabulated for different values of Reynolds number Re_z and the Williamson parameter W_s. From $Table.$(8.1) it is depicted that with the increase in Reynolds number Re_z skinfriction coefficient c_f increases, whereas with the increase in the Williamson parameter W_s, skinfriction coefficient decreases. $Table.$(8.2) shows the values for boundary derivatives of the temperature profile θ, corresponding to the local Nusselt number Nu presented for different values of the Prandtl number Pr and the Williamson parameter W_s. From entries in $Table.$(8.2) it is depicted that increase in the Prandtl number Pr increases local Nusselt number Nu, whereas increase in the Williamson parameter W_s produces slight decrease in local Nusselt numbers.
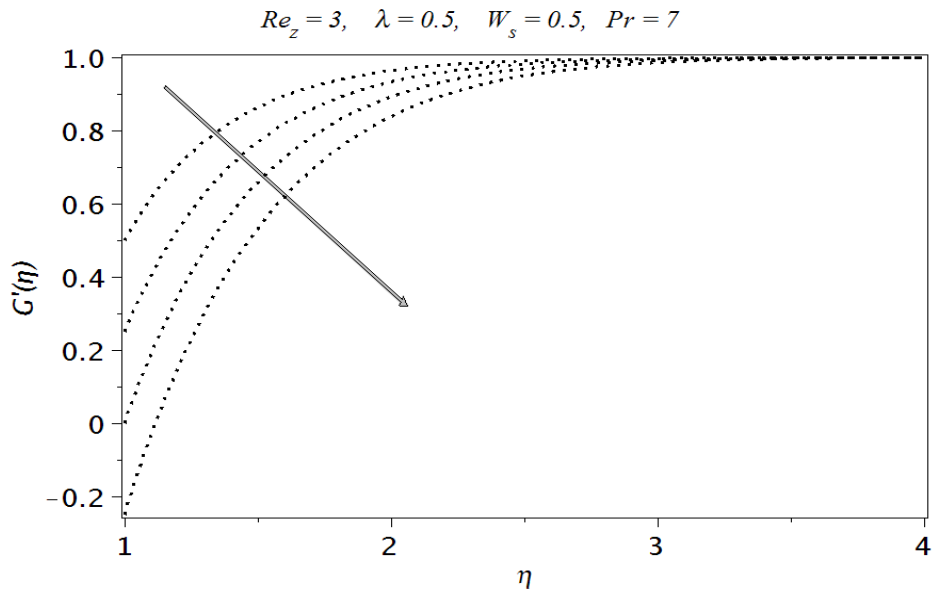

$Fig.$(8.1). Behavior of velocity profile G' for $\varepsilon = 0.5, 0.25, 0, -0.25$
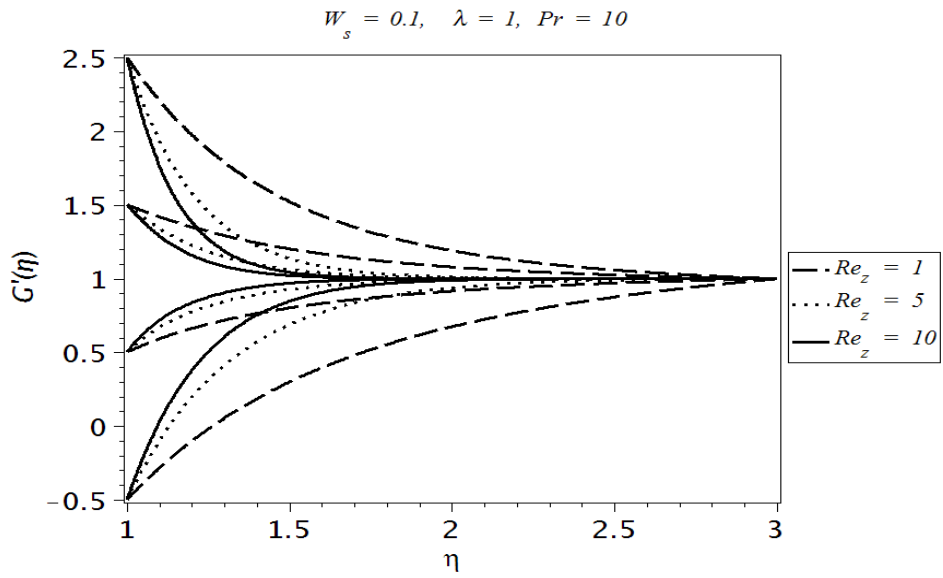
Fig.(8.2). Influence of Reynolds numbers Re_z over velocity profile G' for
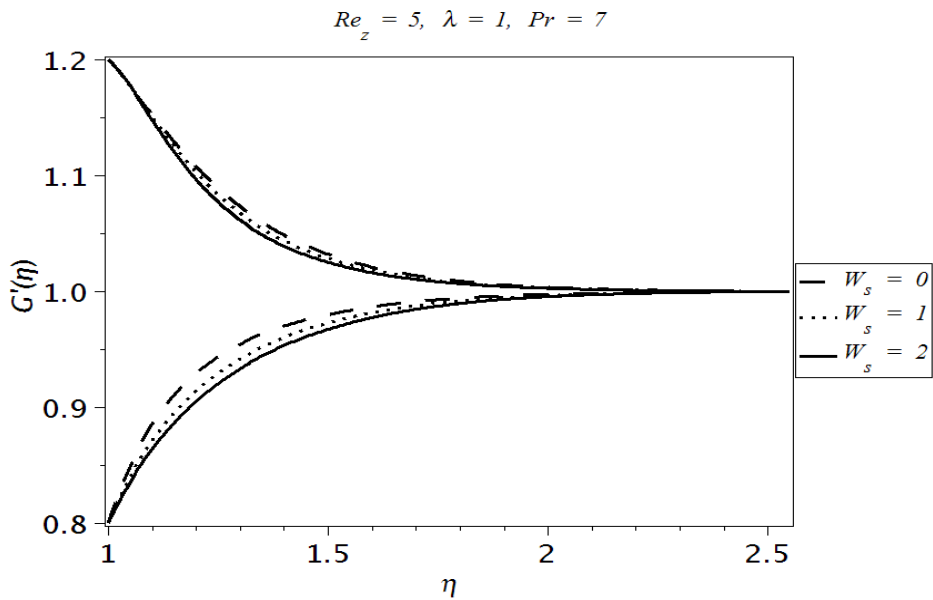
different ε

Fig.(8.3). Influence of Williamson parameter W_s over velocity profile G' for
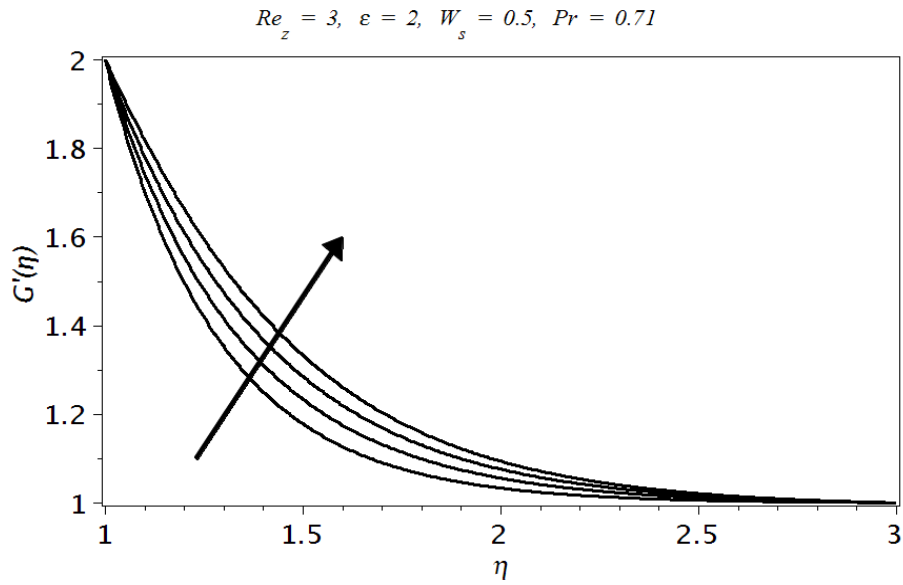
$\varepsilon = 0.8$ and 1.2

139

Fig.(8.4). Influence of natural convection parameter λ over velocity profile
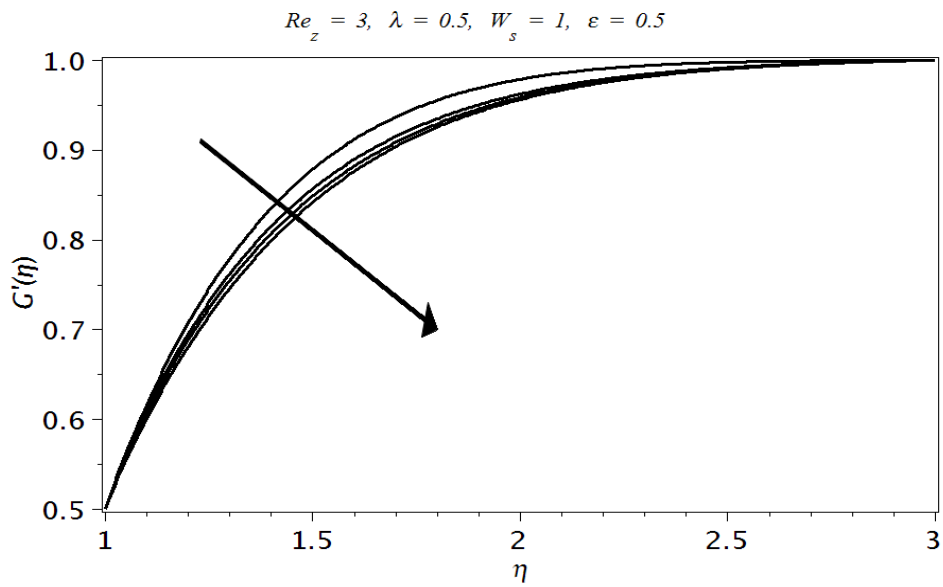
G' for $\lambda = 0, 1, 2$ and 3

Fig.(8.5). Influence of Prandtl number Pr over velocity profile G' for
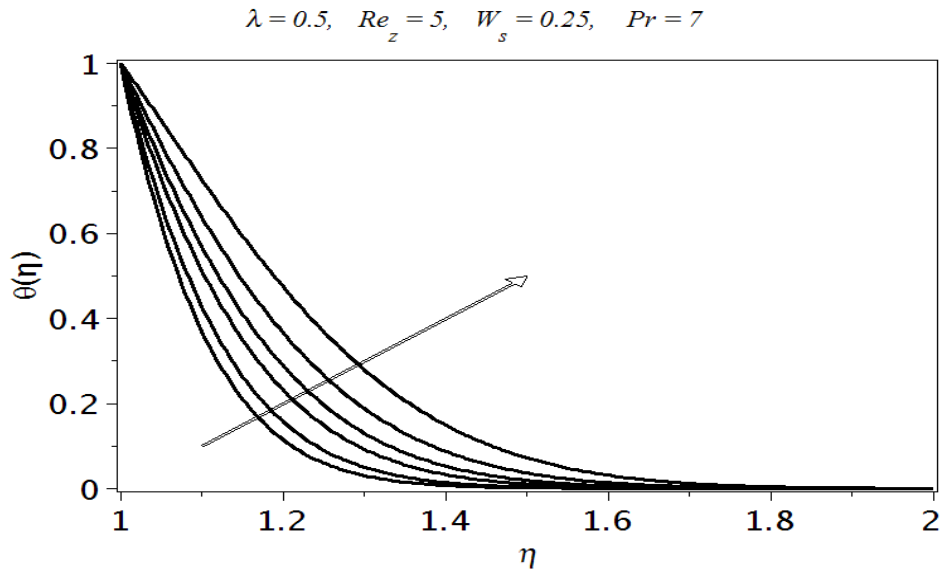
$\text{Pr} = 0.71, 3, 7$ and 70

$Fig.(8.6)$. Influence of stretching ratio ε over temperature profile θ for

$$\varepsilon = 1.5, 1, 0.5, 0.25, 0, -0.25$$
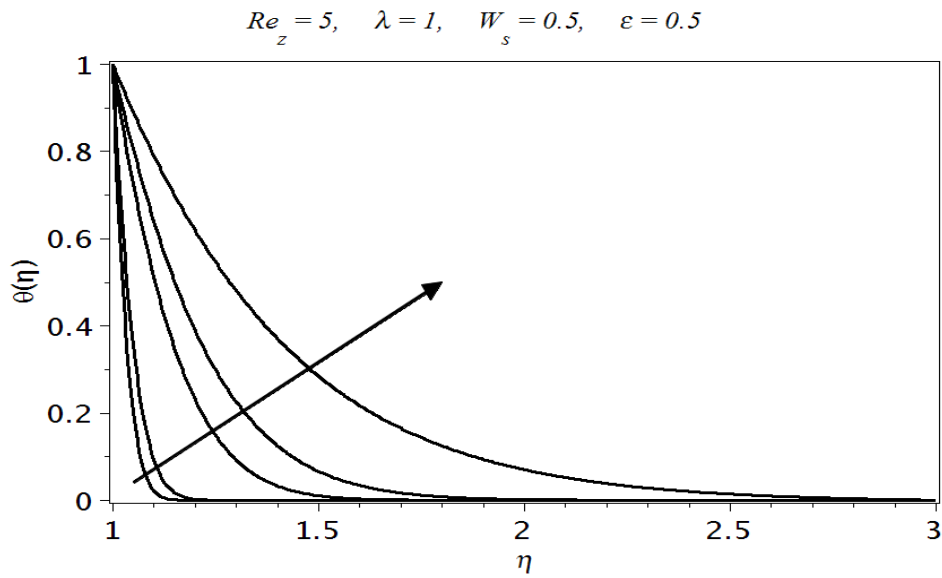
$Fig.(8.7)$. Influence of Prandtl number Pr over temperature profile θ for
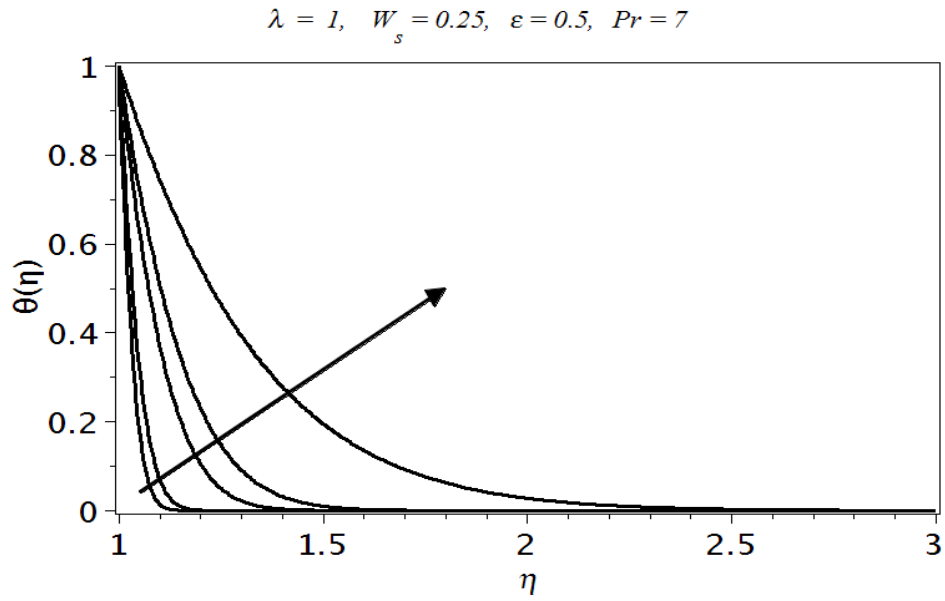
$$Pr = 150, 70, 7, 3, 0.71$$

$\lambda = 1, \quad W_s = 0.25, \quad \varepsilon = 0.5, \quad Pr = 7$

Fig.(8.8). Influence of Reynolds number Re_z over temperature profile θ for

$$\text{Re}_z = 100, 50, 10, 5, 1$$

$Re_z\backslash W_s$	$G''(1)$					
	0	0.25	0.5	0.75	1.0	1.5
1	0.9582	0.9040	0.8636	0.8317	0.8055	0.7645
5	1.9624	1.7379	1.6010	1.5039	1.4295	1.3199
10	2.7250	2.3211	2.1016	1.9539	1.8442	1.6869
20	3.8029	3.0892	2.7485	2.5303	2.3726	2.1521
50	5.9406	4.4721	3.8906	3.5398	3.2943	2.9601
100	8.3494	5.8747	5.0318	4.5429	4.2075	3.7584

Table.(8.1). Behavior of shear stress at the surface of the cylinder for

different values of the involved parameters, when $\lambda = 0.5, \varepsilon = 0.5, \text{Pr} = 7$

$Pr\backslash W_s$	$-\theta'(1)$					
	0	0.25	0.5	1.0	1.5	2.0
0.71	2.6265	2.6260	2.6256	2.6248	2.6241	2.6235
1	3.0668	3.0663	3.0659	3.0651	3.0644	3.0638
7	7.6733	7.6730	7.6727	7.6722	7.6718	7.6714
10	9.1189	9.1187	9.1187	9.1180	9.1177	9.1173
70	23.6943	23.6943	23.6943	23.6941	23.6940	23.6939
100	28.2706	28.2706	28.2706	28.2704	28.2704	28.2703
700	74.3879	74.3879	74.3879	74.3879	74.3879	74.3878

$Table.$(8.2). Behavior of heat flux at the surface of the cylinder for different values of the involved parameters, when $\lambda = 0.5, \varepsilon = 1, \text{Re}_z = 5$

8.5   Conclusion

The main points of results and discussion are summarized as

- The nondimensional velocity profile G' decreases with the increase in the Reynolds number Re_z and the Williamson parameter W_s, when $\varepsilon > 1$.

- The velocity profile G' increases with increase in the natural convection parameter λ.

- The nondimensional temperature profile θ decreases with the increase in the Prandtl number Pr and the Reynolds number Re_z and the natural convection parameter λ.

- Skinfriction coefficient at the surface of the cylinder increases with increase in the Reynolds number Re_z .

- The local Nusselt number at the surface of the cylinder increases with increase in the Prandtl number Pr .

Chapter 9

Boundary layer flow of second grade fluid in a cylinder with heat transfer

9.1 Introduction

In this chapter an analysis is carried to obtain the solution of the steady boundary layer flow and heat transfer of a second grade fluid flowing through a horizontal cylinder. The governing partial differential equations along with the boundary conditions are reduced to dimensionless form by using the boundary layer approximation and applying suitable similarity transformation. The resulting nonlinear coupled system of ordinary differential equations subject to the appropriate boundary conditions is solved by homotopy analysis method (HAM). The effects of the physical parameters on the flow and heat transfer characteristics of the model are presented. The behavior of skinfriction coefficient and Nusselt numbers are studied for different parameters.

9.2 Formulation

Let us consider the problem of natural convection boundary layer flow of a second grade fluid flowing along a horizontal circular cylinder having radius r_0. The temperature at the surface of the cylinder is assumed to be T_w and the uniform ambient temperature is taken to be T_∞ such that the quantity $T_w - T_\infty > 0$ in case of the assisting flow, while $T_w - T_\infty < 0$ in case of the opposing flows, respectively. The allied velocity field, temperature profile and the boundary

conditions are listed in $Eqs.\,(2.1)$, (2.3) and (2.4).

The governing equations of conservation of mass, momentum and energy are

$$\text{div}\,\mathbf{V} \;=\; \mathbf{0}, \tag{9.1}$$

$$\rho\frac{d\mathbf{V}}{dt} \;=\; \text{div}\,\mathbf{S}, \tag{9.2}$$

$$\rho c_p\frac{dT}{dt} \;=\; \mathbf{S}\cdot\boldsymbol{\nabla}\mathbf{V} - \text{div}\,\mathbf{q}, \tag{9.3}$$

where the Cauchy stress tensor $\mathbf{S}$ for second grade fluid is defined as [82]

$$\mathbf{S} \;=\; -p\mathbf{I} + \boldsymbol{\tau}, \tag{9.4}$$

$$\boldsymbol{\tau} \;=\; \mu\mathbf{A}_1 + \alpha_1\mathbf{A}_2 + \alpha_2\mathbf{A}_1^2, \tag{9.5}$$

where $\mathbf{I}$ is the unit tensor, $\boldsymbol{\tau}$ is the extra stress tensor for second grade fluid, α_1 and α_2 are the normal stress moduli, while $\mathbf{A}_1$ and $\mathbf{A}_2$ are the first and second Rivlin-Ericksen tensors and are defined as

$$\mathbf{A}_1 \;=\; (\text{grad}\,\mathbf{V}) + (\text{grad}\,\mathbf{V})^{T_1}, \tag{9.6}$$

$$\mathbf{A}_2 \;=\; \frac{d\mathbf{A}_1}{dt} + (\text{grad}\,\mathbf{V})\cdot\mathbf{A}_1 + \mathbf{A}_1\cdot(\text{grad}\,\mathbf{V})^{T_1}. \tag{9.7}$$

For thermodynamic stability the following restrictions are imposed over the system [80]

$$\mu \geq 0,\ \text{and}\ \alpha_1 + \alpha_2 = 0, \quad \text{and}\ \alpha_1 > 0, \tag{9.8}$$

Using these equations, the following boundary layer equations of motion and heat transfer are obtainedwhere the velocity components

$$(rw)_r + ru_x \;=\; 0, \tag{9.9}$$

$$uu_x + wu_r \;=\; -\rho\frac{\partial p}{\partial x} + \nu(u_{rr} + \frac{1}{r}u_r) + \frac{\alpha_1}{\rho_\infty}[wu_{rrr} + uu_{rrx} + u_x u_{rr} - u_r w_{rr}$$
$$+ \frac{1}{r}(wu_{rr} + uu_{rx} + u_r u_x - u_r w_r)] \tag{9.10}$$

$$wT_r + uT_x \;=\; \alpha(T_{rr} + \frac{1}{r}T_r) + \frac{\nu}{c_p}u_r^2 + \frac{\alpha_1}{c_p\rho_\infty}\left(wu_r u_{rr} + uu_r u_{rx}\right), \tag{9.11}$$

9.3 Solution of the problem

Introduce the following similarity transformations

$$u = \frac{xU_\infty}{l}F'(\eta), \qquad w = -\frac{r_0}{r}\left(\frac{\nu U_\infty}{l}\right)^{\frac{1}{2}}F(\eta), \tag{9.12}$$

$$\theta = \frac{T - T_\infty}{T_w - T_\infty}, \qquad \eta = \frac{r^2 - r_0^2}{2r_0}\left(\frac{U_\infty}{\nu l}\right)^{\frac{1}{2}}, \tag{9.13}$$

where the characteristic temperature ΔT is calculated from the relations $T_w - T_\infty = (x/l)^2 \Delta T$. With the help of transformations (9.12) and (9.13), $Eqs.$ (9.9) to (9.11) take the form

$$(1 + 2\gamma_c\eta)F''' + 2\gamma_c F'' + 1 + FF'' - F'^2 + 4\gamma_c\beta\left(F'F'' - FF'''\right)$$

$$+\beta(1 + 2\gamma_c\eta)\left(F''^2 + 2F'F''' - FF^{iv}\right) = 0, \tag{9.14}$$

$$(1 + 2\gamma_c\eta)\theta'' + 2\gamma_c\theta' + \Pr(F\theta' - F'\theta) - \Pr Ec\beta\gamma_c FF''^2$$

$$+ \Pr Ec(1 + 2\gamma_c\eta)\left[F''^2 - \beta FF''F''' + \beta F'F''^2\right] = 0, \tag{9.15}$$

in which $\gamma_c = \left(\nu l/U_\infty r_0^2\right)^{1/2}$ is the curvature parameter, $\beta = \alpha_1 U_\infty/\rho\nu l$ is the dimensionless viscoelastic (second grade fluid) parameter, $\Pr = v/\alpha$ is the Prandtl number, $Ec = U_\infty^2/c_p\Delta T$ is the Eckert number.

The boundary conditions in nondimensional form are defined as

$$F(0) = c_0, \quad F'(0) = 0, \quad F' \longrightarrow 1, \text{ as } \eta \longrightarrow \infty, \tag{9.16}$$

$$\theta(0) = 1, \quad \theta \longrightarrow 0, \text{ as } \eta \longrightarrow \infty, \tag{9.17}$$

where c_0 is any constant. The coefficient of skinfriction and the Nusselt number are defined as

$$\frac{1}{2}c_f \operatorname{Re}_x^{1/2} = \frac{1}{\rho W_\infty^2}\tau rx \mid_{r\to 0}, \quad Nu/\operatorname{Re}_x^{1/2} = -\theta'(0),$$

where $\operatorname{Re}_x = U_\infty x/\nu$ is the local Reynolds number.

The solution of the above system is obtained by using the analytical technique homotopy

analysis method (HAM). In the present case we seek the initial guesses to be

$$F_0\left(\eta\right) = c_0 - 1 + \eta + e^{-\eta}, \quad \theta_0\left(\eta\right) = e^{-\eta}. \tag{9.19}$$

The corresponding auxiliary linear operators are

$$L_f = \frac{d^3}{d\eta^3} + \frac{d^2}{d\eta^2}, \quad L_\theta = \frac{d^2}{d\eta^2} + \frac{d}{d\eta}, \tag{9.20}$$

satisfying

$$L_f[c_1 + c_2\eta + c_3 e^{-\eta}] = 0, \quad L_\theta[c_4 + c_5 e^{-\eta}] = 0, \tag{9.21}$$

where $c_i\left(i = 1, ..., 5\right)$ are arbitrary constants. Further details of the HAM solutions can be found in chapter 1.

9.4   Results and discussion

The solutions of the problem of stagnation point boundary layer flow and heat transfer of a non-Newtonian second grade fluid flowing through a horizontal cylinder of radius r_0 are obtained through the homotopy analysis method. The convergence of the obtained solutions are examined through the $\hbar'$ curves, while the behavior of the different important parameters, the curvature parameter γ_c, the second grade fluid parameter β, the Prandtl number Pr and the Eckert numbers Ec are studied through graphs, whereas the physical quantities like the shear stress at the surface and the skinfriction coefficient are analyzed through table. $Fig.\,(9.1)$ shows the convergence region of the nondimensional velocity profile F' plotted at the 20th order of iteration, while $Fig.\,(9.2)$ displays the convergence region of the nondimensional temperature profile θ for specified values of the involved parameters. From $Fig.\,(9.2)$ it is noted that the acceptable convergence region for the auxiliary parameter $\hbar_2$ is $-1.8 \leq \hbar_2 \leq -0.5$.

The influence of the curvature parameter γ_c over the nondimensional velocity profile F' is plotted in $Fig.\,(9.3)$. From the sketch it is observed that with an increase in the curvature parameter γ_c, the nondimensional velocity profile F' decreases. $Fig.\,(9.4)$ depicts the impact of the second grade fluid parameter β over the velocity profile F'. From $Fig.\,(9.4)$ it is observed that with an increase in the second grade fluid parameter β the nondimensional velocity profile

increases. $Fig.\,(9.5)$ provides the behavior of the velocity profile F' for different values of the boundary condition c_0 that also shows the suction behavior of the fluid at the surface of the cylinder. From $Fig.\,(9.5)$ it is revealed that by increasing the boundary condition c_0 the velocity profile F' also increases. The influence of the curvature parameter γ_c over the nondimensional temperature flow rate θ is graphed in $Fig.\,(9.6)$. From the figure it is evident that with an increase in the curvature parameter γ_c the nondimensional temperature profile θ increases. $Fig.\,(9.7)$ displays the impact of the second grade fluid parameter β over the temperature flow rate θ. From $Fig.\,(9.7)$ it is noted that with an increase in the second grade fluid parameter β the nondimensional temperature flow rate θ increases. The impact of the Prandtl number Pr over the temperature profile θ is portrayed in $Fig.\,(9.8)$. From the sketch it is observed that with an increase in the Prandtl number Pr the temperature profile θ decreases. The behavior of temperature function θ for different values of the Eckert number Ec is sketched in $Fig.\,(9.9)$. From the figure it is observed that with an increase in the Eckert number Ec the temperature profile θ increases. $Fig.\,(9.10)$ displays the behavior of the boundary condition c_0 over the temperature function θ. From the sketch it is noted that by increasing the boundary condition c_0 the temperature function θ decreases.

The important physical parameters like the shear stress and the skinfriction coefficient are analyzed through table $Table.\,(9.1)$ for different values of the associated parameters. $Table.\,(9.1)$ shows the behavior of boundary derivatives for the velocity profile tabulated for different values of the curvature parameter γ_c, the second grade parameter β and the boundary condition c_0. Entries in $Table.\,(9.1)$ corresponds to the shear stress at the surface of the cylinder and the skinfriction coefficient. From $Table.\,(9.1)$ it is observed that with an increase in the curvature parameter γ_c, the shear stress at the surface of the cylinder increases, whereas the shear stress at the surface of the cylinder decreases with an increase in the second grade fluid parameter β.
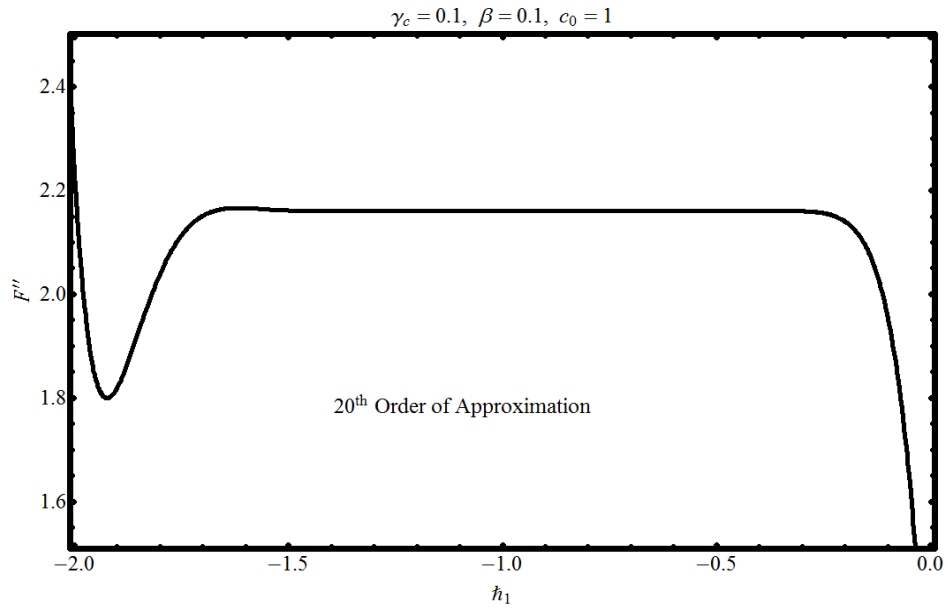
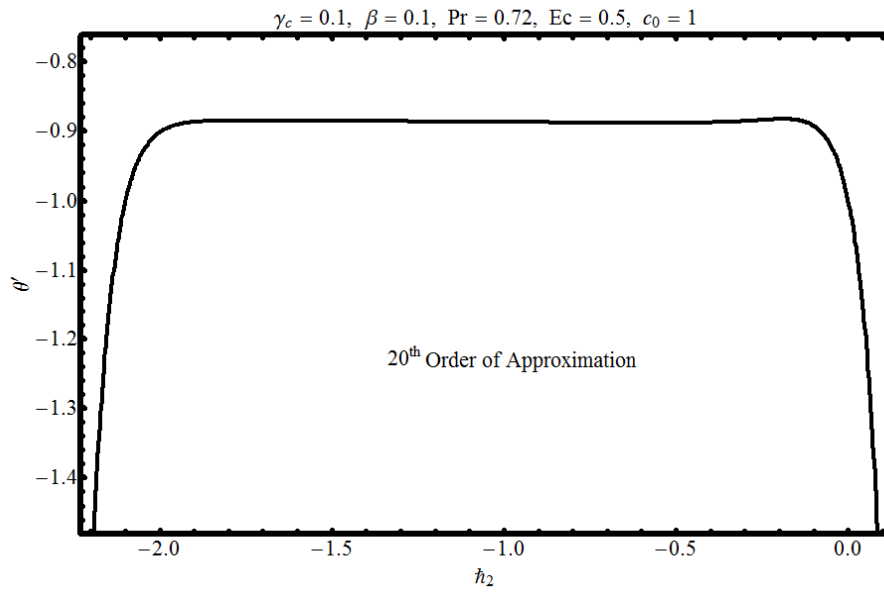$Fig.(9.1)$. $\hbar_1$-curve for the velocity profile F'

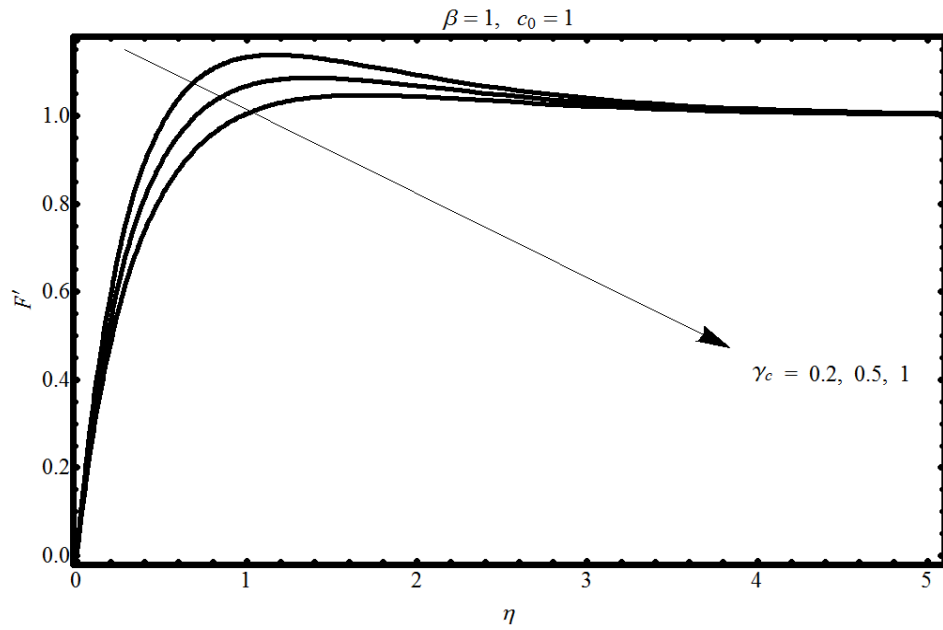$Fig.(9.2)$. $\hbar_2$-curve for the temperature profile θ

Fig.(9.3). Influence of the curvature parameter γ_c over the velocity profile F'
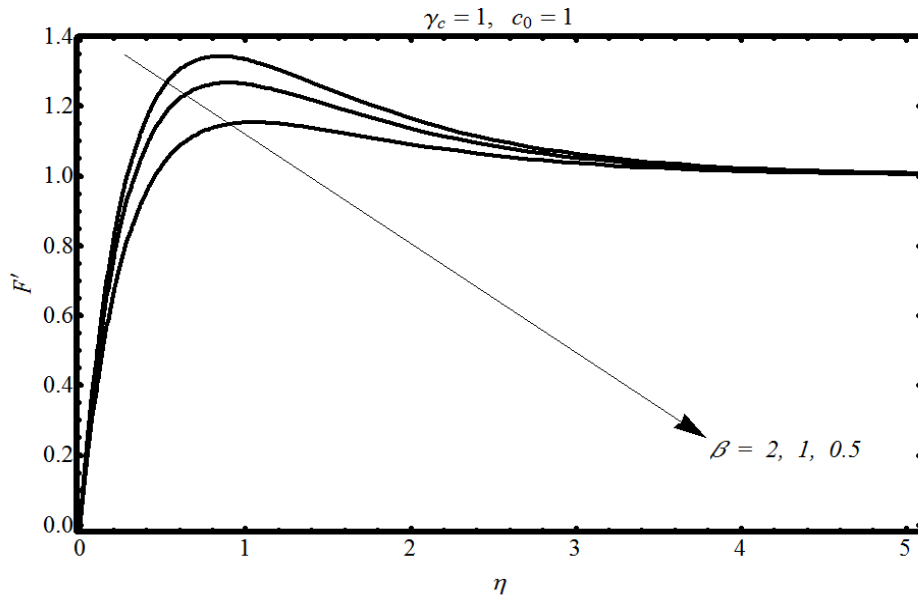

Fig.(9.4). Influence of the second grade parameter β over the velocity profile F'
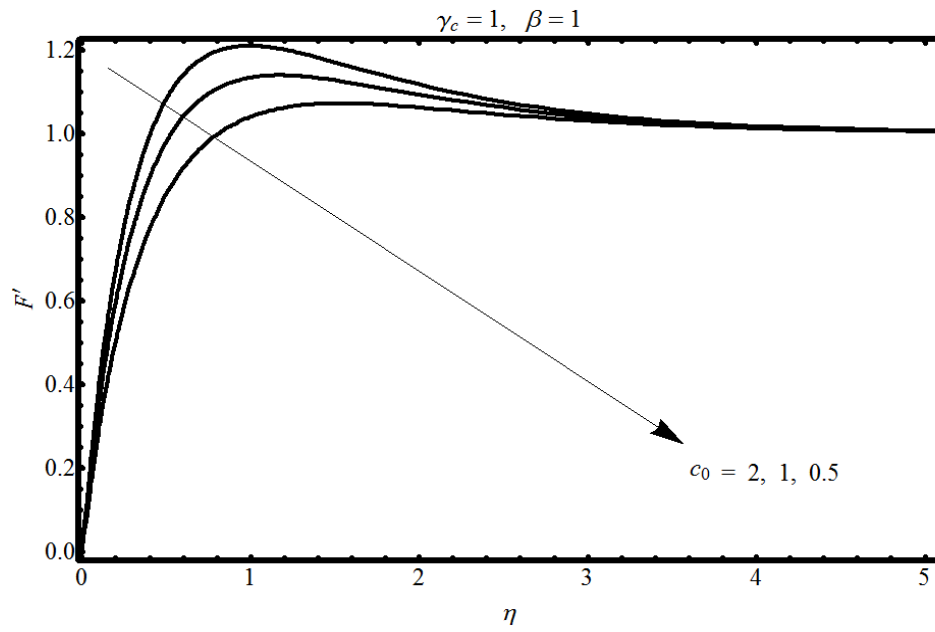
150

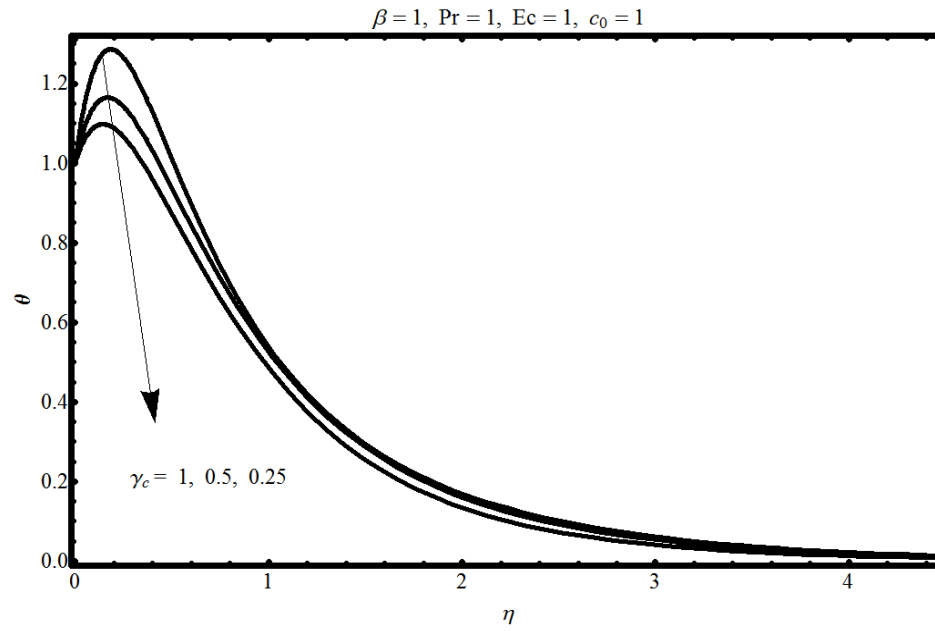$Fig.(9.5)$. Influence of the boundary condition c_0 over the velocity profile F'

$Fig.(9.6)$. Influence of the curvature parameter γ_c over the temperature
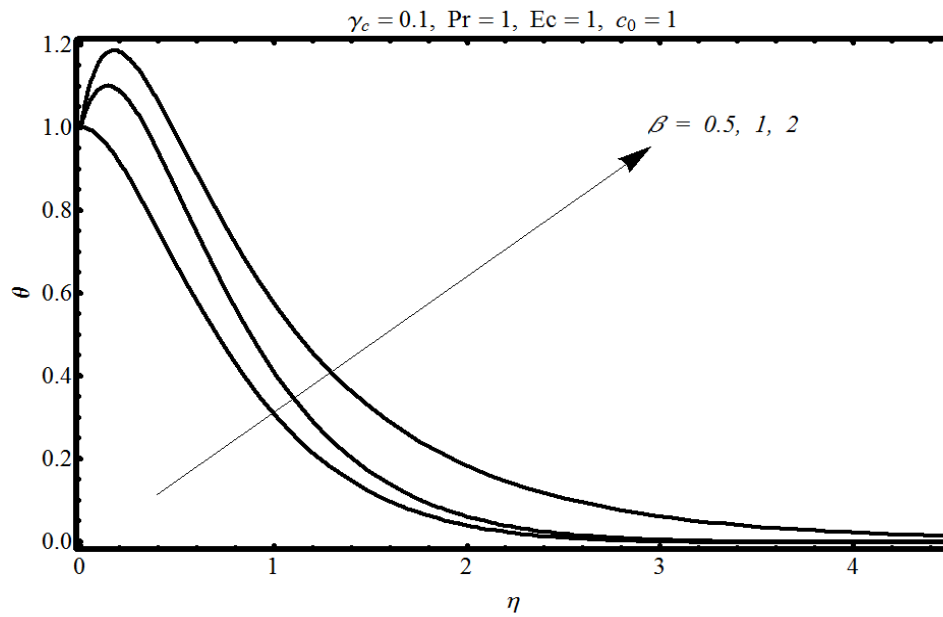
profile θ

151

$Fig.(9.7)$. Influence of the second grade parameter β over the temperature profile θ
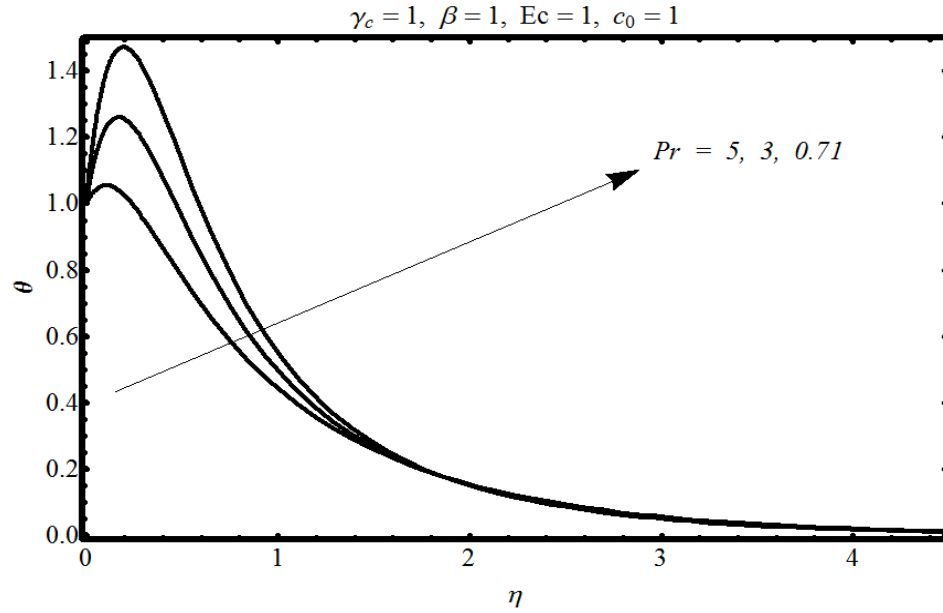

$Fig.(9.8)$. Influence of the Prandtl number Pr over the temperature profile θ
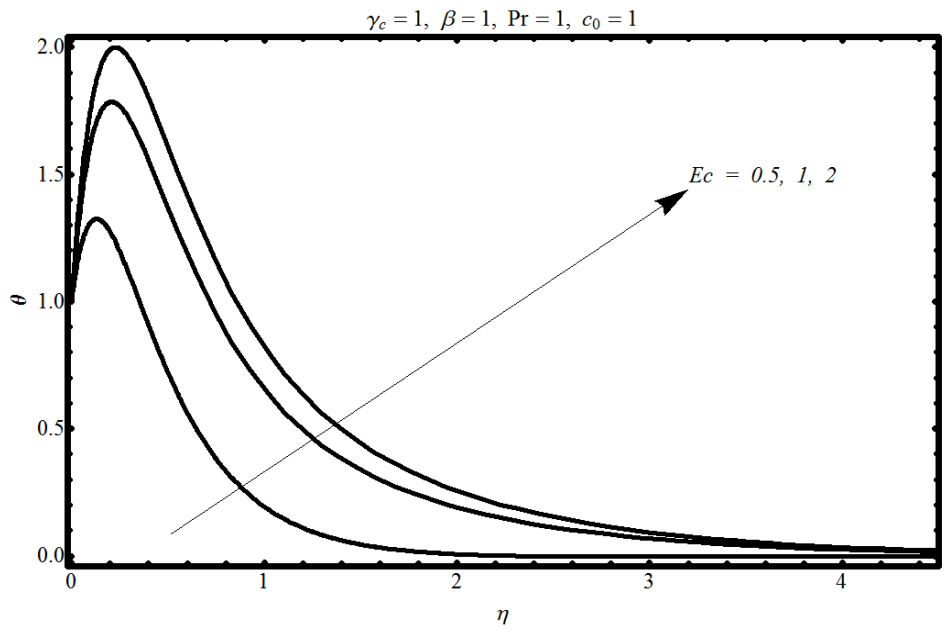
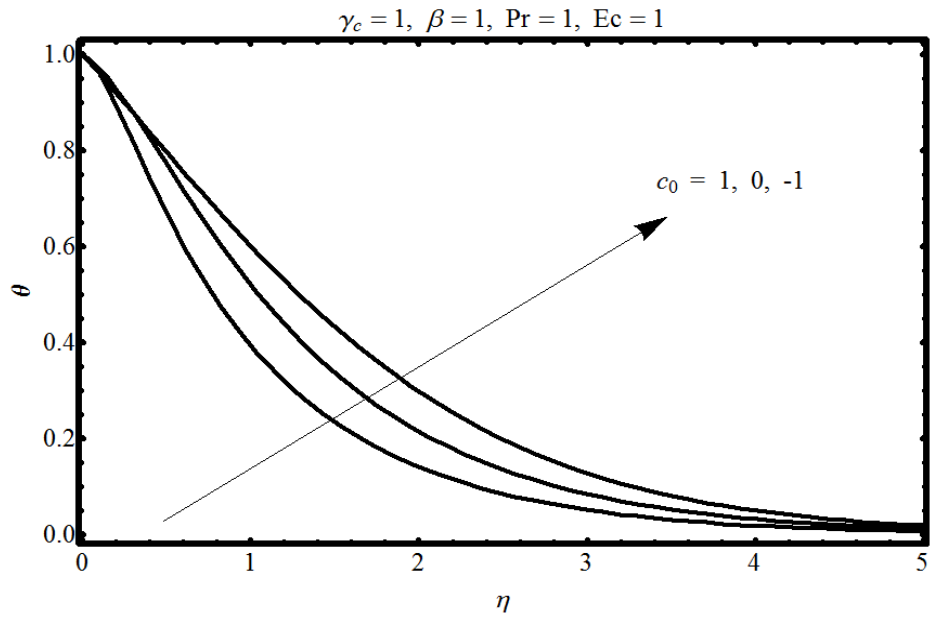$Fig.(9.9)$. Influence of the Eckert number Ec over the temperature profile θ

$Fig.(9.10)$. Influence of the boundary condition c_0 over the temperature profile θ

	$c_0\backslash\gamma_c$	$F''(0)$					
		0.5	1.0	1.5	2.0	2.5	3.0
$\beta = 0$	-1	0.9918	1.1942	1.3729	1.5325	1.6763	1.8067
	0	1.4886	1.7244	1.7954	1.9378	2.0656	2.1810
	1	2.0397	2.1751	2.2982	2.4099	2.5116	2.6044
	2	2.7332	2.8029	2.8746	2.9448	3.0119	3.0752
$\beta = 0.2$	-1	0.8626	0.9205	0.95554	0.9794	0.9958	1.0081
	0	1.5946	1.9137	2.0439	2.2662	2.4626	2.6302
	1	4.2201	5.1146	6.8718	9.1792	11.8742	14.465
	2	8.4914	11.7713	15.6358	24.547	29.4885	38.1896
$\beta = 0.4$	-1	0.7798	0.7935	0.7970	0.80716	0.80754	0.8077
	0	1.5822	1.8917	2.0213	2.2349	2.4119	2.6165
	1	4.5183	6.7654	8.7508	12.368	16.0122	24.2009
	2	9.0899	14.1113	19.8594	28.5561	35.0772	46.7566

Table.(9.1). Behavior of shear stress at the surface for different values of the

involved parameters

9.5 Conclusion

Important observations obtained from the above are

- The nondimensional velocity profile F' increases with the increase in the second grade fluid parameter β and the curvature parameter γ_c.

- The nondimensional temperature profile θ decreases with the increase in the Prandtl number Pr.

- The temperature flow rate θ increases with the increase in the curvature parameter γ_c and the second grade parameter β.

- The shear stress at the surface of the cylinder decreases with increase in the second grade fluid parameter β.

Chapter 10

Boundary layer stagnation-point flow of third grade fluid over an exponentially stretching sheet

10.1 Introduction

This chapter deals with the natural convection steady boundary layer stagnation point flow and heat transfer of a third grade fluid over an exponentially stretching sheet. Both the analytical and numerical solutions are obtained. The analytical solutions are obtained through homotopy analysis method (HAM) while the numerical solutions are computed by using the Keller box technique. Comparison of solutions obtained through the HAM and Keller-box methods are also given. At the end the effects of important physical parameters are presented through graphs and the salient features are discussed.

10.2 Formulation

Consider the stagnation point flow of a steady incompressible third grade fluid over an exponentially stretching sheet. The Cartesian coordinates (x, y) are used such that x is along the surface of the sheet while y is taken as normal to it. The allied velocity profile and the boundary

conditions are

$$\mathbf{V} = (v_x(x, y), v_y(x, y), 0), \tag{10.1}$$

$$v_x = W_{sv}, \quad v_y = 0, \quad T = T_w(x), \quad \text{for } y = 0, \tag{10.2}$$

$$v_x \rightarrow W_\infty, \quad T \rightarrow T_\infty, \quad \text{as } y \rightarrow \infty. \tag{10.3}$$

where W_{sv} is the surface stretching velocity of the sheet, W_∞ is the free-stream velocity, while T_w and T_∞ are the surface temperature and the fluid temperature at infinity, where

$$W_\infty = Ae^{x/L}, \quad W_{sv} = Be^{x/L}, \quad T_w = T_\infty + ce^{x/L}, \tag{10.4}$$

where A and B are constant velocities, c is constant temperature and L is the reference length. The governing equations of conservation of mass, momentum and energy are

$$\text{div } \mathbf{V} = \mathbf{0}, \tag{10.5}$$

$$\rho \frac{d\mathbf{V}}{dt} = \text{div } \mathbf{S}, \tag{10.6}$$

$$\rho c_p \frac{dT}{dt} = \mathbf{S} \cdot \nabla \mathbf{V} - \text{div } \mathbf{q}, \tag{10.7}$$

where $\mathbf{S}$ is the Cauchy stress tensor and for third grade fluid $\mathbf{S}$ is defined as [84]

$$\mathbf{S} = -p\mathbf{I} + \boldsymbol{\tau}, \tag{10.8}$$

$$\boldsymbol{\tau} = \mu \mathbf{A}_1 + \alpha_1 \mathbf{A}_2 + \alpha_2 \mathbf{A}_1^2 + \beta_1 \mathbf{A}_3 + \beta_2 (\mathbf{A}_1 \mathbf{A}_2 + \mathbf{A}_2 \mathbf{A}_1) + \beta_3 \left(trace\mathbf{A}_1^2\right) \mathbf{A}_1, \tag{10.9}$$

where $\boldsymbol{\tau}$ is the extra stress tensor for third grade fluid, α_1 and α_2 are the normal stress moduli and β_1, β_2 and β_3 are the material constants. while $\mathbf{A}_1$ $\mathbf{A}_2$ are the first and second Rivlin-Ericksen tensors stated in $Eqs.$ (9.6) and (9.7), while $\mathbf{A}_3$ is the third Rivlin-Ericksen tensors and is defined as

$$\mathbf{A}_3 = \frac{d\mathbf{A}_2}{dt} + (\text{grad } \mathbf{V})\mathbf{A}_2 + \mathbf{A}_2(\text{grad } \mathbf{V})^{T_1}, \tag{10.10}$$

For thermodynamic stability the following restrictions are imposed over the system [85]

$$\mu \geq 0, \quad \alpha_1 \geq 0, \quad |\alpha_1 + \alpha_2| \leq (24\mu\beta_3)^{1/2}, \tag{10.11}$$

$$\beta_1 = 0, \quad \beta_2 = 0, \quad \text{and } \beta_3 > 0, \tag{10.12}$$

The related boundary layer equations of motion and heat transfer are

$$\frac{\partial v_x}{\partial x} + \frac{\partial v_y}{\partial y} = 0, \tag{10.13}$$

$$v_x \frac{\partial v_x}{\partial x} + v_y \frac{\partial v_x}{\partial y} = W_\infty \frac{dW_\infty}{dx} + v\frac{\partial^2 v_x}{\partial y^2} + \frac{\alpha_1}{\rho}[v_x \frac{\partial^3 v_x}{\partial x \partial y^2} + \frac{\partial v_x}{\partial y}\frac{\partial^2 v_x}{\partial x \partial y} + v_y \frac{\partial^3 v_x}{\partial y^3} + \frac{\partial v_x}{\partial x}\frac{\partial^2 v_x}{\partial y^2}]$$
$$+\frac{2\beta_3}{\rho}[4\left(\frac{\partial v_x}{\partial x}\right)^2 \frac{\partial^2 v_x}{\partial y^2} - \frac{\partial^2 v_x}{\partial x^2}\left(\frac{\partial v_x}{\partial y}\right)^2 + 12\frac{\partial v_x}{\partial x}\frac{\partial v_x}{\partial y}\frac{\partial^2 v_x}{\partial x \partial y} + 6\frac{\partial v_y}{\partial x}\frac{\partial v_x}{\partial y}\frac{\partial^2 v_x}{\partial y^2}], \tag{10.14}$$

$$v_x \frac{\partial T}{\partial x} + v_y \frac{\partial T}{\partial y} = \alpha \frac{\partial^2 T}{\partial y^2}. \tag{10.15}$$

10.3 Solution of the problem

To simplify the above system we make use of the similarity transformations defined in $Eqs.\,(7.13)$, (7.14) and (7.16). The reduced system is then of the form

$$H''' + HH'' - 2H'^2 + 2 + We\left(2\eta H''H''' + 5H'H''' + 3H''^2 - HH^{iv}\right) + \Gamma(68H'H''^2$$

$$+31\eta H''^3 + 22\eta H'H''H''' + 21\eta^2 H''^2 H''' - 6HH''H''' + 16H'^2 H''') = 0, \tag{10.16}$$

$$\theta'' + \Pr(H\theta' - 2H'\theta) = 0, \tag{10.17}$$

in which $We = \alpha_1 W_\infty/2\mu L$ is the weissenberg number, $\Gamma = \beta_3 W_\infty^2/2\nu\rho L^2$ is the third grade fluid parameter and $\Pr = v/\alpha$ is the Prandtl number.

The boundary conditions in nondimensional form are

$$H(0) = 0, \quad H'(0) = \epsilon, \quad H' \longrightarrow 1, \text{ as } \eta \longrightarrow \infty, \tag{10.18}$$

$$\theta(0) = 1, \quad \theta \longrightarrow 0, \text{ as } \eta \longrightarrow \infty, \tag{10.19}$$

157

where $\epsilon = B/A$.

The local Nusselt numbers are obtained in dimensionless form as

$$Nu/\operatorname{Re}_x^{1/2} = -\theta'(0).$$ (10.20)

where $\operatorname{Re} = W_\infty L/2\nu$ and $\operatorname{Re}_x = x^2 W_\infty/2\nu L$ are the Reynolds number and the local Reynolds number, respectively.

The numerical solution of equations (10.16) and (10.17) subject to the boundary conditions (10.18) and (10.19) is obtained through Keller-box scheme. For this scheme we first reduce these equations into a first order system, the obtained system is then approximated by central differences. Further, these difference equations are linearized by Newton's method. The resulting tridiagonal system is then solved using block-elimination technique. Results obtained from Keller-box are discussed and compare with HAM in the next section.

10.4   Results and discussion

The current discussion is based upon the problem of boundary layer stagnation point flow of a non-Newtonian third grade fluid flowing over a stretching surface. The surface stretching velocity of the sheet is assumed to be an exponential function of the distance from the stagnation point. The solutions of the problem are obtained using the Keller box scheme and the homotopy analysis method. The convergence of the HAM solutions are presented through the $\hbar'$ curves, while a comparison of both the numerical and HAM solutions is also included. $Fig.$ (10.1) shows the convergence region for the auxiliary parameter $\hbar_1$ associated with the nondimensional velocity profile H' plotted for different values of the stretching ratio ϵ. $Fig.$ (10.2) shows the convergence region for the auxiliary parameter $\hbar_2$ allied with the nondimensional temperature function θ plotted for different values of the Prandtl number Pr when the stretching ratio $\epsilon = 0.5$. From $Fig.$ (10.2) the acceptable convergence region when Prandtl number Pr $= 3$ is $-0.9 \leq \hbar_2 \leq -0.3$.

$Figs.$ (10.3) to (10.7) show graphical comparison of both the Keller box and HAM solutions for nondimensional velocity and temperature profiles H' and θ graphed for different involved parameters. $Fig.$ (10.3) to (10.5) display comparison of both the solutions for the velocity profile

H' sketched for different values of the stretching ratio ϵ, the Weissenberg number We and the third grade fluid parameter Γ respectively. while $Fig.\,(10.6)$ and (10.7) include the comparison of both the solutions for nondimensional temperature function θ portrayed for different values of the Prandtl number Pr and the stretching ratio ϵ. From these figures it is observed that the Keller box and the HAM solutions are in agreement.

The impact of the stretching ratio ϵ, the Weissenberg number We, the third grade fluid parameter Γ and the Prandtl number Pr over the velocity and temperature profiles H' and θ are presented in $Figs.\,(10.8)$ to (10.12). $Fig.\,(10.8)$ displays the convergence pattern adopted by the nondimensional velocity profile H' for different values of the stretching ratio ϵ. $Fig.\,(10.9)$ depicts the influence of the Weissenberg number We over the nondimensional velocity profile H' for different values of the stretching ratio ϵ. It is observed from $Fig.\,(10.9)$ that the velocity profile H' exhibits dual behavior for different values of the Weissenberg number We against different choices of the stretching ratio ϵ. That is when the stretching ratio $\epsilon < 1$, increase in the Weissenberg number We decreases the velocity profile H', while in the interval when the stretching ratio $\epsilon > 1$, increase in the Weissenberg number We also increases the velocity profile H'. $Fig.\,(10.10)$ shows the behavior of the nondimensional velocity profile H' plotted for different values of the third grade fluid parameter Γ for the choices when the stretching ratio $\epsilon = 0.5, 1.5$. From the graph it is evident that the velocity profile H' has a dual behavior against the third grade fluid parameter Γ for different values of the stretching ratio ϵ. That is for the stretching ratio $\epsilon < 1$, increase in the third grade fluid parameter Γ decreases the velocity profile H', while in the interval when the stretching ratio $\epsilon > 1$, the velocity profile h' increases wit an increase in the third grade fluid parameter Γ. $Fig.\,(10.11)$ inculcates the impact of the Prandtl number Pr over the nondimensional temperature profile θ for the case when the stretching ratio $\epsilon = 0.5$. From the sketch it is observed that with an increase in the Prandtl number Pr the temperature profile θ and the thermal boundary layer thickness both decreases. $Fig.\,(10.12)$ provides an insight in the impact of the stretching ratio ϵ over the temperature flow rate θ. From the plot it is observed that with an increase in the stretching ratio ϵ the temperature profile θ decreases.

The important physical quantities such as the shear stress, the skinfriction coefficient, heat flux and the local Nusselt numbers associated with the problem are examined through tables

for different choices of the allied parameters. $Table.(10.1)$ contains the boundary derivatives showing a comparison of both the Keller box and HAM solutions for different pairs of the stretching ratio ϵ, the Weissenberg number We and the third grade fluid parameter Γ. From $Table.(10.1)$ it is noted that both the solutions are in good agreement. Entries in $Table.(10.1)$ also corresponds to the shear stress at the surface of the stretching sheet and the skinfriction coefficient. From $Table.(10.1)$ it is indicated that with an increase in the Weissenberg number We the shear stress at the surface of the sheet decreases., whereas with an increase in the third grade fluid parameter Γ, shear stress at the surface of the exponentially stretching sheet also increases. $Table.(10.2)$ provides a comparison of the numerical and homotopy analysis method solutions associated with the thermal boundary derivatives tabulated for different choices of the stretching ratio ϵ, the Prandtl number Pr and the third grade fluid parameter Γ. From entries in $Table.(10.2)$ it is observed that both the solutions are in agreement. $Table.(10.2)$ also indicate the behavior of heat flux at the surface and the local Nusselt numbers. From entries in $Table.(10.2)$ it is noticed that with an increase in the Prandtl number Pr the heat flux at the surface of the sheet also increases, whereas with an increase in the third grade fluid parameter Γ heat flux has a dual behavior, that is in case of Weissenberg number $We = 0$, increase in the third grade fluid parameter Γ decreases the heat flux at the surface and the corresponding local Nusselt numbers, while for the other values of the Weissenberg number We, increase in the third grade fluid parameter Γ also increases the heat flux at the surface.
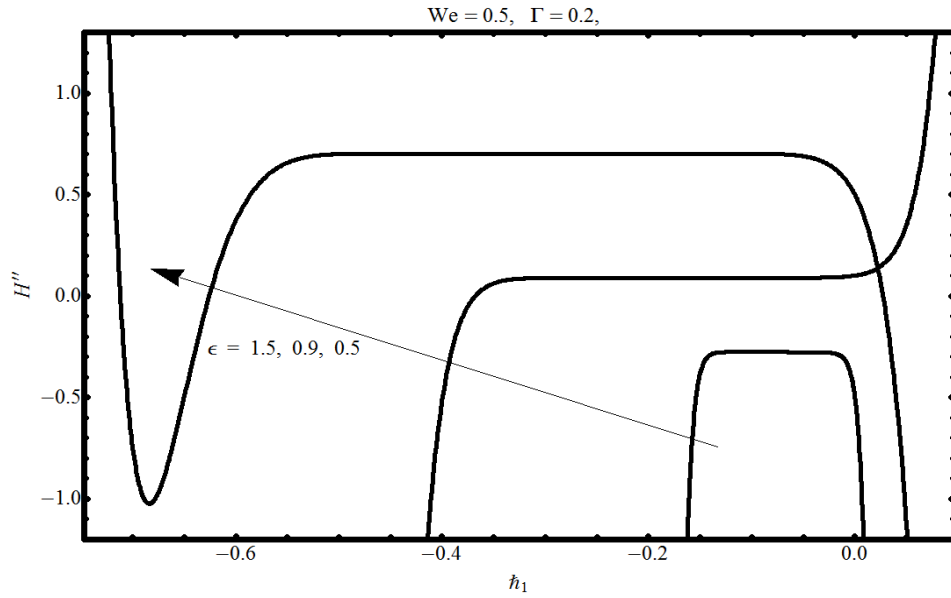
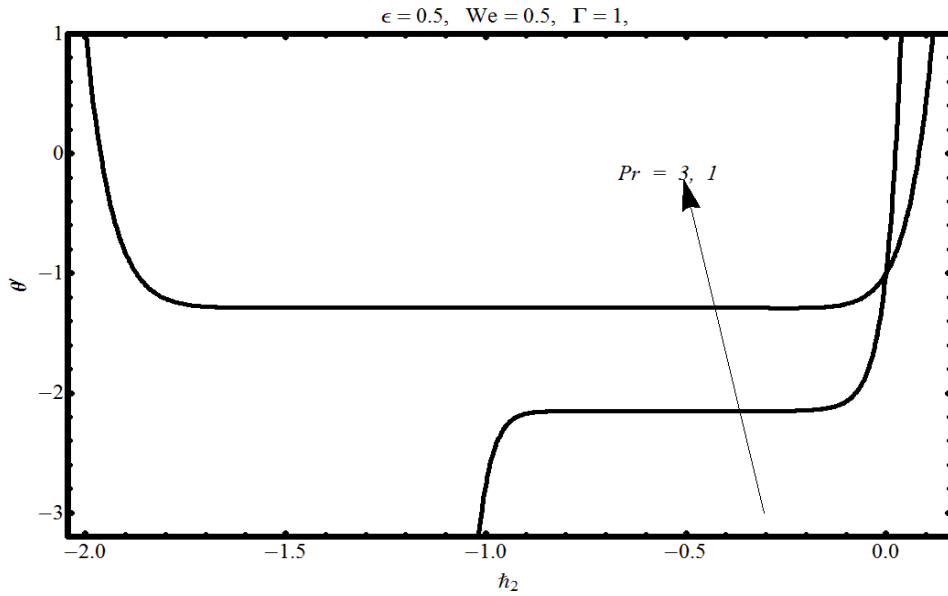$Fig.\,(10.1)$. $\hbar$-curves for velocity profile H' for different values of the stretching ratio ϵ

$Fig.\,(10.2)$. $\hbar$-curves for temperature profile θ for different values of the Prandtl number Pr
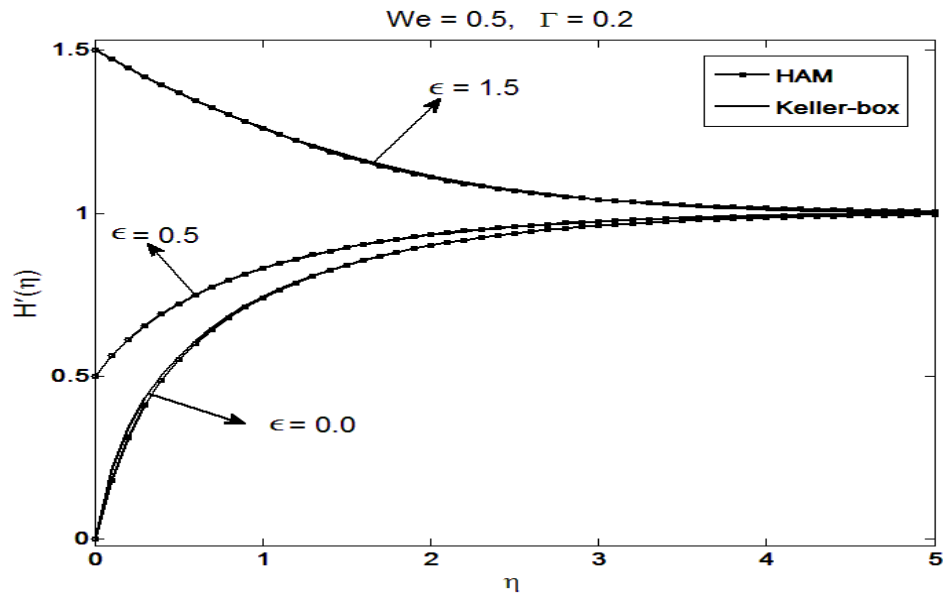
Fig. (10.3). Comparison of numerical and HAM results for different values
of the stretching ratio ϵ over the velocity profile H'
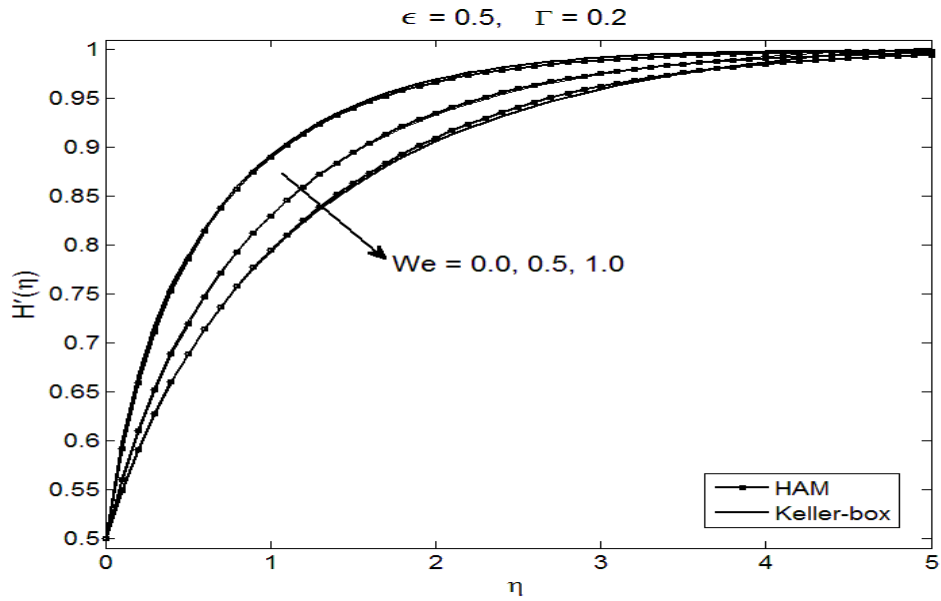

Fig. (10.4). Comparison of numerical and HAM results for different values
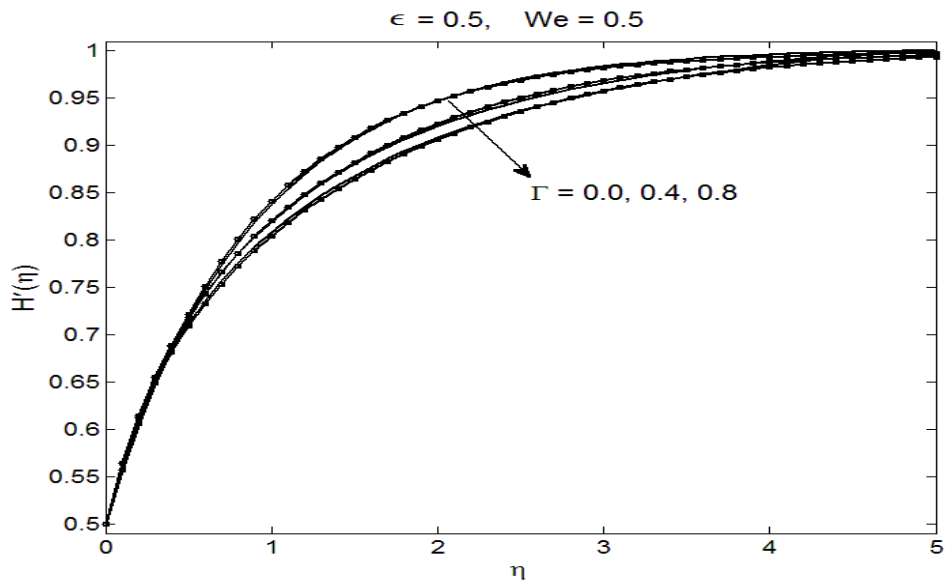of the Weissenberg number We over the velocity profile H'

Fig. (10.5). Comparison of numerical and HAM results for different values of the third grade fluid parameter Γ over the velocity profile H'
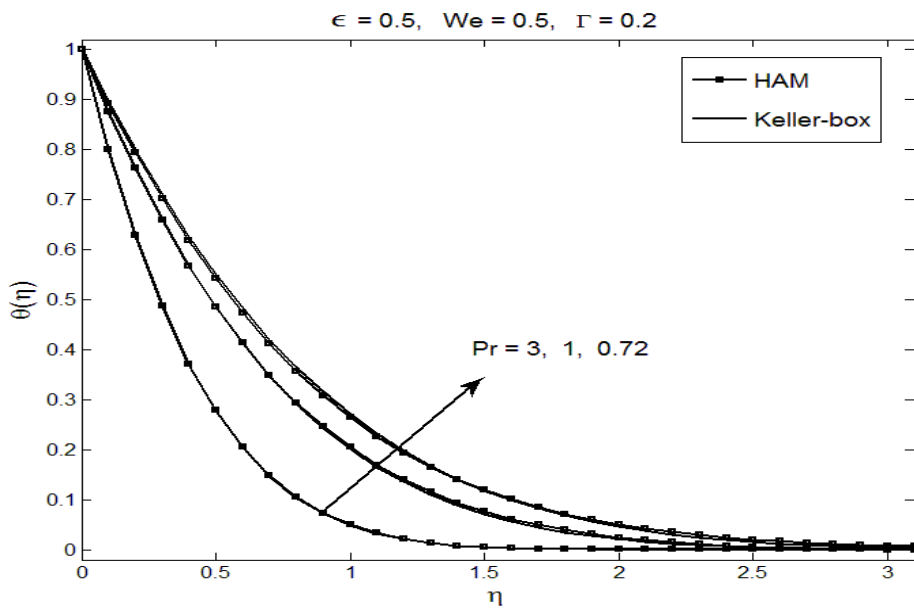

Fig. (10.6). Comparison of numerical and HAM results for different values of the Prandtl number Pr over the temperature profile θ
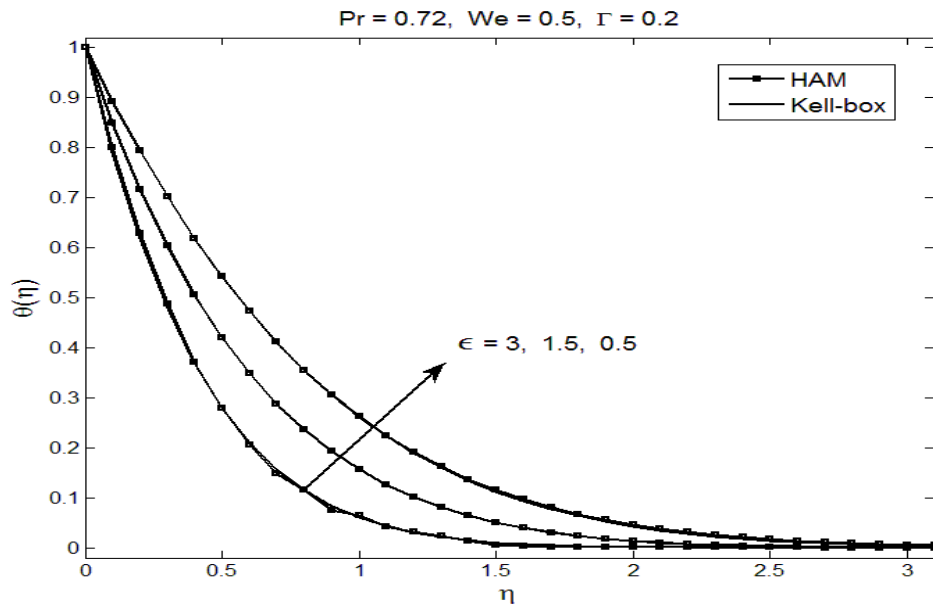
$Fig.\,(10.7)$. Comparison of numerical and HAM results for different values of the stretching ratio ϵ over the temperature profile θ
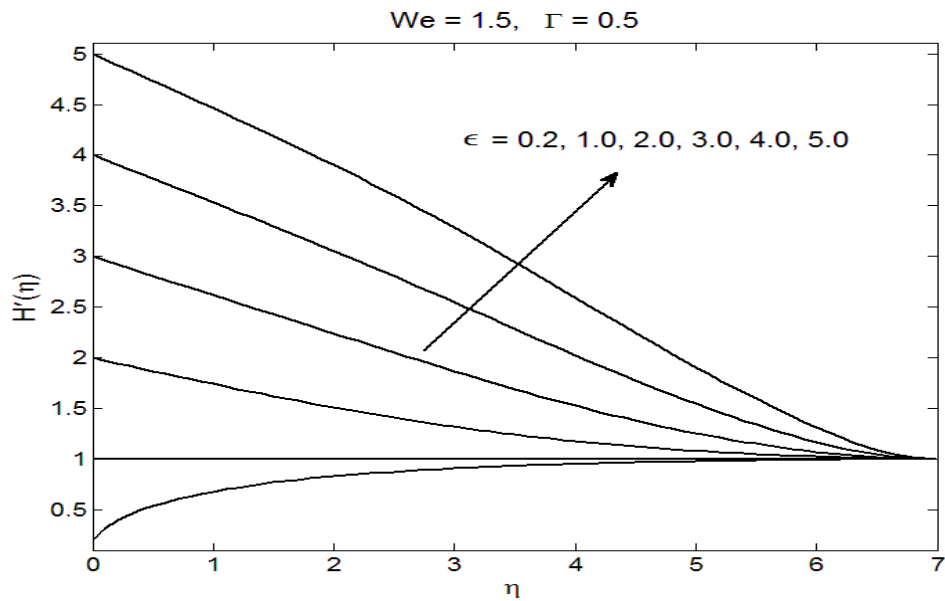
$Fig.\,(10.8)$. Influence of the stretching ratio ϵ over the velocity profile H'
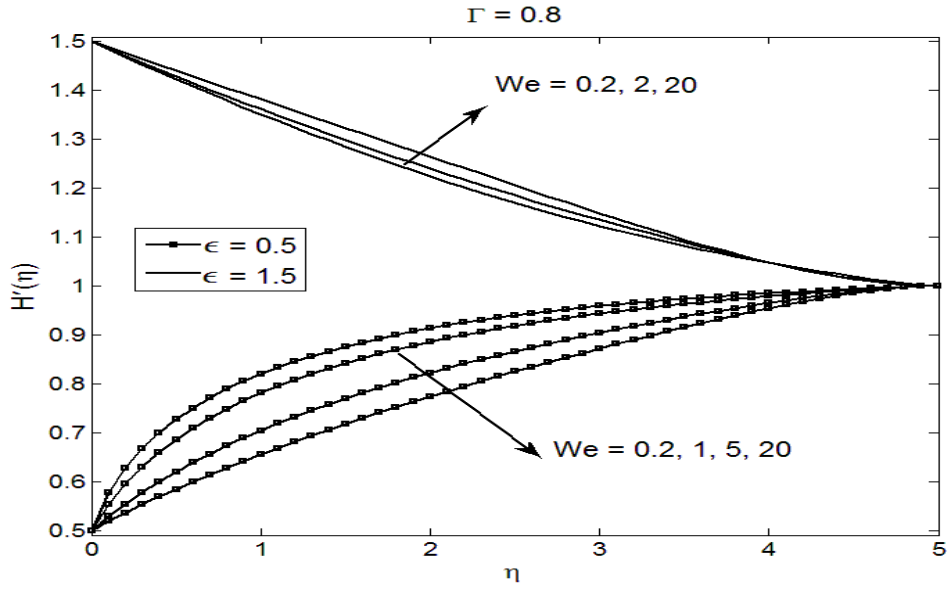
$Fig.$ (10.9). Influence of the Weissenberg number We over the velocity profile H' for different values of the stretching ratio ϵ

$Fig.$ (10.10). Influence of the third grade fluid parameter Γ over the velocity profile H' for different values of the stretching ratio ϵ

$Fig.\,(10.11)$. Influence of the Prandtl number Pr over the temperature

profile θ

$Fig.\,(10.12)$. Influence of the stretching ratio ϵ over the temperature profile

θ

166

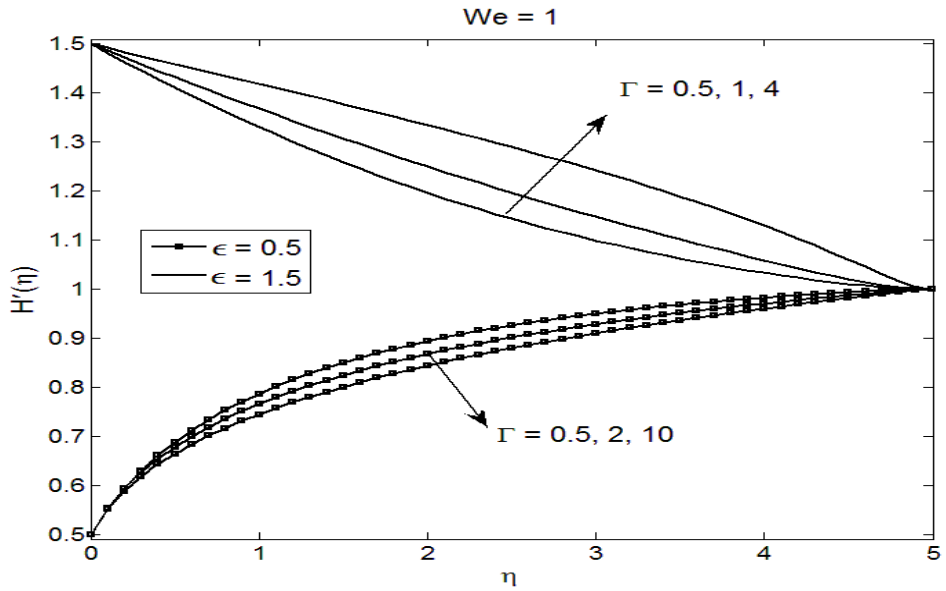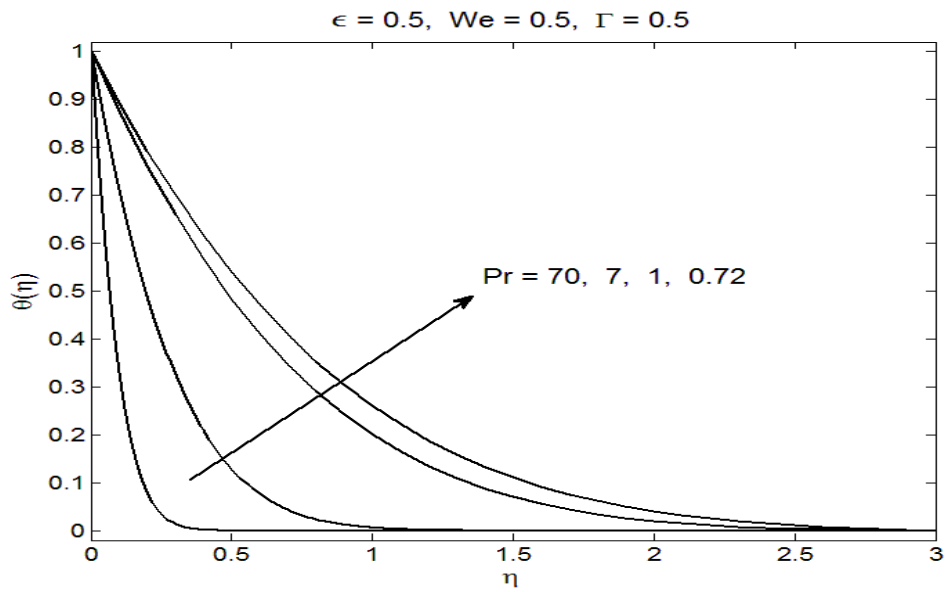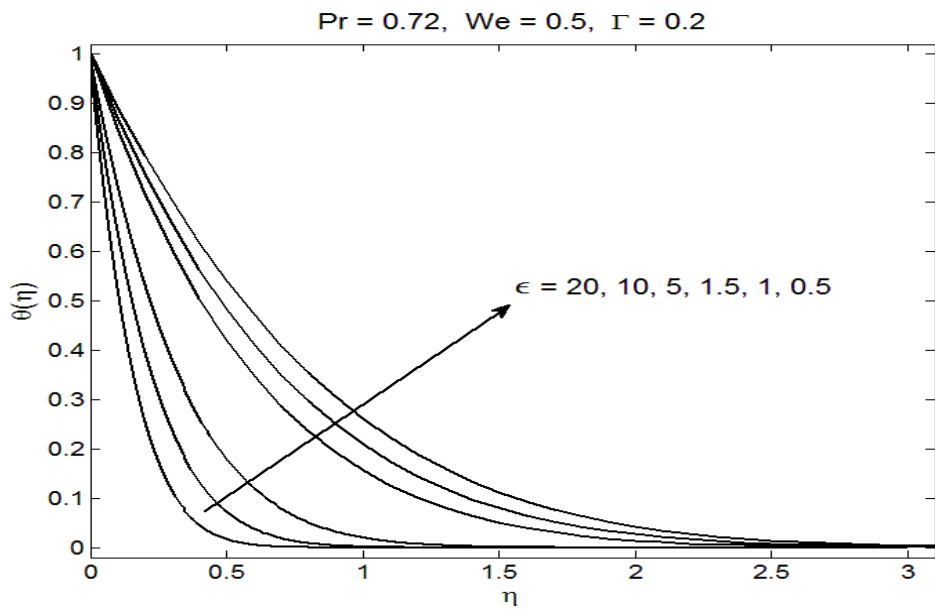|	H''(0)					
	HAM	K-b	HAM	K-b	HAM	K-b
We\ε	0.0		0.5		1.0	
r = 0.0						
0.0	1.6737	1.6737	0.9475	0.9474	0.0207	0.0207
0.5	1.5651	1.5652	0.6141	0.6147	0.0111	0.0111
1.0	1.5084	1.5084	0.4955	0.4955	0.0086	0.0086
10	1.3470	1.3470	0.2710	0.2707	0.0046	0.0046
20	1.3263	1.3263	0.2505	0.2505	0.0010	0.0011
r = 0.5						
0.0	5.1395	5.1394	1.2386	1.2386	0.0074	0.0074
0.5	4.3816	4.3816	0.80472	0.8048	0.0065	0.0066
1.0	4.3726	4.3726	0.6325	0.6325	0.0062	0.0062
10	1.6310	1.6310	0.2957	0.2957	0.0044	0.0044
20	1.4740	1.4739	0.2640	0.2639	0.0042	0.0042
r = 1.0						
0.0	6.8915	6.8915	1.1819	1.1819	0.0057	0.0057
0.5	6.4037	6.4037	0.8699	0.8703	0.0055	0.0055
1.0	6.1075	6.1081	0.7110	0.7111	0.00525	0.0053
10	1.9600	1.9599	0.3193	0.3193	0.0043	0.0043
20	1.6319	1.6319	0.2768	0.2768	0.0041	0.0041

Table. 1. Comparison of behaviour of skin friction coefficient against different

parameters

			-θ'(0)					
			HAM	K-b	HAM	K-b	HAM	K-b
		ε\Pr	0.72		1.0		10	
r = 0.0	*We = 0*	0.5	1.1663	1.1663	1.3475	1.3475	3.9196	3.9196
		1.0	1.3605	1.3605	1.5960	1.5959	5.0597	5.0597
		2.0	1.7040	1.7040	2.0311	2.0311	6.9145	6.9145
	We = .5	0.5	1.1271	1.1272	1.3014	1.3014	3.8242	3.8242
		1.0	1.3595	1.3595	1.5946	1.5946	5.0551	5.0551
		2.0	1.7986	1.7986	2.1367	2.1367	7.0789	7.0789
	We = 1	0.5	1.1149	1.1149	1.2870	1.2869	3.7937	3.7937
		1.0	1.3592	1.3592	1.5943	1.5943	5.0540	5.0540
		2.0	1.8174	1.8174	2.1571	2.1571	7.1072	7.1072
r = 0.5	*We = 0*	0.5	1.1596	1.1596	1.3413	1.3413	3.9460	3.9459
		1.0	1.3590	1.3590	1.5940	1.5940	5.0532	5.0532
		2.0	1.8727	1.8727	1.9835	1.9835	7.1226	7.1226
	We = .5	0.5	1.1399	1.1399	1.3173	1.3173	3.8760	3.8759
		1.0	1.3590	1.3590	1.5939	1.5939	5.0530	5.0529
		2.0	1.8727	1.8727	2.2148	2.2148	7.1771	7.1771
	We = 1	0.5	1.1292	1.1292	1.3044	1.3044	3.8412	3.8412
		1.0	1.3589	1.3589	1.5939	1.5939	5.0527	5.0527
		2.0	1.8707	1.8708	2.2131	2.2131	7.1756	7.1756

Table. 2. comparison of behaviour of Nusselt number against different parameters

10.5   Conclusion

Some important conclusions obtained from the above effort are

- The nondimensional velocity profile H' decreases with the increase in the Weissenberg number We.

- The nondimensional velocity profile H' decreases with the increase in the third grade fluid parameter Γ.

- The nondimensional temperature profile θ decreases with the increase in the Prandtl number Pr.

- The temperature flow rate θ decreases with the increase in the third grade parameter Γ when $\varepsilon < 1$.

- Both the numerical and HAM solutions are in agreement for the velocity and temperature profiles.

- The skinfriction coefficient decreases with incease in the Weissenberg number We.

- The skinfriction coefficient increases with incease in the third grade fluid parameter Γ.

- The local Nusselt number decreases with increase in the Prandtl number Pr, the Weissenberg number We and the third grade fluid parameter Γ.

Chapter 11

Future work

The work presented in this dissertation is focused around the study of stagnation point flows of Newtonian and non-Newtonian fluids flowing through the annular region between two concentric cylinders and fluid flow over exponentially stretching sheets and cylinders. Different techniques are used to obtain results compatible with the available work. Our future interest is to use numerical techniques for solving the problem of fluid flow through the annular region between the concentric cylinders in the limiting case when the radial gap width between the two cylinders approaches to zero. Such minute radial region flow experiencing convective heat transfer would be interesting of engineers in the field of pressure lubricated bearings. Our attention is also towards the study of nanoparticles effect over the boundary layer stagnation point flow of Newtonian and non-Newtonian base fluids flowing over exponentially stretching/shrinking surfaces. More over all the work presented in this thesis is still unexplored for the base fluid model. If we find the properties of different non-Newtonian base fluids then this work will be very useful in many technological applications.

Bibliography

[1] J. D. Anderson, Fundamentals of aerodynamics (3rd ed), McGraw-Hill Series in Aeronautical and Aerospace Eng. (2001)

[2] S. K. Shanmugavelayudam, Numerical modeling of blood flow in human left coronary artery and in vitro study of endothelial cell activation by shear stress, Oklahoma State University, (2009)

[3] G. H. Tang, Y. B. Lu, S. X. Zhang, F. F. Wang, W. Q. Tao, Experimental investigation of non-Newtonian liquid flow in microchannels, J. Non-Newtonian Fluid Mech. (2012) 21-29

[4] L. L. Melton, W. T. Malone, H. Co, Fluid mechanics research and engineering application in non-Newtonian fluid systems, SPE J. 4 (1964) 56-66

[5] N. S. Akbar, T. Hayat, S. Nadeem, A. A. Hendi, Influence of mixed convection on blood flow of Jeffrey fluid through a tapered stenosed artery, Ther. Sci. 17(2) (2013) 533-546

[6] A. W. L. Jay, Viscoelastic properties of the human red blood cell membrane, Bio. J. 3 (1973) 1166-1182

[7] J. D. Humphrey, S. L. Delange, An introduction to biomechanics, Springer (2004)

[8] W. Nichols, M. O'Rourke, C. Vlachopoulos, McDonalds blood flow in arteries: theoretical, experimental and clinical principles (6th ed), Hodder and Stoughton Ltd, (2011)

[9] G. Ooms, C. Vuik, P. Poesio, Core-annular flow through a horizontal pipe: Hydrodynamic counterbalancing of buoyancy force on core, Phy. Fluids, 19 (2007) 092103-17

[10] A. Co, Viscoelastic radial flow between parallel disks, University of Wisconsin–Madison, (1979)

[11] P. W. Carpenter, T. I. Pedley, Flow past highly compliant boundaries and in collapsible tubes, Kluwer Academic Publishers, (2003)

[12] M. Kumari, I. Pop, H. S. Takhar, Free-convection boundary-layer flow of a non-Newtonian fluid along a vertical wavy surface, Int. J. Heat Fluid Flow, 18 (1997) 625-631

[13] F. P. Miller, A. F. Vandome, M. John, Dilatant, VDM Publishing, (2010)

[14] R. P. Chhabra, J. F. Richardson, Non-Newtonian flow and applied rheology engineering applications, Elsevier Ltd, (2008)

[15] K. Hiemenz, Die grenzschicht in einem in dem gleichformingen flussigkeitsstrom einge-tauchten gerade kreiszylinder, Dingler Polytech J. 326 (1911) 321-410

[16] F. Homann, Der einfluss grosser zahighkeit bei der stromung um den zylinder und um die kugel, Z. Angew. Math. Mech. 16 (1936) 153-164

[17] H. A. Attia, On the effectiveness of porosity on stagnation point flow towards a stretching surface with heat generation, Comp. Mat. Sci. 38 (2007) 741-745

[18] S. Nadeem, M. Hussain, M. Naz, MHD stagnation flow of a micropolar fluid through a porous medium, Meccanica 45 (2010) 869-880

[19] T. Fang, W. Jing, Closed-form analytical solutions of flow and heat transfer for an un-steady rear stagnation-point flow, Int. J. Heat Mass Tran. 62 (2013) 55-62

[20] N. Bachok, A. Ishak, I. Pop, The boundary layers of an unsteady stagnation-point flow in a nanofluid, Int. J. Heat Mass Tran. 55 (2012) 6499-6505

[21] H. Schlichting, K. Gersten, Boundary-layer theory, Springer (2000)

[22] H. A. Attia, Steady three-dimensional hydromagnetic stagnation point flow towards a stretching sheet with heat generation, Italian J. Pure App. Math. 27 (2010) 9-18

[23] P. D. Weidman, M. A. Sprague, Flows induced by a plate moving normal to stagnation-point flow, Acta Mech, DOI 10.1007/s00707-011-0458-2

[24] A. Borrelli, G. Giantesio, M. C. Patria, MHD oblique stagnation-point flow of a micropolar fluid, App. Math. Mod. 36 (2012) 3949-3970

[25] B. Zinn, Y. Neumeier, J. Seitzman, J. Jagoda, Y. Weksler, Stagnation point reverse flow combustor, Patent App. Pub. (2005)

[26] J. Crane, Y. Neumeier, J. Jagoda, J. Seitzman, B. T. Zinn, Stagnation-point reverse-flow combustor performance with liquid fuel injection, ASME, (2006) 1-10

[27] A. Mastroberardino, Series solutions of annular axisymmetric stagnation flow and heat transfer on moving cylinder, App. Math. Mech. DOI 10.1007/s10483-013-1726-7

[28] S. Munawar, A. Mehmood, A. Ali, Time-dependent stagnation-point flow over rotating disk impinging oncoming flow, Appl. Math. Mech. -Engl. Ed., 34(1) (2013) 85-96

[29] C. Y. Wang, Axisymmetric stagnation flow towards a moving plate, A. I. Ch. E. Journal, 19 (1973) 1080-1087

[30] T. J. Craft, S. E. Gant, H. Iacovides, B. E. Launder, Development and application of a new wall function for complex turbulent flows, European congress on computational methods in applied sciences and engineering ECCOMAS Computational Fluid Dynamics Conference (2001)

[31] C. Y. Wang, Stagnation slip flow and heat transfer on a moving plate, Che. Eng. Sci. 61 (2006) 7668-7672

[32] M. Renardy, Viscoelastic stagnation point flow in a wake, J. Non-Newtonian Fluid Mech. 138 (2006) 206-208

[33] P. D. Weidman, Mohamed E. Ali, Aligned and nonaligned radial stagnation flow on a stretching cylinder, Eur. J. Mech. B/Fluids 30 (2011) 120-128

[34] L. Hong, C. Y. Wang, Annular axisymmetric stagnation flow on a moving cylinder, Int. J. Eng. Sci. 47 (2009) 141-152

172

[35] A. Ishak, R. Nazar, I. Pop, The effects of transpiration on the boundary layer flow and heat transfer over a vertical slender cylinder, Int. J. Non-Linear Mech. 42 (2007) 1010-1017

[36] C. Y. Wang, Stagnation flow on a plate with anisotropic slip, Eur. J. Mech. B/Fluids 38 (2013) 73-77

[37] Y. Y. Lok, N. Amin, I. Pop, Unsteady mixed convection flow of a micropolar fluid near the stagnation point on a vertical surface, Int. J. Ther. Sci. 45 (2006) 1149-1157

[38] S. Nadeem, Abdul Rehman, Axisymmetric stagnation flow of a nanofluid in a moving cylinder, Comp. Math. Mod. 24(2) (2013) 293-306

[39] S. Wei. Wong, M. Abu O. Awang, A. Ishak, Stagnation-point flow over an exponentially shrinking/stretching sheet, ZNa, 66a (2011) 705-711

[40] M. J. Martin, I. D. Boyd, Falkner–Skan flow over a wedge with slip boundary conditions, J. Ther. Heat Tran. 24(2) (2010) 263-270

[41] J. Zhu, L. Zheng, X. Zhang, Homotopy analysis method for hydromagnetic plane and axisymmetric stagnation-point flow with velocity slip, World Academy Sci. Eng. Tech. 39 (2010) 151-155

[42] S Nadeem, Abdul Rehman, Mohamed E Ali, The boundary layer flow and heat transfer of a nanofluid over a vertical slender cylinder, Proceedings of the Institution of Mechanical Engineers, Part N: J. Nanoeng. Nanosys. (2012) 165-173

[43] Abdul Rehman, S. Nadeem, Mixed convection heat transfer in micropolar nanofluid over a vertical slender cylinder, Chin. Phys. Lett. 29(12) (2012) 124701-5

[44] S. Nadeem, Abdul Rehman, C. Lee, J. Lee, Boundary layer flow of second grade fluid in a cylinder with heat transfer, Math. Prob. Eng. doi:10.1155/2012/640289

[45] L. J. Crane, Flow past a stretching plane, J. Appl. Math. Phys. 21 (1970) 645-647

[46] C. Y. Wang, Stagnation flow towards a shrinking sheet, Int. J. Non-Linear Mech. 43 (2008) 377-382

[47] O. D. Makinde, A. Aziz, Boundary layer flow of a nanofluid past a stretching sheet with a convective boundary condition, Int. J. Ther. Sci. 50 (2011) 1326-1332

[48] T. Fang, S. Yao, Viscous swirling flow over a stretching cylinder, Chin. Phys. Lett. 28(11) (2011) 114702-4

[49] N. Bachok, A. Ishak, Flow and heat transfer over a stretching cylinder with prescribed surface heat flux, Mala. J. Math. Sci. 4(2) (2010) 159-169

[50] T. Altan, H. Gegel, Metal forming fundamentals and applications. Metals Park, OH: American Society of Metals; (1979)

[51] Z. Tadmor, I. Klein, Engineering principles of plasticating extrusion. Polymer science and engineering series. New York: Van Nostrand Reinhold; (1970)

[52] T. C. Chiam, Heat transfer with variable conductivity in a stagnation-point flow towards a stretching sheet, Int. Comm. Heat Mass Tran. 23(2) (1996) 239-248

[53] A. Ishak, K. Jafar, R. Nazar, I. Pop, MHD stagnation point flow towards a stretching sheet, Physica A, 388 (2009) 3377-3383

[54] P. D. Weidman, E. Magyari, Generalized Crane flow induced by continuous surfaces stretching with arbitrary velocities, Acta Mech 209 (2010) 353-362

[55] B. Bidin, R. Nazar, Numerical solution of the boundary layer flow over an exponentially stretching sheet with thermal radiation, Euro. J. Scientific Res. 33(4) (2009) 710-717

[56] S. W. Wong, Md. A. O. Awang, A. Ishak, Stagnation-point flow over an exponentially shrinking/stretching sheet, Z. Naturforsch. 66a (2011) 705-711

[57] K. Bhattacharyya, K. Vajravelu, Stagnation-point flow and heat transfer over an exponentially shrinking sheet, Commun. Nonlinear Sci. Numer. Simulat. 17 (2012) 2728-2734

[58] S. Nadeem, C. Lee, Boundary layer flow of nanofluid over an exponentially stretching surface, Nanoscale Res. Lett. 7 (2012) 94

[59] Abdul Rehman, S. Nadeem, M. Y. Malik, Stagnation flow of couple stress nanofluid over an exponentially stretching sheet through a porous medium, J. Power Tech. 93(2) (2013) 1-11

[60] R. N. Jat, G. Chand, MHD flow and heat transfer over an exponentially stretching sheet with viscous dissipation and radiation effects, App. Math. Sci. 7(4) (2013) 167-180

[61] E. M. A. Elbashbeshy, T. G. Emam, K. M. Abdelgaber, Effects of thermal radiation and magnetic field on unsteady mixed convection flow and heat transfer over an exponentially stretching surface with suction in the presence of internal heat generation/absorption, J. Egyp. Math. Soci. 20 (2012) 215-222

[62] A. Ishak, MHD boundary layer flow due to an exponentially stretching sheet with radiation effect, Sains Malaysiana 40(4) (2011) 391-395

[63] S. Pramanik, Casson fluid flow and heat transfer past an exponentially porous stretching surface in presence of thermal radiation, Ain Shams Eng. J. (2013) pp 8

[64] K. Bhattacharyya, Steady boundary layer flow and reactive mass transfer past an exponentially stretching surface in an exponentially moving free stream, J. Egyp. Math. Soci. 20 (2012) 223-228

[65] K. Bhattacharyya, Boundary layer flow and heat transfer over an exponentially shrinking sheet, Chin. Phys. Lett. 28(7) (2011) 074701-4

[66] U. S. Choi, Enhancing thermal conductivity of fluids with nanoparticles, In: D. A. Siginer and H. P. Wang, (eds) Developments and applications of non-Newtonian flows, ASME FED-Vol. 231/ MD-Vol-66 (1995) 99-105

[67] P. Keblinski, J. A. Eastman, D. G. Cahill, Nanofluids for thermal transport, Review Feature, (2005) 36-44

[68] X. Wang, X. Xu, S. U. S. Choi, Thermal conductivity of nanoparticle-fluid mixture, J. Ther. Heat Tran. 13(4) (1999) 474-480

[69] A. C. Eringen, Simple microfluids, Int. J. Eng. Sci. 2 (1964) 205-217

[70] A. C. Eringen, Theory of micropolar fluids, J. Math. Mech. 16 (1966) 1-18

[71] G. Lukaszewicz, Micropolar Fluids: Theory and Applications, Braun-Brumfield, Inc. Ann, Arbor, Mi (1999)

[72] G. Łukaszewicz, Asymptotic behavior of micropolar fluid flows, Int. J. Eng. Sci. 41 (2003) 259-269

[73] I. Dapra, G. Scarpi, Perturbation solution for pulsatile flow of a non-Newtonian Williamson fluid in a rock fracture, Int. J. Rock Mech. Mining Sci. 44(2) (2007) 271-278

[74] S. Nadeem, S. Akram, Influence of inclined magnetic field on peristaltic flow of a Williamson fluid model in an inclined symmetric or asymmetric channel, Math. Comp. Mod. 52 (2010) 107-119

[75] N. Casson, In rheology of dispersed system, Pergamon Press, Oxford (1959)

[76] W. P. Walwander, T. Y. Chen, D. F. Cala, Biorheology, (1975)

[77] G. V. Vinogradov, A. Y. Malkin, Rheology of Polymers, Mir Publisher, Moscow (1979)

[78] Jaw-Ren Lin, Squeeze film characteristics of finite journal bearings: couple stress fluid model, Tribology Int. 31(4) (1998) 201-207

[79] S. Maiti, J. C. Misra, Peristaltic Transport of a Couple Stress Fluid : Some Applications to Hemodynamics, Phy. Fluid Dyn. (2012) 1-27

[80] D. S. Chauhan, V. Kumar, Unsteady flow of a non-Newtonian second grade fluid in a channel partially filled by a porous medium, Adv. App. Sci. Res. 3(1) (2012) 75-94

[81] K. R. Rajagopal, A. S. Gupta, Flow and stability of a second grade fluid between two parallel plates rotating about noncoincdent axes, Int. J. Eng. Sci. 19(11) (1981) 14O1-1409

[82] S. Baris, Steady three-dimensional flow of a second grade fluid towards a stagnation point at a moving flat plate, Tur. J. Eng. Env. Sci. 27 (2003) 21-29

[83] M. R. Mohyuddin, E. E. Ashraf, On stokes problem for a third-grade fluid for generalized fractional model, Quar. Sci. Vis. 19 (2003) 51-55

[84] K. R. Rajagopal, Viscometric flows of third grade fluids, Mech. Res. Comm. 7(1) (1980) 21-25

[85] A. V. Busuioc, D. Iftimie, M. Paicu, On steady third grade fluids equations, Nonlinearity 21 (2008) 1621-1635

[86] Sj. Liao, Homotopy Analysis Method in Nonlinear Differential Equations, Higher Education Press, Beijing and Springer-Verlag Berlin Heidelberg (2012)

[87] Sj. Liao, Beyond perturbation: introduction to the homotopy analysis method, Chapman & Hall/CRC Press, Boca Raton (2003)

[88] Sj. Liao, On the homotopy multiple-variable method and its applications in the interactions of nonlinear gravity waves, Commun. Nonlinear Sci. Numer. Simulat. 16 (2011) 1274-1303

[89] S. Abbasbandy, The application of homotopy analysis method to nonlinear equations arising in heat transfer, Phy. Lett. 360(1) (2006) 109-113

[90] S. Abbasbandy, Homotopy analysis method for heat radiation equations, Int. Commun. Heat Mass Tran. 34(3) (2007) 380-387

[91] S. Abbasbandy, Y. Tan, S. J. Liao, Newton-homotopy analysis method for nonlinear equations, App. Math. Comp. 188(2) (2007) 1794-1800

[92] M. Turkyilmazoglu, A note on the homotopy analysis method, App. Math. Lett. 23 (2010) 1226-1230

[93] J. I. Ramos, Piecewise homotopy methods for nonlinear ordinary differential equations, App. Math. Comp. 198 (2008) 92-116

[94] T. Y. Na, Computational methods in engineering boundary value problems, Academic press (1979)

[95] H. B. Keller, T. Cebeci, Accurate numerical methods for boundary-layer flows. II: Two-dimensional flows, AIAA Journal 10 (1972) 1193-1199

[96] H. B. Keller, Numerical methods in boundary layer theory, Annu. Rev. Fluid Mech. 10 (1978) 417-433

[97] C. F. Mayo, Implementation of the Runge-Kutta-Fehlberg method for solution of ordinary differential equations on a parallel processor, Defense Tech. Infor. Center, (1987)

[98] J. D. Lambert, Computational methods in ordinary differential equations, Wiley (1973)

[99] E. Hairer, G. Wanner, Solving ordinary differential equations: Stiff and differential-algebraic problems, Springer (1991)

[100] P. Smith, Nonlinear ordinary differential equations: An introduction to dynamical systems, Oxford University Press (1999)